



The University of
Nottingham

UNITED KINGDOM • CHINA • MALAYSIA

A Non-coaxial Theory of Plasticity for Soils with An Anisotropic Yield Criterion

by

Ran Yuan BEng, MSc

Thesis submitted to the University of Nottingham for
the degree of Doctor of Philosophy

June 2015

Dedication

I would like to dedicate this thesis to my loving parents.

Abstract

A novel, non-coaxial soil model is developed in the context of perfect plasticity for the plane strain condition whilst incorporating initial soil strength anisotropy. The anisotropic yield criterion is developed by generalising the conventional isotropic Mohr-Coulomb yield criterion to account for the effects of initial soil strength anisotropy described by the variation of internal friction angles at different principal stress directions. The model is implemented into the commercial finite element (FE) software ABAQUS via the user defined material subroutine (UMAT).

The proposed model is used to predict material non-coaxiality in simple shear tests. The non-coincidence of the directions of principal stresses and plastic strain rates can be reproduced. A faster rate of approaching coaxiality is observed when soil yield anisotropy is presented when compared to the model with an isotropic yield criterion.

A semi-analytical solution of the bearing capacity for a smooth strip footing resting on an anisotropic, weightless, cohesive-frictional soil is developed based on the slip line method. A good match of the bearing capacity can be obtained between numerical and semi-analytical results. The results show that the vertical load at plastic collapse of a strip footing resting on an anisotropic soil is lower than that on an isotropic soil. The settlement prior to collapse is larger when the non-coaxial assumption is involved; however, no significant impacts can be observed on the ultimate failure load.

In addition, the non-coaxial soil model is applied to investigate tunnelling induced displacement. The results are compared with the results from the centrifuge tests performed by Zhou (2015). For equal volume loss, the normalised settlement trough can be improved by adopting the soil anisotropic parameter β as compared to the experimental results. The maximum settlement is larger in light of larger non-coaxial

coefficient for the same degree of the stress reduction.

The cross-section of the anisotropic yield criterion developed is a rotational ellipse. Other types of the ellipse are possible. In addition, for simplicity we only consider the effect of initial anisotropy without considering induced anisotropy, and only the simple case of perfect plasticity is investigated. It is suggested that in order to capture the soil behaviours under more complex stress paths, the non-linear and anisotropic elasticity should be associated with the current model, and the development of hardening/softening rules is worth investigating.

Acknowledgments

The research presented in this thesis was carried out at the University of Nottingham during the period of November 2010 to October 2014. No doubt, this result would only be achieved with the support of many individuals and numerous organisations to whom I would like to express my sincere gratitude.

First and foremost, to my supervisor Prof. Hai-sui Yu: I experienced the freedom I needed to be creative while at the same time I gained constant guidance and assistance when I met with difficulties. His enthusiasm and professional attitude towards both academic and personal aspects encouraged me to always carry on with the project. Most grateful I am to him knowing that the period of my PhD study will be of great profit for my future professional life. My deepest gratitude also extends to Dr. Xia Li. As my PhD internal examiner, she always helped me to build up confidence during regular meetings and provided me with useful tips at the beginning of the project.

Moreover, to my colleagues in NCG: Thank you for being such a good team. I have always enjoyed working and having a good time with you. Particular appreciation should go to Mr. Nian Hu and Dr. Juan Wang, with whom I had valuable discussions on my project.

Special thanks should go to the financial support from the University of Nottingham International Research Excellence Scholarship, which was greatly appreciated.

Finally, but most importantly, to my parents: Mum and Dad, you are always on my side. Without your unconditional support and love, I could not have gotten through this tough but wonderful period of my life.

Table of Contents

Dedication	i
Abstract	iii
Acknowledgments	v
Table of Contents	vii
List of Figures	xi
List of Tables	xix
Nomenclature	xxi
1 Introduction	1
1.1 Overview	1
1.2 Aims and Objectives	2
1.3 Structure of the thesis	3
2 Literature Review	5
2.1 Introduction	5
2.2 Soil anisotropy	6
2.2.1 Inherent anisotropy	6
2.2.2 Induced anisotropy	8
2.3 Anisotropic plasticity theory	10
2.4 Experiment investigations and DEM modelling of non-coaxiality	12
2.5 Non-coaxial plasticity theories	17
2.5.1 Li and Dafalias (2004)	18
2.5.2 Tsutsumi and Hashiguchi (2005)	19

2.5.3	Yu (2008)	20
2.5.4	Comments on current constitutive models	27
2.6	Chapter Summary	28
3	Formulation and numerical implementation of the non-coaxial soil model	31
3.1	Introduction	31
3.2	Constitutive equations of the non-coaxial model	32
3.2.1	Development of the anisotropic Mohr-Coulomb yield criterion	33
3.2.2	Discussion of the type of the ellipse	37
3.2.3	Validation of the anisotropic yield criterion with experimental data	38
3.2.4	Non-coaxial plastic flow rule	39
3.2.5	Stress-strain relationship in the incremental form	44
3.2.6	Summary of the parameters	44
3.3	Numerical implementation of the non-coaxial model	45
3.3.1	The FE computational software: ABAQUS	45
3.3.2	A hyperbolic anisotropic Mohr-Coulomb yield function	46
3.3.3	Numerical integration scheme	48
3.4	Prediction of material non-coaxiality in simple shear tests	58
3.4.1	Model and parameters	62
3.4.2	Results and discussion	64
3.5	Chapter Summary	76
4	Analysis of smooth strip footing problems	81
4.1	Introduction	81
4.1.1	General study of footings	81
4.1.2	Chapter structure	83
4.2	Semi-analytical solutions for a weightless frictional-cohesive soil based on the slip line method	83
4.2.1	Governing equations of stresses	83
4.2.2	Stress boundary conditions	87
4.2.3	Ultimate vertical pressure for a strip footing resting on an anisotropic weightless cohesive-frictional soil	89
4.2.4	Special cases	91

4.2.5	Close-form solutions for a particular case of a purely cohesive material	92
4.2.6	Parametric study of semi-analytical solutions	94
4.2.7	Restrictions of the proposed solutions	97
4.3	Numerical verification of the non-coaxial model with semi-analytical solutions	98
4.3.1	Model and parameters	98
4.3.2	Verification with semi-analytical solutions	100
4.3.3	Results and discussion	108
4.4	Chapter Summary	126
5	Applications of the non-coaxial model in tunnelling	127
5.1	Introduction	127
5.1.1	Tunnelling induced ground deformations	127
5.1.2	Lining forces	129
5.1.3	Installation procedures associated with 2D tunnelling	130
5.1.4	Numerical difficulties of modelling subsurface settlement troughs 133	
5.1.5	Chapter structure	135
5.2	Model and parameters	135
5.3	Stiffness reduction method	137
5.3.1	Subsurface settlements	138
5.3.2	Horizontal displacement	140
5.4	Stress reduction method	141
5.4.1	Subsurface settlements	141
5.4.2	Horizontal displacement	142
5.5	Discussion	143
5.6	Case study compared with centrifuge tests	145
5.6.1	Assumption	145
5.6.2	Volume loss	147
5.6.3	Subsurface settlement troughs	148
5.7	Chapter Summary	157

6	Conclusions and recommendations for future work	159
6.1	Conclusions	160
6.1.1	On simple shear problems	160
6.1.2	On strip footing problems	162
6.1.3	On tunnelling	164
6.2	Recommendations for further work	166
Appendix 1		169
A.1	Eccentric ellipse	169
A.1.1	Numerical results on simple shear tests with an eccentric ellipse yield criterion	171
A.2	Strip footings	176
A.2.1	Calculations of m for Rotational ellipse	176
A.2.2	Calculations of m for Eccentric ellipse	177
A.2.3	Close-form solutions for a rotational ellipse anisotropic Mohr–Coulomb yield criterion	179
A.2.4	Semi-analytical solutions for an eccentric ellipse anisotropic Mohr-Coulomb yield criterion	181
A.2.5	Close form solutions for a purely cohesive soil with the eccentric ellipse yield criterion	182
A.2.6	Parametric study	183
A.2.7	Validation of numerical results and analytical results	184
A.2.8	pressure-displacement curve	186
A.2.9	velocity field	186
References		202

List of Figures

2.1	Major principal stress and strain rate orientations with $\eta_0 = 0.2$ (Ai et al., 2014).	13
2.2	Unit plastic strain increment vectors superimposed on the stress path for: (a) monotonic loading; (b) pure rotation; (c) combined loading (after Gutierrez et al., 1991).	15
2.3	Stress and strain increment directions of : (a) the initial anisotropic sample; (b) the preloaded sample (Li and Yu, 2009).	16
2.4	Mohr-Coulomb yield surface and plastic potential (Yu and Yuan, 2006). 22	
2.5	Numerical results of principal directions of stress and plastic strain rate for $\phi = 35^\circ$, $\psi = 0^\circ$ and $K_0 = 0.43$ (Yu and Yuan, 2006): (a) $\Lambda = 0.00$; (b) $\Lambda = 0.05$	24
2.6	Numerical results of principal directions of stress and plastic strain rate for $\phi = 35^\circ$, $\psi = 0^\circ$ and $K_0 = 3.0$ (Yu and Yuan, 2006): (a) $\Lambda = 0.00$; (b) $\Lambda = 0.05$	25
2.7	The non-coaxial plastic flow rule (after Rudnicki and Rice, 1975).	25
2.8	Results of the coaxial and non-coaxial predictions with perfect plasticity, $K_0 = 0.4$; (a) shear stress ratio; (b) orientations of the principal stress and principal plastic strain rate (after Yang and Yu, 2006 <i>b</i>).	26
2.9	Results of the coaxial and non-coaxial predictions with perfect plasticity, $K_0 = 3.0$; (a) shear stress ratio; (b) orientations of the principal stress and principal plastic strain rate (after Yang and Yu, 2006 <i>b</i>).	27
3.1	Definition of stress orientation angle.	34
3.2	The ellipse anisotropic Mohr-Coulomb yield surface in: a) (X,Y,Z) space; b) (Z,Y) space.	35

3.3	Validation with results of triaxial compression tests carried out by Oda et al. (1978) when: a) $\sigma_3 = 49$ kPa; b) $\sigma_3 = 196$ kPa.	39
3.4	Validation with results of laboratory monotonic loading tests carried out by Yang (2013) when: a) $b = 0.2$; b) $b = 0.4$	39
3.5	The non-coaxial plastic flow rule in: a) $(\frac{\sigma_x - \sigma_y}{2}, \sigma_{xy}, \frac{\sigma_x + \sigma_y}{2})$ space; b) $(\frac{\sigma_x - \sigma_y}{2}, \sigma_{xy})$ space.	40
3.6	The illustration of plastic potential when the nonassociativity is used in: a) $((\sigma_x - \sigma_y)/2, \sigma_{xy}, (\sigma_x + \sigma_y)/2)$; b) $((\sigma_x - \sigma_y)/2, \sigma_{xy})$ space. . .	41
3.7	a) Hyperbolic approximation of the anisotropic Mohr-Coulomb yield curve; b) Parametric study of a	47
3.8	Yield surface intersection: Elastic to plastic transition.	50
3.9	The illustration of the negative plastic multiplier.	53
3.10	Flow chart of the explicit modified Euler algorithm.	59
3.11	Definitions of directions of the principal stress and principal plastic strain rate.	60
3.12	Experimental results showing orientations of principal stress and plastic strain rate (after Roscoe et al., 1967): a) $\sigma_y = 135$ kPa; b) $\sigma_y = 396$ kPa. 62	
3.13	The influence of anisotropic coefficients on the predicted shear stress ratio : a) associativity; b) nonassociativity.	65
3.14	The influence of non-coaxiality on the predicted shear stress ratio with $K_0 = 0.5$ in: a) Test 1; b) Test 2.	67
3.15	The influence of non-coaxiality on the predicted shear stress ratio with $K_0 = 2.0$ in: a) Test 1; b) Test 2.	67
3.16	The influence of non-coaxiality on the predicted shear stress ratio with $K_0 = 0.5$ in: a) Test 7; b) Test 8.	68
3.17	The influence of non-coaxiality on the predicted shear stress ratio with $K_0 = 2.0$ in: a) Test 7; b) Test 8.	69
3.18	The influence of non-coaxiality on the predicted shear stress ratio with $K_0 = 0.5$ in: a) Test 11; b) Test 12.	69
3.19	The influence of non-coaxiality on the predicted shear stress ratio with $K_0 = 2.0$: a) Test 11; b) Test 12.	70

3.20	Numerical results of principal orientations of stress and plastic strain increment for the recovered isotropic Mohr-Coulomb yield condition in Test 1 : a) $k = 0.0$; b) $k = 0.02$	71
3.21	Numerical results of principal orientations of stress and plastic strain increment for the recovered isotropic Mohr-Coulomb yield condition in Test 2 : a) $k = 0.0$; b) $k = 0.02$	72
3.22	Numerical results of principal orientations of stress and plastic strain increment in Test 7 : a) $k = 0.0$; b) $k = 0.02$	72
3.23	Numerical results of principal orientations of stress and plastic strain increment in Test 8 : a) $k = 0.0$; b) $k = 0.02$	73
3.24	Numerical results of principal orientations of stress and plastic strain increment in Test 10 : a) $k = 0.0$; b) $k = 0.02$	73
3.25	Numerical results of principal orientations of stress and plastic strain increment in Test 11 : a) $k = 0.0$; b) $k = 0.02$	74
3.26	Numerical results of principal orientations of stress and plastic strain increment in Test 12 : a) $k = 0.0$; b) $k = 0.02$; c) $k = 0.05$	75
3.27	Stress path for the recovered isotropic Mohr-Coulomb yield surface in: a) Test 1; b) Test 2.	77
3.28	Stress path for the case when $n = 0.707$, $\beta = 45^\circ$ in : a) Test 7; b) Test 8.	77
3.29	Stress path for the case when $n = 0.707$, $\beta = 0^\circ$ in: a) Test 11; b) Test 12.	78
4.1	The coordinate system and stress characteristics for anisotropic plasticity (Yu, 2006).	84
4.2	a) Stress state at failure; b) anisotropic yield curve in $(\frac{\sigma_x - \sigma_y}{2}, \sigma_{xy})$ space.	86
4.3	The stress conditions on a boundary.	88
4.4	The stress conditions on a boundary.	88
4.5	Plastic stress field of strip footing with surcharge on OB	90
4.6	The influence of the anisotropic coefficient on the bearing capacity factor N_c with various friction angles : a) n ; b) β ($n = 0.707$).	95
4.7	The influence of the anisotropic coefficient on the bearing capacity factor N_q with various friction angles: a) n ; b) β ($n = 0.707$).	96

4.8	The bearing capacity factors versus β with different values of n : a) N_c ; b) N_q	96
4.9	Geometry and finite element discretization of the strip footing.	99
4.10	Bearing capacity factor N_c versus various friction angles: a) Test 1; b) Test 2.	102
4.11	Bearing capacity factor N_c versus various friction angles: a) Test 3; b) Test 4; c) Test 5.	102
4.12	Ultimate failure pressure normalised by surface surcharge (q_t/q) versus various friction angles: a) Test 1; b) Test 2.	103
4.13	Ultimate failure pressure normalised by surface surcharge (q_t/q) versus various friction angles : a) Test 3; b) Test 4; c) Test 5.	104
4.14	Load displacement curve of bearing capacity factor N_c in Test 1.	105
4.15	Load displacement curve of bearing capacity factor N_c in Test 3.	106
4.16	Load displacement curve of ultimate failure pressure normalised by surface surcharge q_t/q in Test 1.	106
4.17	Load displacement curve of ultimate failure pressure normalised by surface surcharge q_t/q in Test 3.	107
4.18	The velocity field for the case of isotropic Mohr-Coulomb yield criterion.	107
4.19	The velocity field when $n = 0.707$, $\beta = 45^\circ$	108
4.20	Load displacement curve of bearing capacity N_c in Test 8.	109
4.21	Load displacement curve of bearing capacity N_c in Test 9.	110
4.22	Load displacement curve of bearing capacity N_c in Test 10.	110
4.23	Load displacement curve of bearing capacity N_c in Test 11.	111
4.24	Load displacement curve of bearing capacity N_c in Test 12.	112
4.25	Load displacement curve of bearing capacity N_c in Test 13.	112
4.26	Load displacement curve of bearing capacity N_c in Test 14.	113
4.27	Load displacement curve of bearing capacity N_c in Test 15.	114
4.28	Principal stress rotation regarding different values of the anisotropic coefficient.	115
4.29	Principal stress rotation with regarding associativity and nonassociativity in the conventional plastic flow rule ($n = 0.707$, $\beta = 45^\circ$).	115
4.30	Load displacement curve of bearing capacity N_q in Test 17.	117

4.31	Load displacement curve of bearing capacity N_q in Test 18.	117
4.32	Load displacement curve of bearing capacity N_q in Test 19.	118
4.33	Load displacement curve of bearing capacity N_q in Test 20.	118
4.34	Load displacement curve of bearing capacity N_q in Test 21.	119
4.35	Load displacement curve of bearing capacity N_q in Test 23.	120
4.36	Load displacement curve of bearing capacity N_q in Test 22.	120
4.37	Load displacement curve of bearing capacity N_q in Test 24.	121
4.38	Load displacement curve of bearing capacity N_q in Test 25.	121
4.39	Principal stress rotation with different values of the anisotropic coefficient.	123
4.40	Principal stress rotation with different values of the anisotropic coefficient ($n = 0.707 \beta = 45^\circ$).	123
4.41	Displacement patterns of the soil mass with ($n = 0.85 \beta = 45^\circ n = 0.0$) at $\frac{\Delta}{B} = 0.4$	124
4.42	Displacement patterns of the soil mass with ($n = 0.85 \beta = 45^\circ n = 0.1$) at $\frac{\Delta}{B} = 0.4$	124
4.43	Displacement patterns of the soil mass with ($n = 0.707 \beta = 45^\circ n = 0.0$) at $\frac{\Delta}{B} = 0.6$	125
4.44	Displacement patterns of the soil mass with ($n = 0.707 \beta = 45^\circ n = 0.1$) at $\frac{\Delta}{B} = 0.6$	125
5.1	Ground movements induced by tunnelling (Attewell et al., 1986). . .	128
5.2	Settlement troughs defined by Gaussian distribution curve after Peck (1969).	129
5.3	Different distributions of ground loads on tunnel linings: a) Hewett et al. (1964); b) Windels (1967); c) Fleck and Sklivanos (1978). . . .	130
5.4	Display of the stress reduction method.	131
5.5	Display of the stiffness reduction method.	132
5.6	Illustration of the gap method parameters (after Rowe et al., 1983). . .	133
5.7	Geometry and finite element discretisation of the tunnel model. . . .	137
5.8	The installation of the liner.	138
5.9	Vertical displacement with the influences of n and β ($\alpha = 0.1$). . . .	139
5.10	Vertical displacement with the influence of k ($\alpha = 0.1$).	139
5.11	Horizontal displacement with the influences of n and β ($\alpha = 0.1$). . .	140

5.12	Horizontal displacement with the influence of k ($\alpha = 0.1$).	141
5.13	Vertical displacement with the influences of n and β ($\lambda = 0.1$).	142
5.14	Vertical displacement with the influence of non-coaxiality ($\lambda = 0.1$).	143
5.15	Horizontal displacement with the influences of n and β ($\lambda = 0.1$).	143
5.16	Horizontal displacement with the influence of non-coaxiality ($\lambda = 0.1$). 144	
5.17	Geometry and finite element discretisation: real size with Zhou's cen- trifuge tests.	146
5.18	The illustration of volume loss calculation.	148
5.19	Normalised settlement profiles in terms of $V_l = 0.86\%$	149
5.20	Normalised settlement profiles in terms of $V_l = 2.0\%$	150
5.21	Normalised settlement profiles in terms of $V_l = 3.23\%$	151
5.22	Normalised settlement profiles in terms of $V_l = 5.16\%$	151
5.23	Normalised settlement profiles in terms of $V_l = 3.23\%$ in terms of non- coaxial effects when $n = 0.707$ $\beta = 0^\circ$	152
5.24	Normalised settlement profiles in terms of $V_l = 3.23\%$ in terms of non- coaxial effects when $n = 0.707$ $\beta = 45^\circ$	153
5.25	Normalised settlement profiles in terms of $V_l = 5.16\%$ in terms of non- coaxial effects when $n = 0.707$ $\beta = 0^\circ$	153
5.26	Normalised settlement profiles in terms of $V_l = 5.16\%$ in terms of non- coaxial effects when $n = 0.707$ $\beta = 45^\circ$	154
5.27	Vertical displacement with the influence of n ($\lambda = 0.92$).	154
5.28	Vertical displacement with the influence of n ($\lambda = 0.6$).	156
5.29	Vertical displacement with the influence of β ($\lambda = 0.92$).	156
5.30	Vertical displacement with the influence of β ($\lambda = 0.6$).	157
1	The eccentric ellipse anisotropic Mohr-Coulomb yield surface in: a) (X, Y, Z) space; b) (Z, Y) space.	170
2	Shear stress ratio obtained from various values of anisotropic coeffi- cient n : a) associativity in the conventional plastic flow rule; b) nonas- sociativity in the conventional plastic flow rule.	172
3	Shear stress ratio obtained from various values of non-coaxial coeffi- cient k with $K_0 = 0.5$ in : a) Test 15; b) Test 16.	173

4	Shear stress ratio obtained from various values of non-coaxial coefficient k with $K_0 = 3.0$ in: a) Test 15; b) Test 16.	173
5	Numerical results of principal orientations of stress and plastic strain increment in Test 15 : a) $k = 0.0$; b) $k = 0.02$; c) $k = 0.05$	174
6	Numerical results of principal orientations of stress and plastic strain increment in Test 16: a) $k = 0.0$; b) $k = 0.02$; c) $k = 0.05$	175
7	The bearing capacity factors versus friction angle ϕ_{max} with different values of n (eccentric ellipse): a) N_c ; b) N_q	183
8	Bearing capacity factor N_c versus various friction angles: a) Test 6; b) Test 7.	184
9	Ultimate failure pressure normalised by surface surcharge (q_t/q) versus various friction angles: a) Test 6; b) Test 7.	185
10	Load displacement curve of bearing capacity factor N_c in Test 2.	186
11	Load displacement curve of bearing capacity factor N_c in Test 4.	187
12	Load displacement curve of bearing capacity factor N_c in Test 5.	187
13	Load displacement curve of ultimate failure force normalised by surface surcharge q_t/q in Test 2.	188
14	Load displacement curve of ultimate failure force normalised by surface surcharge q_t/q in Test 4.	188
15	Load displacement curve of ultimate failure force normalised by surface surcharge q_t/q in Test 5.	189
16	Load displacement curve of bearing capacity factor N_c in Test 7.	189
17	Load displacement curve of ultimate failure pressure normalised by surface surcharge q_t/q in Test 7.	190
18	The velocity field for the case of eccentric ellipse Mohr-Coulomb yield criterion when $n = 0.932$	190

List of Tables

3.1	Experimental results from Oda et al. (1978) triaxial compression tests of Toyoura sand.	38
3.2	Experimental results from Yang (2013) monotonic shear tests of Leighton Buzzard sand.	38
3.3	Summary of the parameters	44
3.4	Material properties for all numerical simulations	64
4.1	Typical material constants and loading conditions	101
4.2	Cases of simulations for rotational ellipse	101
4.3	Material properties for all numerical simulations	108
4.4	Material properties for all numerical simulations	113
4.5	Material properties for all numerical simulations	116
4.6	Material properties for all numerical simulations	122
1	Material properties for all numerical simulations	171
2	Cases of simulations for eccentric ellipse	184

Nomenclature

Roman Symbols

f	yield surface
g	plastic potential
k, nc	non-coaxial coefficient
n	ratio of the minor axis to the major axis of the anisotropic ellipse
p	mean pressure
q_t	vertical pressure at collapse
B	half width of the strip footing
K_0	coefficient of earth pressure at rest
N_c	bearing capacity factor contribution from cohesion
N_q	bearing capacity factor contribution from surface surcharge
R_r	highest difference of pressure-displacement results between coaxial and non-coaxial modelling
S_v	surface settlement of tunnelling
S_{vmax}	maximum surface settlement of tunnelling
V_l	volume loss

Greek Symbols

α	stiffness reduction factor
β	angle between the major axis of ellipse and the x-axis
$\dot{\epsilon}_p^c$	coaxial plastic strain rate
$\dot{\epsilon}_p^n$	non-coaxial plastic strain rate
$\dot{\epsilon}_p$	total plastic strain rate
$\dot{\lambda}$	a positive scalar
λ	stress reduction factor
ν	Poisson's ratio of soil
ϕ	friction angle
ϕ_Ω	peak internal friction angle when the major principal stress is perpendicular to the deposition direction
ϕ_{max}	maximum peak internal friction angle
ϕ_{min}	minimum peak internal friction angle
ψ	dilation angle
ψ_{max}	maximum dilation angle
σ_x, σ_y	horizontal and vertical stress
σ_{xy}	shear stress
Θ, Θ_p	angle between the major principal stress direction and the loading direction

Abbreviations

DEM	Discrete Element Method
FEM	Finite Element Method
HCA	Hollow Cylinder Apparatus
NCG	Nottingham Centre for Geomechanics

Chapter 1

Introduction

1.1 Overview

Extensive experimental and micromechanics-based evidences have proven that non-coaxiality, which refers to the non-coincidence of the directions of the principal stress and principal plastic strain rate, is an intrinsic characteristic of granular materials. In addition, these fundamental insights have been employed to guide the development of more realistic continuum material models. The fabric tensor has been incorporated in the constitutive modelling of non-coaxial behaviour. These constitutive models have been successfully applied to study the bifurcation and strain localisation of granular materials under different loading conditions.

However, very few studies have been made on the application of non-coaxiality in the analysis of practical soil-structure problems. Subsequent research has been made by Yu (2006); Yu and Yuan (2006); and Yu (2008) to develop non-coaxial constitutive models by using the conventional plasticity theory. These models were then numerically applied in geotechnical applications, e.g. shallow foundations, anchor plates and silo problems. Conclusions were drawn that failure to account for non-coaxial soil behaviour would result in an unsafe design in geotechnical applications. This raises the attention for further investigations on the impact of ignoring non-coaxial soil behaviour in geotechnical modelling. No doubt that this is a great step leading to applications of non-coaxiality in modelling geotechnical problems. Nevertheless, work of the above researchers is restricted to the framework of soil strength isotropy. It is generally accepted that the natural characteristic of soils is anisotropic and recent experimental observations have demonstrated that non-coaxiality is a significant aspect

of soil anisotropy. Assuming non-coaxiality in the context of soil isotropy may result in poor predictions of stability and serviceability problems in geotechnical engineering. With particular emphasis on tunnel excavations, non-coaxial effects are not addressed sufficiently in the literature during the excavation procedure, where severe principal stress rotations can be expected in a non-homogeneous material.

1.2 Aims and Objectives

The aim of this project is to develop a non-coaxial soil model taking into account initial soil strength anisotropy. The strength anisotropy is described by assuming an elliptic yield curve in the deviatoric space. The axis of the ellipse is dependent on the peak internal friction angles that are measured in different principal stress directions. The project will develop and implement the non-coaxial soil model into FE code ABAQUS via the user-defined material subroutine (UMAT), and apply the non-coaxial soil model to investigate geotechnical problems.

This will be achieved through the attainment of the following objectives:

- To develop a novel plane strain, elastic perfectly plastic non-coaxial soil model in which the isotropic Mohr-Coulomb yield criterion is generalised by accounting for the effects of initial strength soil anisotropy. The strength anisotropy is described by the variation of peak internal friction angles with the direction of principal stresses.
- To develop a method for finite element implementation of the newly proposed non-coaxial soil model. Emphasis is drawn on the selection of non-linear algorithms and integration methods.
- To numerically assess the non-coaxial soil model by using simple shear problems. In particular, the effects of the initial stress state, the dilation angle, degree of soil anisotropy and non-coaxiality will be investigated.
- To develop a semi-analytical solution for strip footings resting on an anisotropic soil, including a special case for a purely cohesive material.

- To numerically apply the non-coaxial soil model to analyse practical soil-structure problems, e.g. strip footings and tunnel excavations.
- To verify the numerical predictions for strip footings with those obtained from the semi-analytical results as well as to compare the numerical results of the sub-surface settlement of tunnelling with centrifuge results from Zhou (2015). In addition, the effects of the degree of soil anisotropy and non-coaxiality on the soil behaviour of these geotechnical problems will be investigated.

1.3 Structure of the thesis

This thesis consists of seven chapters as outlined below:

Chapter 1 presents an overview of the research. The objectives and the outline of the research are introduced.

Chapter 2 reviews some of the voluminous literature on the subject of non-coaxial behaviour of granular soils. The definition of non-coaxiality, experimental and micro-mechanical studies are provided, with a particular reference to finite element modelling of non-coaxiality based on plasticity theory.

Chapter 3 concerns the development of a non-coaxial soil model in the context of initial soil strength anisotropy, where the soil strength anisotropy is described by the variation of peak internal friction angles with the direction of principal stresses. In addition, the commercial FE software ABAQUS is adopted as a platform for the implementation of the newly proposed non-coaxial model. The stress-strain increment is integrated via the user-defined material subroutine (UMAT).

Chapter 4 assesses the model using a simple shear problem in light of experimental observations under simple shear conditions.

Chapter 5 introduces a semi-analytical solution for strip footings resting on an anisotropic soil based on the slip line method with a particular reference to a close form solution for a purely cohesive soil. A parametric study is performed on the influence of anisotropic coefficients. The verification of numerical results excluding non-coaxiality

with semi-analytical results, is provided. The effects of degree of soil anisotropy and non-coaxiality on the bearing capacity and displacement patterns of strip footings are then investigated.

Chapter 6 provides a series of numerical simulations on tunnelling in terms of the stiffness reduction method and the stress reduction method. A case study is conducted and numerical results of the subsurface settlement are compared with centrifuge experimental and Gaussian empirical results.

Chapter 7 draws the conclusion of the research and highlights areas for further research on this topic.

Chapter 2

Literature Review

2.1 Introduction

The foundation of classical plasticity theory can be dated back to the 1950s and 1960s. One of the key concepts of the theory is the assumption of coaxiality of principal axes of stress and plastic strain rate tensors (reviewed by Yu, 2006). However, more recent research has found that soil behaviour is generally non-coaxial. Non-coaxiality refers to the non-coincidence of the principal axes of stress and plastic strain rate tensors. Extensive experimental (Roscoe et al., 1967; Drescher and De Josselin de Jong, 1972; Drescher, 1976; Arthur et al., 1977; 1980; Christoffersen et al., 1981; Yang, 2013) and micromechanics-based (Zhang, 2003; Jiang and Yu, 2006; Li and Yu, 2010) evidence has demonstrated that non-coaxiality is distinctly observed at the initial stage of the shear stress level, and the degree of non-coaxiality decreases with an increase in the shear stress level. It is a significant aspect of anisotropic granular materials.

A literature review regarding soil anisotropy and non-coaxiality, particularly anisotropic and non-coaxial plasticity theories is provided in this chapter. Soil anisotropy is briefly introduced in Section 2.2; a particular reference is drawn on the anisotropic plasticity theory described by the variation of strength parameters with loading directions in Section 2.3. Previous studies of non-coaxiality are presented in Section 2.4, including experimental and micromechanics-based evidences in support of the non-coaxial behaviour of granular soils. The plasticity theories associated with non-coaxial soil behaviour are compared and analysed in Section 2.5. Concluding remarks are presented in Section 2.6.

2.2 Soil anisotropy

It is generally accepted that soils are intrinsically anisotropic in nature. The term soil anisotropy corresponds to any directional-dependence on mechanical properties such as dilatancy, strength and stiffness of soil mass. It is attributed to the geological depositional process, grain, void characteristics, associated contacts as well as external loading. There are two main types of soil anisotropy by Casagrande and Carillo (1944); namely: inherent anisotropy and induced anisotropy. From a microscopic view, the anisotropy of granular material is mainly due to the anisotropic internal fabric. The spatial arrangement of soil particles and the associated voids were firstly referred to fabric by Brewer (1964). Popular concepts of fabric consist of (ODA et al., 1985):

- Orientation distributions of elongated particles;
- Contact normal distributions between interacting particles;
- Void distributions.

2.2.1 Inherent anisotropy

In nature, soil particles tend to be aligned in some preferred directions during deposition. This is treated as initial anisotropy and can affect material properties of granular soils (e.g. shear strength and deformation characteristics). Casagrande and Carillo (1944) were among the first to model strength anisotropy in soils and gave a definition of inherent anisotropy as ‘a physical characteristic inherent in the material and entirely independent of the applied stresses and strains’.

This geometrical anisotropy of grain orientation was studied and understood in the laboratory. Phillips and May (1967) presented a specially constructed shear box fitted with removable sides and ends, in which the sample was able to be poured in each of the corresponding three orthogonal directions. Conclusions were drawn that inherent anisotropy affects shear strength by demonstrating a variation of approximately 5° in the angle of shearing resistance ϕ' when comparing the samples pour through a side or end and the samples pour to the same porosity in the normal way through the top of the box. The difference of maximum shear stress ratio was up to 24%. Apart from the shear box apparatus, Arthur and Menzies (1972) developed a cubical, triaxial cell apparatus to investigate the inherent anisotropy of non-cohesive granular materials.

Samples were prepared in a tilting mould. The three principal stresses were controlled independently through flexible stress controlled boundaries. They found that rotating the directions of pouring through 90° in drained triaxial compression tests on rounded Leighton Buzzard sand, led to about 2° of variance in the shearing resistance or 10% of the maximum shear stress ratio. Parkin et al. (1968) performed a series of hydrostatic compression tests on triaxial samples and found that the radial strain of the sample is always much larger than the vertical strain. Following their work, Lade and Duncan (1973) and Lade (1978) developed a cubical triaxial apparatus. Using the developed cubical triaxial apparatus with a number of modifications, Abelev and Lade (2003); Lade and Abelev (2003) performed a series of true triaxial tests on dense Santa Monica beach sand on cubical specimens. It was apparent that the peak internal friction angle is various with different sectors (different sectors corresponded to different direction of the principal stress) even when the intermediate principal stress ratios is constant. More recently, the hollow cylinder apparatus has been widely applied to study soil anisotropy of granular materials. Kumruzzaman and Yin (2010) performed a series of consolidated undrained tests on remoulded hollow cylinder specimens of completely decomposed granite. A fixed principal stress direction with an angle deviating from the vertical direction was maintained. Results showed strong strength anisotropy due to material inherent anisotropy. There were significant variations in the friction angle ϕ' .

In addition to such experimental works, other studies have been made on the inherent anisotropy based on micro-mechanics. The contact normal distribution of granular materials is difficult to test in a laboratory. Hence, the fabric is represented by the preferred orientation of a non-spherical particle long axes. Results from the hydrostatic compression tests conducted by Parkin et al. (1968), as aforementioned, showed that the long axes (fabric) of the grains tend to be aligned in the horizontal plane and are symmetrically disposed about the vertical axis after impregnation of the samples. Oda et al. (1978) performed a series of plane strain tests on sand. They prepared natural sand samples and fixed the particle arrangement by infiltrating polyester resin binder into voids after oven-dried. Then the samples were cut into a vertical section (V-section) and a horizontal section (H-section). In support of Oda (1972*b*), they found that the preferred orientation of long axes of particles can be found to be parallel to the

horizontal direction in sands and the intensity of such a preferred orientation of particles is closely related to the shape characteristic of particles and gravitational force and so forth. In addition, they also proved that particle alignment has a vital influence on shear strength. Numerical studies based on the Discrete Element Method (DEM) have flourished to study micro-mechanics of inherent soil anisotropy. DEM was first developed by Cundall and Strack (1979) to investigate micro-mechanic behaviour of rock mass problems and then granular materials. Li and Yu (2009) presented a series of two dimensional (2D) DEM modelling of granular materials subjected to monotonic loading condition. An initially anisotropic specimen was generated using the deposition method. Results indicated evidence of the initial fabric anisotropy produced during particle depositions by showing differences in strengths and deformations when the loading direction changes. Similar DEM conclusions were also pointed out by other researchers that different preferred orientation of particles and contact normal can affect the mechanical behaviour of soil mass. The initial fabric anisotropy demonstrates significant effects on the shear strengths and deformations (Ting and Meachum, 1995; Ng, 2004; Yang et al., 2008; Sazzad and Suzuki, 2010; Seyedi, 2012).

2.2.2 Induced anisotropy

With an increase in the loading condition, particles may structurally rearrange which may alter the fabric. In this case, induced anisotropy becomes dominant. It is generally accepted that defining induced anisotropy is an essential part of the straining process of a soil. Even an initially isotropic material can develop induced anisotropy when subjected to external loading. Casagrande and Carillo (1944) defined induced anisotropy as ‘a physical characteristic due exclusively to the strain associated with an applied stress’.

Since induced anisotropy is directly related to the directional redistribution of particles and inter-particle contacts during shearing and plastic deformation, one pivotal feature of the experimental study of induced anisotropy is the control of principal stress directions during shear. Early experiments (e.g. Bishop, 1966) on cohesive soils achieved principal stress rotations by cutting samples at chosen orientations from larger blocks of the soil. It was reviewed by Arthur et al. (1977) that there exist two special cases of major principal stress rotations as reported in the literature:

- Arthur and Menzies (1972) controlled the rotation of major principal stress in the interchange of major and minor principal stress directions in the axisymmetric triaxial test;
- Roscoe et al. (1967) controlled the rotation of the principal stress in a gradual monotonic change in a Cambridge Simple Shear Apparatus.

Another challenge is to separate induced anisotropy from inherent anisotropy. Based on these ideas, Arthur et al. (1977) developed a useful apparatus to study induced soil anisotropy. In their tests, dense sand samples were deposited in the direction of the intermediate principal stress, conveniently eliminating the influence of inherent anisotropy. Then they were monotonically loaded to a high pre-failure stress ratio before unloading to an isotropic stress state. Further on, the prepared samples were monotonically sheared at various principal stress states. The induced anisotropy was found to have a large influence on the strain required to achieve a given stress ratio. The major principal strain and the stress ratio varied with the rotation of the principal stress direction. However, it showed negligible influence on the angle of shearing resistance ϕ' when compared with inherent anisotropy. This observation is supported by the work of Oda (1972c) from microscopic view. It was explained that the soil fabric constantly changed and aligned in a new direction during the process of shearing. As a result, particle contact normals and the voids between the particles formed load resisting columns. After achieving the peak stress, the columns consisting of contact normals and the voids began to break down, resulting in an alteration of the soil fabric.

Li and Yu (2009) presented 2D DEM simulations of the monotonic behaviour of granular materials with fixed strain increment directions to provide associated particle scale information. The initially anisotropic specimen was sheared in the deposition direction and unloaded to the isotropic stress state to prepare preloaded samples. The samples were monotonically sheared at different loading directions. The loading directions varied from vertical to horizontal at 15° intervals. It was argued that the directional distributions of contact normal probability and normal contact force are the main fabric information to show the stress anisotropy. Microscopic observations from their tests elaborated that the distribution of contact normals changed relative to the loading direction upon shearing, which results in a slower decrease in the stress ratio. This can be explained as the changes of soil fabric leading to induced anisotropy in the soil

structure to resist the loads applied.

The experimental results and micro-mechanical observations shown above certainly demonstrate inherent and induced anisotropy in real granular materials. These fundamental insights obtained from experimental and micromechanics-based investigations have also been employed to guide the development of more realistic continuum material models.

2.3 Anisotropic plasticity theory

The plasticity theory has been introduced in the anisotropic field in order to simulate the evolution of material anisotropy. The conventional constitutive models have been advanced by incorporating the influence of initial as well as induced anisotropy for a more accurate description than what can be achieved from isotropic theories (Amerasinghe and Parry, 1975; Ko and Sture, 1981; Mitchell, 1972). Perhaps there are two most popular ways to achieve this: one is to rotate the original well known yield surface and plastic potential in the stress space due to previous anisotropic stress history, e.g. the bounding surface constitutive model; the other is to introduce a rotational hardening rule to model the evolution of stress-induced anisotropy (Prevost, 1978; Hashiguchi, 1979). These methods are based on the macro-mechanic theory. From the micromechanic view, Kavvadas (1983) introduced an anisotropic tensor in a non-associated kinematic hardening rule expressed in terms of the plastic volumetric strain rate. Anandarajah and Dafalias (1986) developed a constitutive model incorporating both the initial anisotropy and the induced anisotropy by combining the rate-independent bounding surface soil plasticity and the critical state concepts. More recently, a number of constitutive models based on anisotropic plasticity theory have been developed to investigate a various particular cases, e.g. Kowalczyk and Gambin (2004) developed a model of evolution of plastic anisotropy due to crystallographic texture development, describing metals subjected to large deformation processes. The trend attempts to account for more effects into the model to make the model more accurate and capable of predicting. On the other hand, the model becomes more complicated in terms of formulations and calibration for input parameters. Hence, we should think of their usability as the purpose of constitutive modelling is to apply it to solve

boundary value problems.

Many papers reported in the literature (e.g. Duncan and Seed, 1966; Baker and Krizek, 1970) defined the anisotropy of cohesive and frictional materials as the change in 'strength' on a plane as the orientation of this plane changed. The strength parameters mainly refer to cohesion and friction angles. Reddy and Srinivasan (1970) presented a study of anisotropy on the ultimate bearing capacity of rough strip footings associated with the slip line method. The soil was assumed to be rigid plastic at failure. The anisotropy was described by the variation of cohesion, according to Casagrande and Carillo (1944). The cohesion was obtained corresponding to the condition when a major principal stress is coincident with and perpendicular to the horizontal direction. Similarly, Yu and Sloan (1994) studied the influence of strength anisotropy described by the variation of cohesion with a direction based on a finite element formulation of the bound theorems. Their expression of the cohesion was based on the studies of Lo (1965). Only cohesion on the horizontal and vertical planes were accounted for in their study. Their method can be readily applied to investigate boundary value problems, e.g. footing problems. However, it is obvious these methods are applicable to clay other than sand. Perhaps earlier shear tests to investigate inherent soil anisotropy were performed on specimens cut at different orientations. More extensive studies have been presented on the influence of anisotropy in clay than in sand under plane conditions. It is understandable hence why the inherent anisotropy represented by the variation of cohesion with direction, was much more pivotal than the influence of friction angles.

However, more recent experimental observations performed on sand from the HCA indicate that the friction angles show an apparent variation with a change in the principal stress direction α for different controlled b (intermediate principal stress ratio) values. The largest range of friction angle ϕ_p occurs when $b = 1.0$, which is $\phi_p = 31^\circ$ for the minimum and $\phi_p = 45^\circ$ for the maximum corresponding to $\alpha = 75^\circ$ and $\alpha = 0^\circ$ respectively. Therefore, there exists an increasing interest in describing plastic anisotropy by the variation of friction angles. Booker and Davis (1972) presented a class of slip line equations for a plane strain plastic material having a general anisotropic Mohr-Coulomb yield condition, in which the hydrostatic stress was considered. For a special case, Hill (1950) proposed a treatment for materials with strength independent of hy-

drostatic pressure. Following their study, we will try to present a general form of an anisotropic yield criterion by treating a changing friction angle with the direction of principal stresses. Both clay and sand will be taken into consideration in our project. The newly proposed anisotropic yield criterion is extended from the original isotropic Mohr-Coulomb yield criterion, which demonstrated a good balance between the predictive ability and usability for various geotechnical problems. Obviously, only a few material parameters will be introduced.

In the past decades, the study of soil anisotropy has enjoyed a fruitful outcome in a variety of fields. Non-coaxiality, as a particular significant aspect of soil anisotropy, is the main subject in our project and will be reviewed in the subsequent section in detail.

2.4 Experiment investigations and DEM modelling of non-coaxiality

One of the earliest experimental investigations into non-coaxiality was made by Roscoe et al. (1967) and Roscoe (1970), where it was demonstrated that non-coaxiality is distinctly observed during the initial state of the shear stress level in the simple shear tests. The traditional preparation of samples to achieve the principal stress rotation is to rotate the materials themselves in a simple shear or direct shear apparatus. Drescher and De Josselin de Jong (1972) described an experimental micro-mechanical study performed on an assembly of photo-elastic discs constituting a two-dimensional analogue of a granular material. Oda and Konishi (1974*b*) performed a series of simple shear and direct shear tests respectively with an assembly of cylinders made of photoelastic material packed randomly in a two-dimensional simple shear apparatus. The results indicated that a possible non-coaxiality of stress and strain-rate tensors was induced and hence could be observed in actual practice as well. The contact normals tend to concentrate towards the maximum principal stress axis during an increase in the shear stress level. The preferred direction of the concentration gradually rotated when the shear stress was gradually applied up to the peak value; and this rotation is due to the rotation of the principal stress axes as described by Roscoe et al. (1967). In the past twenty decades, the simple shear and direct shear apparatus have been improved and a similar non-coaxial behaviour of granular materials when subjected to a rotation of principal stresses (Arthur et al., 1977; 1980; Airey et al., 1985).

However, one of the limitations of the simple shear/direct shear apparatus is that it is practically difficult to impose a uniform normal and shear stress field on the shearing plane. Arthur et al. (1977) tried to control the normal and shear stresses on the plane of deformation but also on the plane that is normal to the shearing plane to improve the Cambridge simple shear apparatus. However, the rearrangement of granular materials still remains unpredictable. More recently, there has been a growing interest in applying DEM to study the non-coaxial behaviour of granular assemblies (e.g. (Zhang, 2003)). Ai et al. (2014) developed a discretised-wall confined granular cell in their 2D DEM study of quasi-static non-steady simple shear flows. These modifications to the boundary configuration allowed for synchronised dilations between the boundary and the confined solid. Thus sufficient and uniform distributions of the stress-strain across the whole assembly was achieved. Results from these tests are plotted in Figure 2.1 and indicate a similar evolution of orientations of principal stress and principal strain rate increment when compared with aforementioned experimental studies (e.g. Roscoe et al., 1967), where a significant non-coincidence in the principal directions of stress and strain rate increment occurred at small values of shear strain and decreased with an increase in the shear strain (η_0 refers to the initial stress ratio of deviatoric stress q over mean stress p). From a micro-mechanic view, the fabric and the direction of the principal stress coincident at the limit stage of shear loading.

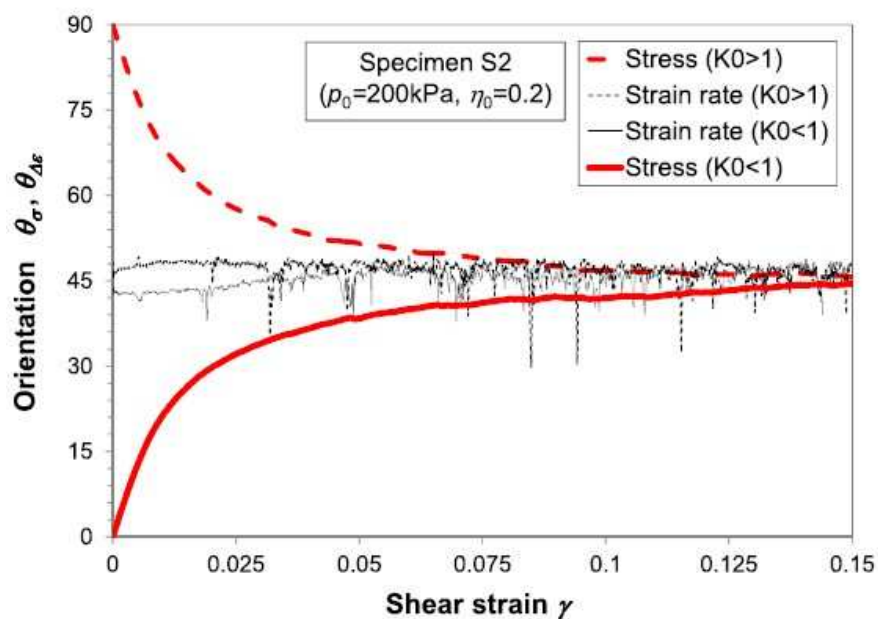


Figure 2.1 Major principal stress and strain rate orientations with $\eta_0 = 0.2$ (Ai et al., 2014).

Another way to achieve the principal stress rotation is to control and rotate the direction of the principal stress itself, which can be achieved by the hollow cylinder apparatus (HCA) (Saada and Baah, 1967; Lade and Duncan, 1975; Hight et al., 1983; Gutierrez et al., 1991). The apparatus makes it possible to monitor and control the principal stresses and the direction of the major principal stress independently. It is capable of controlling the relative magnitude of the intermediate principal stress as well. In a very significant paper, Gutierrez et al. (1991) investigated the effect of the principal stress rotation on the plastic behaviour of sand by using the hollow cylinder apparatus. Three different stress paths were followed in his study, namely monotonic loading tests at different fixed principal stress directions, pure rotation of principal stress directions at constant mobilised angles of friction (i.e. at constant stress ratios) and combined loading paths involving a simultaneous increase in the shear stress level and rotation of the principal stress direction. The stress paths and the plastic strain rate vectors from the above three types of tests are presented in Figure 2.2 in the $(X - Y)$ space. Both the total strain increment and the plastic strain increment directions are plotted in these figures. It is demonstrated that the difference between the directions of the total strain increment and the plastic strain increment is minute and can be neglected. Figure 2.2 a shows details of monotonic loading tests. The directions of the principal stress are presented by straight lines, and are very close as compared to the direction of the plastic strain increment, i.e. the total strain increment direction. Figures 2.2 b and 2.2 c exhibit results from the pure rotation and combined loading tests, where the combined stress paths are plotted as spirals in the $(X - Y)$ stress space. For both figures, it is apparent that the degrees of non-coaxiality are exaggerated in the initial stage of the tests and decrease with an increase in the shear stress level.

The HCA has been widely applied to investigate the non-coaxial behaviour of granular materials. Cai (2010) performed 24 tests on Portaway sand and 2 tests on Leighton Buzzard sand to study the non-coaxial soil behaviour of granular materials. Yang (2013) performed a series of drained monotonic shear tests and drained rotational shear tests on Leighton Buzzard sand to investigate drained anisotropic behaviour of sand under generalised stress conditions. The features that affect the degree of non-coaxiality were proposed as the density of the specimen, the stress path followed, the stress level and the material particle properties. These test results also indicated that non-coaxiality

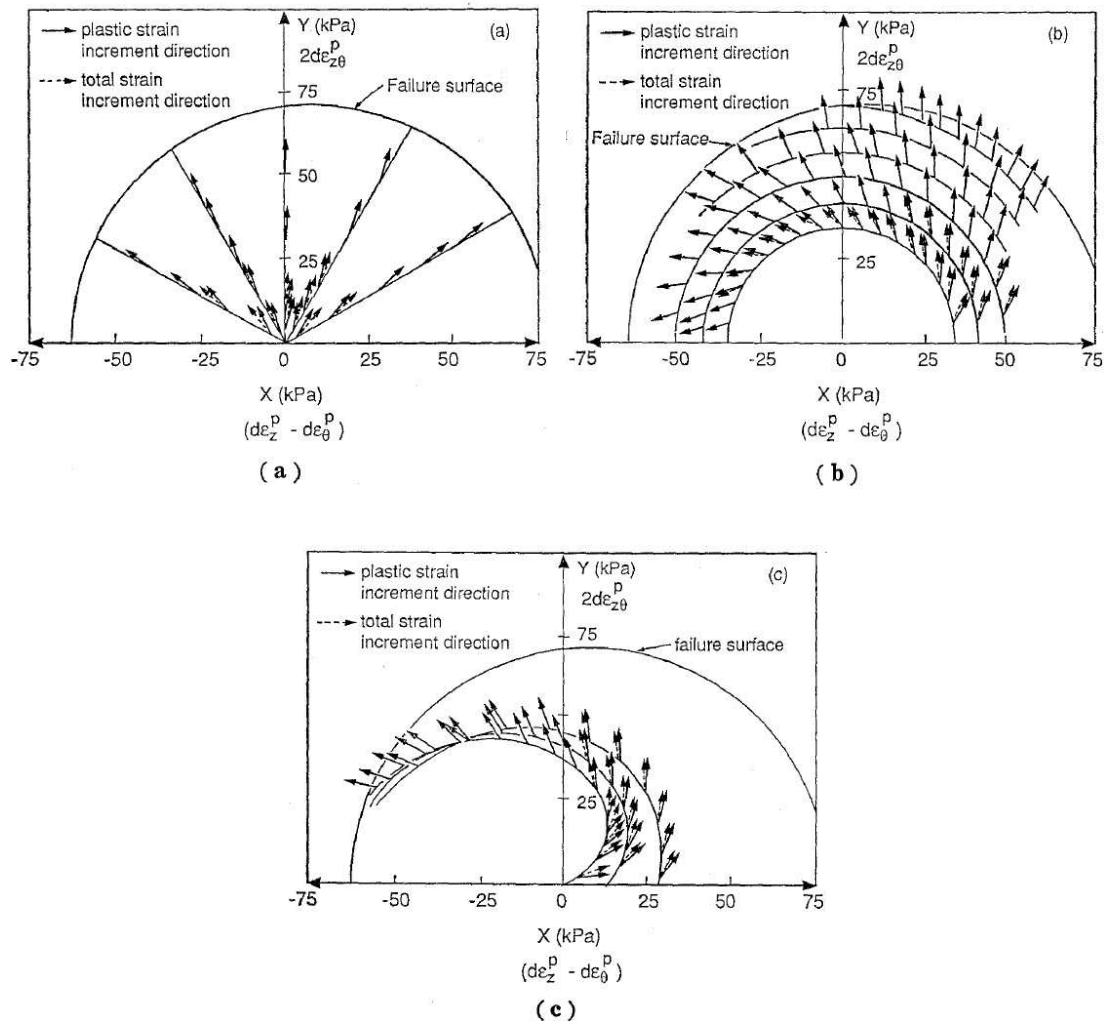
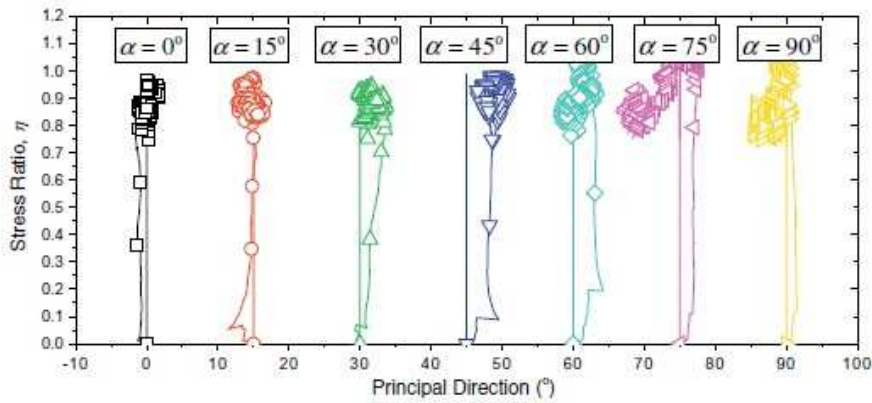
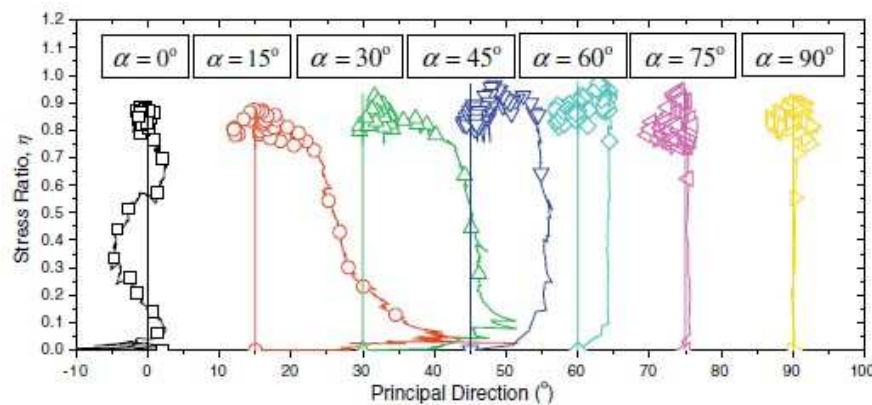


Figure 2.2 Unit plastic strain increment vectors superimposed on the stress path for: (a) monotonic loading; (b) pure rotation; (c) combined loading (after Gutierrez et al., 1991).

is more significant in pure rotation tests than in monotonic loading tests. However, as our project is concerned with initial anisotropy, the rotational shear tests will not be deeply reviewed.



(a)



(b)

Figure 2.3 Stress and strain increment directions of : (a) the initial anisotropic sample; (b) the preloaded sample (Li and Yu, 2009).

In addition, DEM simulations have been performed on the HCA. As reviewed in the previous section, Li and Yu (2009) performed 2D DEM simulations under monotonic loading to explore the underlying mechanisms of non-coaxiality. Two samples were tested; namely the initially anisotropic specimen and the preloaded specimen, describing the behaviour of inherent anisotropy and induced anisotropy. The loadings were monotonically applied in the strain-controlled mode. Results illustrating stress and strain increment directions are shown in Figure 2.3. α represents the loading directions. The vertical straight lines represent the direction of the principal strain increment, whereas the lines with hollow symbols indicate the direction of the principal stress. As shown in Figure 2.3 a, non-coincidence is small for the case of initial

anisotropy. However, it is pronounced in Figure 2.3 b for the cases when the loading direction is further away from the previous loading direction in terms of the preloaded specimen. It was argued by Li and Yu (2009) from the micro-mechanic view that the direction of major principal stress was dependent on the principal directions of contact normal and contact force, and also their relative magnitudes. For the initially anisotropic sample, the principal directions of anisotropic fabrics were vertical. The principal direction of the contact normal was close to the principal direction of the contact force when the loading direction was closer to $\alpha = 90^\circ$. This time the non-coaxiality was not obvious as indicated in Figure 2.3 a. When the sample was subjected to loading, the resulted stress direction was close to the principal contact force direction, i.e. the loading direction. This time, non-coaxiality was significant as indicated in Figure 2.3 b. More analyses can be found in some further work, e.g. Li and Yu (2010) performed 2D DEM simulations in which the samples were subjected to different loading path (i.e. pure rotation); and Yang (2014) extended 2D into a 3D realm.

The conclusions drawn from the experimental and micro-mechanic evidence, confirm the non-coaxial nature of soil behaviour. These findings can be assimilated to advance current constitutive models. These models can then be used to investigate geotechnical applications. In recent years, FE simulations have been widely used to analyse complicated geotechnical problems.

2.5 Non-coaxial plasticity theories

The majority of existing constitutive models encompassing granular materials have been generalised based on continuum mechanics. A high proportion of continuum models for granular materials are based on plasticity theory. Prager and Drucker (1952) established a continuum model of dilatant granular materials which was then applied by Shield (1953). Two useful assumptions were associated with their model:

- The plastic potential is very similar to the formulation of the Coulomb yield function;
- It is assumed to be associated and coaxial with the principal orientations of stress and plastic strain rate.

This approach has found some success in geotechnical engineering. Over the past a few decades and in most cases, the coincidence of the principal directions of stress and plastic strain rate during the period of plastic deformation, has been assumed when predicting soil behaviour using these models. In other words, these models have been developed from the results of experiments subject to fixed principal stress directions. Experiment results (e.g. Yang, 2013) indicated that a significant plastic deformation is induced during rotational shear despite the magnitude of principal stress remaining constant. Cumulative permanent deformation may result in unsafe design in geotechnical applications. It is thus required to improve the current constitutive models to include non-coaxial soil behaviour, which is a missing component to ensure more accurate predictions of soil behaviour.

2.5.1 Li and Dafalias (2004)

Over the past a few decades, the fabric tensor has been a link between micromechanics and the continuum theory (e.g. (Cambou, 1993; Cambou et al., 2000)). The macroscopic mechanical behaviour of granular materials is then directly related to the evolution of the internal structure. Structural or multi-scale approaches based on micromechanics have been proposed to develop constitutive relationship accounting for microscopic information. Recently, many constitutive models are modified by introducing the fabric tensor, in which the material parameters are defined at the macroscopic scale. The fabric anisotropy is characterised as a fabric tensor. The effects of the fabric anisotropy are considered in terms of making material parameters as a function of the fabric tensor, or incorporating the fabric tensor into the yield surface and flow law directly. Thereafter, a flow rule or a hardening law is hypothesised or obtained through the experimental data on the evolution of fabric tensor with stress, strain etc (Li and Dafalias, 2002; Zhu et al., 2006a;b). For example, Li and Dafalias (2004) modified an existing platform model which is a double-hardening bounding surface sand model with a state-dependent dilatancy by introducing the deviatoric plastic modulus functions of a scalar-valued anisotropic parameter to make it capable to simulate anisotropic sand including non-proportional loading. In their model, the inherent anisotropy is described by making the soil dilatancy a function of fabric anisotropy. A new third loading mechanism, which can be called the 'rotational loading mechanism' is associated with the dilatancy and plastic potential. In this load-

ing mechanism which produced additional plastic deformation, the unit tensor which defined the loading direction contained two mutually orthogonal parts, one coaxial and the other in general non-coaxial with the principal stress axes. Their model was able to describe the response of sand subjected to monotonic or cyclic loading, proportional or non-proportional paths. However, the incorporation of fabric anisotropy into the plasticity model is highly complicated and intractable, even the simplest of them without any anisotropic features may already be complicated, largely because of their shear-dilatancy coupling. On the other hand, these models consider the effects of microstructure in indirect way where the micro information is estimated using on phenomenological method, which may still be unrevealed in microstructures. Hence, these models haven't been widely applied to investigate geotechnical problems.

2.5.2 Tsutsumi and Hashiguchi (2005)

Tsutsumi (e.g (Hashiguchi, 1977; Hashiguchi and Tsutsumi, 2001; Tsutsumi and Hashiguchi, 2005)) and his group made a systemic study of constitutive models incorporating the tangent (vertex) effect and the anisotropy of soils described concisely by the concept of the rotation of the yield surface around the origin of the stress space. Thereafter, in a significant paper (Tsutsumi and Hashiguchi, 2005), Tsutsumi and Hashiguchi tried to examine the non-coaxial behaviour in the stress probe test subjected to non-proportional loading paths. Four different plasticity models to predict the measured strain path were analysed by either incorporating the yield vertex (tangent) effect or the yield anisotropy described by the concept of the rotation of the yield surface. They found that although it is possible to predict non-coaxiality of soils if the plastic potential is assumed to be an anisotropic function of the stress tensor; the plastic strain rate which is dependent on the stress state that is tangential to the yield surface, cannot be modelled. The calibration of the model to predict the measured strain path was compared with the probe tests performed by Gutierrez et al. (1991). The model with both the tangent effect and the anisotropy can simulate well the dependence of the strain path. Hence, both the tangent effect and the yield anisotropy incorporating the subloading surface model should be incorporated into constitutive equations for the description of the general loading behaviour of materials. However, we should notice here that they were trying to propose a constitutive model which is capability of reproducing the non-coaxiality of soil behaviour, they did not give any evidence to model

the non-coincidence of the direction of the principal stress and principal plastic strain rate. Perhaps as Tsusumi pointed out himself that their models are mainly developed to predict the plastic instability phenomena of geomaterials. On the other hand, the stress-strain response in the pre-failure range is still of interest.

2.5.3 Yu (2008)

Yu (2008) and his group have made great efforts to study the stress-strain behaviour of granular materials under non-coaxial plasticity in the context of pre-failure deformation. In particular, they developed a number of non-coaxial constitutive models based on the combined double shearing and plastic potential theory (Yuan, 2005; Yu and Yuan, 2006) and the yield vertex theory (Yang and Yu, 2006*b*). The simple formulations of these models made it possible to be numerically applied to geotechnical applications (Yuan, 2005; Yang and Yu, 2006*a*; 2010*b*; *a*; Yang et al., 2011).

Double shearing theory

An early kinematic model for granular material flow was developed by De Josselin de Jong (1971), and is known as the ‘double-sliding, free rotation’ model. This model assumes that shear flow occurs along two surfaces where the available shear resistance has been exhausted. Based on the concept of the ‘double-sliding, free rotation’ model, Spencer (1964) proposed a set of kinematic equations termed as ‘the double shearing model’. He stated that ‘the double shearing theory is based on the Coulomb failure criterion, supplemented by a kinematic constitutive assumption that the deformation mechanism is by simultaneous shearing on the two families of surfaces on which the critical shear stress is mobilised’. The kinematic model originated by Spencer (1964) was developed for incompressible, rigid-plastic plane flow of granular materials. Further research has extended the theory in various ways, among which Mehrabadi and Cowin (1978) established a ‘dilatant double-shearing theory’ obeying the Butterfield and Harkness (1972) hyperthesis by introducing a dilatancy parameter χ . The two theories have common basis that the deformation is postulated to occur by shearing along stress/velocity characteristics. However, the main difference lies in that the definition of the rotation-rate is different. Harris (1993; 1995) proposed a method that gives a unified derivation of the equations for the double sliding, free rotating model; the double shearing model and the plastic potential model for granular materials. He interpreted

the rotation-rate as ‘the rate of rotation of the sliding elements’ or ‘the local fabric’ for the double sliding, free rotating model; as ‘the rate of rotation of principal stresses’ for the double shearing model and as zero for the plastic potential model. However, the rate of rotation of the local fabric was both unknown and unknowable in terms of the model. This may explain why the double shearing theory is more popular in the following applications.

Following Spencer (1964) and Harris (1993; 1995), Yu and Yuan (2006) argued that one significant part of the plastic strain rate was generated from the plastic potential theory. Another component was taken to be tangential to the yield surface as shown in Figure 2.4 (with tension positive notation in complying with the sign convention in continuum mechanics). Taking small strain cases into consideration, the Jaumann time derivative of $\dot{\boldsymbol{\epsilon}}$ was replaced by the material derivative $\dot{\boldsymbol{\epsilon}}$ by neglecting the spin tensor ω_{12} . In addition, they relaxed the original kinematic hypothesis of the coincidence of stress and velocity field, and gave Λ a reasonable positive dimensionless scalar in agreement with the findings from Savage and Lockner (1997), who pointed out that slip lines in the velocity field do not generally coincide with the Coulomb results in the stress field. The model was developed under plane strain conditions.

As indicated in Figure 2.4, the yield criterion f was taken as the isotropic Mohr-Coulomb criterion, of which the shape is taken as a circle in the deviatoric plane. By combining the double shearing theory and the plastic potential theory, a formulation of a class of non-coaxial models was proposed and took the following general form in terms of plastic strain rates:

$$\dot{\boldsymbol{\epsilon}}_{ij}^p = \dot{\boldsymbol{\epsilon}}_{ij}^{pc} + \dot{\boldsymbol{\epsilon}}_{ij}^{pn} = \dot{\lambda} \frac{\partial g}{\partial \sigma_{ij}} + \Lambda \dot{t}_{ij} \quad \text{if} \quad f = 0 \quad \text{and} \quad \dot{f} = 0 \quad (2.1)$$

where f and g denote the yield function and the plastic potential, $\dot{\lambda}$ and Λ denote scalar functions and Λ is dimensionless. The superscripts pc and pn refer to the coaxial component normal to the yield curve and non-coaxial component tangential to the yield curve respectively. The normal tensor can be expressed as the vector \mathbf{T} :

$$\mathbf{T} = [\cos 2\Theta_\sigma, -\cos 2\Theta_\sigma, 0, 2\sin 2\Theta_\sigma]^T \quad (2.2)$$

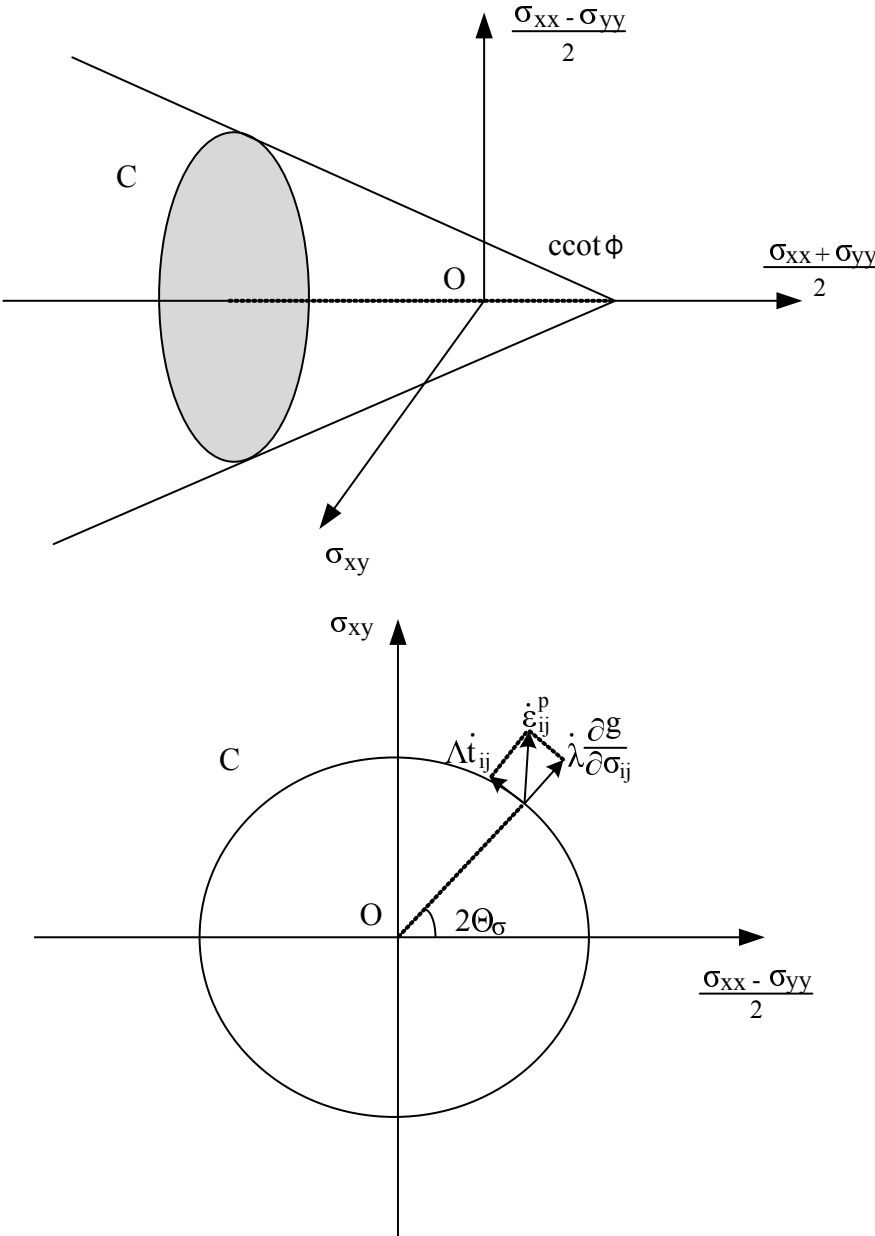


Figure 2.4 Mohr-Coulomb yield surface and plastic potential (Yu and Yuan, 2006).

where Θ_σ denotes the direction of the major principal stress.

It is obvious that t_{ij} can be rewritten in terms of planar stress:

$$t_{ij} = \frac{1}{\Lambda} H_{ijkl} \dot{\sigma}_{kl} \quad (2.3)$$

and the tensor H_{ijkl} can be expressed in terms of matrix \mathbf{H} :

$$\mathbf{H} = \begin{bmatrix} a_1 & -a_1 & 0 & a_2 \\ -a_1 & a_1 & 0 & -a_2 \\ 0 & 0 & 0 & 0 \\ a_2 & -a_2 & 0 & a_3 \end{bmatrix} \quad (2.4)$$

where

$$a_1 = \frac{4\Lambda\sigma_{xy}^2}{\sqrt{(\sigma_{xx} - \sigma_{yy})^2 + 4\sigma_{xy}^2}} \quad (2.5)$$

$$a_2 = -\frac{4\Lambda\sigma_{xy}(\sigma_{xx} - \sigma_{yy})}{\sqrt{(\sigma_{xx} - \sigma_{yy})^2 + 4\sigma_{xy}^2}} \quad (2.6)$$

$$a_3 = -\frac{4\Lambda(\sigma_{xx} - \sigma_{yy})^2}{\sqrt{(\sigma_{xx} - \sigma_{yy})^2 + 4\sigma_{xy}^2}} \quad (2.7)$$

The isotropic elasticity is assumed and the expression for the elastic stiffness modulus tensor is given as:

$$D_{ijkl}^e = \frac{Ev}{(1+\nu)(1-2\nu)} \delta_{ij} \delta_{kl} + \frac{2E}{(1+\nu)} (\delta_{ik} \delta_{jl} + \delta_{il} \delta_{jk}) \quad (2.8)$$

where E is Young's Modulus, ν is Poisson's ratio and δ_{ij} is Kronecker's delta, i.e., $\delta_{ij} = 1$ for $i = j$ and $\delta_{ij} = 0$ for $i \neq j$.

The relationship between total strain rates and stress states is obtained as:

$$\dot{\sigma}_{ij} = D_{ijkl}^{ep} \dot{\epsilon}_{kl} \quad (2.9)$$

and the elasto-plastic modulus tensor is defined as:

$$D_{ijkl}^{ep} = \bar{D}_{ijkl}^e - \frac{\bar{D}_{ijpq}^e \frac{\partial g}{\partial \sigma_{pq}} \bar{D}_{klmn}^e \frac{\partial f}{\partial \sigma_{mn}}}{\frac{\partial f}{\partial \sigma_{\mu\nu}} \bar{D}_{uvst}^e \frac{\partial g}{\partial \sigma_{st}}} \quad (2.10)$$

where \bar{D}_{ijkl}^e is introduced as the modified elastic modulus tensor and can be related to the conventional elastic modulus tensor:

$$\bar{D}_{ijkl}^e = (I_{ijkl} + D_{ijkl}^e H_{ijkl})^{-1} D_{ijkl}^e \quad (2.11)$$

where I_{ijkl} is the identity tensor.

The non-coaxial model based on the combined plastic potential and double shearing theory was then implemented in the finite element code ABAQUS via user-defined material subroutine UMAT. Figures 2.5 and 2.6 show the evolutions of orientations of the principal stress and the principal plastic strain rate for normally consolidated soil and over-consolidated soil respectively. K_0 represents the lateral stress ratio, which is defined as σ_{xx}/σ_{yy} . The results demonstrate a very good agreement with experimental observations (e.g. Roscoe et al., 1967).

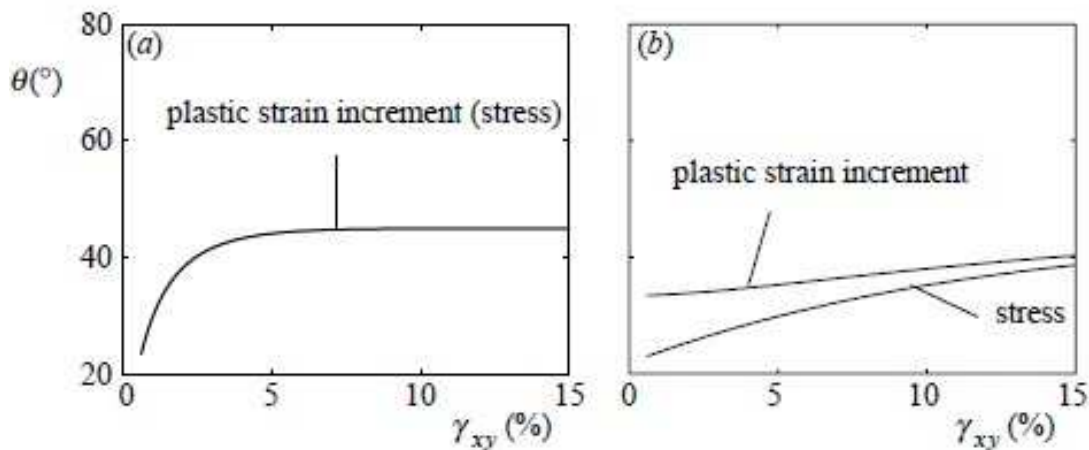


Figure 2.5 Numerical results of principal directions of stress and plastic strain rate for $\phi = 35^\circ$, $\psi = 0^\circ$ and $K_0 = 0.43$ (Yu and Yuan, 2006): (a) $\Lambda = 0.00$; (b) $\Lambda = 0.05$.

This model made a plane strain, elastic perfectly plastic assumption. In addition, Yuan (2005) have extended the previous model to axisymmetric problems and strain hardening problems.

Yield vertex (tangent) theory

The yield vertex (tangent) theory was initially proposed by Rudnicki and Rice (1975). The core of the yield vertex (tangent) theory states that when the stress state lies on

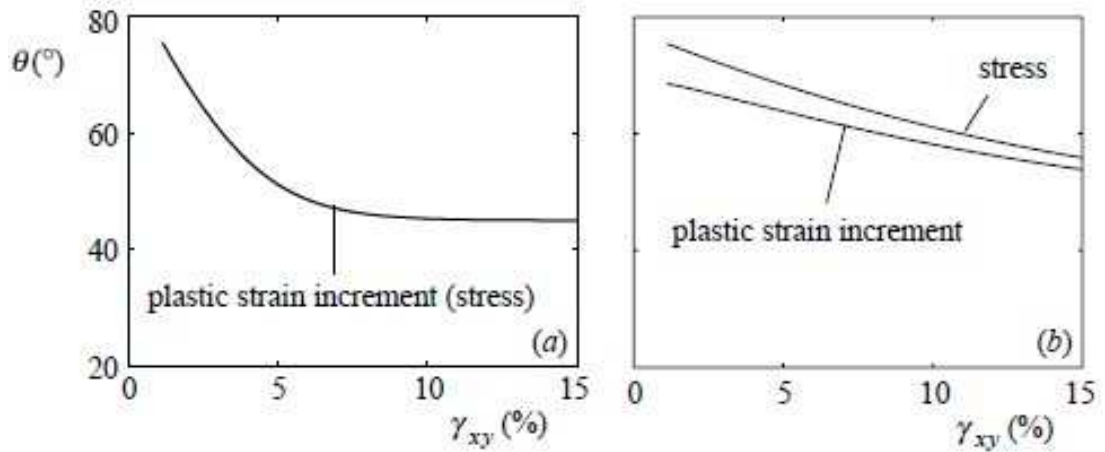


Figure 2.6 Numerical results of principal directions of stress and plastic strain rate for $\phi = 35^\circ$, $\psi = 0^\circ$ and $K_0 = 3.0$ (Yu and Yuan, 2006): (a) $\Lambda = 0.00$; (b) $\Lambda = 0.05$.

the current yield surface, plastic deformation is produced by both components of the normal and tangential stress rates. In other words, a second hardening modulus that governs the response to that part of a stress increment directed tangentially to the yield surface, is proposed in addition to the plastic hardening modulus governing ‘straight ahead’ stressing in the conventional plasticity theory.

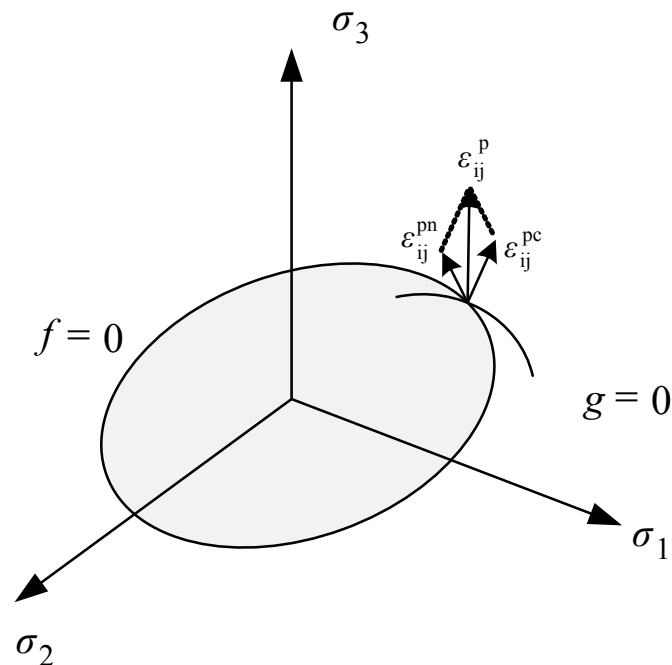


Figure 2.7 The non-coaxial plastic flow rule (after Rudnicki and Rice, 1975).

Yang and Yu (2006b) proposed a general elastic-plastic formulation for implementing the yield vertex theory proposed by Rudnicki and Rice (1975) to investigate non-

coaxial modelling on stress-strain responses of granular materials. The total strain rate includes the elastic strain rate derived by the classic Hooke's law as well as the plastic strain rate. As shown in Figure 2.7, the plastic strain rate is composed of the coaxial plastic strain rate $\dot{\epsilon}_{ij}^{pc}$ and the non-coaxial strain rate $\dot{\epsilon}_{ij}^{pn}$. The yield surface associated with the non-coaxial theory is characterised by a conical Drucker-Prager yield surface in general stress space.

Figures 2.8 and 2.9 illustrate the results of the coaxial and non-coaxial predictions of the shear stress ratio and principal directions of stress and plastic strain rate with different values of lateral stress ratio $K_0 = 0.4$ and $K_0 = 3.0$. The evolutions of the shear stress ratio are presented in Figures 2.8 and 2.9 a, whereas the orientations of the principal stress and the principal plastic strain rate are shown in Figure 2.8 and 2.9 b. It is concluded that the use of the non-coaxial model decreases the hardening or softening of shear stress ratio evolutions as compared with the coaxial model, and the predictions by the coaxial and non-coaxial models tend to be identical at the end of the shear stage. The coaxiality of the principal stress and the principal plastic strain rate is observed in Figures 2.8 and 2.9 b (see solid line). The dash lines show the non-coincidence of the principal stress and principal plastic strain rate. As expected, the degree of non-coaxiality is pronounced at the initial stage of the shear stress level and diminishes with the increase in the shear stress level.

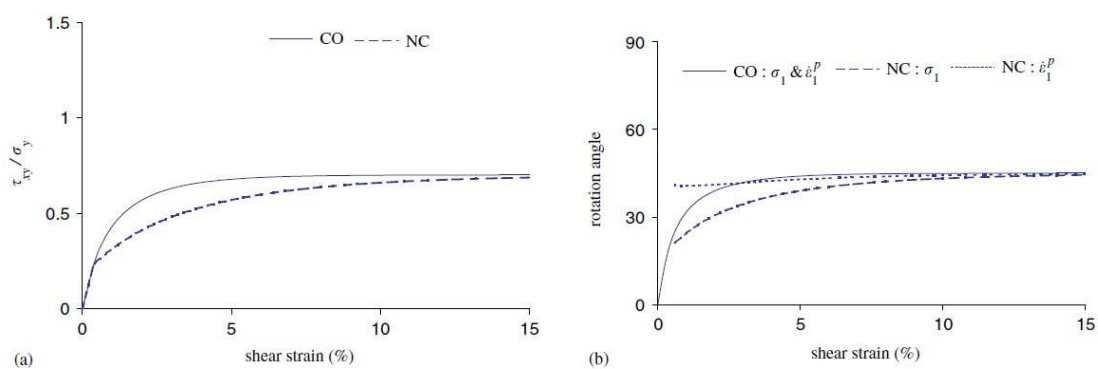


Figure 2.8 Results of the coaxial and non-coaxial predictions with perfect plasticity, $K_0 = 0.4$; (a) shear stress ratio; (b) orientations of the principal stress and principal plastic strain rate (after Yang and Yu, 2006b).

The non-coaxial stress-strain relationship in terms of the non-circular yield surface was then applied to the critical state model CASM (Yu, 1998). The CASM is a unified clay

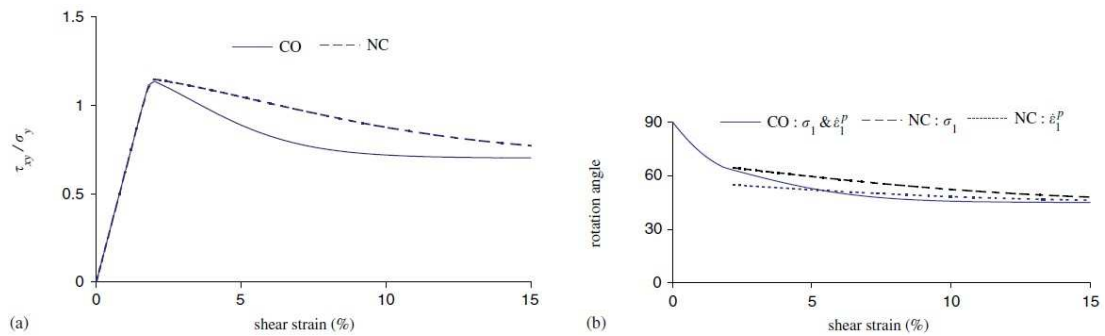


Figure 2.9 Results of the coaxial and non-coaxial predictions with perfect plasticity, $K_0 = 3.0$; (a) shear stress ratio; (b) orientations of the principal stress and principal plastic strain rate (after Yang and Yu, 2006b).

and sand model that can simulate the behaviour of both clay and sand without losing simplicity. The non-coaxial CASM can compensate for the previous non-coaxial Drucker-Prager model. The newly proposed non-coaxial model was applied to analyse simple shear problems.

The relationship between yield vertex and double shearing theories

Yu (2008) made a brief comparison between the yield vertex and the double shearing theories. He concluded that at least in form, a constant non-coaxial coefficient Λ from the double shearing theory may be equivalent to a pressure dependent plastic modulus from the yield vertex theory (and vice versa).

Therefore, non-coaxiality can simply be described in the formulation of plastic strain which consists of two components, namely: the coaxial part normal to the yield curve that is generated by the conventional plastic potential and the non-coaxial part that is tangential to the yield curve and is stress dependent.

2.5.4 Comments on current constitutive models

Generally, constitutive models that have been reviewed in this section can be classified as two groups. One group is developed from conventional plastic theory that the elasto-plastic constitutive models for granular materials are normally constructed using the following ingredients: the yield function or loading surface, the hardening law, the flow rule or plastic potentials usually derived from the stress-dilatancy relationship. Another group is to use fabric tensor to link the micro-mechanism and macro behaviour

of granular materials. Further, the numerical models based on many soil parameters characterising many aspects of soil fabric would not be directly useful for in-situ oriented engineering design at the present. As we argued before, the latter group requires a list of complicated mathematical formulations. For Tsutsumi and Hashiguchi (2005), they have shown the ability to capture the evolution of the strain path. However, they have introduced too many parameters without physical meanings and are difficult to be calibrated. In addition, The stress-strain response of granular materials under non-coaxial plasticity hasn't been studied. And then, Yu (2008) and his group presented a systemic study of non-coaxial behaviour in the context of pre-failure based on the double shearing theory and yield vertex theory. The simple formulations of these models made it possible for them to be applied into geotechnical applications. However, these fond models are restricted to the framework of soil strength isotropy. Therefore, it should be interesting and necessary to extend their work to account for the effects of soil anisotropy as granular soils are intrinsically anisotropic. In addition, intensive numerical applications of non-coaxial models into geotechnical problems remain an interesting research aspect. These are the main scopes of our project.

2.6 Chapter Summary

Previous research on the study of soil anisotropy and non-coaxiality of principal stresses and principal plastic strain rates was outlined in this chapter, and the relevant methods adopted in this research were presented in detail to provide an insight into non-coaxiality and soil anisotropy. The literature review can be summarised as follows:

- It is generally acknowledged that the natural behaviour of soil is anisotropic. Soil anisotropy, in reference to the inherent soil anisotropy and induced soil anisotropy, has been reviewed in detail, using both experimental investigations and micro-mechanic evidence.
- The anisotropic plasticity theory described by the variation of strength parameters with loading directions was briefly discussed in this section. It was identified that more literature is found to investigate the strength anisotropy described by the variation of cohesion with direction. However, recent experimental results on sand indicated a significance of soil anisotropy described by the variation of friction angles with the direction of principal stresses.

- Non-coaxial behaviour has been extensively observed in experiments over the decades. Some of the noted experimental apparatuses reported in the literature are the simple shear device and the hollow cylinder apparatus (HCA). The simple shear tests performed by Roscoe et al. (1967) and Roscoe (1970) were among the earliest experimental investigations that demonstrated that non-coaxiality is distinctly observed during the initial stage of shearing. The degree of non-coaxiality decreased when the shear strain increased. Results from hollow cylinder torsional shear tests showed that non-coaxiality is pronounced in pure rotational tests rather than monotonic loading tests. Previous research on the applications of DEM to investigate non-coaxial behaviour of granular soils was also presented. The micromechanics-based evidence and those experimental findings could be used to guide the development of more realistic continuum material models, through which non-coaxiality can be applied into analysing soil-structure interaction.
- Many plasticity theories have been extended to include the influence of non-coaxiality. Some phenomenological models and the soil models incorporated the fabric/loading interaction theory were briefly reviewed, with emphasis on the yield vertex (tangent) theory and double shearing theory developed by Yu (2008) and his group. Despite many researchers having applied non-coaxial models based on these theories to investigate shear banding and strain localisation, the roles of non-coaxial models in stress-strain responses and evolutions of orientations of principal stress and principal plastic strain rate were highlighted in this section. For the reason that current non-coaxial models within anisotropic regime required a number of parameters without physical meanings and were difficult to be calibrated, the development of a simple non-coaxial theory to be formulated in an anisotropic framework was shown to be required for granular materials. More extensive, complicated numerical applications of non-coaxial soil models into geotechnical engineering were shown to be required as it is one of the preliminary tools for the design of geotechnical projects.

Chapter 3

Formulation and numerical implementation of the non-coaxial soil model

3.1 Introduction

The literature review in Chapter 2 provided an overview of previous research on one aspect of the fundamental mechanics of soils, non-coaxial behaviour; with a particular focus on constitutive modelling using plasticity theory. Several authors including Bardet (1991); Hashiguchi and Tsutsumi (2003); Lashkari and Latifi (2008) have developed non-coaxial constitutive models that can be applied to study bifurcation and strain localisation of granular materials. On the other hand, Yuan (2005); Yu (2006); Yu and Yuan (2006); Yang and Yu (2006*a*; *b*); and Yu (2008) have made great efforts to study the stress-strain behaviour of granular materials under non-coaxial plasticity. However, their work is restricted to the assumption of soil strength isotropy. Generally, the natural characteristics of soils are anisotropic. This fact has been widely accepted during recent studies of soil behaviour. Non-coaxial behaviour of soils has been proven to be an aspect of soil anisotropy by many researchers (e.g. Yang, 2013). Hence, we are facing a challenge to develop a non-coaxial soil model within the framework of soil anisotropy, and the model should be simple and brief and the parameters should have clear physical meanings. Hence, it can be easily implemented into numerical platforms and applied to model complicated geotechnical problems. Taking these all into consideration, in this section, we present a plane strain, elastic-perfect-plastic

non-coaxial soil model with an anisotropic Mohr-Coulomb yield criterion following the general idea of Booker and Davis (1972). The out-of-plane stresses and strains are assumed irrelevant to the in-plane material responses. The formulation of non-coaxial constitutive equations is described by a general form in terms of plastic strain rates. In this form, the plastic strain rate is divided into two parts: the conventional component that is derived from the plastic potential theory and the non-coaxial component that is assumed to be tangential to an anisotropic yield surface (Yuan, 2005; Yu and Yuan, 2006). The anisotropic yield criterion is developed by generalising the conventional isotropic Mohr-Coulomb yield criterion to account for the effects of inherent soil anisotropy. The anisotropy is described by the variation of internal friction angles (angles of shearing resistance) with the direction of principal stresses. Two shape parameters n and β are introduced to define the yield curve in the deviatoric space. For simplicity, we only consider an initial anisotropy which remains unchanged throughout the loading process. Both the associativity and nonassociativity in the conventional plastic flow rules are used. The signs of the stress (rate) are chosen to be positive for compression. The proposed model can be reduced to the existing non-coaxial model developed by Yuan (2005) and Yu and Yuan (2006) when the shape parameter $n = 1.0$.

This chapter is concerned with the formulation and numerical implementation of the newly proposed non-coaxial soil model in the framework of soil anisotropy. The model is then numerically applied to predict the material non-coaxiality in simple shear tests. The development of constitutive equations of the non-coaxial model is detailed in Section 3.2; followed by the numerical implementation of the non-coaxial model presented in Section 3.3. The model is then used to investigate the simple shear problems in Section 3.4. Section 3.5 is the conclusion to the key findings of the previous sections.

3.2 Constitutive equations of the non-coaxial model

The total strain rate includes the elastic strain rate and the plastic strain rate, and is shown as:

$$\dot{\epsilon}_{ij} = \dot{\epsilon}_{ij}^e + \dot{\epsilon}_{ij}^p \quad (3.1)$$

where the superscripts e and p denote the elastic and plastic strains respectively.

The general rate equation for an elasto-plastic relationship is:

$$\dot{\sigma}_{ij} = D_{ijkl}^e (\dot{\epsilon}_{kl} - \dot{\epsilon}_{kl}^p) \quad (3.2)$$

where D_{ijkl}^e denotes the elastic stiffness modulus tensor. In our model, the elastic component is assumed to follow Hooke's law under plane strain conditions. The isotropic elastic stiffness modulus tensor is shown as:

$$D_{ijkl}^e = \frac{E\nu}{(1+\nu)(1-2\nu)} \delta_{ij} \delta_{kl} + \frac{2E}{(1+\nu)} (\delta_{ik} \delta_{jl} + \delta_{il} \delta_{jk}) \quad (3.3)$$

where E is Young's Modulus, ν is Poisson's ratio and δ_{ij} is Kronecker's delta, i.e., $\delta_{ij} = 1$ for $i = j$ and $\delta_{ij} = 0$ for $i \neq j$.

3.2.1 Development of the anisotropic Mohr-Coulomb yield criterion

Booker and Davis (1972) presented a general anisotropic Mohr-Coulomb yield condition in which they assumed that the curve in the deviatoric space $(\frac{\sigma_x - \sigma_y}{2}, \sigma_{xy})$ was a known function of the mean pressure p and the direction of the principal stress. As shown in Figure 3.1, Θ_p refers to the angle of deviation of the principal direction, where the only stresses are normal stresses, to the x -axis. Stresses are denoted $(\sigma_x, \sigma_y, \sigma_{xy})$, and it is impossible to attain states of stress lying outside the yield surface. The equation of the anisotropic Mohr-Coulomb yield criterion in Booker and Davis (1972) can be written in the following general form:

$$f(\sigma_x, \sigma_y, \sigma_{xy}) = R - F(p, \Theta_p) = 0 \quad (3.4)$$

where

$$R = \frac{1}{2} \sqrt{(\sigma_x - \sigma_y)^2 + 4\tau_{xy}^2} \quad (3.5)$$

$$p = \frac{1}{2}(\sigma_x + \sigma_y) \quad (3.6)$$

$$\tan(2\Theta_p) = \frac{2\sigma_{xy}}{\sigma_x - \sigma_y} \quad (3.7)$$

Recalling that for the isotropic Mohr-Coulomb yield criterion, the shape in the deviatoric space is a circle, where the radius of the circle depends on the value of mean

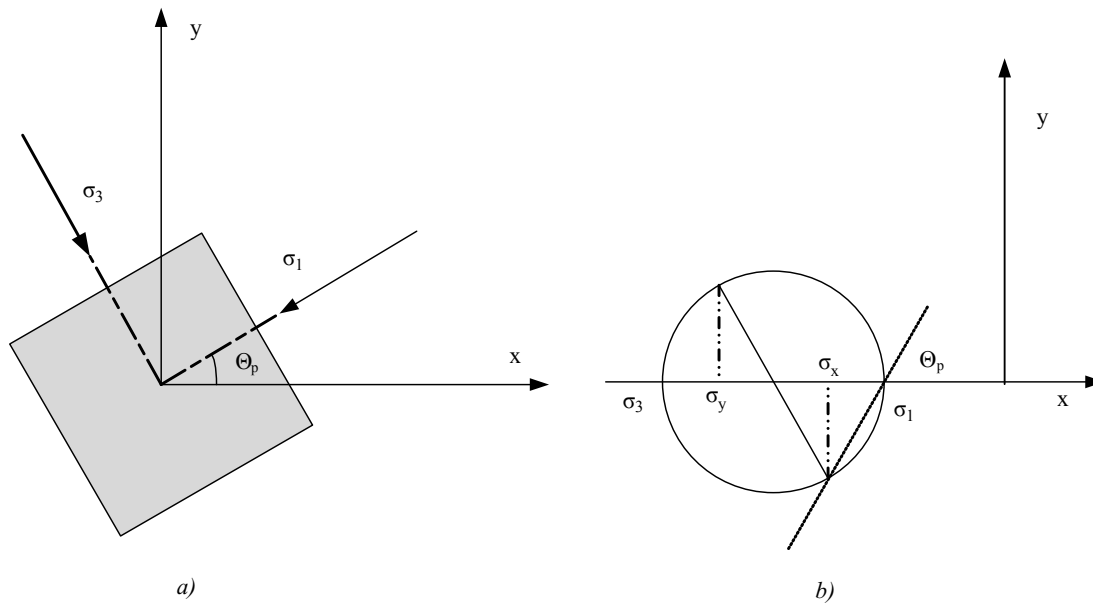


Figure 3.1 Definition of stress orientation angle.

pressure p . However, for the anisotropic Mohr-Coulomb yield criterion, the shape in the deviatoric space is assumed to be an ellipse for mathematical convenience, where the radius of the ellipse depends on the value of mean pressure and the direction of the principal stress (see Figure 3.2). As aforementioned, experimental evidence demonstrated that the peak internal friction angle (angle of shearing resistance) varies with the direction of the principal stress. This will help to develop clear expressions of the anisotropic Mohr-Coulomb yield criterion by geometric calculations.

As indicated in Figure 3.2, the cross section of the anisotropic yield criterion with a constant Z is assumed to be a rotational ellipse in the deviatoric space of (Z, Y) , with $X = (\sigma_x + \sigma_y)/2 = p$, $Y = \sigma_{xy}$ and $Z = (\sigma_x - \sigma_y)/2$. The yield surface in the (X, Y, Z) space is a cone. The centre of the anisotropic ellipse is assumed to be located at the base point of O . The major axis of the ellipse rotates 2β degree from the original Cartesian coordinate $X - Y$ to a new one $X' - Y'$. Now consider a point D which lies on the yield curve; the length OD is dependent on the mean pressure and the direction of the principal stress. In addition, it changes due to the variation of peak internal friction angles with the direction of the principal stress. Here we set the half length value of the major axis of the ellipse as A and the minor axis as B . The angle of rotation of the ellipse deviating from the x -axis is set as 2β .

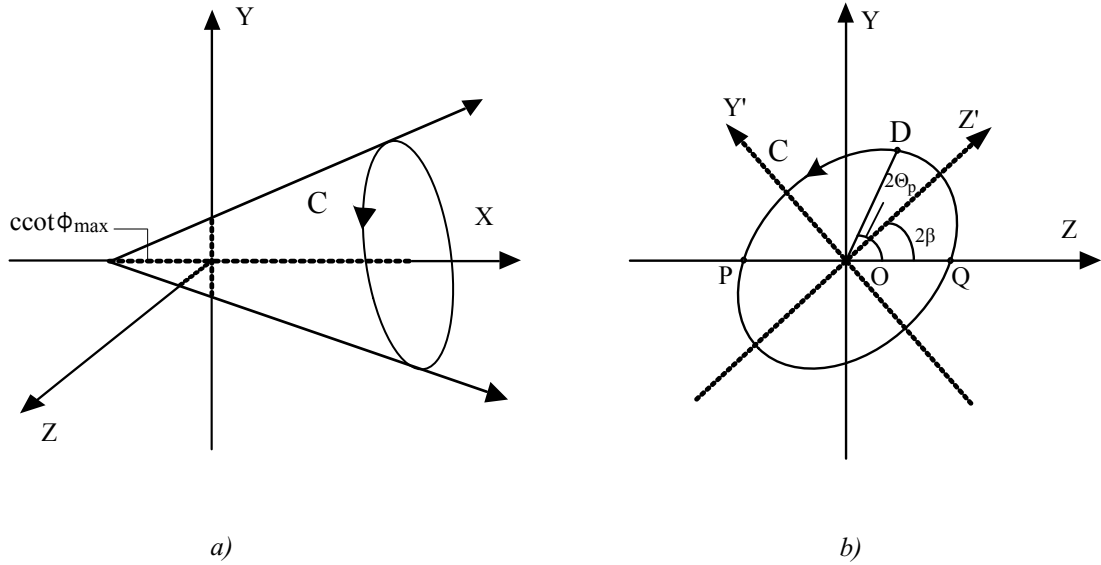


Figure 3.2 The ellipse anisotropic Mohr-Coulomb yield surface in: a) (X, Y, Z) space; b) (Z, Y) space.

ϕ_{max} and ϕ_{min} refer to the maximum and minimum peak internal friction angle respectively. The major (A) and minor (B) length of the ellipse depend on the maximum and minimum magnitude of the peak internal friction angle respectively. Two shape parameters n and β are added to the general isotropic Mohr-Coulomb yield criterion to form the anisotropic yield criterion:

1. $n = \frac{B}{A} = \frac{\sin\phi_{min}}{\sin\phi_{max}}$, where the range of n is between 0 and 1. In particular, the isotropic Mohr-Coulomb yield criterion is retrieved when $n = 1.0$.
2. β refers to an angle when the major principal stress, corresponding to the case of the maximum peak internal friction angle, is inclined to the deposition direction; and β ranges from 0 to $\frac{\pi}{2}$.

As shown in Figure 3.2, the value of A can be geometrically obtained as:

$$A = (p + ccot\phi_{max}) \cdot \sin\phi_{max} \quad (3.8)$$

where c is the cohesion of materials.

Using parametric equations of an ellipse and assuming a point D on the ellipse, we have:

$$\begin{cases} \overline{OD}\cos(2\Theta_p - 2\beta) = A\cos\alpha \\ \overline{OD}\sin(2\Theta_p - 2\beta) = nA\sin\alpha \end{cases} \quad (3.9)$$

where α denotes the geometrically parametric angle of an ellipse.

By eliminating the parametric angle α in Equation 3.9, the expression of \overline{OD} can be obtained as:

$$\overline{OD} = \frac{nA}{\sqrt{n^2 \cos^2(2\Theta_p - 2\beta) + \sin^2(2\Theta_p - 2\beta)}} \quad (3.10)$$

The yield curve takes the form in terms of (p, Θ_p) as follows:

$$F(p, \Theta_p) = \frac{nA}{\sqrt{n^2 \cos^2(2\Theta_p - 2\beta) + \sin^2(2\Theta_p - 2\beta)}} \quad (3.11)$$

Substituting A from Equation 3.8 into Equation 3.11 gives us:

$$F(p, \Theta_p) = \frac{n \sin \phi_{max}}{\sqrt{n^2 \cos^2(2\Theta_p - 2\beta) + \sin^2(2\Theta_p - 2\beta)}} \cdot (p + c \cot \phi_{max}) \quad (3.12)$$

Here we can also define friction angles with the direction of the principal stress as:

$$\sin \phi(\Theta_p) = \frac{n \sin \phi_{max}}{\sqrt{n^2 \cos^2(2\Theta_p - 2\beta) + \sin^2(2\Theta_p - 2\beta)}} \quad (3.13)$$

In summary, simple forms of the anisotropic Mohr-Coulomb yield condition can be defined as follows:

$$f(\sigma_x, \sigma_y, \sigma_{xy}) = R - F(p, \Theta_p) = 0 \quad (3.14)$$

where

$$F(p, \Theta_p) = (p + c \cot \phi_{max}) \cdot \sin \phi(\Theta_p) \quad (3.15)$$

and,

$$\sin \phi(\Theta_p) = \frac{n \sin \phi_{max}}{\sqrt{n^2 \cos^2(2\Theta_p - 2\beta) + \sin^2(2\Theta_p - 2\beta)}} \quad (3.16)$$

3.2.2 Discussion of the type of the ellipse

Oda (1972c) mentioned that the void and contact normal columns begin to break down and the soil fabric is altered when the peak stress is achieved. In this situation, it seems that induced anisotropy has a negligible effect on the internal friction angle of the soil. In addition, Symes et al. (1984) performed a series of torsional shear tests on medium-loose Ham River sand. They determined that the friction angle is relatively unaffected by previous stress rotation if the loading direction is given; which corroborated the findings from Oda (1972a). Hence in this chapter, attention is drawn to materials with an initial anisotropy which remains unchanged throughout the loading process. In other words, the perfect plasticity theory is used.

As simplified from Booker and Davis (1972), the proposed ellipse anisotropic Mohr-Coulomb yield criterion can be used to describe initial soil strength anisotropy. Moreover, the additional two parameters demonstrate clear physical meanings. However, it should be noted that it is only a particular case to determine the yield curve in the deviatoric space. It assumes that the centre of the anisotropic ellipse to be located at the base point O . Recent experimental observations by using the HCA have suggested that for a given value of b ($b = (\sigma_2 - \sigma_3)/(\sigma_1 - \sigma_3)$ is the intermediate principal stress parameter), the friction angle reduces with an increase in α (α is an orientation of the minor principal compressive stress with respect to the horizontal direction) and it has a slight rebound at $\alpha = 90^\circ$ (Oda et al., 1978; Van Dyck, 2012; Yang, 2013). Hence, it seems in reality the maximum magnitude of the peak internal friction angle is obtained when the orientation of the major principal stress (i.e. the minor compressive stress) is parallel to the deposition direction. When the intermediate principal stress is taken into consideration, the maximum length from base point O to the failure envelope is observed for cases when $\alpha \approx 60^\circ$. The above observation was presented by Yang (2013) who carried out a series of drained monotonic shear tests on a Buzzard sand sample and Glass Ballotini with various α and b values in a HCA. Based on the above findings, a rotational ellipse is insufficient in describing the yield curve since it gives an equal length from the base point O to the failure envelope for both cases when the major principal stress is parallel (i.e. $\alpha = 0^\circ$) and perpendicular (i.e. $\alpha = 90^\circ$) to the deposition direction respectively. Hence, other types of the ellipse should be introduced to complement the rotational type. We give an example of an eccentric ellipse

anisotropic Mohr-Coulomb yield criterion in the Appendix.

3.2.3 Validation of the anisotropic yield criterion with experimental data

Experimental investigations from the laboratory can help to test the accuracy and limitations of the proposed anisotropic Mohr-Coulomb yield criterion. Oda et al. (1978) performed a series of plane strain tests to investigate the shear strength of sand by taking into account its initial fabric anisotropy. In their tests, the specimens had different values of tilting angle δ . δ refers to the angle of the bedding plane with respect to the maximum principal stress axis. Different values of the tilting angle led to significant variations in the peak deviatoric stress ($\sigma_1 - \sigma_3$) when the cell pressures (i.e. the minor principal stress σ_3) were equal to 49 and 196 kPa. Subsequently the failure envelope in the deviatoric space ($\frac{\sigma_x - \sigma_y}{2}, \sigma_{xy}$) was plotted. The friction angles obtained with different tilting angles from Oda's (1978) tests are presented in Table 3.1. It should be noted that $\Theta_p = \frac{\pi}{2} - \delta$.

Table 3.1 Experimental results from Oda et al. (1978) triaxial compression tests of Toyoura sand.

tilting angle $\delta(^{\circ})$	0	15	24	30	45	60	90
friction angle ($^{\circ}$) ($\sigma_3 = 49$ kPa)	46.857	47.39	48.59	48.622	49.337	50.496	51.534
friction angle ($^{\circ}$) ($\sigma_3 = 196$ kPa)	44.3	44.21	41.847	42.535	45.615	46.737	49.524

The correlations on the failure envelopes are performed between the anisotropic yield criterion and the experimental results as illustrated in Figure 3.3. The figures are plotted in the deviatoric space with (Z, Y) normalised by the mean pressure p . As indicated in both of the figures, it is obvious that the anisotropic yield failure model shows satisfactory agreement with the experimental data.

Table 3.2 Experimental results from Yang (2013) monotonic shear tests of Leighton Buzzard sand.

loading direction $\alpha(^{\circ})$	0	15	30	45	60	90
friction angle ($^{\circ}$) ($b = 0.2$)	40	39.15	38.693	37.712	34.837	35.163
friction angle ($^{\circ}$) ($b = 0.4$)	46.311	43.492	42.639	39.098	38.246	37.918

Yang (2013) conducted a range of monotonic shear tests on Leighton Buzzard sand with the b value ranging from 0.2 to 1.0 at different loading directions. The aim was

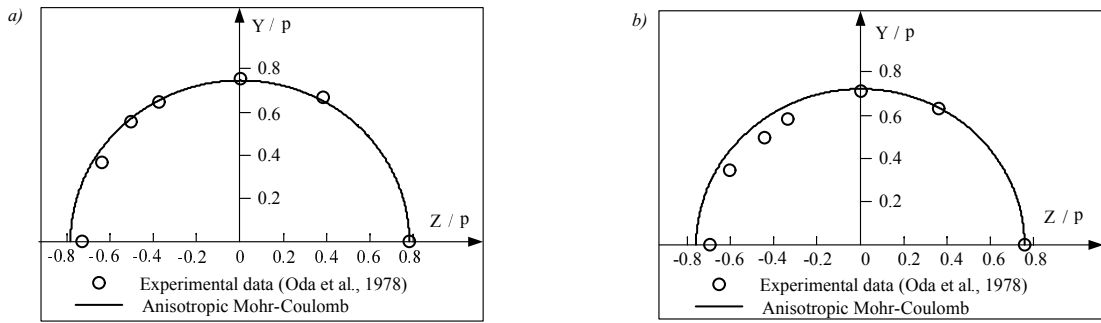


Figure 3.3 Validation with results of triaxial compression tests carried out by Oda et al. (1978) when: a) $\sigma_3 = 49$ kPa; b) $\sigma_3 = 196$ kPa.

to investigate the influence of b on the frictional shear resistance of soils. As the plane strain condition ($b \approx 0.2 - 0.4$) is taken into consideration, the peak internal friction angle varies with different values of α for a given value of b as presented in Table 3.2. The correlations on the failure envelopes are performed between the anisotropic yield criterion and the experimental results as illustrated in Figure 3.4. The findings are consistent with Oda et al. (1978). In general, it can be concluded that the newly proposed anisotropic Mohr-Coulomb yield criterion is a reasonable hypothesis.

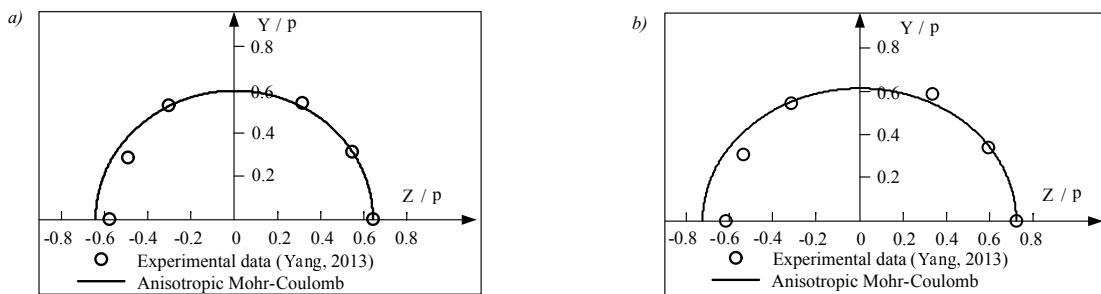


Figure 3.4 Validation with results of laboratory monotonic loading tests carried out by Yang (2013) when: a) $b = 0.2$; b) $b = 0.4$.

3.2.4 Non-coaxial plastic flow rule

It has been argued by Hashiguchi and Tsutsumi (2003) that it is possible to predict non-coaxiality of soils if the plastic potential is assumed to be an anisotropic function of the stress tensor. However, the plastic strain rate which is dependent on the stress state that is tangential to the yield curve, cannot be modelled under this assumption. Hence in our analysis, following Yu and Yuan (2006), the plastic strain rate is divided into two parts; where the coaxial component is generated by the plastic potential theory and the tangential non-coaxial component is assumed to be tangential to the anisotropic Mohr-

Coulomb yield surface proposed in the previous section. As shown in Figure 3.5, the general form of the plastic strain rate $\dot{\epsilon}_{ij}^p$ is shown as:

$$\dot{\epsilon}_{ij}^p = \dot{\epsilon}_{ij}^{pc} + \dot{\epsilon}_{ij}^{pt} \quad \text{if} \quad f = 0 \quad \text{and} \quad \dot{f} = 0 \quad (3.17)$$

where the superscripts *pc* and *pt* denote the conventional and tangential plastic strain rates respectively, and *f* denotes the yield surface.

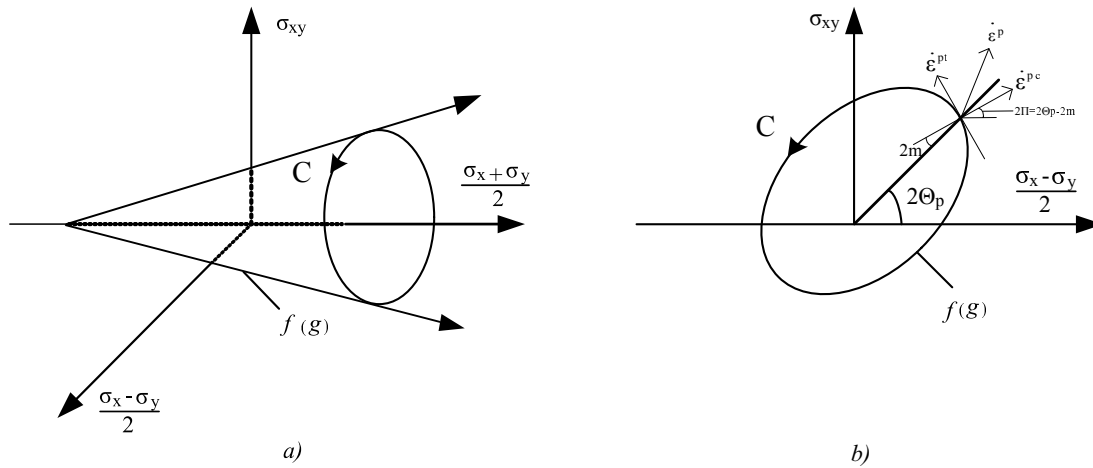


Figure 3.5 The non-coaxial plastic flow rule in: a) $(\frac{\sigma_x - \sigma_y}{2}, \sigma_{xy}, \frac{\sigma_x + \sigma_y}{2})$ space; b) $(\frac{\sigma_x - \sigma_y}{2}, \sigma_{xy})$ space.

Conventional component of the plastic strain rate

The conventional part of the plastic strain rate is normal to the yield curve, which is derived from the classic plastic potential theory:

$$\dot{\epsilon}_{ij}^{pc} = \dot{\lambda} \frac{\partial g}{\partial \sigma_{ij}} \quad (3.18)$$

where $\dot{\lambda}$ denotes a positive scalar and *g* denotes the plastic potential. If *g* = *f* then the associativity in the conventional plastic flow rule is used, otherwise the nonassociativity in the plastic flow rule is used.

Nonassociativity in the conventional plastic flow rule

As shown in Figure 3.6, *f* represents the anisotropic Mohr-Coulomb yield surface and *g* represents the plastic potential. The plastic potential takes into account the effect of the dilation angle. The dilation angle is assumed to vary with the direction of principal stresses. However, the flow direction in the deviatoric plane is assumed to be coinci-

dent with the direction of principal stresses for the nonassociativity in the conventional plastic flow rule. It should be noted this time the plastic potential is various corresponding to different stress states as shown in Figure 3.6. In the meantime, the range of the dilation angle drops between zero and the value of the internal friction angle. The plastic potential takes the following form:

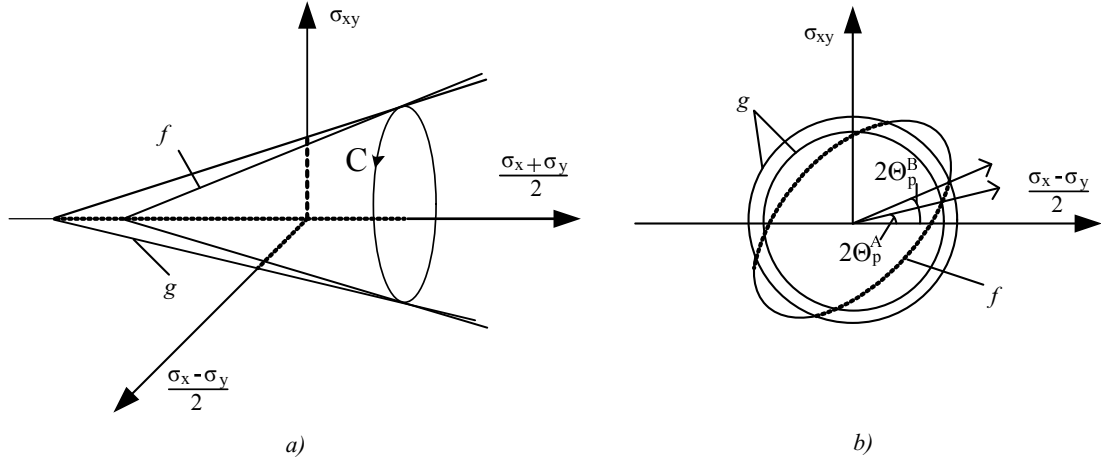


Figure 3.6 The illustration of plastic potential when the nonassociativity is used in: a) $((\sigma_x - \sigma_y)/2, \sigma_{xy}, (\sigma_x + \sigma_y)/2)$; b) $((\sigma_x - \sigma_y)/2, \sigma_{xy})$ space.

$$g = \sqrt{\frac{1}{4}(\sigma_y - \sigma_x)^2 + \sigma_{xy}^2} - \frac{1}{2}(\sigma_x + \sigma_y)\sin\psi(\Theta_p) = \text{constant}, \quad (3.19)$$

and,

$$\sin\psi(\Theta_p) = \frac{n \cdot \sin\psi_{max}}{\sqrt{n^2 \cdot \cos^2(2\Theta_p - 2\beta) + \sin^2(2\Theta_p - 2\beta)}} \quad (3.20)$$

where ψ_{max} denotes the maximum dilation angle.

Tangential component of the plastic strain rate

We introduce a tensor t_{ij} normal to the yield curve in the deviatoric plane, and the material derivative \dot{t}_{ij} can be expressed in terms of the stress rate tensor $\dot{\sigma}_{ij}$. The tangential non-coaxial plastic strain rate tensor can be written in terms of \dot{t}_{ij} as:

$$\dot{\epsilon}_{ij}^{pt} = k \cdot \dot{t}_{ij} \quad (3.21)$$

where k is a dimensionless scalar.

To simplify the mathematics, the variable m that is geometrically illustrated in Figure 3.5, will be introduced using the following definition:

$$\tan(2m) = \frac{1}{2F} \frac{\partial F}{\partial \Theta_p} \quad (3.22)$$

where F is as defined in Equation 3.15.

The orientation of the normal tensor t_{ij} with respect to the anisotropic Mohr-Coulomb yield curve in the deviatoric space can be defined as follows:

$$2\Pi = 2\Theta_p - 2m \quad (3.23)$$

where Θ_p is the angle between the direction of the major principal stress and the x -axis:

$$\cos(2\Theta_p) = \frac{\sigma_x - \sigma_y}{2q} \quad (3.24)$$

$$\sin(2\Theta_p) = \frac{\sigma_{xy}}{q} \quad (3.25)$$

and, the tensor t_{ij} can be expressed in terms of the vector \mathbf{T} :

$$\mathbf{T} = \begin{bmatrix} \cos 2\Pi & -\cos 2\Pi & 0 & 2\sin 2\Pi \end{bmatrix}^T \quad (3.26)$$

Based on the above definition, the material derivative \dot{t}_{ij} can be expressed in terms of the vector $\dot{\mathbf{T}}$ as:

$$\dot{\mathbf{T}} = \begin{bmatrix} \dot{t}_x & \dot{t}_y & \dot{t}_z & \dot{t}_{xy} \end{bmatrix}^T = \begin{bmatrix} \dot{\cos} 2\Pi & -\dot{\cos} 2\Pi & 0 & 2 \dot{\sin} 2\Pi \end{bmatrix}^T \quad (3.27)$$

By combining Equations 3.27, 3.23, 3.24, 3.25 and 3.22, these mathematical equations can be solved and the derivative \dot{t}_{ij} can be displayed in light of expressions of principal stress increments. Hence:

$$\dot{t}_{ij} = \frac{1}{k} \Lambda \dot{\sigma}_{ij} \quad (3.28)$$

The matrix Λ can be defined as:

$$\Lambda = \begin{bmatrix} a & -a & 0 & b \\ -a & a & 0 & -b \\ 0 & 0 & 0 & 0 \\ c & -c & 0 & d \end{bmatrix} \quad (3.29)$$

The expressions of a , b , c , d are listed below:

$$a = k \cdot H \cdot \left[-\frac{\sigma_{xy}}{4\sigma_{xy}^2 + (\sigma_x - \sigma_y)^2} \right] \quad (3.30)$$

$$b = k \cdot H \cdot \left[\frac{\sigma_x - \sigma_y}{4\sigma_{xy}^2 + (\sigma_x - \sigma_y)^2} \right] \quad (3.31)$$

$$c = k \cdot I \cdot \left[-\frac{\sigma_{xy}}{4\sigma_{xy}^2 + (\sigma_x - \sigma_y)^2} \right] \quad (3.32)$$

$$d = k \cdot I \cdot \left[\frac{\sigma_x - \sigma_y}{4\sigma_{xy}^2 + (\sigma_x - \sigma_y)^2} \right] \quad (3.33)$$

where

$$H = -2(\sin 2\Theta_p \cos 2m + \cos 2\Theta_p \sin 2m) \cdot (1 + m_{\Theta_p}) \quad (3.34)$$

$$I = 2(\cos 2\Theta_p \cos 2m - \sin 2\Theta_p \sin 2m) \cdot (1 + m_{\Theta_p}) \quad (3.35)$$

Recalling the anisotropic Mohr-Coulomb yield criterion, the definition of m_{Θ_p} is:

$$m_{\Theta_p} = \frac{4(1 - n^2) \cdot \cos(4\Theta_p - 4\beta) \cdot C - 4D^2}{C^2} \quad (3.36)$$

where

$$C = 2(n^2 - 1)\cos^2(2\Theta_p - 2\beta) + 2 \quad (3.37)$$

$$D = (1 - n^2)\sin(4\Theta_p - 4\beta) \quad (3.38)$$

Table 3.3 Summary of the parameters

Elastic model		
Young's modulus		E
Poission's ratio		ν
Plastic model		Data obtained
Shape parameter	$n = \frac{\sin\phi_{min}}{\sin\phi_{max}}$ β	ratio regarding the minimum and maximum internal friction angle rotation of the major length of the ellipse from the x-axis
non-coaxial coefficient	k	a positive scalar, following Harris (1993; 1995) and Yuan (2005)
nonassociativity	Ψ_{max}	simple/direct shear tests; HCA
cohesion	c	

3.2.5 Stress-strain relationship in the incremental form

The general rate equation for an elasto-plastic relationship is shown as:

$$\dot{\sigma}_{ij} = D_{ijkl}^{ep} \dot{\epsilon}_{kl} = D_{ijkl}^e (\dot{\epsilon}_{kl} - \dot{\lambda} \frac{\partial g}{\partial \sigma_{kl}} - N_{klmn} \dot{\sigma}_{mn}) \quad (3.39)$$

and the consistency condition equation for perfect plasticity is:

$$\left(\frac{\partial f}{\partial \sigma_{ij}} \right)^T \cdot \dot{\sigma}_{ij} = 0 \quad (3.40)$$

Substituting $\dot{\sigma}$ from Equation 3.39 into Equation 3.40, we can obtain the expression of the scalar multiplier $\dot{\lambda}$ as:

$$\dot{\lambda} = \frac{\overline{D_{ijkl}^e} \frac{\partial f}{\partial \sigma_{kl}} \epsilon_{ij}}{\frac{\partial f}{\partial \sigma_{uv}} \overline{D_{uvst}^e} \frac{\partial g}{\partial \sigma_{st}}} \quad (3.41)$$

in which a modified elasto-plastic matrix $\overline{D_{ijkl}^e}$ is introduced as:

$$\overline{D_{ijkl}^e} = (I_{ijuv} + D_{ijpq}^e N_{pquv})^{-1} D_{uvkl}^e \quad (3.42)$$

The non-coaxial elasto-plastic stress-strain matrix is shown as:

$$D_{ijkl}^{ep} = \left[\overline{D_{ijkl}^e} - \frac{\overline{D_{ijpq}^e} \frac{\partial g}{\partial \sigma_{pq}} \overline{D_{klmn}^e} \frac{\partial f}{\partial \sigma_{mn}}}{\frac{\partial f}{\partial \sigma_{uv}} \overline{D_{uvst}^e} \frac{\partial g}{\partial \sigma_{st}}} \right] \quad (3.43)$$

3.2.6 Summary of the parameters

In summary, there were two new shape parameters added to the general isotropic Mohr-Coulomb yield criterion to form the anisotropic yield criterion. An additional non-

coaxial plastic strain rate that due to the stress state tangential to the anisotropic yield criterion was introduced with a non-coaxial coefficient describing its degree. All the parameters that are used in this model are listed in the following table.

3.3 Numerical implementation of the non-coaxial model

3.3.1 The FE computational software: ABAQUS

ABAQUS is a suite of software applications for finite analysis and computer-aided engineering. It was originally written and maintained by Hibbitt, Karlsson and Sorensen, Inc in 1978, and is employed to simulate the behaviour of solids and structures under externally applied load. The developers of ABAQUS demonstrated a thorough understanding of continuum mechanics and thus ABAQUS is generally known as a highly sophisticated, general purpose finite element program. Its main strength is that it is satisfactory for non-linear calculations. The ABAQUS product consists of four core software products. They are listed as ABAQUS/CAE, ABAQUS/CFE, ABAQUS/Standard and ABAQUS/Explicit.

ABAQUS has a very extensive elemental library. It can provide a sufficient amount of material modelling capabilities. It was initially designed to address non-linear physical behaviour, and it currently allows for a user-defined stress-strain law to be incorporated with the user-defined material subroutine (UMAT), which can be written in Fortran language. Hence, it is chosen as the numerical platform for the implementation of the newly proposed non-coaxial model.

The UMAT can be used to define the mechanical, constitutive behaviour of a material. It will be called at all material points at each iteration of every increment. At the start of each increment, the material state (e.g. stress, solution-dependent state variables and predefined field variables) is transferred to UMAT from ABAQUS main program. The material state should then be updated to its new value at the end of the increment. In the meantime, the material Jacobian matrix $\partial\Delta\boldsymbol{\sigma}/\partial\Delta\boldsymbol{\epsilon}$ must be returned to the main program via UMAT. This matrix will be dependent on the integration scheme used if the constitutive model is in rate form and is integrated numerically in the subroutine. It is worth noting that one major determinant of the convergence of the solution should be the accuracy of determining the Jacobian matrix. In other words, the accuracy has

a significant influence on computational efficiency. Therefore, the main task of the following subsection is to determine the Jacobian matrix and the integration scheme of the constitutive equations.

3.3.2 A hyperbolic anisotropic Mohr-Coulomb yield function

For the sake of implementation of geotechnical constitutive laws into finite element analysis, many technical problems must be taken into consideration. Great efforts must be made for parametric control in finite element analysis allowing the newly proposed theory to run successfully in finite element codes.

For the plane strain assumption, the yield curve of the proposed anisotropic Mohr-Coulomb yield condition is a cone. When it is used in displacement finite element analysis, we should note that the yield surface presents computational difficulties due to the gradient discontinuities which occur at the tip when intersecting with the p -axis (see point *A* in Figure 3.7 a). To avoid such difficulties, a hyperbolic approximation at the tip of the yield curve can be used to eliminate singularity. The curve then becomes both continuous and differentiable and can be fitted to the anisotropic Mohr-Coulomb yield locus by adjusting just one parameter a (Abbo, 1997). A further advantage of this type of approximation is that it asymptotes rapidly to the anisotropic Mohr-Coulomb yield surface when the compressive hydrostatic stress increases.

When the tangential part of the plastic strain due to non-coaxiality, is perpendicular to the p -axis at the tip when cutting the p -axis, careful attention must be paid. Under this situation, the direction of the plastic strain is not distinctly determined. Hence, for simplicity, we treat the non-coaxial plastic strain to be zero at this very special point (see point *B* in Figure 3.7 a).

The expression of the straight line can be determined directly from Equation 3.15 and the slope of the straight line is given by $\sin\phi_{\Theta_p}$. As shown in Figure 3.7 a, the straight line intercepts the p -axis at $p = -ccot\phi_{max}$. Following Zienkiewicz and Pande (1977) and Abbo (1997), a close straight line which defines the Mohr-Coulomb yield surface can be obtained by using an asymptotic hyperbola. The general equation of such a

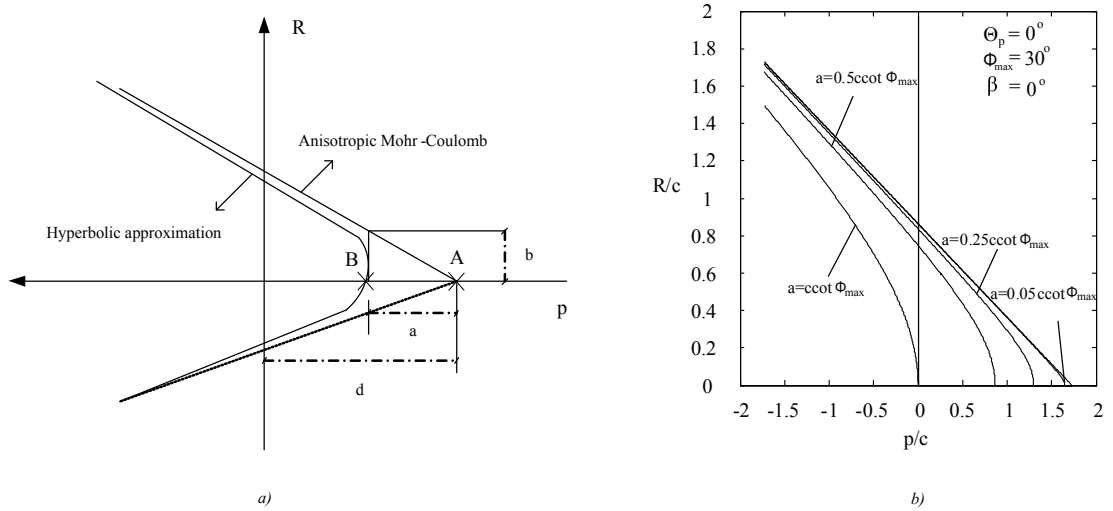


Figure 3.7 a) Hyperbolic approximation of the anisotropic Mohr-Coulomb yield curve; b) Parametric study of a .

hyperbola, in (p, R) space, is shown as follows:

$$\frac{(p-d)^2}{a^2} - \frac{R^2}{b^2} = 1 \quad (3.44)$$

where a , b and d are distances shown in Figure 3.7 a.

Equating the slope, the intercept of the anisotropic Mohr-Coulomb yield surface to the slope and the intercept of the hyperbolic asymptote yields the relation as:

$$\frac{b}{a} = \sin\phi_\Theta, d = -ccot\phi_{max} \quad (3.45)$$

Then substituting Equation 3.45 into Equation 3.44 gives the yield criterion as:

$$f = \sqrt{\left(\frac{\sigma_x - \sigma_y}{2}\right)^2 + \sigma_{xy}^2} + a^2 \sin^2 \phi_\Theta - (p + ccot\phi_{max}) \sin \phi_\Theta = 0 \quad (3.46)$$

where the positive branch of the hyperbola has been chosen. This function can be made to model the anisotropic Mohr-Coulomb yield function as closely as desired by adjusting the parameter a . Moreover, the anisotropic Mohr-Coulomb yield function is recovered if a is set as zero. As indicated in Figure 3.7 b, the asymptotic hyperbola is almost identical to the anisotropic Mohr-Coulomb straight line when $|a| = 0.05ccot\phi_{max}$. Abbo (1997) pointed out that for $|a| \leq 0.25ccot\phi$, the hyperbolic surface closely represents the isotropic Mohr-Coulomb surface.

3.3.3 Numerical integration scheme

The stress-strain behaviour at each numerical integration point is generally nonlinear in elastoplastic problems. To determine the stresses at the end of a given displacement increment, it is necessary to integrate the stress-strain relationships over a known strain interval. One method for doing this is to integrate the constitutive law by automatically dividing the strain increment into a number of subincrements. The number of sub-steps required for each iteration point is usually determined by an empirical rule, whereas the determination of the size of the sub-step is found dependent on local non-linearity of the yield surface and the hardening law. For each of the above cases, the governing equations are formulated as a system of ordinary differential equations and are solved using adaptive integration procedures. Explicit and implicit methods are two approaches used in numerical analysis for obtaining numerical solutions of time-dependent ordinary and partial differential equations, as required in computational simulations of physical processes.

Perhaps one of the main advantages of the explicit method over implicit method is that this algorithm only requires first derivatives (in terms of stresses) of the yield surface and plastic potential. This makes the explicit method simpler to implement for complex constitutive laws. However, the implicit method requires second derivatives, which are both difficult and expensive to compute for many geotechnical models. Abbo (1997) concluded that the implicit schemes do not perform well in the vicinity of the corners of the Tresca and Mohr-Coulomb yield criteria, even when they were rounded, through analysing their results for footing problems. Under these considerations, the explicit method is used in our project.

The explicit forward Euler/modified Euler pair is a family of explicit methods. It requires determination of the intersection with the yield surface when the stresses experience a transition from an elastic state to a plastic state. It is usually invoked with some form of sub-incrementation and stress correction to improve its accuracy and efficiency. Details of the integration algorithm used in this project will be presented in the subsequent sections.

Yield surface intersection of elastic to plastic transition

During a typical iteration or load increment of an elastic-plastic analysis, the strain increments at each Gauss point are found from the nodal displacement increment using the strain-displacement relations. The equation of the relationship between the strain increment and the displacement increment can be defined as:

$$\Delta \boldsymbol{\varepsilon} = \mathbf{B} \Delta \boldsymbol{\mu} \quad (3.47)$$

where $\Delta \boldsymbol{\mu}$ represents nodal displacement increments, \mathbf{B} denotes the strain-displacement matrix and $\Delta \boldsymbol{\varepsilon}$ is the vector of incremental strains.

After computing the strains, the corresponding elastic stress increment can be defined as:

$$\Delta \boldsymbol{\sigma} = \mathbf{D}_e \Delta \boldsymbol{\varepsilon} \quad (3.48)$$

where \mathbf{D}_e is the elastic stress-strain matrix.

It should be noted that perfect plasticity is studied in this thesis, for which the subsequent yield surface at any instant is assumed to be unchanged. The hardening parameter is not included in the initial state. The initial stress $\boldsymbol{\sigma}_0$, the yield function f and the subsequent stress $\boldsymbol{\sigma}_0 + \Delta \boldsymbol{\sigma}$ are factors that should be taken into consideration when deciding whether or not the stress increment $\Delta \boldsymbol{\sigma}$ will induce a change of the stress state from elastic to plastic behaviour. As shown in Figure 3.8, the change from elastic behaviour to plastic behaviour must occur at $\boldsymbol{\sigma}_{int}$, i.e. $f(\boldsymbol{\sigma}_0) < 0$ and $f(\boldsymbol{\sigma}_0 + \Delta \boldsymbol{\sigma}_e) > 0$. We should further ascertain the fraction of $\Delta \boldsymbol{\sigma}_e$ which causes purely elastic behaviour. Such a situation may arise several times during the course of an elastoplastic finite element analysis and needs to be handled efficiently and accurately.

Here we introduce a parameter $FTOL$ as the small positive yield surface tolerance. Abbo (1997) has ascertained that suitable values for the yield surface tolerance typically range from 10^{-6} to 10^{-9} . As indicated in Figure 3.8, the exact yield condition $f(\boldsymbol{\sigma}) = 0$ has been replaced by the approximation $|f(\boldsymbol{\sigma})| \leq FTOL$. This allows for the effects of finite precision arithmetic and modifies the transition conditions shown above to $f(\boldsymbol{\sigma}_0) < -FTOL$ and $f(\boldsymbol{\sigma}_0 + \Delta \boldsymbol{\sigma}_e) > +FTOL$.

A problem now exists regarding the determination of which portion of $\Delta\sigma_e$ lies inside the yield surface. The onset of yielding when the stresses are at the yield surface intersection point, allows for σ_{int} to be determined. By introducing a scalar quantity Γ , the condition of the non-linear equation below is satisfied as follows:

$$f(\sigma_0 + \Gamma\Delta\sigma_e) = f(\sigma_{int}) = 0 \quad (3.49)$$

$\Gamma = 0$ indicates that $\Delta\sigma_e$ induces purely plastic deformation, while $\Gamma = 1$ indicates that $\Delta\sigma_e$ causes purely elastic deformation. Therefore, for a transition from elastic behaviour to plastic behaviour, the value of Γ drops between 1 and 0.

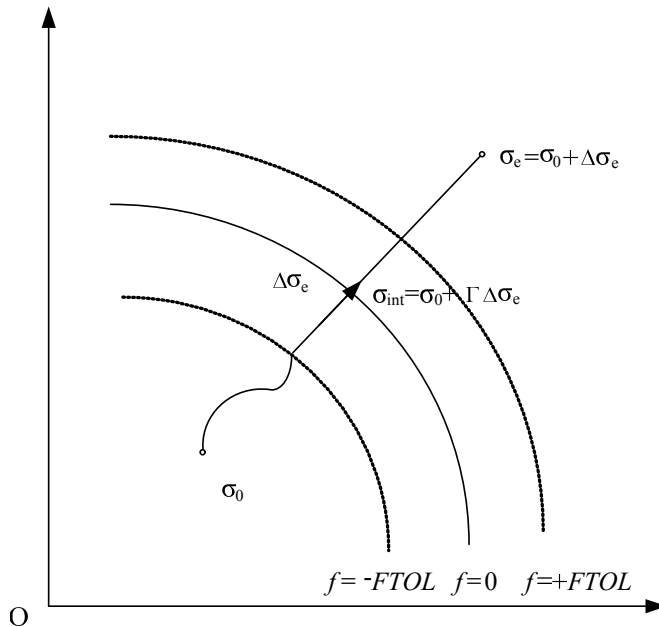


Figure 3.8 Yield surface intersection: Elastic to plastic transition.

The non-linear equation in light of variable Γ can be solved using several techniques. Sloan (1987) introduced the secant and Newton-Raphson method because in practice he found this algorithm typically converged within 4 to 5 iterations even with large load increments and a tight error tolerance on the stresses. However, as argued by Abbo (1997), the drawback of this algorithm is that it may diverge in some circumstances as it does not constrain the solution. The modified regula-falsi procedure proposed by Abbo (1997) demonstrates a suitable method to solve the non-linear equation of the yield surface intersection since it does not require the use of derivatives, and typically converges in four or five iterations even when used with stringent values of the toler-

ance $FTOL$. Hence, in this thesis, the modified regula-falsi intersection scheme is used and the procedure is shown below:

1. The stress $\boldsymbol{\sigma}_0$ and the stress increment $\Delta\boldsymbol{\sigma}_e$ are transferred from ABAQUS and entered into the user-defined material subroutine (UMAT). In the meantime, initial values of Γ_0 and Γ_1 are set to bound the intersection with the yield surface. The maximum number of iterations is set as $MAXITS = 50$.
2. The yield functions in terms of the three stress states are assigned as:

$$f_{save} = f(\boldsymbol{\sigma}_0) \quad (3.50)$$

$$f_0 = f(\boldsymbol{\sigma}_0 + \Gamma_0 \Delta\boldsymbol{\sigma}_e) \quad (3.51)$$

$$f_1 = f(\boldsymbol{\sigma}_0 + \Gamma_1 \Delta\boldsymbol{\sigma}_e) \quad (3.52)$$

3. Obtaining the value of Γ by solving the following non-linear equation:

$$\Gamma = \Gamma_1 - \frac{f_1}{f_1 - f_0} (\Gamma_1 - \Gamma_0) \quad (3.53)$$

and set:

$$f_{new} = f(\boldsymbol{\sigma}_0 + \Gamma \Delta\boldsymbol{\sigma}_e) \quad (3.54)$$

4. If $|f_{new}| \leq FTOL$ then go to step 8, else continue.
5. If $f_{new} \cdot f_0 < 0$ then:
 - set $\Gamma_1 = \Gamma$ and $f_1 = f_{new}$.
 - If f_{new} is of the same sign as f_{save} then set $f_0 = \frac{f_0}{2}$
 - else
 - set $\Gamma_0 = \Gamma_0$ and $f_0 = f_{new}$.
 - If $f_{new} \cdot f_{save} > 0$ then set $f_1 = \frac{f_1}{2}$.
6. Set $f_{save} = f_{new}$.
7. Repeat steps 3 to 6 for $MAXITS = 50$.

8. If convergence is not achieved after $MAXISTS = 50$, print error message and stop; if convergence is achieved, exit with Γ , and the fraction of $\Delta\boldsymbol{\sigma}_e$ that lies within the yield surface is ascertained.

In the absence of better information, the algorithm is started by specifying $\Gamma_0 = 0$ and $\Gamma_1 = 1$. The loop is terminated until the stress satisfies the condition $|f(\boldsymbol{\sigma}_0 + \Gamma\Delta\boldsymbol{\sigma}_e)| \leq FTOL$.

Negative plastic multiplier

An elastic to plastic transition may also occur if a stress point, initially lying on the yield surface, is subject to an unloading and reloading condition, particularly if the trial stress increment $\Delta\boldsymbol{\sigma}_e$ is large (Figure 3.9). This is indicated by a negative plastic multiplier which is defined in Equation 3.56 and $f(\boldsymbol{\sigma}_e) > +FTOL$. As indicated in Figure 3.9, there are two points when the stress path cuts the yield surface. Because the fraction of the stress that lies inside the yield surface is elastic, only the elastoplastic constitutive law beyond the last intersection point (see B in Figure 3.9) is required to be integrated.

In order to avoid the need to compute $\Delta\lambda$ explicitly, Abbo (1997) gave a discriminant of the negative plastic multiplier in terms of the cosine of the angle between a_0 and $\Delta\boldsymbol{\sigma}_e$, and the discriminant should be within a suitable tolerance. The equation is shown below:

$$\cos\theta = \frac{a_0^T \Delta\boldsymbol{\sigma}_e}{\|a_0\|_2 \|\Delta\boldsymbol{\sigma}_e\|_2} < LTOL \quad (3.55)$$

where $LTOL$ is the tolerance and $a_0 = \frac{\partial f}{\partial \boldsymbol{\sigma}}$. Similarly,

$$\Delta\lambda = \frac{a_0^T \Delta\boldsymbol{\sigma}_e}{a_0^T \mathbf{D}_e b_0} \quad (3.56)$$

where $b_0 = \frac{\partial g}{\partial \boldsymbol{\sigma}}$. They are evaluated at the initial stress state $\boldsymbol{\sigma}_0$.

This time the stress increment may cross the yield surface twice (see A and B in Figure 3.9). The procedure is comparable to the modified regula-falsi intersection scheme. However, the only difference is that the starting values Γ_0 and Γ_1 will be recalculated to guarantee that Γ_0 and Γ_1 bracket the second crossing. As $\Delta\boldsymbol{\sigma}_e$ is large in this

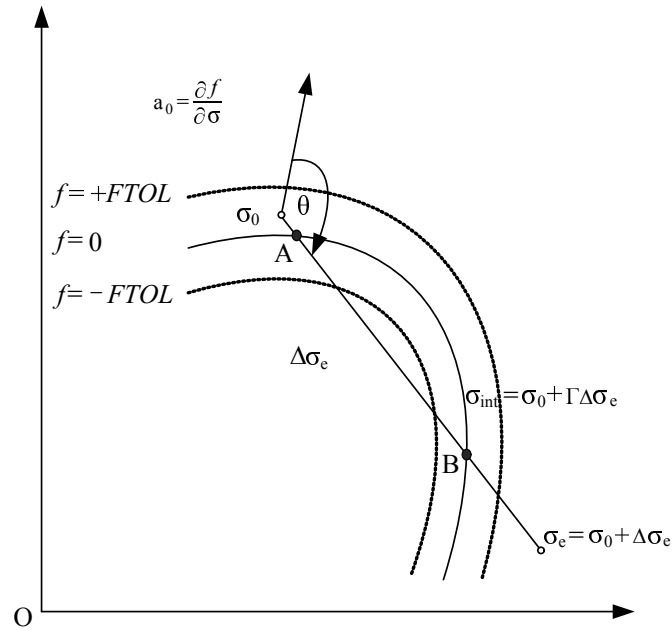


Figure 3.9 The illustration of the negative plastic multiplier.

situation, one way which is used to determine the starting values which bracket the desired crossing, is based on dividing the trial stress increment $\Delta\sigma_e$ into a number of smaller subincrements ($NSUB$). Hence, in the first iteration, the subincrement size is $\Delta\sigma_e/NSUB$, which corresponds to subincrements in Γ of $\Delta\Gamma = 1/NSUB$. Since the benefit gained from each subsequent restart diminishes fairly rapidly, these types of iterations should be limited in number, namely $MAXITS = 3$ and $NSUB = 10$ in our user subroutine. Details of determining the negative plastic multiplier are shown below:

1. Firstly, the stress σ_0 and the stress increment $\Delta\sigma_e$ are transferred from ABAQUS and entered into the user-defined material subroutine (UMAT).
2. Set $\Gamma_0 = 0$, $\Gamma_1 = 1$, $f_0 = f(\sigma_0)$ and $f_{save} = f_0$.
3. Do steps 4 to 5 $MAXITS$ times.
4. Find a suitable smaller size of Γ :

$$\Delta\Gamma = \frac{\Gamma_1 - \Gamma_0}{NSUB} \quad (3.57)$$

5. Do steps 6 to 7 $NSUB$ times.
6. Then calculate:

$$\sigma_1 = \sigma_0 + \Gamma\Delta\sigma_e \quad (3.58)$$

and

$$\Gamma = \Gamma_0 + \Delta\Gamma \quad (3.59)$$

7. If $f(\boldsymbol{\sigma}_1) > FTOL$, then

set $\Gamma_1 = \Gamma$.

If $f_0 < -FTOL$,

set $f_1 = f(\boldsymbol{\sigma}_1)$ and go to step 9.

else

set $\Gamma_0 = 0$ and $f_0 = f_{save}$ and the loop is terminated over steps 6 and 7.

else

set $\Gamma_0 = \Gamma$ and $f_0 = f(\boldsymbol{\sigma}_1)$.

8. If the iteration fails, print error message and stop.

9. Exit with new Γ_0 and Γ_1 .

10. Call the modified regula-falsi algorithm with the new Γ_0 and Γ_1 to locate the yield surface intersection.

The substepping scheme

As mentioned previously, the explicit method is advantageous as compared to the implicit method. This is because the former computes intermediate stresses using the elastoplastic stress-strain law instead of requiring to solve a system of nonlinear equations at each Gauss point. For a given strain, if the stresses at an integration point cause plastic yielding at each stage in the solution process, the unknown stresses can be found by solving Equation 3.60 (non-coaxial plasticity is included). The modified Euler explicit sub-stepping scheme proposed by Sloan (1987) and modified by Abbo (1997) is used here. The aim of this approach is to compute the stress-strain response over each substep by integrating the elastic-plastic constitutive matrix \mathbf{D}_{ep} . It is worth noting that the modified Euler scheme is accurate for very small time steps, and thus smaller substeps are required by subdividing ΔT ($0 < \Delta T < 1$). The error is controlled in the integration process of elastoplastic constitutive laws by selecting the size of each substep automatically over each time interval. This error control can be achieved by using a local error measure to automatically subincrement the imposed strain increment $\Delta \boldsymbol{\varepsilon}$. Obviously, the size of each subincrement may vary throughout the integration process instead of assuming substeps to an empirical standard and of the same size. The

stress-strain relationship in the incremental form is shown as:

$$\dot{\boldsymbol{\sigma}} = \mathbf{D}_{ep} \dot{\boldsymbol{\varepsilon}} = \Delta \boldsymbol{\sigma}_e - \Delta \lambda \mathbf{D}_e b - \mathbf{D}_e \Lambda \dot{\boldsymbol{\sigma}} \quad (3.60)$$

where $\boldsymbol{\sigma}$ denotes a vector of stresses, $\boldsymbol{\varepsilon}$ denotes a vector of strains, \mathbf{D}_{ep} denotes the elasto-plastic stress strain matrix, \mathbf{D}_e denotes the elastic stress strain matrix, Λ denotes the tangential non-coaxial matrix which can be found in Equation 3.29 and the superior dot represents a derivative with respect to time.

And recalling that:

$$\Delta \lambda = \frac{a^T \mathbf{D}_e \Delta \boldsymbol{\varepsilon}}{a^T \mathbf{D}_e b} = \frac{a^T \Delta \boldsymbol{\sigma}_e}{a^T \mathbf{D}_e b} \quad (3.61)$$

to begin with, the initial stress $\boldsymbol{\sigma}_0$ and the strain increment $\Delta \boldsymbol{\varepsilon}$ are used as inputs for the user-defined subroutine. As explained previously, the modified regula-falsi intersection scheme is used to determine the intersection point Γ with the yield surface when the stresses experience a transition from an elastic state to a plastic state (note that the negative multiplier λ should be checked at this stage). The stress $\boldsymbol{\sigma}_0 + \Gamma \Delta \boldsymbol{\sigma}_e$ lies within the yield surface which corresponds to the purely elastic component; whereas the stress increment $(1 - \Gamma) \Delta \boldsymbol{\sigma}_e$ induces purely plastic stress behaviour. Consequently $(1 - \Gamma) \Delta \boldsymbol{\varepsilon}$ causes purely plastic deformation. The elastoplastic stiffness matrix \mathbf{D}_{ep} will be integrated over the plastic strain step $(1 - \Gamma) \Delta \boldsymbol{\varepsilon}$. For the sake of obtaining smaller substeps, the substep strain is set as $\Delta T \cdot (1 - \Gamma) \cdot \Delta \boldsymbol{\varepsilon}$ ($0 \leq \Delta T \leq 1$). T is initially set as zero to ensure that only one substep is necessary during computation while ΔT is set as one to minimise the number of strain subincrements for each Gaussian point.

With the above given substep strain, the first estimate of the associated stress with a first order Euler approximation can be calculated as:

$$\Delta \boldsymbol{\sigma}_1 = \mathbf{D}_{ep}(\boldsymbol{\sigma}_0) \Delta T (1 - \Gamma) \Delta \boldsymbol{\varepsilon} \quad (3.62)$$

where,

$$\mathbf{D}_{ep} = \left(\overline{\mathbf{D}_e} - \frac{\overline{\mathbf{D}_e} \frac{\partial g}{\partial \boldsymbol{\sigma}_0} (\frac{\partial f}{\partial \boldsymbol{\sigma}_0})^T \overline{\mathbf{D}_e}}{(\frac{\partial f}{\partial \boldsymbol{\sigma}_0})^T \overline{\mathbf{D}_e} \frac{\partial g}{\partial \boldsymbol{\sigma}_0}} \right) \quad (3.63)$$

The second estimate of the associated stress can be evaluated at the end of the above substep as:

$$\Delta\boldsymbol{\sigma}_2 = \mathbf{D}_{ep}(\boldsymbol{\sigma}_0 + \Delta\boldsymbol{\sigma}_1)\Delta T(1 - \Gamma)\Delta\boldsymbol{\epsilon} \quad (3.64)$$

where,

$$\mathbf{D}_{ep} = \left(\overline{\mathbf{D}_e} - \frac{\overline{\mathbf{D}_e} \frac{\partial g}{\partial \boldsymbol{\sigma}_1} (\frac{\partial f}{\partial \boldsymbol{\sigma}_1})^T \overline{\mathbf{D}_e}}{(\frac{\partial f}{\partial \boldsymbol{\sigma}_1})^T \overline{\mathbf{D}_e} \frac{\partial g}{\partial \boldsymbol{\sigma}_1}} \right) \quad (3.65)$$

By using the modified Euler procedure, a more accurate estimate of the stresses at the end of the time interval can be obtained as:

$$\Delta\boldsymbol{\sigma} = \frac{1}{2}(\Delta\boldsymbol{\sigma}_1 + \Delta\boldsymbol{\sigma}_2) \quad (3.66)$$

It was proposed by Sloan (1987) and Abbo (1997) that there is a local truncation error in the Euler explicit procedure for a given strain increment $\Delta T(1 - \Gamma)\Delta\boldsymbol{\epsilon}$. The values are $O(\Delta T^2)$ and $O(\Delta T^3)$ for a Euler and a modified Euler solution respectively. We can subtract Equation 3.64 from Equation 3.66 to provide an estimation of the local error in terms of $\boldsymbol{\sigma}$:

$$M \approx \frac{1}{2}(\Delta\boldsymbol{\sigma}_2 - \Delta\boldsymbol{\sigma}_1) \quad (3.67)$$

It should be noted that the estimation of the local truncation error is only accurate to $O(\Delta T^2)$. This error can be used to select each substep of ΔT . Here a suitable tolerance $STOL$ is introduced to bound the relative error (shown in Equation 3.68). In other words, if the local truncation error $R_{error} \leq STOL$, the current strain subincrement is accepted and the stress increments are updated using Equation 3.66.

$$R_{error} = \frac{\|M\|}{\|\boldsymbol{\sigma}_0 + \Delta\boldsymbol{\sigma}\|} \quad (3.68)$$

Otherwise if $R_{error} > STOL$, the local truncation error is rejected and a smaller size of the substep is applied. Consider the next pseudo time step:

$$\Delta T_{new} = m\Delta T \quad (3.69)$$

where m is a scalar.

As aforementioned, since the local error estimate is accurate only to $O(\Delta T^2)$, the new local truncation error can be expressed associated with Equation 3.69 as:

$$(R_{error})_{new} \approx m^2 R_{error} \quad (3.70)$$

Since $(R_{error})_{new}$ is bounded by $STOL$, we can then obtain the range of m :

$$m \approx \left(\frac{STOL}{R_{error}} \right)^{\frac{1}{2}} \quad (3.71)$$

Generally, local extrapolation may lose accuracy due to strong non-linear behaviour, and hence a conservative value of m is chosen to minimise the number of rejected strain subincrements. Sloan (1987) introduced a factor of 0.8; however, Abbo (1997) found that a factor of 0.9 was reasonable and can reduce the computing time. The latter value had been verified by multiple numerical experiments on a wide variety of plasticity problems. m can now be re-written as:

$$m \approx 0.9 \left(\frac{STOL}{R_{error}} \right)^{\frac{1}{2}} \quad (3.72)$$

where the range of m should be from 0.1 to 1.1:

$$0.1 \leq m \leq 1.1 \quad (3.73)$$

Thus:

$$0.1\Delta T \leq \Delta T_{new} \leq 1.1\Delta T \quad (3.74)$$

Then the loop is terminated until $R_{new} \leq STOL$ and the process continues to the next step. The stresses are updated according to:

$$\boldsymbol{\sigma}_{T+\Delta T} = \boldsymbol{\sigma}_T + \Delta \boldsymbol{\sigma} \quad (3.75)$$

The newly updated stresses state should be checked whether they lie within the yield surface or diverge from the yield condition ($|f(\boldsymbol{\sigma})| > FOTL$). Potts and Gens (1985) found that it is necessary to apply some forms of stress correction because a cumulative effect does not satisfy the yield condition. They proposed a consistent correction method with a consistent total strain increment and successfully employed this method

to critical state soil models. The stress correction should obey the expression as shown below:

$$\delta \boldsymbol{\sigma} = -\delta \lambda \overline{\mathbf{D}}_e b_0 \quad (3.76)$$

$$\delta \lambda = \frac{f_0}{a_0^T \overline{\mathbf{D}}_e b_0} \quad (3.77)$$

However, Abbo (1997) pointed out that for cases that occur close to the vertices of the Mohr-Coulomb surface for a material when the nonassociativity in the conventional plastic flow rule is used, convergence may not be achieved. This behaviour is noticed when the corrected stress state is further from the yield surface than that of the uncorrected one. Hence, for these situations, the consistent correction method is abandoned for one iteration and the normal correction method is used with the total applied strain increment not preserved. Then Equation 3.76 is replaced by :

$$\delta \boldsymbol{\sigma} = -\frac{f_0 a_0}{a_0^T a_0} \quad (3.78)$$

Once the above condition is satisfied, the process is passed on to the next substep and then repeated from the estimate of the associated stress until the entire increment of strain is $\sum \Delta T = 1$.

The detailed procedure of the integration scheme is presented with the flow chart in Figure 3.10.

3.4 Prediction of material non-coaxiality in simple shear tests

The constitutive soil model is advanced by crystallising findings from laboratory tests. The measurements of soil parameters obtained from the laboratory are applied to computer-based analyses. The observations and data from laboratory testing can be used to check the validity of the proposed constitutive model and verify its performance under severe principal stress rotations.

We should be aware that the non-coaxial soil model proposed in this project is developed under plane strain assumptions. The simple shear tests with their rigid confine-

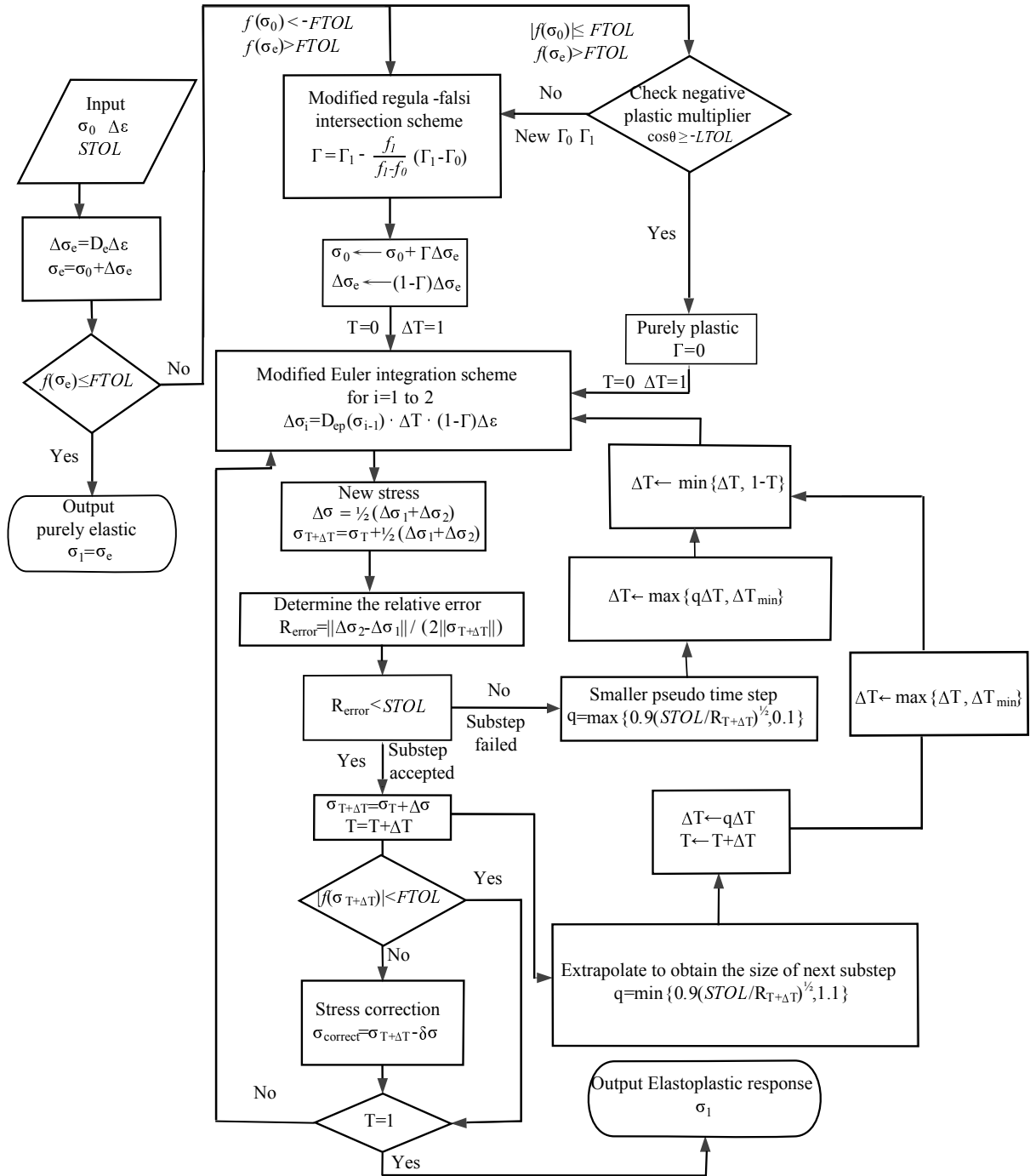


Figure 3.10 Flow chart of the explicit modified Euler algorithm.

ment parallel to the shear direction, are similar to many geotechnical problems that occur due to failure under plane strain conditions. Hence, simple shear tests will be used to assess the proposed non-coaxial soil model.

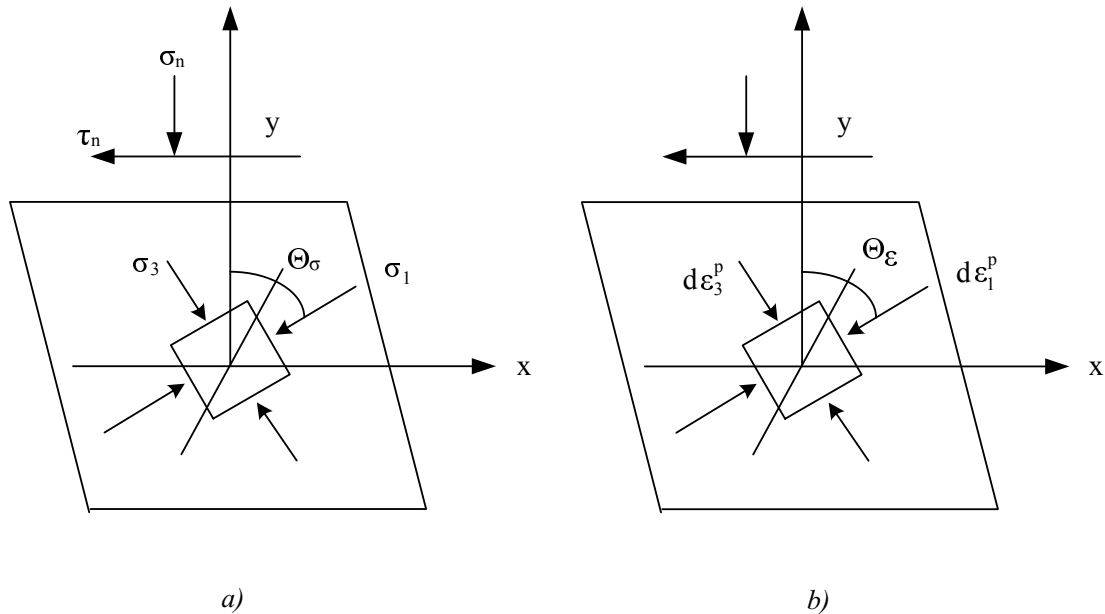


Figure 3.11 Definitions of directions of the principal stress and principal plastic strain rate.

There are two main types of simple shear test devices. The first one was initially developed by Kjellman (1951), who used a cylindrical specimen (80 mm in diameter and 20 mm in height). The system was laterally confined with a reinforced rubber membrane and a bunch of thin and evenly spaced rings. A prescribed simple shear strain was then applied by displacing the top boundary. Later, the device developed by Kjellman (1951) was further refined by Bjerrum and Landva (1966) at the Norwegian Geotechnical Institute (NGI). They replaced the thin rings by wires embedded in rubber membrane. The second device, as previously mentioned, was originally proposed by Roscoe (1953) for the development of critical state soil mechanics at Cambridge University. The specimen tested by the device was a parallel-piped, cylindrical specimen having dimensions 100 mm \times 100 mm \times 20 mm. The top and bottom of the specimen were enclosed by two rigid platens. Two hinged end flaps located on the two sides of the device were used to constrain vertical displacement. Simple shear strain was applied by rotating the two hinged end flaps when the bottom boundary of the device was displaced horizontally. The inner walls of these end flaps were assumed frictionless in order to avoid significant shear stresses.

Researchers at both Cambridge University and the NGI have made great efforts to study simple shear experiments. Airey et al. (1985) provided a general review of simple shear testing and highlighted both advantages and disadvantages of the test. They hypothesised that one significant limitation of all different techniques within the shear test ambit was that imposing a uniform normal and shear stress field on the shearing plane is non-achievable. In addition, neither of the two main types of simple shear techniques allowed for the development of complementary shear stresses on the vertical sides that were normal to the plane of deformation. As a result, the shear and normal stresses were consequently non-uniform corresponding to the experimental procedure. However, with respect to the simple shear apparatus developed at Cambridge University, certain middle sections of the sample have been observed to deform uniformly (Budhu, 1984; Airey et al., 1985; Budhu and Britto, 1987).

One of the earliest simple shear investigations made by Roscoe et al. (1967) and Roscoe (1970) showed that the axes of the corresponding principal strain increment did not coincide with the axes of the principal stress when subject to principal stress rotations. Their experimental results agree with Hill's (1950) elucidation that both of these two principal axes are in general non-coincident in an anisotropic material. Figure 3.11 illustrates the direction of the principal stress (Θ_σ) and the direction of the principal plastic strain rate (Θ_ϵ) in a Cartesian coordinate system $0(x,y)$. Θ_σ refers to the angle between the major principal stress and the y -axis (or the loading direction), whereas Θ_ϵ is expressed as the angle between the major principal plastic strain rate and the y -axis. Figure 3.12 shows the typical non-coaxial behaviour of the principal axes of stress and strain rate tensors (after Roscoe et al., 1967). It is evident from Figure 3.12 that non-coaxiality is distinctly observed during the initial stage of shear stress level subject to simple shear deformations. The degree of non-coaxiality then gradually reduces with an increasing shear strain. Finally the principal axes of stress and strain rate tensors become identical. Oda and Konishi (1974*b*) studied simple shear behaviour from a theoretical point of view. The relationship between the granular fabric, the orientation of principal stress axes and the mobilised stress ratio ($\frac{\tau}{\sigma_n}$) in the granular mass were obtained. They drew a conclusion that at least before the peak stress ratio $(\frac{\tau}{\sigma_n})_{peak}$, both the principal axes of stress and strain increments were non-

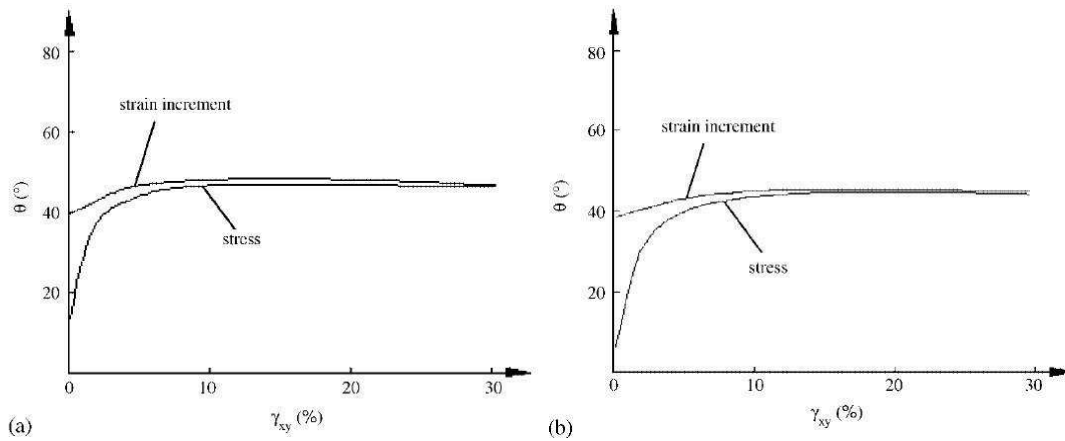


Figure 3.12 Experimental results showing orientations of principal stress and plastic strain rate (after Roscoe et al., 1967): a) $\sigma_y = 135\text{kPa}$; b) $\sigma_y = 396\text{kPa}$.

coincident. In parallel with Oda and Konishi (1974b), Oda and Konishi (1974a) built up a two-dimensional granular model using photoelastic cylinders packed randomly in a loading frame to simulate the shear deformation of sand. Non-coaxial behaviour of this granular material was observed through their research. In addition, as reviewed by Yu (2006), other studies reported in the literature demonstrated a similar non-coaxial behaviour in simple shear tests (e.g. Airey et al., 1985; Arthur et al., 1977; Matsuoka et al., 1988).

3.4.1 Model and parameters

For simplicity, a single isoparametric, eight-noded, plane strain reduced element *CPE8R* is used. All of the sides remain linear, and the top and bottom are kept parallel to their original directions throughout loading. The bottom nodes are fixed and both vertical and horizontal movements are not allowed under this assumption. A prescribed shear strain γ_{xy} is employed and the x -direction is constrained to have zero direct strain ($\epsilon_x = 0$). Hence, the sample is subjected to a rotation of the principal stress caused by the change in the induced shear stress τ_{xy} . A constant surface surcharge of $p = 100$ kPa is applied throughout the simulation. Loading and boundary conditions are both based on ideal assumptions since the objective is to validate numerically the proposed non-coaxial soil model. It should be noted here that σ_x is equal to σ_z throughout the shearing due to the adoption of plane strain conditions in the z -direction and full constraining of the movement in the x -direction. This follows the work by Yang and Yu (2006b). In addition, Hu (2015) in his constitutive modelling suggested that for simple

shear problems, it's more like that $\sigma_x = \sigma_z$ for plane strain conditions. The prescribed shear strain γ_{xy} is encountered in two sub-steps until it reaches 20% of its original value.

Since the directions of principal stresses and principal strain rate increments are different for a non-coaxial behaviour, the definition of the plastic strain rate direction is different from that of the principal stress direction (Figure 3.11 b):

$$\tan 2\Theta_\varepsilon = \frac{2\dot{\varepsilon}_{xy}^p}{\dot{\varepsilon}_x^p - \dot{\varepsilon}_y^p} \quad (3.79)$$

A cohesionless material is assumed in this section. A lateral stress ratio ($K_0 = \sigma_x/\sigma_y$) is taken as $K_0 = 0.5$ for normally consolidated soil. With respect to over-consolidated soil, it is taken as $K_0 = 2.0$. In order to avoid the singularity problem for numerical modelling in ABAQUS, the value of cohesion is set as 0.001 kPa to simulate a cohesionless material. One should note here that it has negligible effect on the results when $c < 0.1$ kPa. Hence, we choose a relative smaller value of c to confirm the cohesionless of the soil. Typical elastic constants are always assumed: Young's modulus $E = 2.6 \times 10^4$ kPa, Poisson's ratio $\nu = 0.3$. The maximum internal friction angle is set as $\phi_{max} = 30^\circ$ for all cases of simulation. The Young's modulus and internal friction angle are consistent with the same set of soil parameters as those used by Hansen (1961) since the analytical results of Hansen (1961) will be used to validate the numerical results. When the associativity in the conventional plastic flow rule is used, $\psi(\Theta_p) = \phi(\Theta_p)$; otherwise $\psi(\Theta_p) = 0^\circ$ as the nonassociativity in the conventional plastic flow rule is used. The parametric study is performed to investigate the influence of the initial stress state, the degree of soil anisotropy, the associativity/nonassociativity and the degree of non-coaxiality on the predictions of the stress-strain behaviours and principal stress and strain rate orientations under non-coaxial modelling. Material properties for all cases are shown in Table 3.4.

The tests are classified into two categories of groups; the first group presents the validation of the proposed non-coaxial model with analytical results of the stress ratio when the isotropic Mohr-Coulomb yield criterion is recovered (i.e. $n = 1.0$). The second group investigates the influence of initial stress states (K_0), soil anisotropy (n and β) and non-coaxiality (k) on the predictions of shear stress ratio and stress-strain be-

Table 3.4 Material properties for all numerical simulations

Cases	Anisotropic coefficient		associativity/ nonassociativity	Dilation angle	Non-coaxial coefficient	lateral stress ratio	
	n	$\beta(\circ)$	0-asso 1-non-asso	$\psi_{\Theta_p}(\circ)$	k	K_0	
Test 1	1.0	N/A	0	30	(0.0, 0.02)	(0.5, 2.0)	
Test 2			1	0			
Test 3	0.85	45	0	30	(0.0, 0.02)	(0.5, 2.0)	
Test 4			1	0			
Test 5			22.5	1			0
Test 6			0	1			0
Test 7	0.707	45	0	30	(0.0, 0.02, 0.05)	(0.5, 2.0)	
Test 8			1	0			
Test 9			22.5	0			30
Test 10	0	22.5	1	0	(0.0, 0.02, 0.05)	(0.5, 2.0)	
Test 11			0	30			
Test 12			1	0			

Note: the maximum peak internal friction angle $\phi_{max} = 30^\circ$, $c = 0.001\text{kPa}$, and $q = 100\text{kPa}$.

haviour.

3.4.2 Results and discussion

Yuan (2005) in his thesis reviewed the ratio of shear stress to normal stress acting on the slip line. Davis (1968) pointed out that for a purely frictional soil on the slip line, the Mohr-Coulomb failure criterion can be expressed in terms of the following stress ratio:

$$\left(\frac{\sigma_{xy}}{\sigma_y}\right)_{ultimate} = \frac{\sin\phi \cos\psi}{1 - \sin\phi \sin\psi} \quad (3.80)$$

where ϕ denotes the friction angle and ψ denotes the dilation angle.

In addition, the peak point of the stress ratio was defined by Hansen (1961) as follows:

$$\left(\frac{\sigma_{xy}}{\sigma_y}\right)_{peak} = \tan\phi \quad (3.81)$$

Oda and Konishi (1974a) hypothesised that the stress ratio $\frac{\sigma_{xy}}{\sigma_y}$ on the horizontal plane is related to the inclination of the major stress direction to the horizontal direction based on their simple shear tests. However, Davis (1968) identified that the horizontal plane can be classified as velocity characteristic and is therefore inclined at an orientation of $45^\circ + \frac{\psi}{2}$ to the direction of the major principal stress when the ultimate failure (i.e. the start of plastic deformation) is reached.

Shear stress ratio

The shear stress ratio is expressed as the shear stress (σ_{xy}) divided by the vertical stress (σ_y). All the figures (Figures 3.13 - 3.19) below are plotted as the shear stress ratio versus the shear strain.

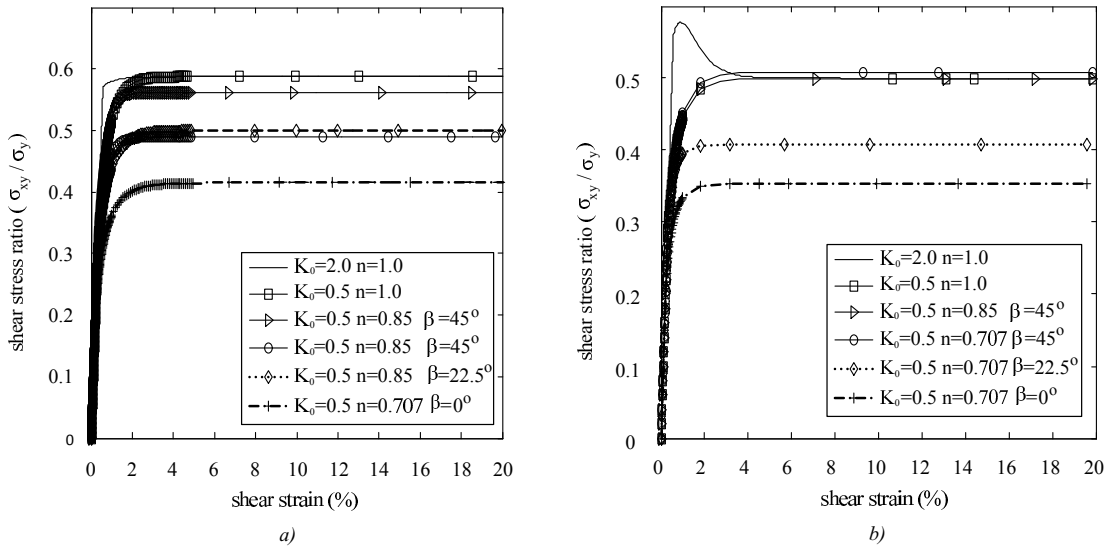


Figure 3.13 The influence of anisotropic coefficients on the predicted shear stress ratio : a) associativity; b) nonassociativity.

As indicated in Figure 3.13, the influence of the anisotropic coefficients (n , β) on the predictions of the shear stress ratio, is presented. In this case, the non-coaxial coefficient k is always set as zero. When the isotropic Mohr-Coulomb yield criterion is recovered, i.e. n equals 1.0, the ultimate value of the shear stress ratio $(\frac{\sigma_{xy}}{\sigma_y})_{ultimate} = 0.577$ and $(\frac{\sigma_{xy}}{\sigma_y})_{ultimate} = 0.499$ by assuming the associativity in the conventional plastic flow rule and the nonassociativity respectively, is irrespective of the magnitude of the lateral stress ratio K_0 . If the lateral stress ratio $K_0 = 2.0$, a distinct stress-strain softening tendency is observed when the nonassociativity in the conventional plastic flow rule is invoked with both $\phi_{max} = 30^\circ$ and $\psi_{max} = 0^\circ$ as shown in Figure 3.13 b. It is argued by Yuan (2005) that for the nonassociativity when $\psi < \phi$, it is possible that the coaxial material model can exhibit a strain-softening response with the combination of a high K_0 value and a low value of ψ in simple shear problems. This is consistent with the observation obtained in our analysis even if the perfect plasticity is assumed. The reason can be explained that in our analysis, the perfect plasticity is only described in terms of that the yield surface do not expand or contract. Hence,

the peak shear stress ratio should be distinctly determined for the same value of internal friction angle following Equation 3.80. It is independent of the dilation angle. However, the ultimate stress ratio is determined by the internal friction angle and the dilation angle following Equation 3.81. Here if the associativity in the conventional plastic flow rule is used (i.e. $\phi = \psi$), hence, the peak stress ratio equals to the ultimate stress ratio (i.e. $(\frac{\sigma_{xy}}{\sigma_y})_{ultimate} = (\frac{\sigma_{xy}}{\sigma_y})_{peak}$), there is no strain softening as shown in Figure 3.13 a. However, if the non-associativity in the conventional plastic flow rule is used, the ultimate stress ratio and the peak stress ratio are not the same. The stress path may pass the peak point to reach the ultimate point on the yield surface, which is dependent on the starting point (the lateral stress ratio K_0). Hence the strain softening can be observed. In our case, we can see that if $K_0 = 2.0$, the material can exhibit a stress-strain softening tendency even the perfect plasticity is assumed. Recalling the definition of the ultimate shear stress ratio defined in Equation 3.80, the analytical solutions should be 0.577 and 0.5 for the associativity and nonassociativity in the conventional plastic flow rules respectively. The analytical solution of the peak value is 0.577 as calculated from Equation 3.81. It is evident that the aforementioned numerical results shown in Figure 3.13 are consistent with these analytical calculations.

The two shape parameters n and β demonstrate a marked effect on numerical predictions of the ultimate shear stress. Smaller values of n and lower degrees of β result in a lower shear stress ratio excluding a particular case (i.e. $n = 1.0$ and $n = 0.85$ for the nonassociativity in the conventional plastic flow rule). However, the two parameters show negligible effect on the shape of the stress-strain response. In contrast, the initial lateral stress ratio K_0 affects the shape of the stress-strain curve by producing a strain-softening response.

Figures 3.14 - 3.19 present the influence of the non-coaxial coefficient k on the evolutions of the stress-strain relationship in the framework of both soil isotropy and soil anisotropy. In general, non-coaxial modelling leads to an apparent softening in stress-strain response at the early stage of shearing. A larger value of the non-coaxial coefficient results in a softer response in the stress-strain behaviour. However, with the increase in the shear stress level, all of the predicted stress-strain curves tend to be coincident at a limit state, irrespective of coaxial and non-coaxial modelling. These

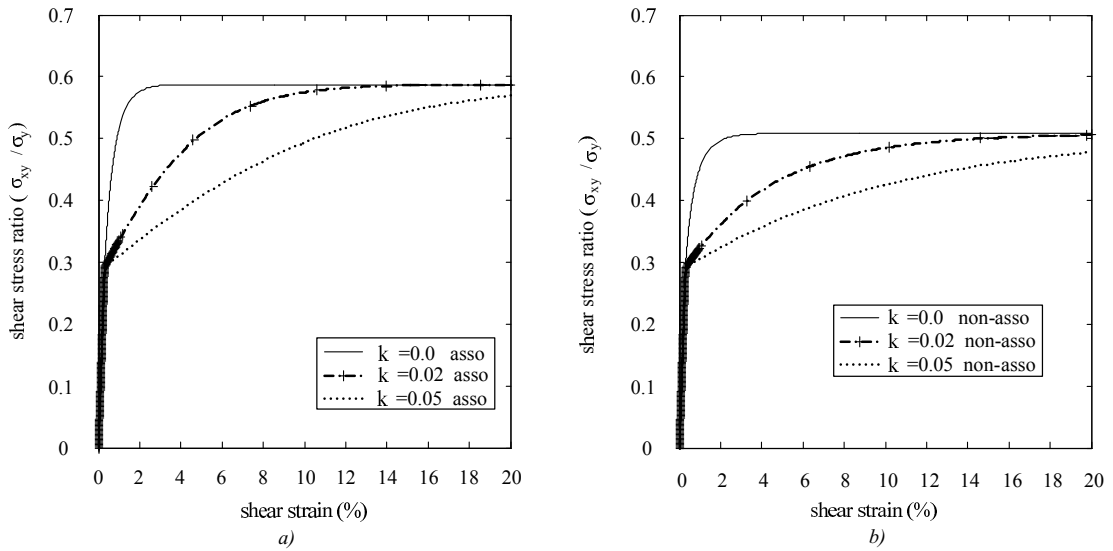


Figure 3.14 The influence of non-coaxiality on the predicted shear stress ratio with $K_0 = 0.5$ in: a) Test 1; b) Test 2.

findings are similar to conclusions drawn by Yuan (2005) and Yu and Yuan (2006) and consistent with experimental observations that prove non-coaxiality is distinct when the soil sample is subject to severe principal stress rotations. It should be noted that for cases when $n = 0.707$ and $\beta = 45^\circ$, the soil quickly develops plasticity. This is evident from plots of the stress path in latter analyses.

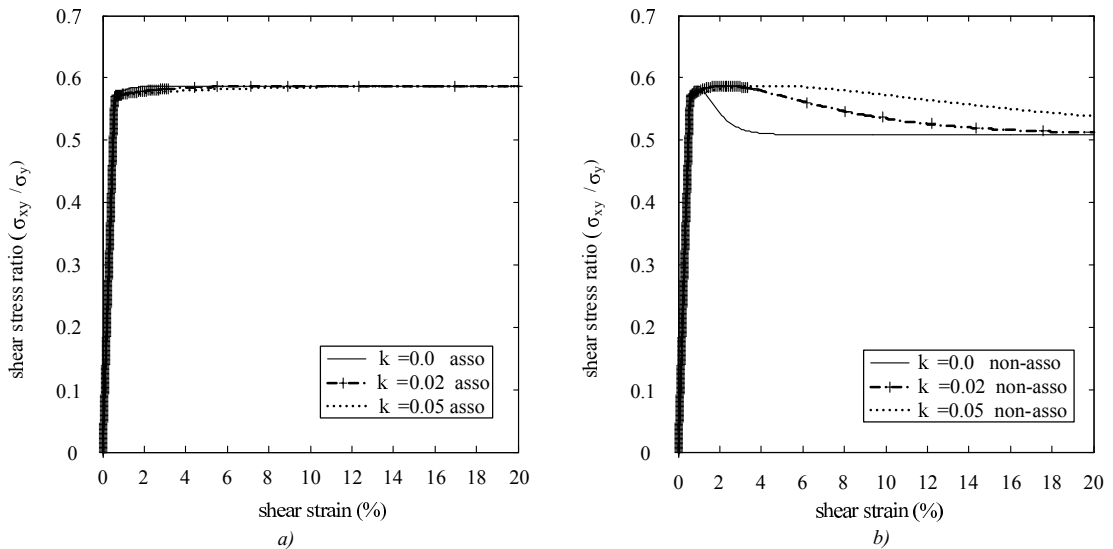


Figure 3.15 The influence of non-coaxiality on the predicted shear stress ratio with $K_0 = 2.0$ in: a) Test 1; b) Test 2.

With respect to the effect of the lateral stress ratio K_0 , the shape of the stress-strain evolution is different when the initial value of the lateral stress ratio K_0 is changed.

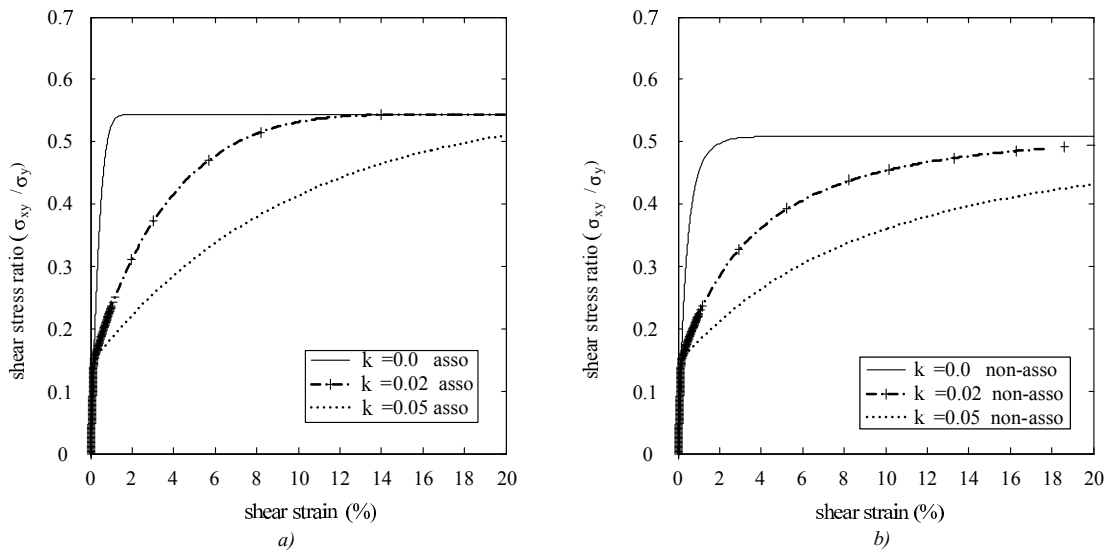


Figure 3.16 The influence of non-coaxiality on the predicted shear stress ratio with $K_0 = 0.5$ in: a) Test 7; b) Test 8.

However, no effects on the ultimate shear stress state are observed. For some particular cases, i.e. $K_0 = 2.0$ for over-consolidated soils; there is negligible difference between the shear stress ratios for coaxial and non-coaxial modelling when $n = 1.0$ (Figure 3.15 a) and $n = 0.707$, $\beta = 0^\circ$ (Figure 3.19 a) for the associativity in the conventional plastic flow rule. In other words, it can be expected that there are few principal stress rotations under this circumstance, which may result in the coincidence of the direction of the principal stress and principal plastic strain rate. It is interesting to see that for over-consolidated soils ($K_0 = 2.0$) using the nonassociativity in the conventional plastic flow rule, a strain softening behaviour is observed, and the ultimate stress ratios tend to be larger with larger values of k . This numerical observation recommends further studying as it has not yet been discussed in other research.

Orientations of the principal stress and principal plastic strain rate

Figures 3.20 and 3.21 show the pattern of orientations of the principal stress and principal plastic strain rate versus the shear strain when the anisotropic yield surface is reduced to its isotropic counterpart (i.e. $n = 1.0$). When the nonassociativity in the conventional plastic flow rule is used, the dilation angle ψ_{max} is set to be zero. With coaxial plasticity, the direction of the corresponding principal plastic strain rate always follows the change in the direction of the principal stress (see Figure 3.20 a and Figure 3.21 a). The ultimate orientations of the principal stress and principal plastic strain rate approach 60° when the associativity in the conventional plastic flow rule is used, and

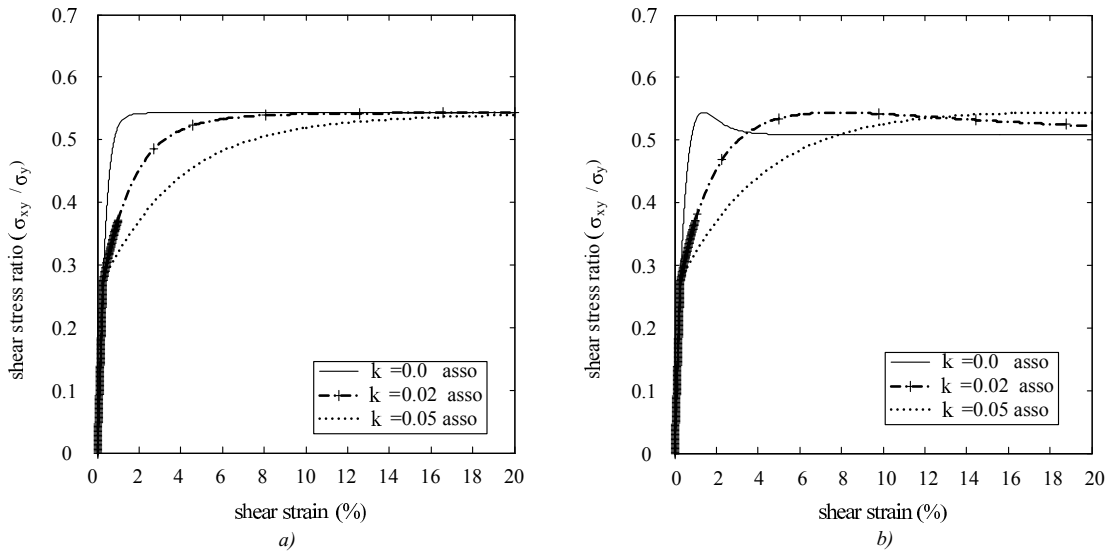


Figure 3.17 The influence of non-coaxiality on the predicted shear stress ratio with $K_0 = 2.0$ in: a) Test 7; b) Test 8.

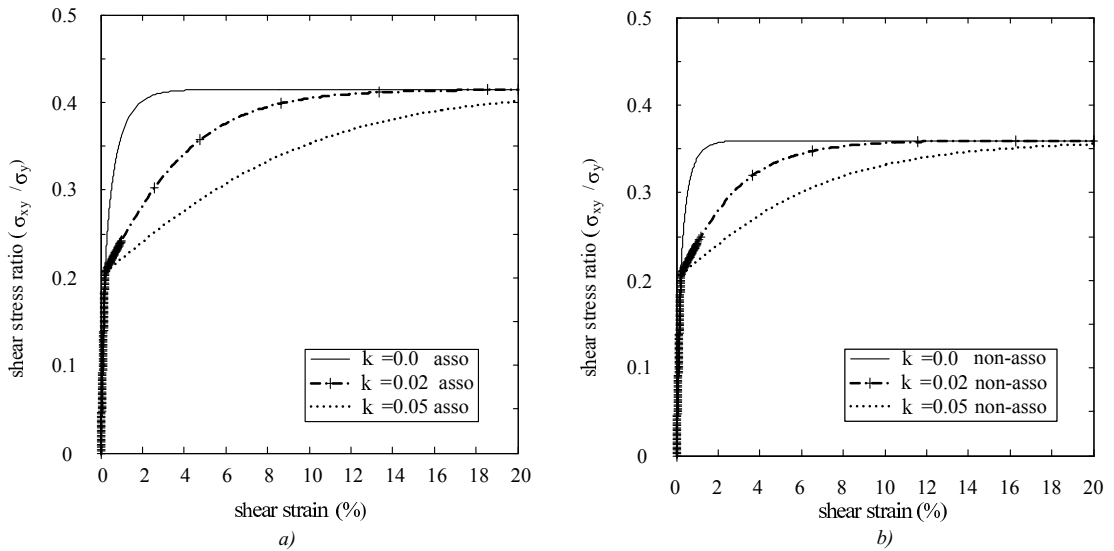


Figure 3.18 The influence of non-coaxiality on the predicted shear stress ratio with $K_0 = 0.5$ in: a) Test 11; b) Test 12.

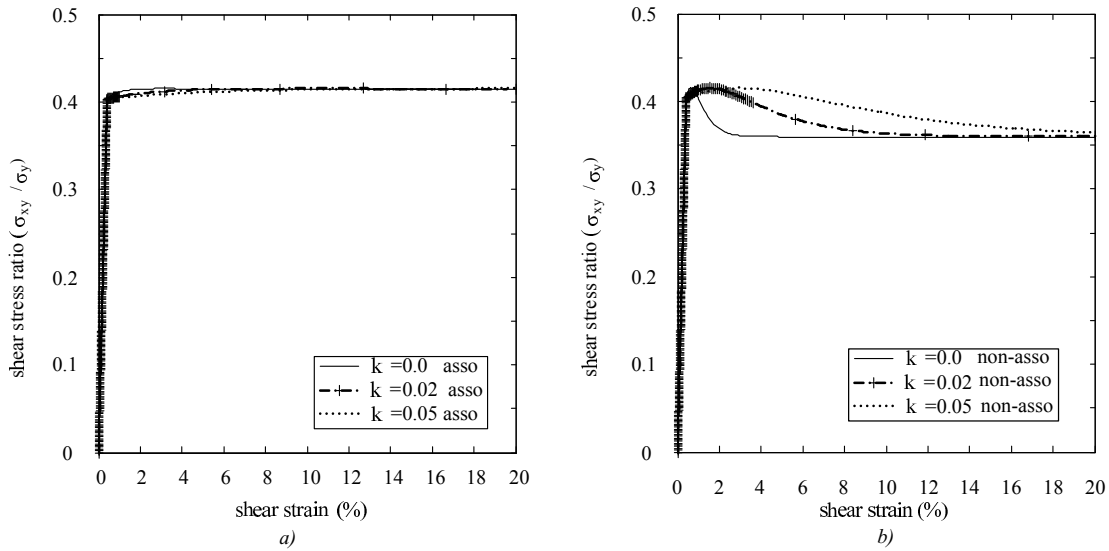


Figure 3.19 The influence of non-coaxiality on the predicted shear stress ratio with $K_0 = 2.0$: a) Test 11; b) Test 12.

45° when the nonassociativity in the plastic flow rule is used. This is in agreement with the study of Davis (1968), who pointed out that at the ultimate failure, any horizontal plane is always inclined at $45^\circ + \frac{\psi}{2}$.

Figures 3.22 - 3.26 present numerical results in the framework of soil anisotropy. It is interesting to see in Figures 3.22 a and 3.25 a that the directions of the principal stress and the principal plastic strain rate are not identical even if the tangential non-coaxial plasticity is assumed to be zero with the associativity in the plastic flow rule. This is because the function of the plastic potential for the associativity in the conventional plastic flow rule follows the same pattern as the function of the yield surface, which is an anisotropic function of the stress tensors. It is possible to predict non-coaxiality of soils if the plastic potential is assumed to be an anisotropic function of the stress tensors as mentioned by Tsutsumi and Hashiguchi (2005). However, the non-coincidence continues throughout the shear loading, which has not been shown in experimental observations. The reason may be the limitations of the proposed yield criterion as it is just one particular type of the ellipse. Results from the eccentric yield criterion are presented in the Appendix. It is obvious that the eccentric ellipse performs relatively better as the directions of the principal stress and principal plastic strain rate are almost identical for coaxial modelling when the associativity in the conventional plastic flow rule is assumed. However, as aforementioned, the formulation is complicated for the eccentric ellipse. Therefore, we would not go in details even the eccentric ellipse

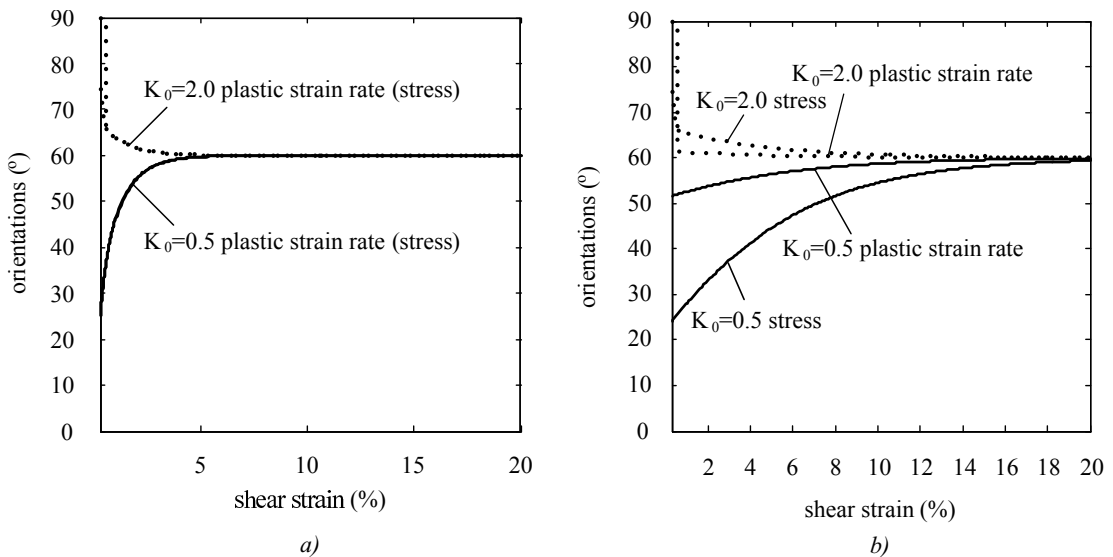


Figure 3.20 Numerical results of principal orientations of stress and plastic strain increment for the recovered isotropic Mohr-Coulomb yield condition in Test 1 : a) $k = 0.0$; b) $k = 0.02$.

performs better in this particular situation. In addition, it should be noticed that the model only accounts for initial soil anisotropy; strain hardening and strain softening which are induced by induced soil anisotropy, are neglected. In other words, we only consider the elastic perfectly plastic material behaviours. The yield cannot expand or contract. Hence, there always exists a deviation between the direction of the principal stress and the direction that is normal to the yield surface (i.e. the gradient of the plastic potential). Generally, since the direction of the plastic strain rate follows the gradient of the plastic potential, the direction of the principal stress and the direction of the plastic strain rate may not coincident even at a limit state when the deformation is plastic. In order to overcome the drawbacks of the proposed non-coaxial model to simulate simple shear tests, the nonassociativity in the conventional plastic flow rule is developed. The nonassociativity theory allows the direction of the principal stress and the gradient of the plastic potential to be identical. As shown in Figures 3.23 a, 3.24 a and 3.26 a, the directions of the principal stress and the direction of the principal plastic strain rate are coincident when the tangential non-coaxial plasticity is negligible.

In general, when the tangential non-coaxial coefficient is not equal to zero, a distinct non-coincidence of the direction of the principal stress and principal plastic strain rate is observed during initial shear stress levels. Nevertheless, the degree of non-coincidence decreases with the increase in the shear strain. The orientations tend to be identical at the limit state approaching the end of the shearing loading (see Figures

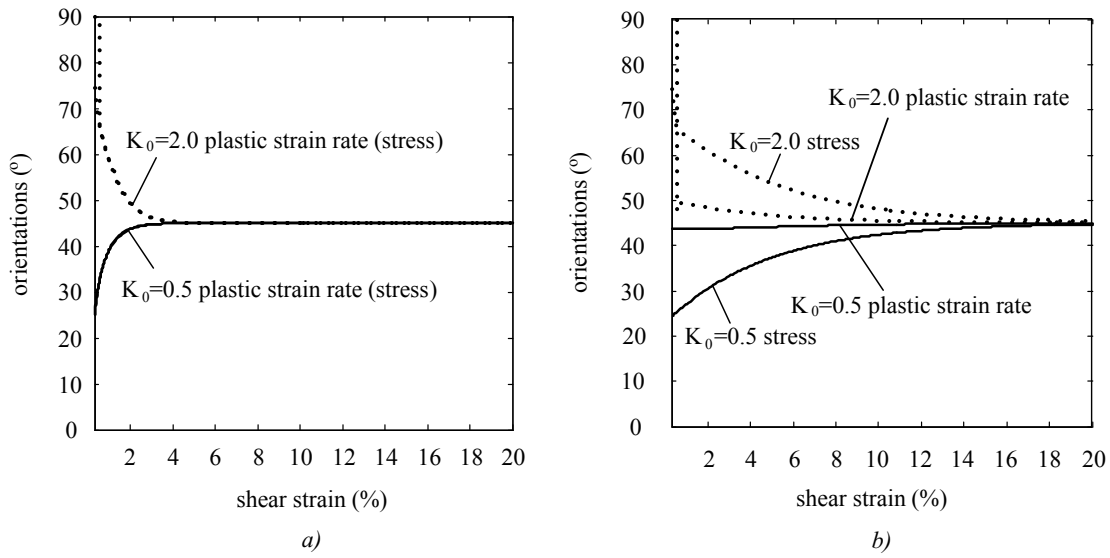


Figure 3.21 Numerical results of principal orientations of stress and plastic strain increment for the recovered isotropic Mohr-Coulomb yield condition in Test 2 : a) $k = 0.0$; b) $k = 0.02$.

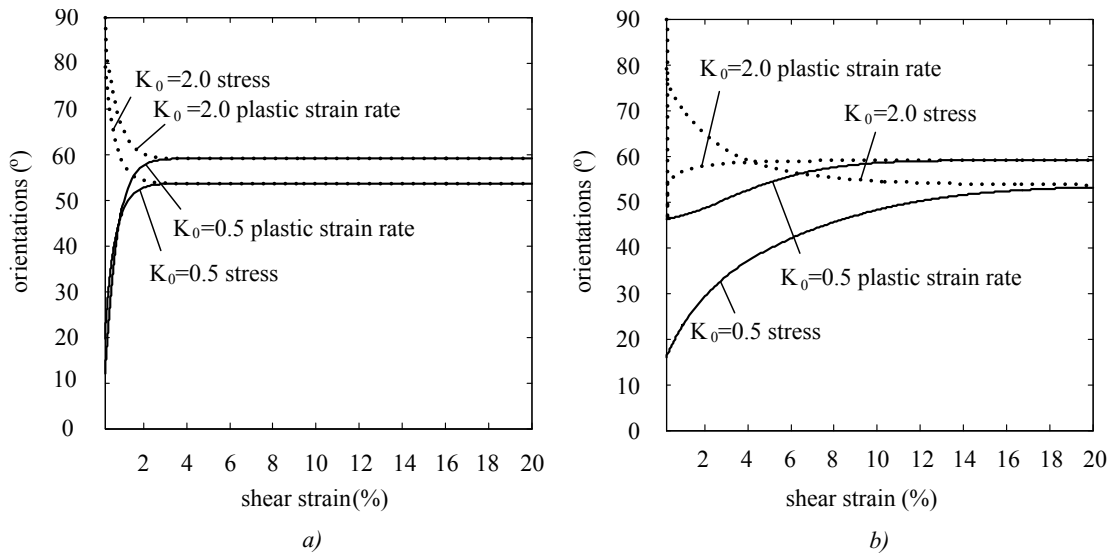


Figure 3.22 Numerical results of principal orientations of stress and plastic strain increment in Test 7 : a) $k = 0.0$; b) $k = 0.02$.

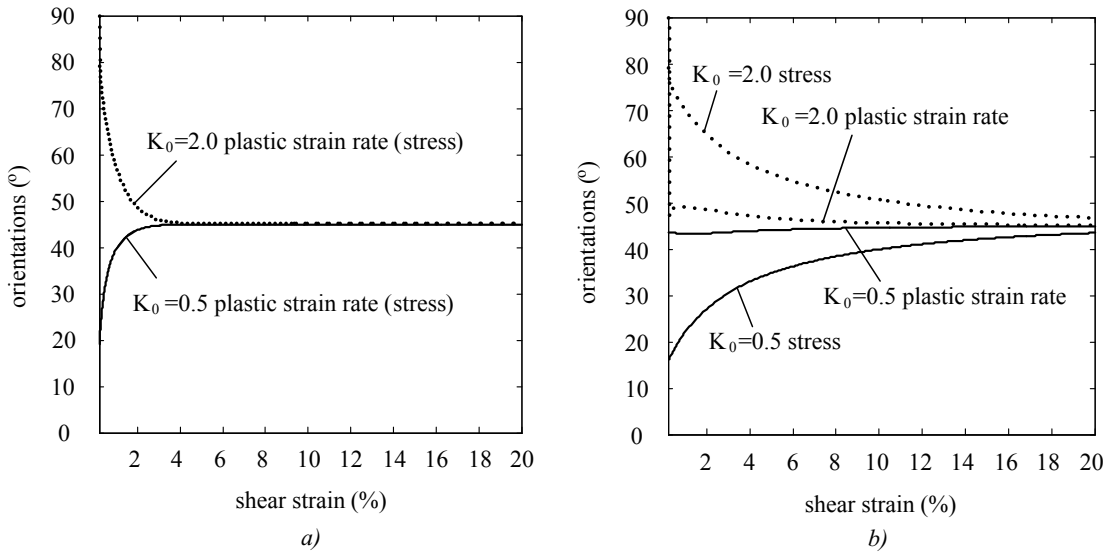


Figure 3.23 Numerical results of principal orientations of stress and plastic strain increment in Test 8 :
 a) $k = 0.0$; b) $k = 0.02$.

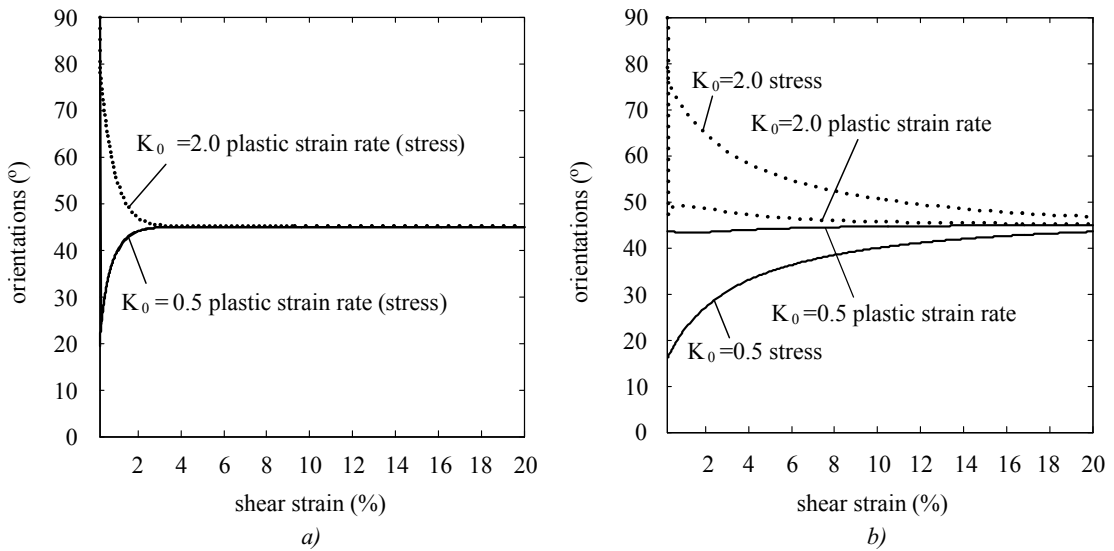


Figure 3.24 Numerical results of principal orientations of stress and plastic strain increment in Test 10 :
 a) $k = 0.0$; b) $k = 0.02$.

3.23 b, 3.24 b and 3.26 b, c). The angle of the direction is between 0° and $45^\circ + \frac{\psi}{2}$ for normally consolidated soil with $K_0 < 1.0$; whereas for over-consolidated soil with $K_0 > 1.0$, the angle is between $45^\circ + \frac{\psi}{2}$ and 90° as expected. In addition, the degree of non-coaxiality increases with a larger value of the non-coaxial coefficient when comparing Figures 3.26 b and 3.26 c. It is interesting to see that the ultimate orientation of the principal stress goes beyond that of the principal plastic strain rate for cases when assumptions of an anisotropic soil and the associativity in the conventional plastic flow rule hold true, and when the non-coaxial coefficient k is equal to zero (Figure 3.25 a). This phenomenon can be caused by the diverse angle between the vector of the principal stress and the principal plastic strain rate tangential to the yield loci in the deviatoric space. The angle is strongly dependent on the initial stress state and the stress path.

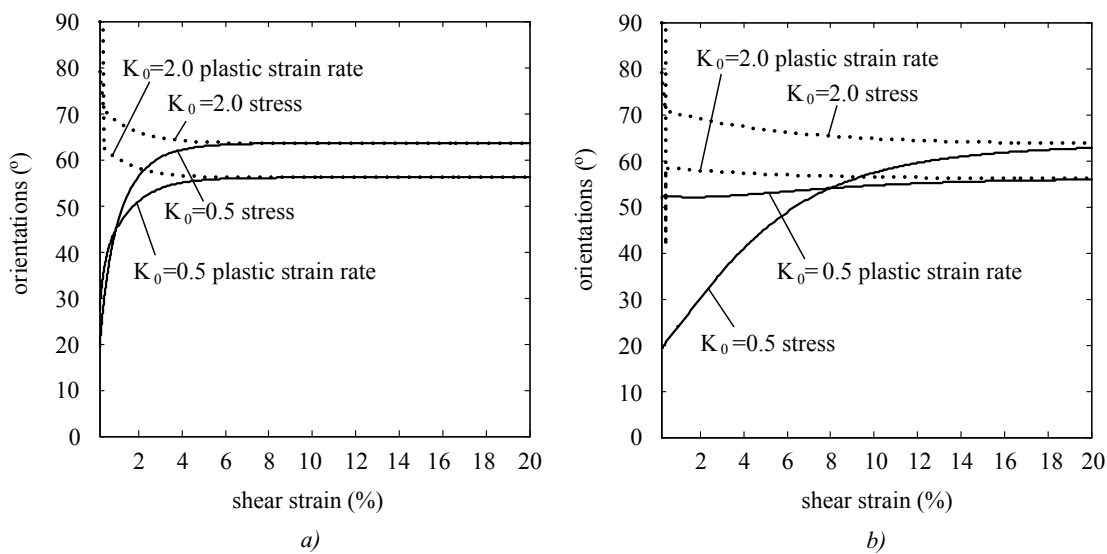


Figure 3.25 Numerical results of principal orientations of stress and plastic strain increment in Test 11 :
a) $k = 0.0$; b) $k = 0.02$.

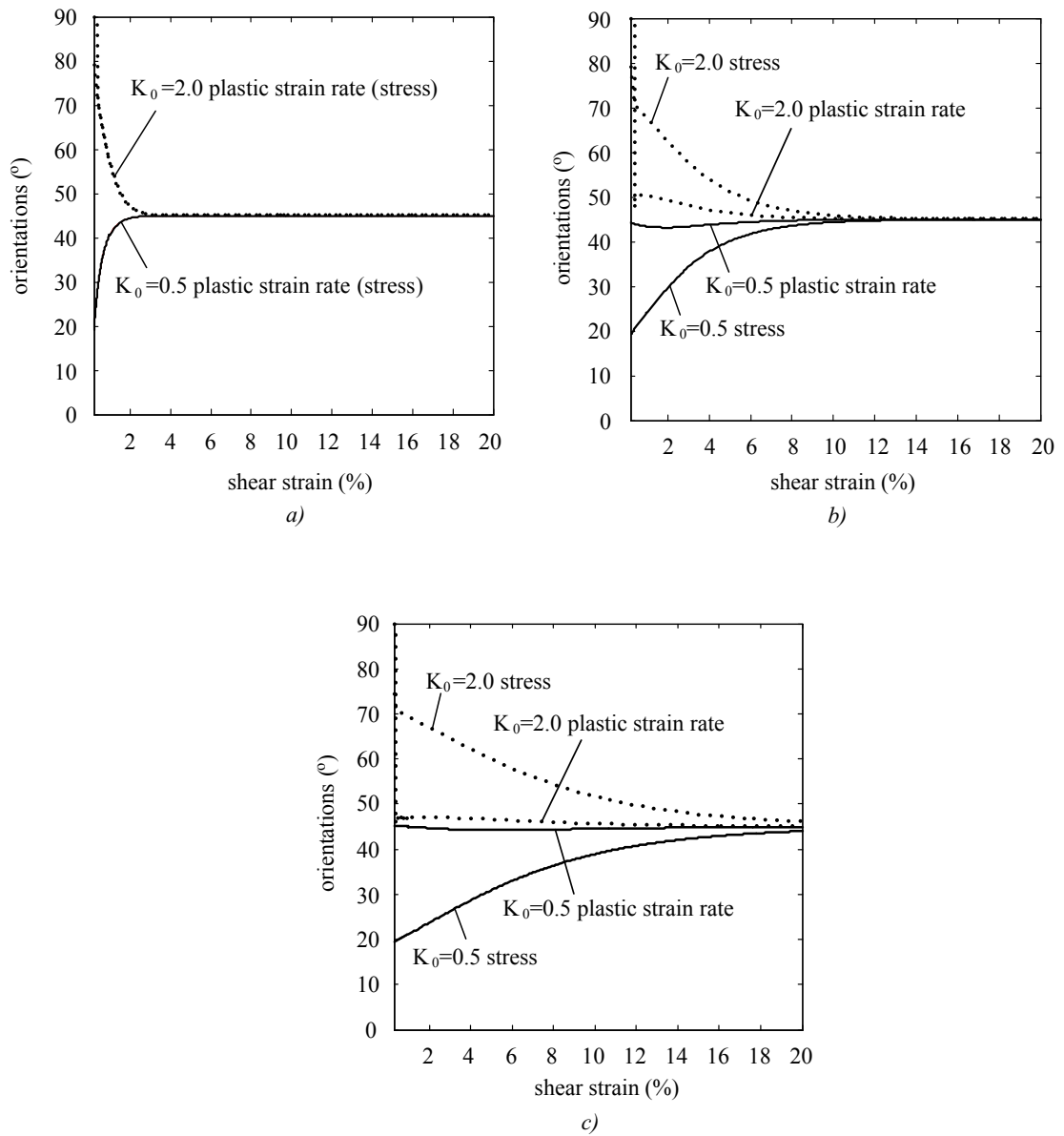


Figure 3.26 Numerical results of principal orientations of stress and plastic strain increment in Test 12 :
a) $k = 0.0$; b) $k = 0.02$; c) $k = 0.05$.

Stress path

Plastic stress paths may move along the yield surface since perfect plasticity is assumed. The onset of plastic strain may affect the relative directions of the principal stress and the principal plastic strain rate when the associativity in the conventional plastic flow rule is used. In addition, the ultimate position of the stress path determines the ultimate orientations of the principal stress and principal plastic strain rates when the nonassociativity in the conventional plastic flow rule is used. Hence, the stress path is a vital factor providing insight into how the stress and orientations develop.

It is interesting to identify that the ultimate orientations of the principal stress and the principal plastic strain rate tend to be identical, irrespective of the values of the non-coaxial coefficient and the lateral stress ratio. This can be evident in the following figures (Figures 3.27 - 3.29) in which the stress paths reach the same final position on the yield curve for each case with the same flow rules. It is obvious that the anisotropic coefficients demonstrate a pivotal effect on the time span between the start of loading and the onset of plastic deformation. In addition, by comparing Figures 3.29 and 3.28, the plastic stress path for the case when $n = 0.707$ and $\beta = 0^\circ$ travels a lot longer in the elastic region than the case when $n = 0.707$ and $\beta = 45^\circ$. This affects non-coaxial behaviour by increasing the time span for reaching coaxiality.

3.5 Chapter Summary

Since experimental observations have shown that non-coaxiality is an aspect of soil anisotropy, a non-coaxial soil model was developed in the framework of soil anisotropy. The anisotropic Mohr-Coulomb yield criterion was generated from the original isotropic Mohr-Coulomb yield criterion by assuming that the peak internal friction angle varies with the direction of principal stresses. Two shape parameters n and β were added to the general isotropic Mohr-Coulomb yield criterion to form the anisotropic yield criterion. The non-coaxial plastic strain was assumed to be induced by the combination of the normal component generated from the plastic potential and tangential component to an anisotropic Mohr-Coulomb yield surface. Both the associativity and nonassociativity in the conventional plastic flow rule were used. Conditions of plane strain and perfect plasticity were firstly investigated for simplicity.

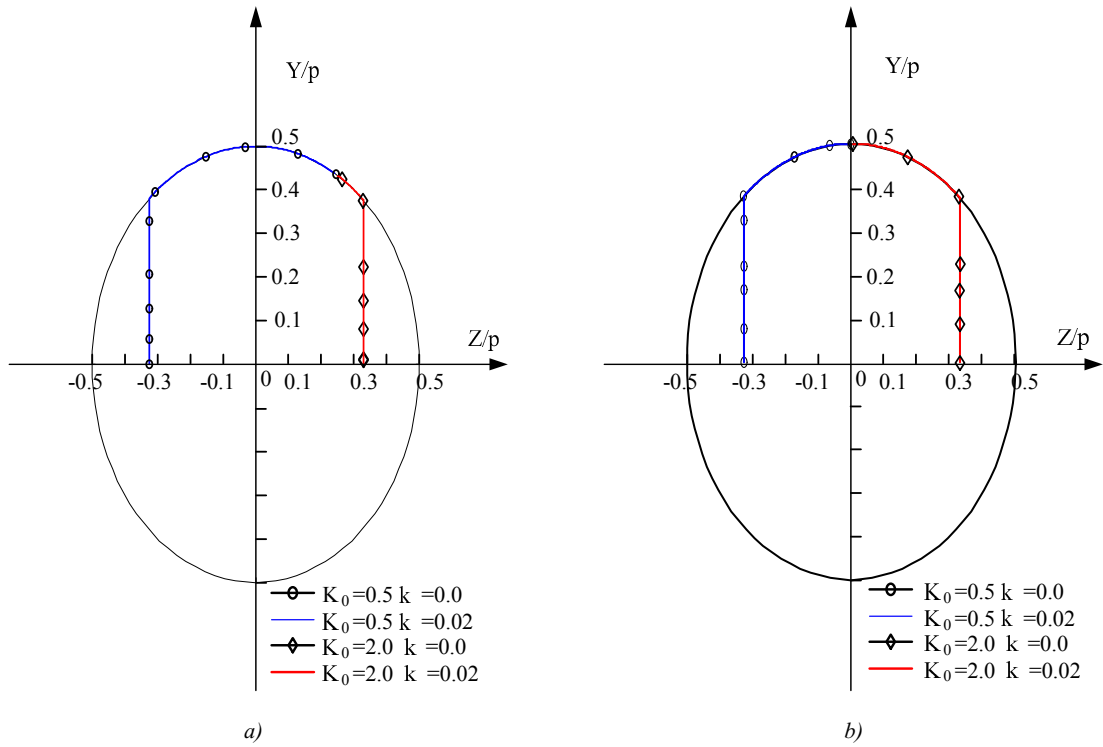


Figure 3.27 Stress path for the recovered isotropic Mohr-Coulomb yield surface in: a) Test 1; b) Test 2.

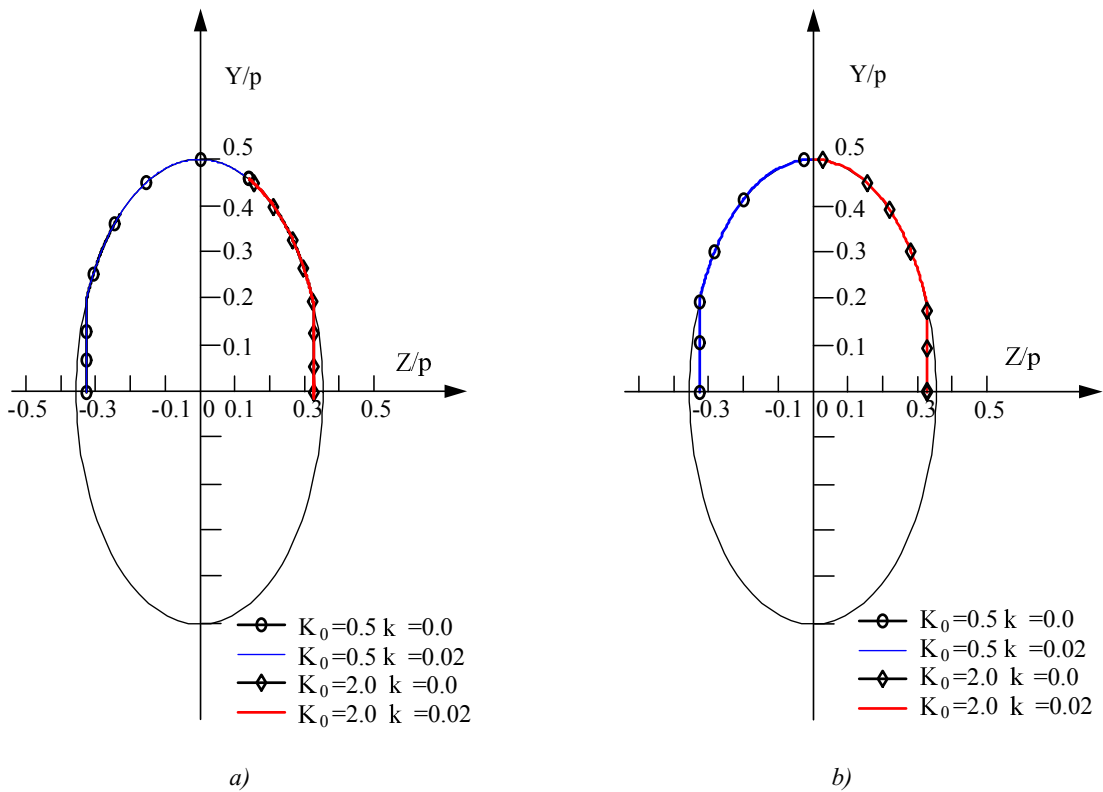


Figure 3.28 Stress path for the case when $n = 0.707$, $\beta = 45^\circ$ in : a) Test 7; b) Test 8.

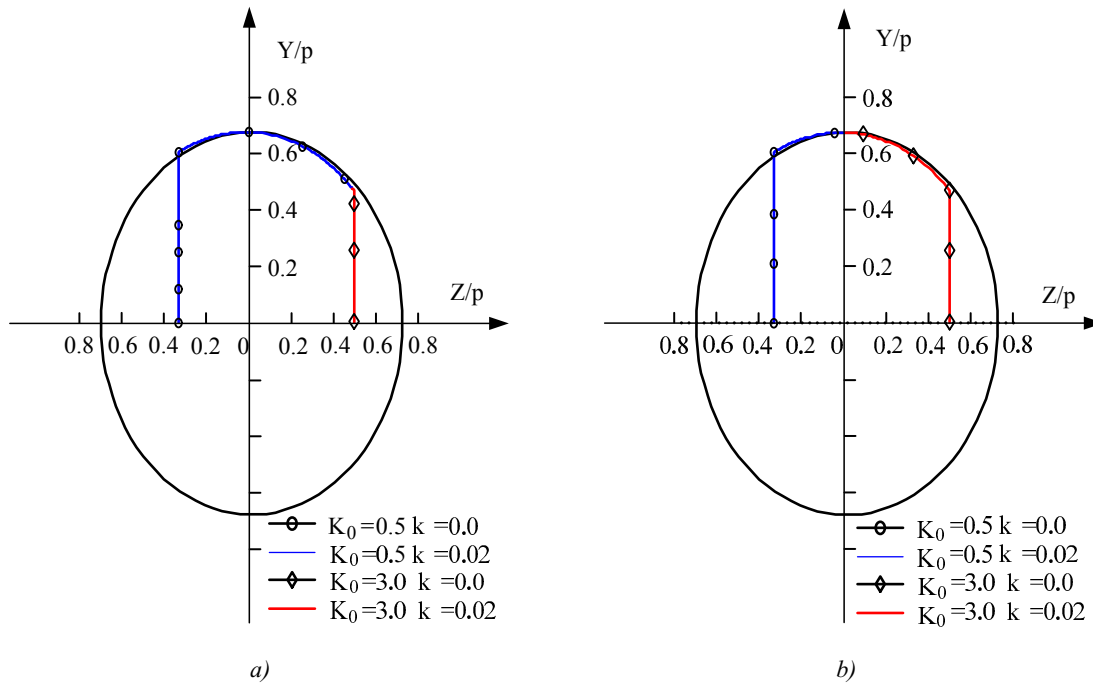


Figure 3.29 Stress path for the case when $n = 0.707$, $\beta = 0^\circ$ in: a) Test 11; b) Test 12.

For the sake of validating the proposed non-coaxial soil model, the finite element software ABAQUS was chosen as the platform. ABAQUS has the capability to integrate complex constitutive models via the user-defined material subroutine (UMAT). A hyperbolic approximation was introduced to remove the tip of the yield surface. The explicit modified Euler integration scheme with stress correction during each substep was employed to integrate the constitutive law. The intersection point while transitioning from the elastic state to the plastic state, was found by the modified regula-falsi method. The negative plastic multiplier was also investigated. This explicit scheme was robust and demonstrated high efficiency.

Numerical simulations have been performed on simple shear tests using the newly proposed non-coaxial soil model. Numerical results obtained from recovering the isotropic Mohr-Coulomb yield condition were in good agreement with analytical calculations, and the patterns were similar to experimental investigations and results drawn by Yuan (2005). This testifies the correctness of the finite element implementation procedures of the newly proposed model. The ultimate shear stress ratio predicted by anisotropic modelling, was lower than that predicted by isotropic modelling. A faster rate of approaching coaxiality was observed when anisotropic coefficients were

not equal to zero. In addition, the angle of non-coaxiality depended on the initial stress state, the dilation angle and the stress path.

The model has its limitations when modelling coaxial behaviour of soils when the associativity in the conventional plastic flow rule is assumed. In the future, strain-hardening and strain softening should be associated with the current model to overcome these limitations.

Chapter 4

Analysis of smooth strip footing problems

4.1 Introduction

4.1.1 General study of footings

It is generally acknowledged that there are two categories of foundations, namely shallow foundations and deep foundations. Shallow foundations consist of pads (isolated) footings, strip footings and rafts; whereas deep foundations consist of piles, pile walls etc. The study of foundations has enjoyed a fruitful outcome over the course of previous decades of research. Both conventional design methods based on stress field solutions and limit analysis have been combined with empirical correlations and the finite-element method in parallel to study the bearing capacity of foundations. It should also be noted that a complete analysis of elastic-plastic problems is only possible for basic cases where loading and geometry are simple. In particular, a strip footing that refers to a continuous foundation in which all loads occur in a straight line, is always treated as a benchmark for other complicated footings.

Most of the research regarding footing problems is under the assumption of soil isotropy and coaxiality of the principal stress and plastic strain rate tensors. Studies carried out by a number of researchers have further built upon the aspect of strength soil anisotropy by introducing a variation of cohesion with direction, for analysing the bearing capacity of footings (Lo, 1965; Reddy and Srinivasan, 1970; Davis and Christian, 1971; Chen, 1975; Yu and Sloan, 1994). Surprisingly though, very little work has been

done on the bearing capacity including soil anisotropy that is described by a variety of friction angles. Yu and Sloan (1994) pointed out that it may be partly due to the fact that more extensive studies focused on the influence of anisotropy in clays rather than in sands. Experimental investigations using hollow cylinder tests conducted by Yang (2013) however demonstrated that internal friction angles vary significantly with a change in the direction of principal stress. On the other hand, it is generally accepted that soils in the vicinity of footing corners experience severe principal stress rotations; hence, it is necessary to investigate its material response under non-coaxial modellings.

Work has been seldom performed on analysing footing problems in the framework of non-coaxial behaviour of granular soils. It is still generally accepted though that the soil mass underneath a footing, especially in the vicinity of footing edges, experiences a large amount of stress rotations under loading. The soil mass can be expected to exhibit non-coaxial behaviour in general. Yu and other authors (Yuan, 2005; Yu, 2006; Yu and Yuan, 2006; Yang and Yu, 2006*b;a*; Yu, 2008; Yang and Yu, 2010*b*) numerically applied their non-coaxial constitutive models which are in the framework of soil strength isotropy assumptions, to investigate footing settlement and stability. In their work, the application of non-coaxial models could predict a higher settlement prior to collapse in comparison with conventional coaxial models. The ultimate failure stress was still not significantly affected in the above mentioned cases. The conclusions drawn from this study clearly stated that without accounting for the non-coaxial behaviour of soil, a high chance for unsafe design exists in geotechnical applications.

Hence, it remains a key issue to provide an insight into what different aspects may be introduced to strip footing problems that are modelled by non-coaxial plasticity in the framework of soil anisotropy when compared to coaxial plasticity. In this chapter, the numerical results are compared with the developed upper bound analytical results. However, the validations of the numerical results with laboratory tests and in-situ observations are highly recommended in the future work. Likewise, the signs of the stress (rate) are chosen to be positive for compression.

4.1.2 Chapter structure

The chapter begins with the development of a semi-analytical solution for the bearing capacity of a rigid smooth strip footing that is assumed to rest on an anisotropic, weightless, cohesive-frictional soil based on the slip line method (Section 4.2). The following Section 4.3 considers the numerical applications of the newly proposed non-coaxial soil model to investigate the bearing capacity and pressure-displacement relationship of smooth strip footing problems. In addition, the influence of the initial stress state, the dilation angle, the degree of soil anisotropy and non-coaxiality will be evaluated, followed by concluding remarks in 4.4.

4.2 Semi-analytical solutions for a weightless frictional-cohesive soil based on the slip line method

It is necessary to validate the results obtained from a newly developed model with analytical solutions in order to ascertain usability in practical, large scale applications. In order to achieve this, semi-analytical solutions of the bearing capacity of a strip footing resting on an anisotropic soil mass, are developed based on the slip line method. The initial soil strength anisotropy is considered and represented by the change in the friction angles with the direction of the principal stress. Furthermore, a parametric study in terms of the anisotropic coefficients n and β is performed and results from numerical simulations and semi-analytical calculations are compared. For simplicity, a cohesive-frictional, weightless soil is considered for all analyses.

4.2.1 Governing equations of stresses

For many practical geotechnical problems, the elastic component of the strain is not the major concern as the failure load is not sensitive to this component of the strain. Therefore, the elastic strain in the plastic region may not be taken into consideration since a complete elastic-plastic treatment is very complex. For the sake of consistency, the elastic strain in the non-plastic zone is also disregarded. Considering soil as a rigid-plastic body under the plain strain assumption, the problem of the plane strain plastic flow rule becomes statically determined since that there will be three stress equations

for three unknown stress components provided that the stresses are prescribed on the boundary. It should be noted here that the rigid-plastic soil refers to a material that is rigid when the stress is below the yield stress and perfectly plastic when the stress reaches the yield stress. In order to solve these stress equations, the stress characteristics (velocity field) are assumed to be along potential slip surfaces. Thus, this type of approach is named as the slip line analysis or the theory of slip line fields (Hill, 1951; Yu, 2006).

In the literature, slip line analysis is best used to analyse materials obeying Tresca's yield criterion since a simple form of slip line can be obtained when the friction angle ϕ equals zero. Yu (2006) provided a thorough investigation of slip line analysis, in which cohesive materials, frictional material, axisymmetric problems and anisotropic problems are presented and analysed in detail.

In this section, equations will be presented in terms of stress fields which must be satisfied in the plastic region of a rigid, plastic body. In this case, the magnitude of elastic strains is disregarded. The rigid, plastic body is modelled using the anisotropic Mohr-Coulomb failure criterion.

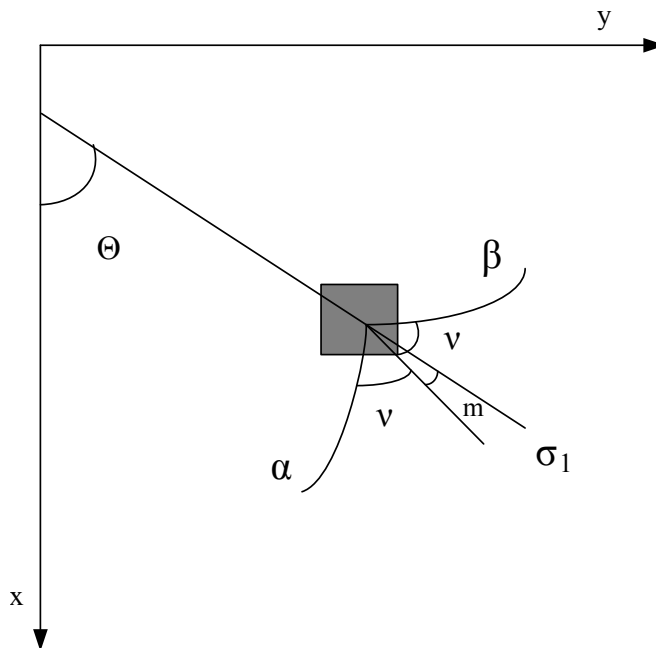


Figure 4.1 The coordinate system and stress characteristics for anisotropic plasticity (Yu, 2006).

Figure 4.1 shows a rectangular Cartesian coordinate system (x,y) and stress charac-

teristics for anisotropic plasticity under plane strain conditions. Θ refers to the angle between the direction of the major principal stress (σ_1) and the x - axis. α and β are two stress characteristic curves and the angle m has a simple geometric interpretation as defined in Section 3.

Referring to the coordinate system shown in Figure 4.1, two equations of equilibrium under plane strain conditions can be obtained:

$$\frac{\partial \sigma_x}{\partial x} + \frac{\partial \sigma_{xy}}{\partial y} = 0 \quad (4.1)$$

$$\frac{\partial \sigma_{xy}}{\partial x} + \frac{\partial \sigma_y}{\partial y} = \gamma \quad (4.2)$$

where γ is the unit weight of the material in the y direction.

Assuming there exists a point in the plastic region where the stress Mohr circle touches the failure envelope, it proves useful to express the stresses using Mohr's stress representation as shown in Figure 4.2 a:

$$\sigma_x = p + R \cos 2\Theta \quad (4.3)$$

$$\sigma_y = p - R \cos 2\Theta \quad (4.4)$$

$$\sigma_{xy} = R \sin 2\Theta \quad (4.5)$$

where $p = \frac{1}{2}(\sigma_x + \sigma_y)$ is the mean stress and $R = (p + c \cot \phi_{max}) \sin \phi(\Theta)$ is the radius of the Mohr stress circle.

If the values of stress from Equations 4.3 - 4.5 are substituted into Equations 4.1 and 4.2, it can be found that the resultant equations are hyperbolic in nature. Booker and Davis (1972) pointed out that the characteristics of the resultant equations are:

$$\frac{dy}{dx} = \tan(\xi_\alpha) = \tan(\Theta - m - \nu) \quad (4.6)$$

$$\frac{dy}{dx} = \tan(\xi_\beta) = \tan(\Theta - m + \nu) \quad (4.7)$$

It should be noted here that the variable m has a simple geometric interpretation and is introduced purely to ensure simplicity of the mathematics involved (shown in Figure

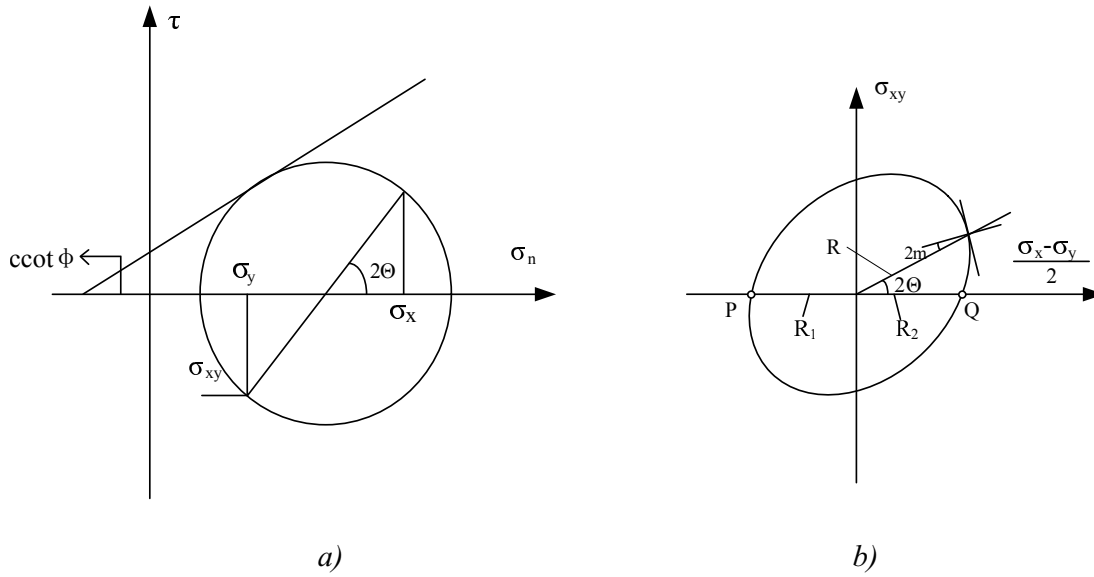


Figure 4.2 a) Stress state at failure; b) anisotropic yield curve in $(\frac{\sigma_x - \sigma_y}{2}, \sigma_{xy})$ space.

4.2 b). m and ν are defined by:

$$\tan(2m) = \frac{1}{2F} \frac{\partial F}{\partial \Theta} \quad (4.8)$$

$$\cos(2\nu) = \cos(2m) \frac{\partial F}{\partial p} \quad (4.9)$$

The two characteristic lines: α -lines and β -lines, as illustrated in Figure 4.1, are integrals of Equations 4.6 and 4.7 respectively. Hence, the canonical form of the equilibrium equations can be written as follows:

$$\sin[2(m - \nu)] \frac{\partial p}{\partial \alpha} + 2F \frac{\partial \Theta}{\partial \alpha} + \gamma \cos(2m) \left[\sin(2\nu) \frac{\partial x}{\partial \alpha} + \cos(2\nu) \frac{\partial y}{\partial \alpha} \right] = 0 \quad (4.10)$$

$$\sin[2(m + \nu)] \frac{\partial p}{\partial \beta} + 2F \frac{\partial \Theta}{\partial \beta} + \gamma \cos(2m) \left[-\sin(2\nu) \frac{\partial x}{\partial \beta} + \cos(2\nu) \frac{\partial y}{\partial \beta} \right] = 0 \quad (4.11)$$

Here for a cohesive-frictional soil with no self-weight, γ is neglected. Then the Equations 4.10 and 4.11 are reduced to the definitions shown below:

$$\sin[2(m - \nu)] \frac{\partial p}{\partial \alpha} + 2F \frac{\partial \Theta}{\partial \alpha} = 0 \quad (4.12)$$

$$\sin[2(m + \nu)] \frac{\partial p}{\partial \beta} + 2F \frac{\partial \Theta}{\partial \beta} = 0 \quad (4.13)$$

which are hyperbolic if the characteristics defined in Equations 4.6 and 4.7 are real and distinct.

In previous chapters, a general form of an anisotropic yield criterion in terms of inherent anisotropy for plane strain conditions is presented. Under this assumption, the variation of the stress state in a plastic region can be shown as:

$$dp + (p + ccot\phi_{max}) \frac{2\sin\phi(\Theta)}{\sin 2(m - \nu)} d\Theta = 0 \quad (4.14)$$

$$dp + (p + ccot\phi_{max}) \frac{2\sin\phi(\Theta)}{\sin 2(m + \nu)} d\Theta = 0 \quad (4.15)$$

The subsequent equations of m and ν for the above are:

$$\cos(2\nu) = \cos(2m) \frac{\partial F}{\partial p} = \cos(2m) \sin(\phi(\Theta)) \quad (4.16)$$

$$\sin(2\nu) = \sqrt{1 - \cos^2(2\nu)} \quad (4.17)$$

$$\tan(2m) = \frac{1}{2F} \frac{\partial F}{\partial \Theta} = \frac{d\sin\phi(\Theta)}{2\sin\phi(\Theta)d\Theta} \quad (4.18)$$

where the calculations of $d\sin\phi(\Theta)$, $\sin(2m)$ and $\cos(2m)$ will be presented in Appendix 1.

4.2.2 Stress boundary conditions

The solutions to the governing stress Equations 4.1 and 4.2 require sufficient stress boundary conditions in terms of the mean stress and the direction of the principal stress (p, Θ). It is useful to consider a boundary (see the bold line) as shown in Figure 4.3. As indicated in Figure 4.3, the normal direction of the boundary deviates from the y direction with an angle of δ . σ_n and τ_n denote the normal stress and shear stress respectively.

The normal and shear stresses at the boundary must be on the Mohr circle that touches the failure envelope. As shown in Figure 4.4, these stresses can be geometrically calculated as:

$$\sigma_n = p + R\cos 2(\delta - \Theta) \quad (4.19)$$

$$\tau_n = R\sin 2(\delta - \Theta) \quad (4.20)$$

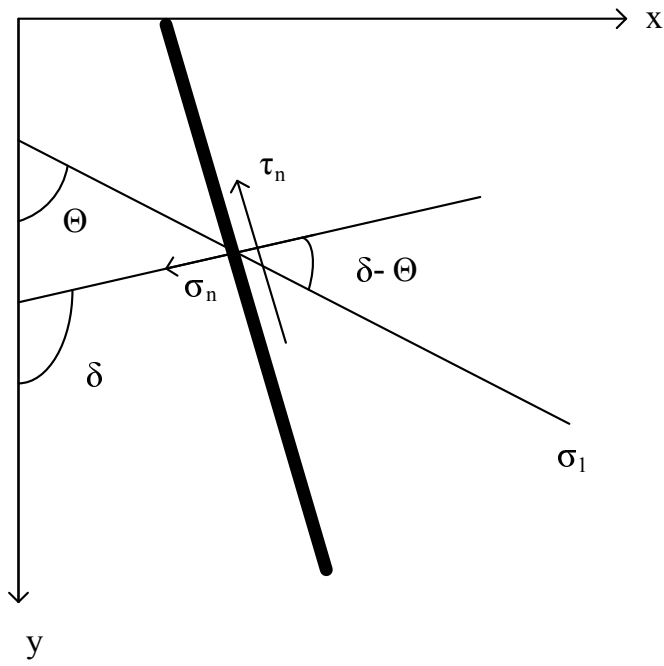


Figure 4.3 The stress conditions on a boundary.

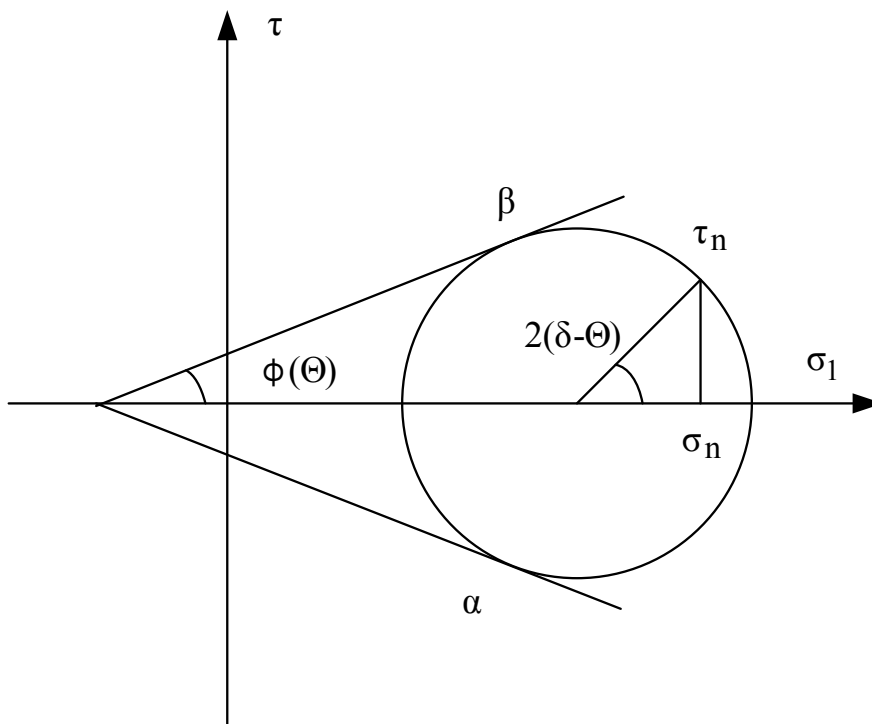


Figure 4.4 The stress conditions on a boundary.

Based on the equations shown above, the mean stress p and the radius R can be solved and expressed in terms of the given values of σ_n and τ_n :

$$(\sigma_n - p)^2 + \tau_n^2 = (p + c \cot \phi_{max})^2 \sin^2 \phi(\Theta) \quad (4.21)$$

Once the mean stress is determined, the value of Θ can be calculated by combining Equation 4.21 with either Equation 4.19 or Equation 4.20.

In particular, for a strip footing problem, Equation 4.21 can be simplified since the shear stress acting on the boundary is zero. Hence:

$$\Theta = (-1)^n \cdot n \cdot \frac{\pi}{2} + \delta \quad (4.22)$$

In Equation 4.22, n assumes the value 1 or 2 depending upon the conditions in a given problem (i.e. determining whether σ_n is the major principal stress or not). Thus the mean stress p can be solved as:

$$p = \frac{\sigma_n \mp c \cot \phi_{max} \sin \phi(\Theta)}{1 \pm \sin \phi(\Theta)} \quad (4.23)$$

with the first sign $n = 1.0$ is for the case when σ_n is the major principal stress, and the second sign $n = 2.0$ is for the case when σ_n is the minor principal stress.

4.2.3 Ultimate vertical pressure for a strip footing resting on an anisotropic weightless cohesive-frictional soil

The illustration of the bearing capacity of a smooth strip footing is shown in Figure 4.5. It should be noted that only a symmetrical footing problem is presented. AO is half of the strip footing. The material immediately beneath and adjacent to the footing (area bounded by the curve $\overline{ADC\overline{B}}$) is in a state of plastic failure. The plastic region is supposed to extend as far as B . AB is a non-characteristic line on which the traction is specified, and it hence defines a Cauchy problem. There exists a surface surcharge of q applied on OB . Based on the corollary of Hencky's theory, all α -lines in this field must be straight lines; and all these lines must pass through the edge point of the footing at O . The family of straight α -lines are the characteristics within the region OCD , which demonstrate an angle of Θ . The extent of the region OCD is governed by

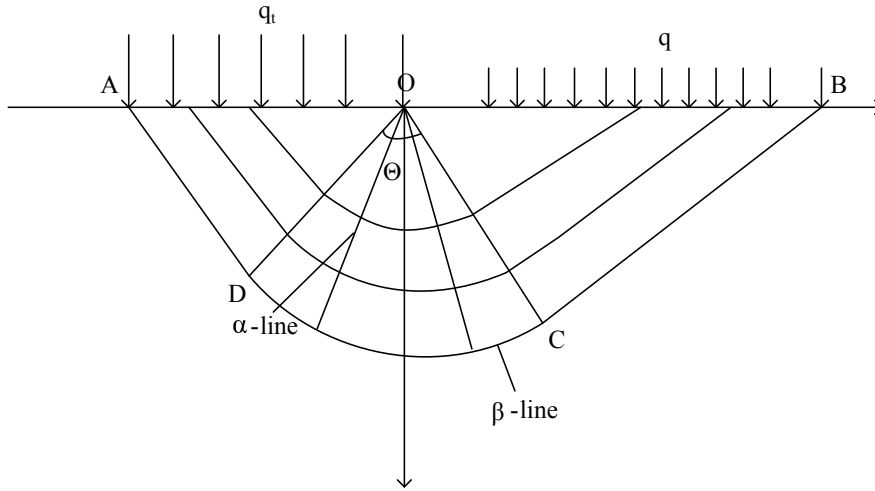


Figure 4.5 Plastic stress field of strip footing with surcharge on OB .

the condition that OA is smooth. In other words, $\Theta = 0^\circ$ on OA . This implies that the angle COD is a right angle.

Following Equation 4.23, the mean stress on OB where $\Theta = \frac{\pi}{2}$ can be calculated as:

$$\Theta_1 = \frac{\pi}{2} \quad (4.24)$$

$$p_1 = \frac{q + ccot\phi_{max}\sin\phi(\Theta_1)}{1 - \sin\phi(\Theta_1)} \quad (4.25)$$

and the mean stress on OA can be obtained as:

$$\Theta_2 = 0 \quad (4.26)$$

$$p_2 = \frac{q_t - ccot\phi_{max}\sin\phi(\Theta_2)}{1 + \sin\phi(\Theta_2)} \quad (4.27)$$

The families of α -lines and β -lines are illustrated in Figure 4.5. For the β -lines, the two stress variables (p_1, Θ_1) and (p_2, Θ_2) at two points along the same family of stress characteristics can be linked by the following equations:

$$\ln(p_2 + ccot\phi_{max}) = \int_0^{\frac{\pi}{2}} \left(\frac{2\sin\phi(\Theta)}{\sin 2(m+\nu)} \right) d\Theta + \ln(p_1 + ccot\phi_{max}) \quad (4.28)$$

Thus the mean stress p can be solved as:

$$p_2 = e^{\int_0^{\frac{\pi}{2}} \left(\frac{2\sin\phi(\Theta)}{\sin 2(m+\nu)} \right) d\Theta} (p_1 + ccot\phi_{max}) - ccot\phi_{max} \quad (4.29)$$

Then substituting for p_2 from Equation 4.29 into Equation 4.27 provides us with the

value of vertical pressure at plastic collapse as:

$$q_t = (1 - \sin\phi(\Theta_2)) \left(e^{\int_0^{\frac{\pi}{2}} \left(\frac{2\sin\phi(\Theta)}{\sin^2(m+v)} \right) d\Theta} \right) (p_1 + ccot\phi_{max}) - ccot\phi_{max} \sin\phi(\Theta_2) \quad (4.30)$$

The above solution can be further expressed in terms of contributions from cohesion and surcharge as follows:

$$q_t = N_c c + N_q q \quad (4.31)$$

where N_c denotes the bearing capacity factor contribution from cohesion and N_q denotes the bearing capacity factor contribution from surcharge.

4.2.4 Special cases

For the rotational anisotropic Mohr-Coulomb yield criterion, the expression of $\sin\phi_\Theta$ is shown as:

$$\sin\phi(\Theta) = \frac{n \cdot \sin\phi_{max}}{\sqrt{n^2 \cdot \cos^2(2\Theta - 2\beta) + \sin^2(2\Theta - 2\beta)}} \quad (4.32)$$

Then substituting for $\sin\phi_\Theta$ into Equation 4.30, we can readily obtain solutions for the vertical pressure at plastic collapse:

$$q_t = \left(1 + \sqrt{\frac{2}{M}} n \sin\phi_{max} \right) \left(e^{\int_0^{\frac{\pi}{2}} G(\Theta) d\Theta} \cdot \frac{q\sqrt{M} + \sqrt{M}ccot\phi_{max}}{\sqrt{M} - \sqrt{2}n\sin\phi_{max}} \right) - ccot\phi_{max} \quad (4.33)$$

and:

$$G(\Theta) = \frac{2\sqrt{2}n\sin\phi_{max}(C^2 + D^2)}{\sqrt{2}n\sin\phi_{max}DC + \sqrt{C^5 + D^2C^3 - 2C^4(n\sin\phi_{max})^2}} \quad (4.34)$$

$$C = 2[(1 - n^2)\sin^2(2\Theta - 2\beta) + n^2] \quad (4.35)$$

$$D = (n^2 - 1)\sin(4\Theta - 4\beta) \quad (4.36)$$

$$M = 2[(1 - n^2)\sin^2(2\beta) + n^2] \quad (4.37)$$

Further on, the bearing capacity factor contribution from surcharge can be expressed

as:

$$N_q = e^{\int_0^{\frac{\pi}{2}} G(\Theta) d\Theta} \cdot \left(1 + \sqrt{\frac{2}{M}} n \sin \phi_{max}\right) \cdot \frac{\sqrt{M}}{\sqrt{M} - \sqrt{2} n \sin \phi_{max}} \quad (4.38)$$

and the bearing capacity factor contribution from cohesion can be expressed as:

$$N_c = (N_q - 1) \cot \phi_{max} \quad (4.39)$$

It should be noted here that when $n = 1.0$, Prandtl's solution will be recovered from Equation 4.33, namely:

$$q_t = (q + c \cot \phi) \tan^2 \left(\frac{\pi}{4} + \frac{\phi}{2} \right) e^{\pi \tan \phi} - c \cot \phi \quad (4.40)$$

likewise,

$$q_t = N_c c + N_q q \quad (4.41)$$

and,

$$N_q = \tan^2 \left(\frac{\pi}{4} + \frac{\phi}{2} \right) e^{\pi \tan \phi} \quad (4.42)$$

$$N_c = (N_q - 1) \cot \phi. \quad (4.43)$$

in which the friction angle is constant as soil isotropy is assumed; hence ϕ_{max} is replaced by ϕ .

4.2.5 Close-form solutions for a particular case of a purely cohesive material

As shown in Section 4.2.1, a semi-analytical solution for q_t using numerical methods is obtained since direct integration is highly complicated. However, for a particular case of a purely cohesive material when the yield criterion is independent of hydrostatic pressure, i.e. $\nu = \frac{\pi}{4}$, it is obvious that in the region OCD , the β -characteristics are circles. In this particular case, the yield surface is a cylinder generated by straight lines parallel to the line corresponding to $\sigma_x = \sigma_y, \tau_{xy} = 0$. The solution becomes much simpler and can readily be obtained analytically.

Booker and Davis (1972) and Yu (2006) provided a general solution of the ultimate failure load of a smooth strip footing in purely cohesive soil mass without surface surcharge and modelled on a general anisotropic yield surface. The authors suggested that the ultimate bearing capacity could be simply expressed as follows:

$$q_t = \overline{PQ} + S \quad (4.44)$$

where S is the minimum arc length between points P and Q (see Figure 4.2 b).

In previous sections, an expression of q_t for a general, cohesive-frictional soil is obtained in terms of p_2 and the maximum internal friction angle ϕ_{max} . The failure load q_t in this case under the assumption that the limit value of ϕ_{max} is approaching zero, can be obtained as follows:

$$q_t = \lim_{\phi_{max} \rightarrow 0} q_t \quad (4.45)$$

The close-form solutions in this case can be obtained by using *L'Hospital's* rule, and details of the calculations can be found in Appendix 1.

With respect to the rotational anisotropic Mohr-Coulomb yield criterion, the solution can be obtained as:

$$q_t = \pi n c + 2(1 - n)c + 2nc \sqrt{\frac{2}{M}} \quad (4.46)$$

where $M = 2[(1 - n^2)\sin^2(2\beta) + n^2]$.

In addition, for a special case of an anisotropic Tresca model with $\phi = 0$, the solution can be expressed by the following well-known form:

$$q_t = (2 + \pi) \cdot c \quad (4.47)$$

It should be noted that this is consistent with Equation 4.46 if the isotropic Mohr-Coulomb yield criterion is recovered (i.e. $n = 1.0$).

4.2.6 Parametric study of semi-analytical solutions

Mathematical integration of Equation 4.33 is too complicated to achieve a complete analytical solution; however, part of the integration can be done numerically. By combining numerical and integral methods, semi-analytical solutions of a smooth strip footing on a weightless frictional-cohesive soil can be obtained. It is necessary to perform a parametric study to verify the semi-analytical solutions and investigate the influence of the anisotropic coefficients.

Two separate categories of loading conditions are solved for in this section. The first case involves a footing resting on an anisotropic frictional-cohesive soil without surface surcharge, where $c = 30$ kPa and $q = 0$ kPa. The second case involves a footing resting on a cohesion-less soil with surface loading q taken as 100 kPa and $c = 0.01$ kPa in order to avoid the singularity problem for numerical modelling in ABAQUS. Results of the ultimate bearing capacity factor expressed in terms of contributions from cohesion (N_c) and surcharge (N_q) have been plotted versus different values of anisotropic coefficients n and β . The maximum peak internal friction angle is always set as 30° unless otherwise specified from 5° to 40° for the parametric study of bearing capacity factors in terms of peak internal friction angles.

Results from semi-analytical solutions are presented below. Figure 4.6 shows the influence of the anisotropic coefficients n and β on the bearing capacity factor N_c corresponding to different values of friction angles. The bond lines without markers are obtained from Prandtl's solution as shown in Equation 4.43. As indicated in Figure 4.6 a, the line obtained from Prandtl's solution is identical with the line obtained when $n = 1.0$ because the isotropic Mohr-Coulomb yield criterion will be recovered if the anisotropic coefficient n is equal to 1.0. With respect to the influence of n (Figure 4.6 a), the bearing capacity is lower when soil anisotropy is considered and the difference between the isotropic and anisotropic condition is dramatic with a larger value of the maximum peak internal friction angle ϕ_{max} . With respect to the influence of β (Figure 4.6 b), the same conclusion can be drawn when compared to the influence of n , i.e. the bearing capacity is lower when soil anisotropy is involved and much smaller with a higher value of the friction angle. In addition, a larger value of n and a lower value of β result in a larger bearing capacity factor N_c . Comparing the two bearing capacity

factors N_c and N_q ; the value of N_c is larger than the value of N_q for smaller values of friction angles (e.g. $\phi_{max} \leq 30^\circ$). For larger values of friction angles, the difference is insignificant.

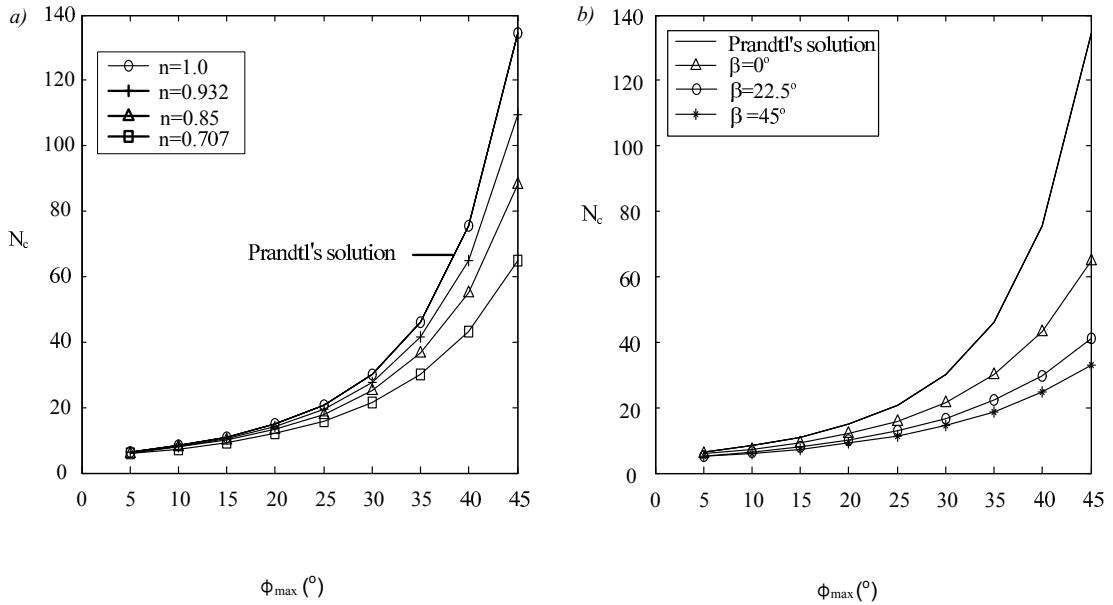


Figure 4.6 The influence of the anisotropic coefficient on the bearing capacity factor N_c with various friction angles : a) n ; b) β ($n = 0.707$).

Figure 4.7 presents the influence of the anisotropic coefficients n and β on the bearing capacity factor N_q with various magnitudes of the maximum peak internal friction angle ϕ_{max} . Likewise, the bond lines without markers are obtained from Prandtl's solution, and are coincident with the line results from semi-analytical solutions when $n = 1.0$. Similar conclusions such as the influence of anisotropic coefficients on the bearing capacity N_c , can be drawn in this regard.

Figure 4.8 plots the bearing capacity factors N_c and N_q versus β with different values of n . The bond lines without markers are obtained from Prandtl's solution. It shows that the line of results obtained from semi-analytical solutions and the bond lines obtained from Prandtl's solution are the same as expected, irrespective of the values of β . It is self-evident from the two figures that the predicted results of bearing capacity decrease with an increase in β ; however, they increase with an increase in n .

From the above analysis, it can be concluded that the proposed semi-analytical solutions can be applied to investigate smooth strip footing problems. Soil anisotropy is a

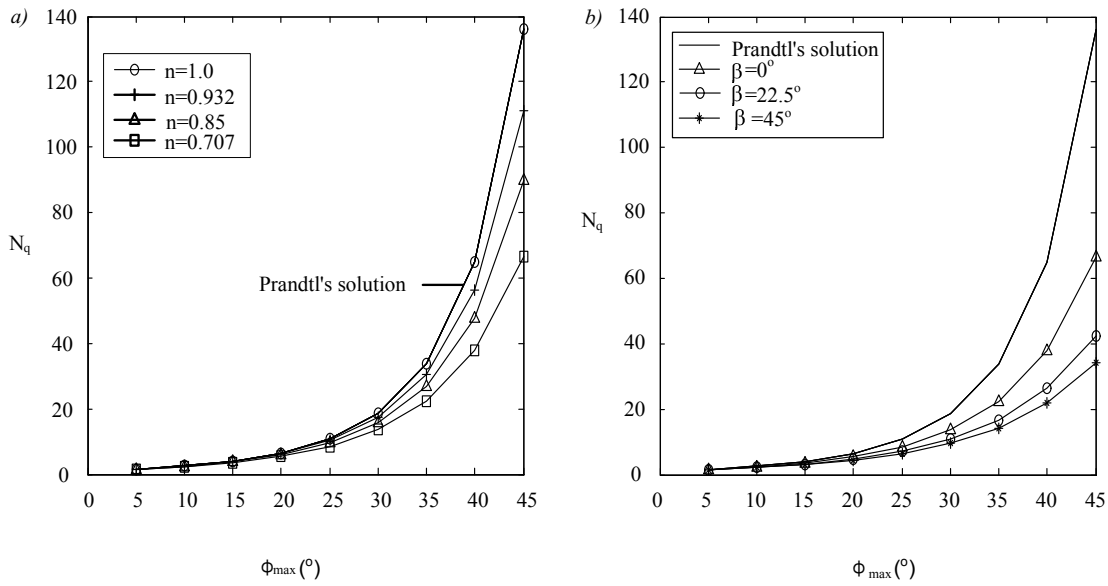


Figure 4.7 The influence of the anisotropic coefficient on the bearing capacity factor N_q with various friction angles: a) n ; b) β ($n = 0.707$).

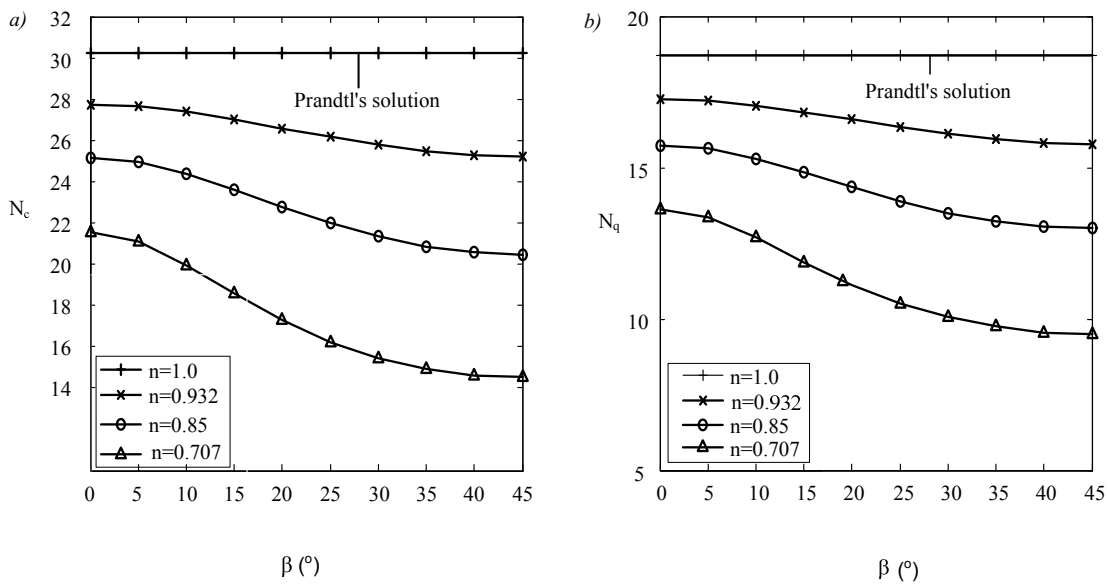


Figure 4.8 The bearing capacity factors versus β with different values of n : a) N_c ; b) N_q .

significant addition to the overall calculations and should be taken into consideration for the bearing capacity of strip footing problems.

4.2.7 Restrictions of the proposed solutions

The solutions shown above are under the assumption that the associated flow rule is valid. In this case, the stress characteristics and velocity characteristics are coincident so the determination of a velocity field is not essential. However, for problems that involve both kinematic and static boundary conditions, the stress field must be compatible with some form of movement and this aspect must be checked initially. Booker and Davis (1972) argued that in most die indentation problems, the failure load will be rarely affected by the nature of the flow rule; however, in problems where the velocity boundary conditions are more constrictive, the failure load for a material with a non-associated flow rule may demonstrate a drastically lower value as compared to the corresponding material with an associated flow rule. Hence, further work can be carried out to take into consideration boundary conditions as well as to analyse the velocity field. The cases involving the non-associated flow rule can then be investigated.

As noticed by Bishop (1953), the stresses in the plastic stress solutions have only been demonstrated to satisfy the yield condition and equilibrium equations in the plastic zone; and these stresses are termed as a partial stress field or incomplete solutions. Such incomplete solutions are termed as an upper bound solution. The upper bound solution is defined if sufficient assumptions are made to determine the stress field, and these assumptions can be validated by showing that a velocity field involving no negative plastic work can be found. If, the partial stress field satisfies the equilibrium equations, yield criterion and the stress boundary conditions, and can be extended to the entire body, it is termed as a lower bound solution. If the solution is proved to be both an upper bound and a lower bound solution, an exact solution can then be obtained. Since the solution proposed in our research may be regarded as an upper bound solution, further steps can be taken to develop a lower bound solution.

Nevertheless, the upper bound solution for the bearing capacity of strip footings is very close to the exact solution in practice. Hence, it can be, not strictly speaking, used to represent the exact solution for the sake of simplicity.

4.3 Numerical verification of the non-coaxial model with semi-analytical solutions

4.3.1 Model and parameters

In this section, the non-coaxial soil model is applied to investigate smooth strip footing problems. Firstly, the numerical results using the non-coaxial soil model are verified using the previous semi-analytical solutions of vertical load at plastic collapse developed from the theory of the slip line method. Then the influence of the degree of soil anisotropy, the initial stress state and the degree of non-coaxiality will be analysed in detail. Both the associativity in the conventional plastic flow rule and the nonassociativity in the conventional plastic flow rule will be used.

Perfect plasticity and plane strain conditions are assumed for this case. The model size for half of the base soil is assumed to be 60 m in length and 30 m in depth, with the half width B of the footing setting as 1 m (Figure 4.9). This negates the impact of the boundary conditions. Model size has been tested that the boundary conditions have negligible effects on the numerical modelling even if the half model size is set as 20 m in length and 10 m in depth. The mesh density follows the assumption of Yang and Yu (2006b). The material of the base soil is discretised with first order 8-node plane strain reduced elements (element type *CPE8R*). The left-hand boundary represents a vertical symmetry axis, whereas the far-field condition on the right-hand side boundary allows for vertical movement. The condition on the bottom boundary is fixed in both vertical and horizontal directions. The nodes immediately underneath the footing are tied to the top node on the left edge to guarantee identical downward movement. These nodes are then applied in a gradually increasing, downward vertical displacement to simulate the movement of the footing. The downward movement is applied incrementally until it reaches 10 - 15 cm. The horizontal movements of these nodes are restricted although they are subject to the same vertical downward displacement. Hence, there should be no relative displacements and strains in the footing, and the footing is regarded as a rigid strip footing. This setting can reduce the stress localisation which will occur adjacent to the edge of the footing, which may cause convergence problem.

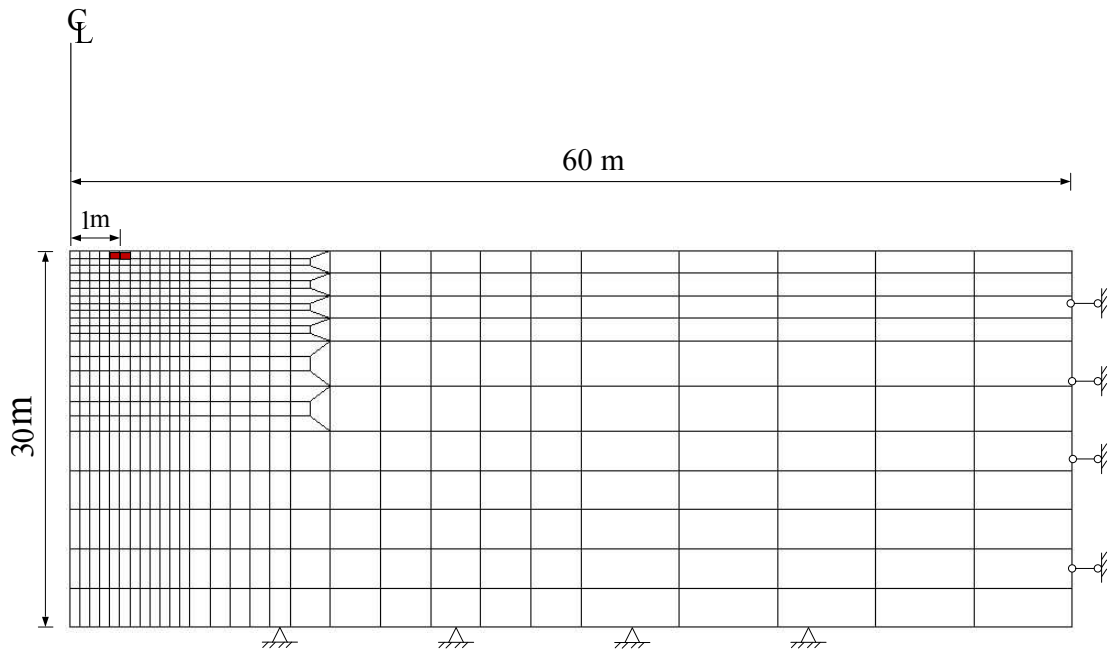


Figure 4.9 Geometry and finite element discretization of the strip footing.

The average value of the vertical stresses (s_{22}) obtained from the Gauss points of the elements just underneath the footing, is used to represent the footing pressure.

Two categories of simulations are performed: the first with a footing located on a weightless, cohesive soil without surface surcharge; while the second involves a footing located on a weightless, cohesive soil with 100 kPa surface surcharge. It should be noted here that in order to avoid the singularity problem for numerical modelling in ABAQUS, especially for cases with small friction angles, cohesion is always set as 30 kPa, otherwise $c = 0.01$ kPa. Typical elastic constants are fixed; such as Youngs modulus $E = 10.0 \times 10^4$ kPa and Poissons ratio $\nu = 0.3$.

The computation of N_c is performed. The contributions of other bearing capacity factors are not taken into consideration. The footing is displaced incrementally immediately before numerical convergence fails. N_c is expressed by the ultimate vertical load at plastic collapse normalised by cohesion:

$$N_c = \frac{q_t}{c} \quad (4.48)$$

The semi-analytical solution of the N_c value is then expressed as:

$$N_c = (N_q - 1) \cdot \phi_{max} \quad (4.49)$$

Another bearing capacity factor N_q is evaluated, and in this situation, contributions from other bearing capacity factors are ignored e.g. $c = 0.01$ kPa. N_q is defined as the ultimate failure load normalised by surface surcharge:

$$N_q = \frac{q_t}{q} \quad (4.50)$$

It should be noted here that the semi-analytical solutions of bearing capacity N_q and N_c are expressed in Equations 4.38-64.

Special attention should be paid to the cases of parametric study of bearing capacity factors with various friction angles, where singularity problems may occur for small values of the friction angle. Cohesion is set as 30 kPa, even for the computation of ultimate failure normalised by surface surcharge. Attention should be paid to those cases where severe nonassociativity in the conventional plastic flow rule is applied. For these situations, negative eigenvalues may be obtained in the solution of global finite-element equations. This scenario is especially prevalent for footing problems in which severe discontinuity of the stress field occurs in the vicinity of footing corners. Thus in order to solve or relax non-convergence problems in ABAQUS in these situations, the default force residual tolerance $R_n = 5 \times 10^{-3}$ and the default displacement correction tolerance $C_n = 1 \times 10^{-2}$ are adjusted to some larger number (e.g. $R_n = 5 \times 10^{-2}$ and $C_n = 4 \times 10^{-2}$), which may reduce accuracy; however within a tolerable range. The default time incremented parameters $I_0 = 4$ and $I_R = 8$, which have a direct effect on convergence, are increased to some acceptable values (e.g. $I_0 = 8$ and $I_R = 10$) as well. The parametric study has been done in the author's first year report, in which it showed that such modifications of these parameters would not affect the final numerical results; however, can improve the convergence of simulations.

4.3.2 Verification with semi-analytical solutions

In this section, the non-coaxial coefficient k is always set as zero. Verification of results from numerical simulations and semi-analytical solutions will be presented. As shown

in Tables 4.1 - 2, the investigation is classified into two categories, each encompassing seven separate cases of simulation during which different values of the anisotropic coefficients n and β are investigated. The maximum peak internal friction angle ϕ_{max} is varied from 5° to 40° , and different values of anisotropic coefficients n and β are shown in Tables 4.2 and 2 for the parametric study of bearing capacity factors. The lateral stress ratio K_0 is always set as 0.5, and the associativity in the conventional plastic flow rule is used.

Table 4.1 Typical material constants and loading conditions

Scenario	Young's Modulus	Poisson's ratio	Cohesion	Surface surcharge	Lateral stress ratio
	E (kPa)	ν	c (kPa)	q (kPa)	K_0
Category 1	10.0×10^4	0.3	30	0	N/A
Category 2				100	0.5

Table 4.2 Cases of simulations for rotational ellipse

Cases	The maximum friction angle	Anisotropic coefficient	Direction of the principal loading corresponding to ϕ_{max}
	$\phi_{max}(\circ)$	n	$\beta(\circ)$
Test 1	(40, 35, 30, 25, 20, 15, 10, 5)	1.0	N/A
Test 2	(40, 35, 30, 25, 20, 15, 10, 5)	0.85	0
Test 3			45
Test 4	(40, 35, 30, 25, 20, 15, 10, 5)	0.707	22.5
Test 5			0

Note: coefficient of earth pressure at rest $K_0 = 0.5$, $n = \frac{\sin\phi_{min}}{\sin\phi_{max}}$ and the associativity in the conventional plastic flow rule is used

Ultimate failure pressure

The comparison of the ultimate failure pressure normalised by cohesion (N_c) obtained from semi-analytical solutions and numerical simulations for a rotational ellipse yield curve, is illustrated in Figures 4.10 and 4.11. The maximum friction angle ϕ_{max} is varied from 0° to 40° . A good match of the predicted bearing capacity factor N_c can be observed between numerical simulations and semi-analytical calculations for all cases with different values of anisotropic coefficients n and β . In particular, for a special case when $n = 1.0$, which reduces to Prandtl's solution as shown in Equation 4.43, the numerical results of the bearing capacity factor N_c are close to the analytical results. With the increase in friction angles, the numerical results deviate further from the analytical results.

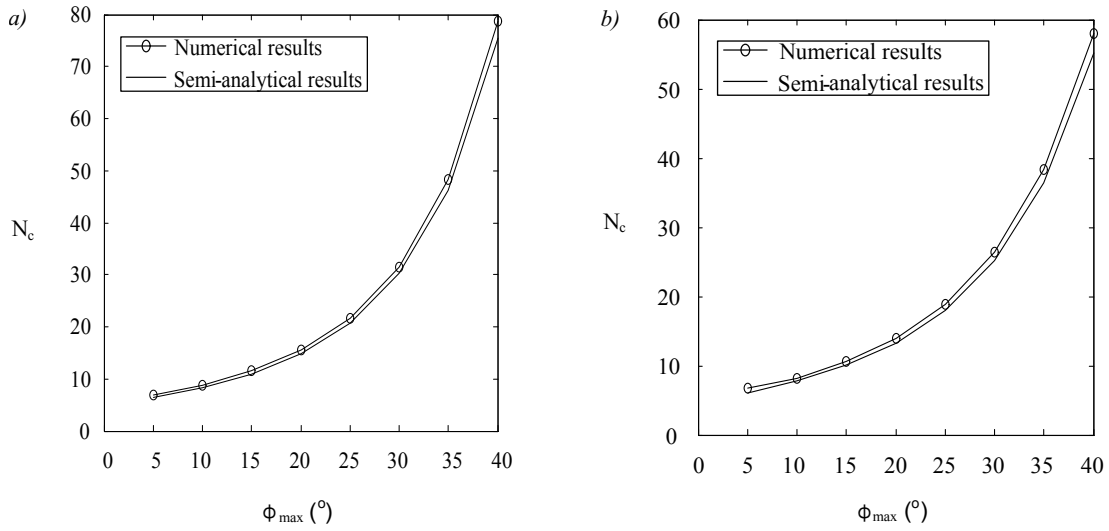


Figure 4.10 Bearing capacity factor N_c versus various friction angles: a) Test 1; b) Test 2.

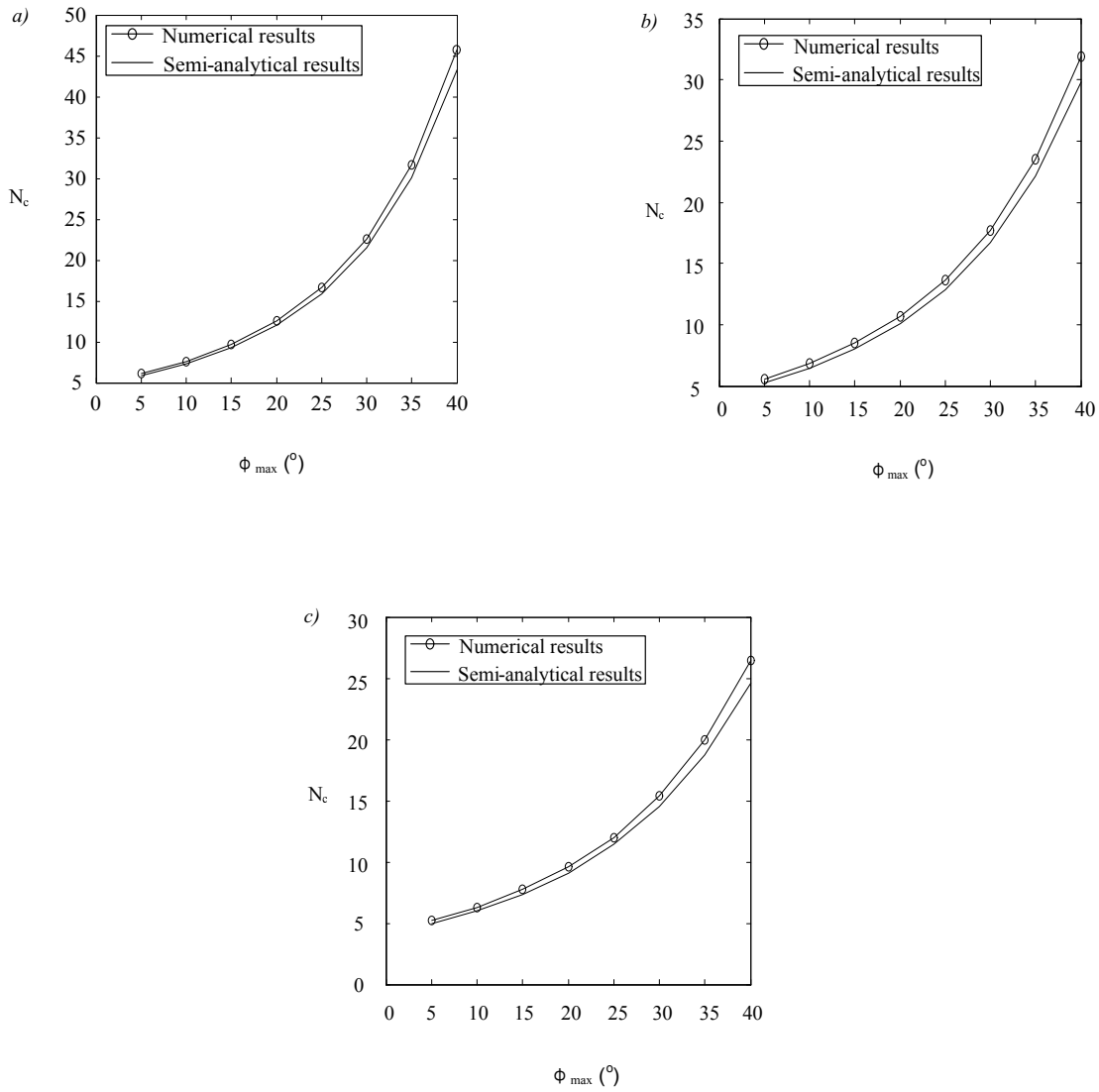


Figure 4.11 Bearing capacity factor N_c versus various friction angles: a) Test 3; b) Test 4; c) Test 5.

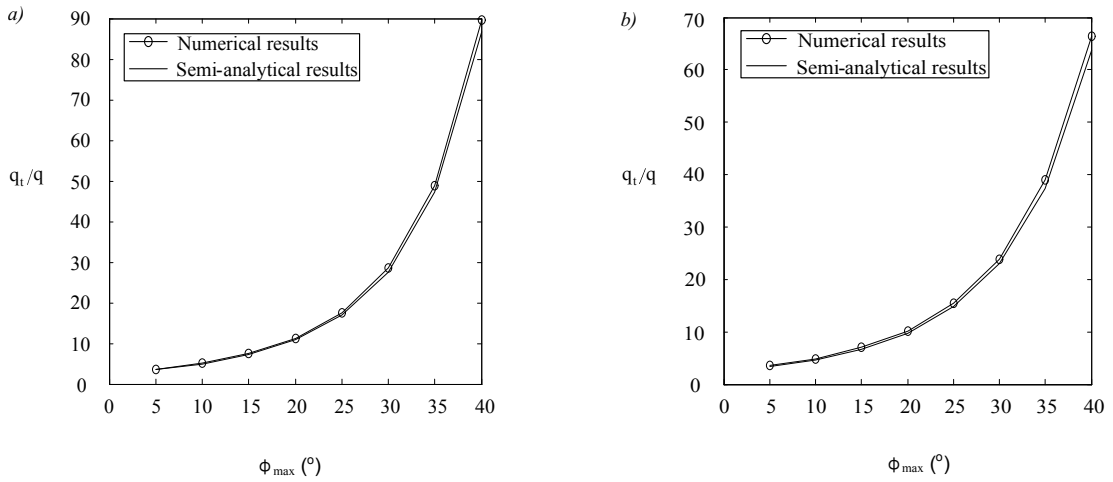


Figure 4.12 Ultimate failure pressure normalised by surface surcharge (q_t/q) versus various friction angles: a) Test 1; b) Test 2.

The comparison of the ultimate failure pressure normalised by the surface surcharge (q_t/q) obtained from semi-analytical solutions and numerical simulations for a rotational ellipse yield curve, is illustrated in Figures 4.12 and 4.13. As shown in Table 4.1, the contribution of the cohesion is not neglected and is set as $c = 30$ kPa for computational convergence with smaller values of friction angle ϕ_{max} . This time the uniform surface surcharge is set as $q = 100$ kPa. A good match of the predicted ultimate failure pressure normalised by the surface surcharge q_t/q can be observed between numerical simulations and semi-analytical calculations for all cases as presented in Figures 4.12 and 4.13.

In summary, the proposed non-coaxial soil model is robust in analysing strip footing problems when the tangential non-coaxial plastic part is not involved.

The pressure-displacement curve

Figures 4.14 - 4.15 show the load displacement curve obtained by applying a rotational ellipse yield criterion for the simulations in each category respectively. The maximum friction angle ϕ_{max} is varied from 5° to 30° .

The y -axis represents the footing pressure normalised by cohesion p/c , and the x -axis represents the vertical displacement (Δ) normalised by the half-length of the footing B . The soil is stiffer with larger values of β and n . In addition, the influence of the anisotropic coefficient β is much more significant than that of n .

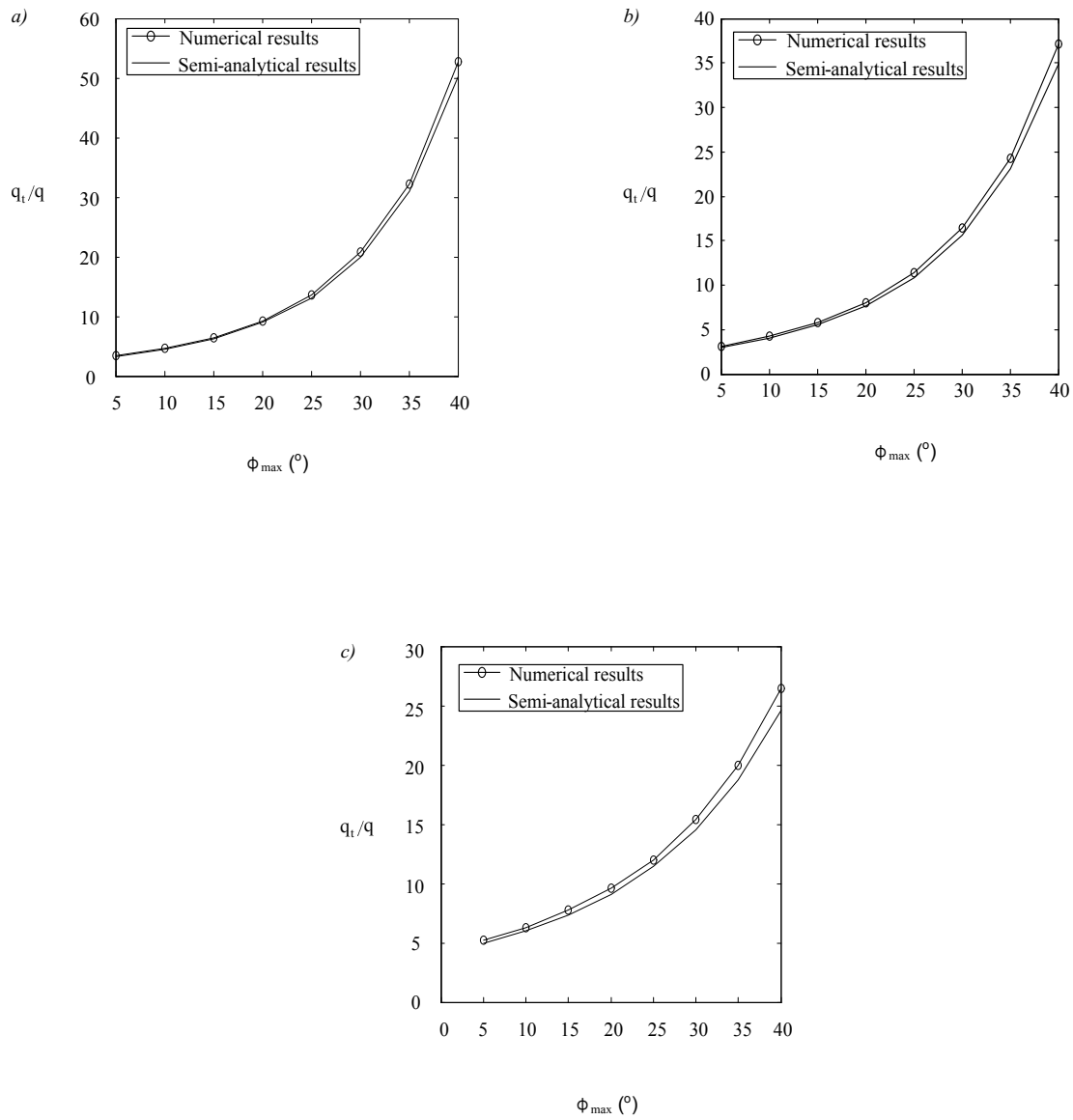


Figure 4.13 Ultimate failure pressure normalised by surface surcharge (q_t/q) versus various friction angles : a) Test 3; b) Test 4; c) Test 5.

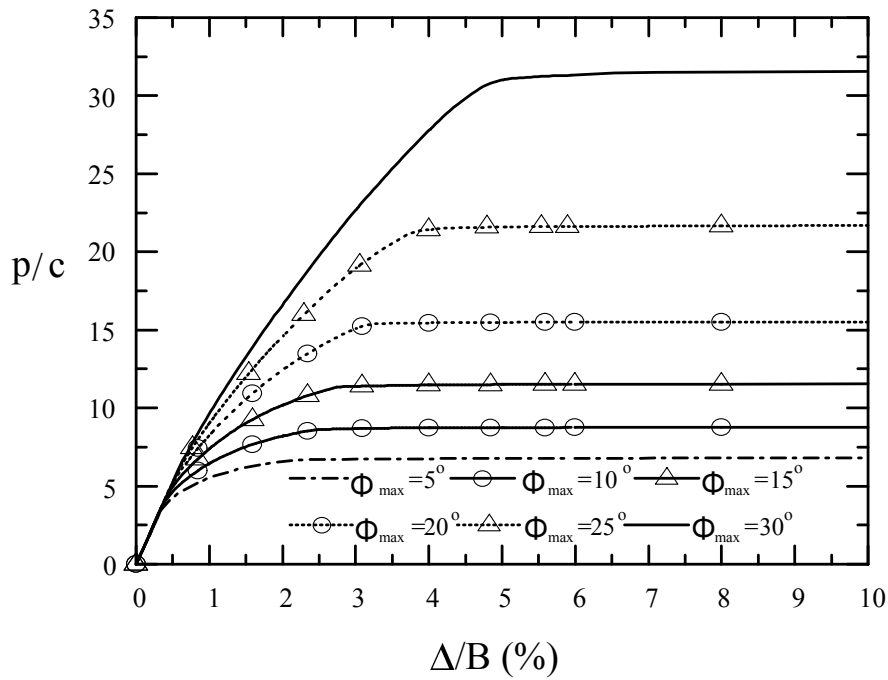


Figure 4.14 Load displacement curve of bearing capacity factor N_c in Test 1.

Figures 4.16 - 4.17 show the load displacement curve obtained by applying a rotational ellipse yield criterion for the simulations in each category respectively. The maximum friction angle ϕ_{max} is varied from 5° to 30° . The y-axis represents the pressure normalised by the surface surcharge p/q , and the x-axis represents the vertical displacement (Δ) normalised by the half-length of footing (B). Similar patterns can be observed as those from the investigations of N_c . The soil is stiffer with an increase in β . The anisotropic coefficient n significantly influences the ultimate failure load, which has been proven in previous analyses.

The velocity field

Figures 4.18 - 4.19 show the velocity field obtained when $\phi_{max} = 30^\circ$. The velocity pattern for the isotropic Mohr-Coulomb yield criterion is presented in Figure 4.18, whereas the velocity patterns for the anisotropic Mohr-Coulomb yield criterion are presented in Figures 4.19. The directions of the arrows represent the flow of the velocity and the length and colour of the arrows represents the magnitude of the displacement. The aim is to verify the velocity field as illustrated by the slip line method. Hence, the exact magnitude of the displacement is not the main concern, and is thus not shown in the figures. The flow pattern of the velocity field can be approximately represented

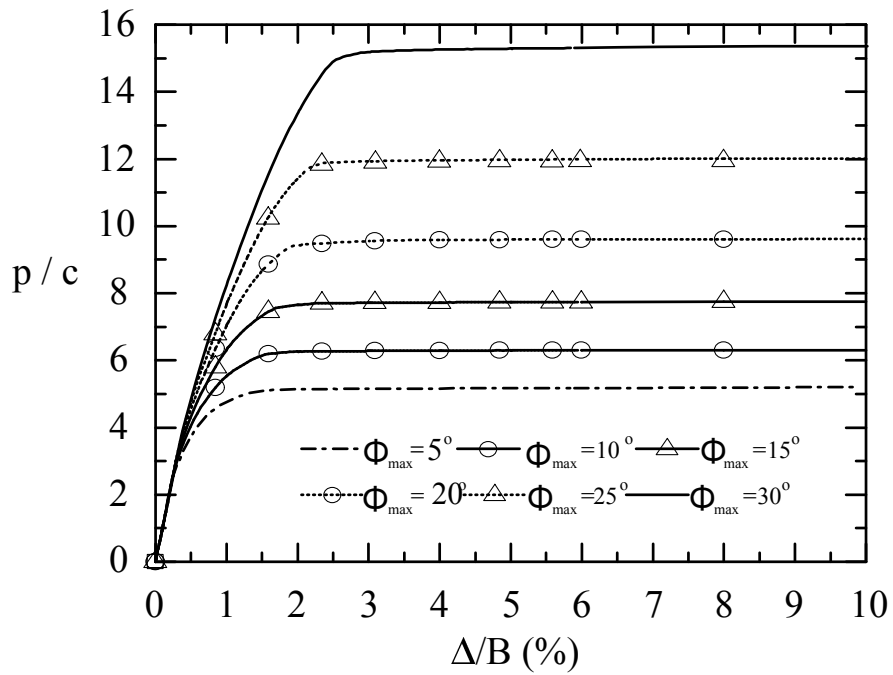


Figure 4.15 Load displacement curve of bearing capacity factor N_c in Test 3.

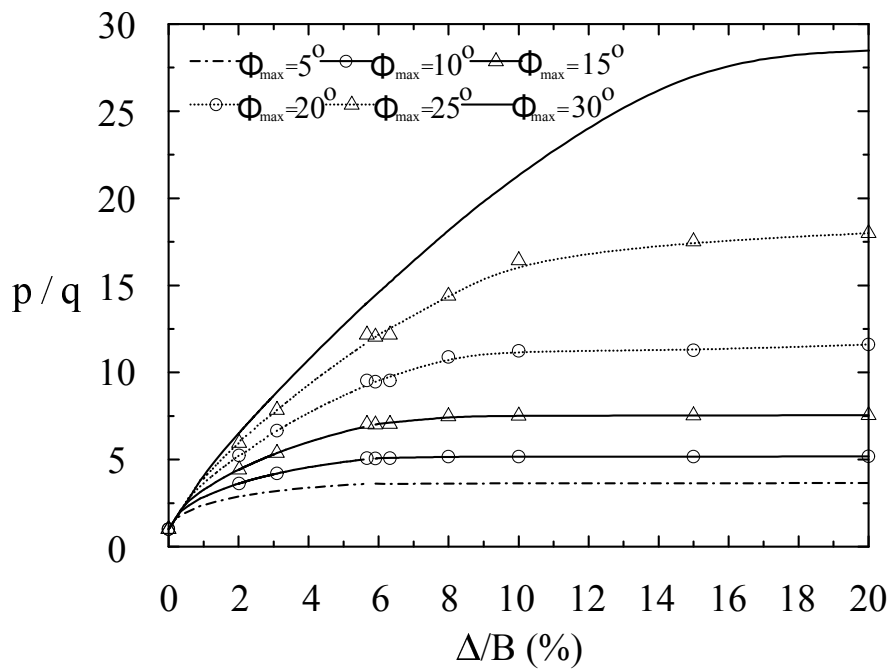


Figure 4.16 Load displacement curve of ultimate failure pressure normalised by surface surcharge q_i/q in Test 1.

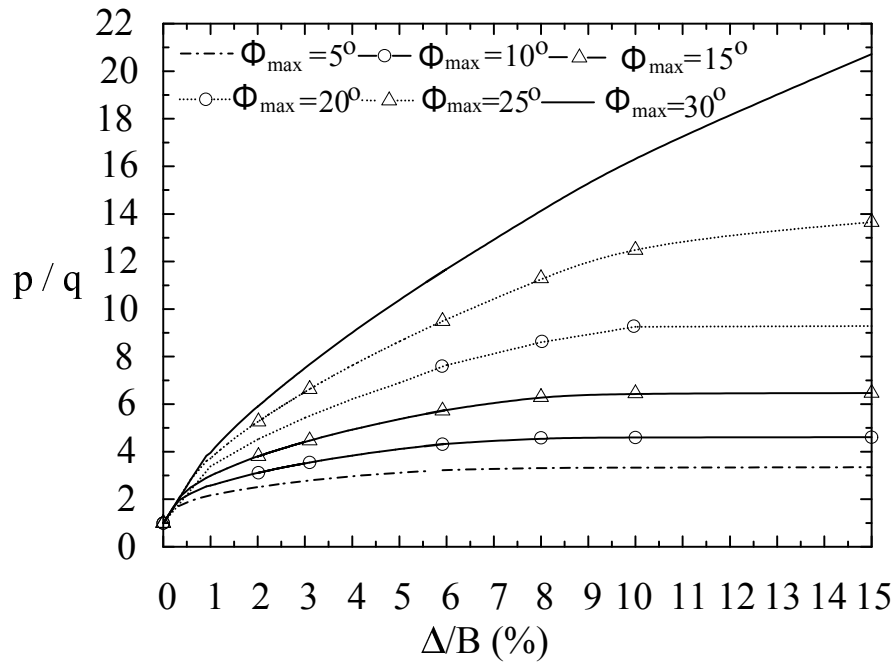


Figure 4.17 Load displacement curve of ultimate failure pressure normalised by surface surcharge q_t/q in Test 3.

by the black dash curves as shown in the figures. When compared to Figure 4.5, the black dash curves can be referred to as the β -lines. They are consistent with the theoretic pattern predicted by the slip line method. In addition, the failure zones indicated by the anisotropic Mohr-Coulomb yield criterion are wider than those indicated by its isotropic counterpart. The horizontal displacements are as well visually larger.

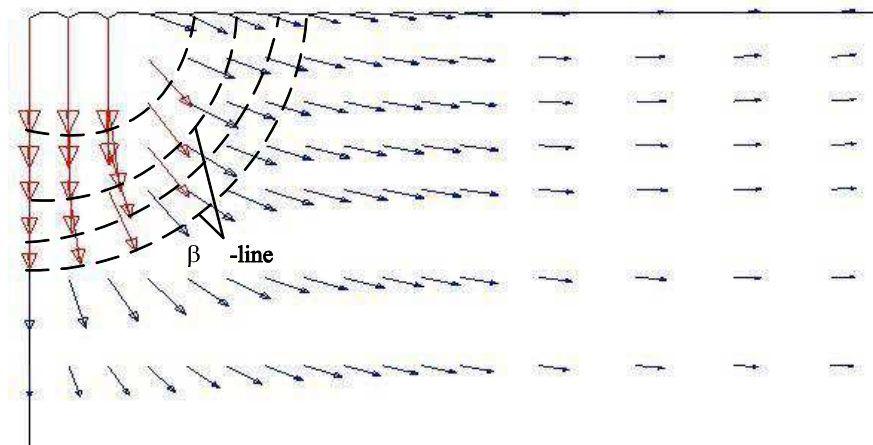


Figure 4.18 The velocity field for the case of isotropic Mohr-Coulomb yield criterion.

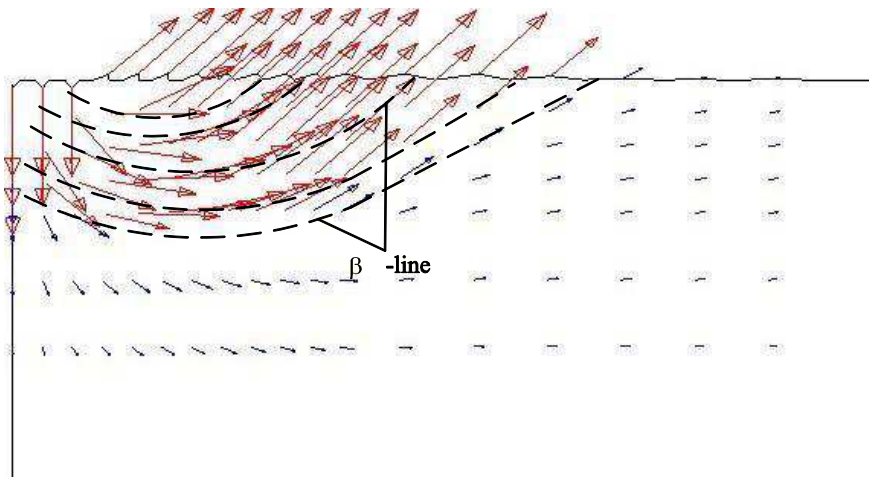


Figure 4.19 The velocity field when $n = 0.707$, $\beta = 45^\circ$.

4.3.3 Results and discussion

4.3.3.1 The computation of bearing capacity due to the contribution of cohesion

$$N_c$$

In this subsection, a thorough investigation of N_c is presented using the newly proposed non-coaxial soil model. For the computation of bearing capacity N_c , contributions of other bearing capacity factors are neglected. The soil underneath the footing is assumed purely frictional-cohesive. In particular, the influence of soil anisotropy, the initial stress state and non-coaxiality on the bearing capacity of a smooth strip footing is analysed. Load-displacement curves are presented below. The displacement is normalised by the half width of footing B . Details of the material properties for numerical simulations under these conditions are shown in Table 4.3.

Table 4.3 Material properties for all numerical simulations

Cases	Anisotropic coefficient		Flow rule	Dilation angle	Non-coaxial coefficient
	n	$\beta(^{\circ})$	0-asso 1-non-asso	$\psi_{max}(^{\circ})$	
Test 8	1.0	N/A	0	30	(0.0, 0.02, 0.1)
Test 9			1	20	
Test 10	0.85	45	0	30	(0.0, 0.02, 0.1)
Test 11			1	20	
Test 12	0.707	22.5	0	30	(0.0, 0.02, 0.1)
Test 13			0	30	
Test 14			0	30	
Test 15		0	1	20	

Note: the maximum friction angle $\phi_{max} = 30^\circ$, $c = 30$ kPa, and $q = 0$ kPa.

Figures 4.20 and 4.21 show the evolution of the resulted pressure normalised by cohesion versus the normalised footing displacement when the anisotropic coefficient

$n = 1.0$. In other words, the isotropic Mohr-Coulomb yield criterion is retrieved. Results by using the associativity and nonassociativity in the conventional plastic flow rules respectively are compared. The dilation angle is set as $\psi_{max} = 20^\circ$ for computational convenience. As shown in Figure 4.20, the maximum difference of the normalised pressure between coaxial ($k = 0.0$) and non-coaxial predictions ($k = 0.1$) is $R_r = 12.4\%$ ($R_r = \frac{N_c(k=0.1) - N_c(k=0.0)}{N_c(k=0.0)}$) when the associativity in the conventional plastic flow rule is used, while the maximum difference of the normalised displacement corresponding to the maximum normalised pressure ($R_s = \frac{\Delta(k=0.1) - \Delta(k=0.0)}{\Delta(k=0.0)}$), as shown in Figures 4.20, is $R_s = 26.9\%$. In Figure 4.21 however, the maximum difference of the normalised pressure is $R_r = 13.1\%$ when the nonassociativity in the conventional plastic flow rule is employed, which is 0.7% larger than the value calculated for the previous case. The maximum difference of the displacement is $R_s = 34.3\%$, which is 7.4% larger than the associativity one. In Figure 4.20, the footing reaches the ultimate failure at $\frac{\Delta}{B} = 0.5$, and at $\frac{\Delta}{B} = 0.6$ in Figure 4.21. It shows that the material with a greater dilation angle shows a greater volume increase than the material with a smaller dilation angle. This makes the soil with the associativity in the conventional plastic flow rule slightly stiffer than the non-dilatant material.

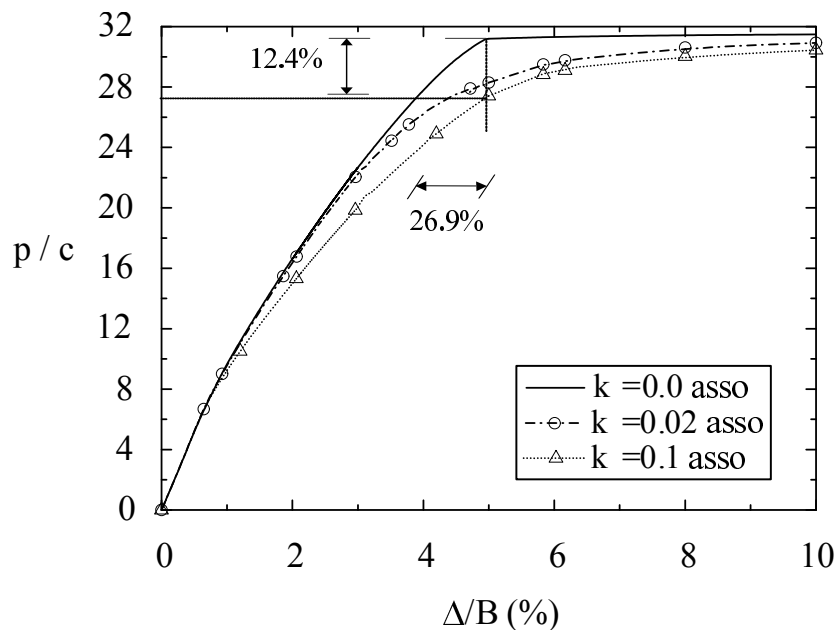


Figure 4.20 Load displacement curve of bearing capacity N_c in Test 8.

Then the investigation of the non-coaxial theory with an anisotropic yield criterion is analysed in Figures 4.22 - 4.27. The influences of different values of anisotropic coef-

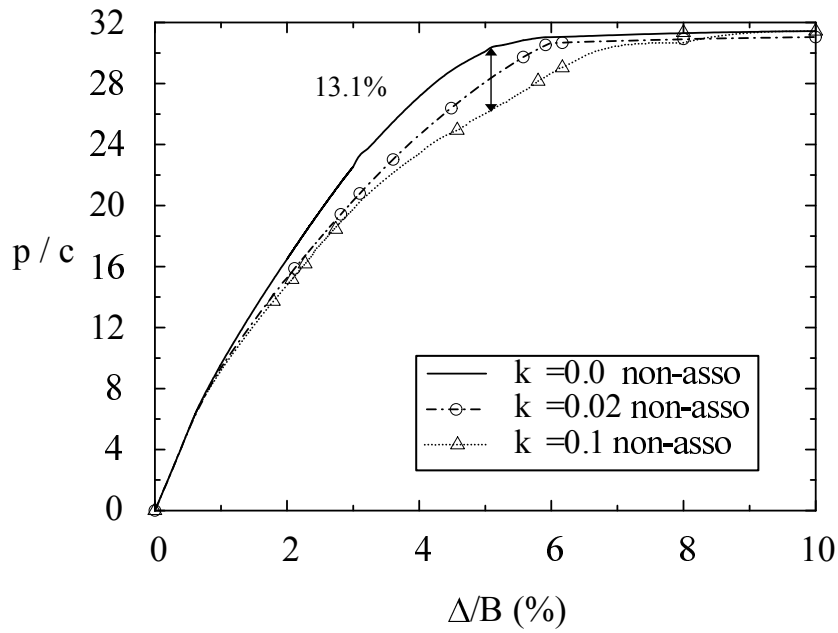


Figure 4.21 Load displacement curve of bearing capacity N_c in Test 9.

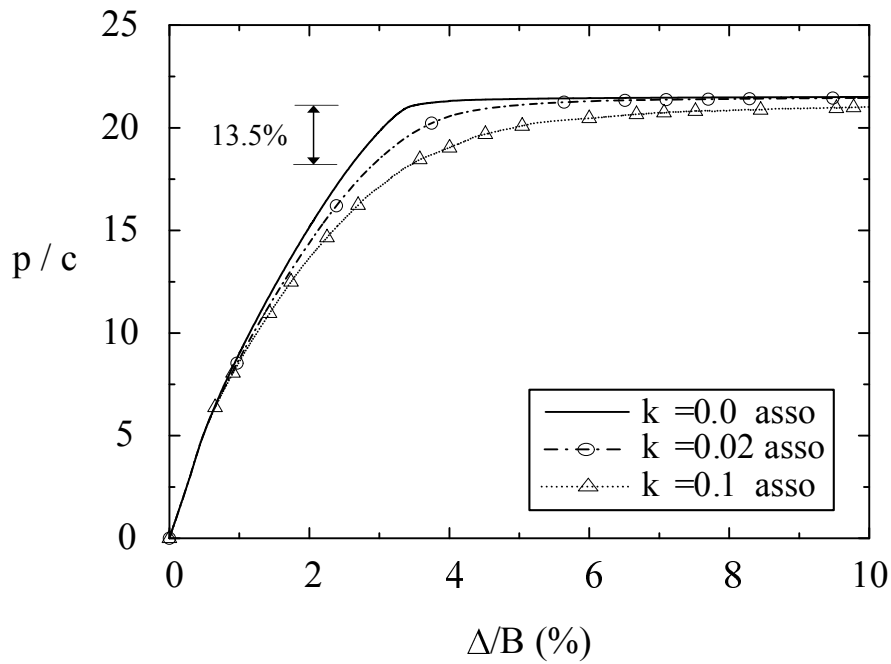


Figure 4.22 Load displacement curve of bearing capacity N_c in Test 10.

ficients n and β and flow rules on the pressure-displacement curves are also examined.

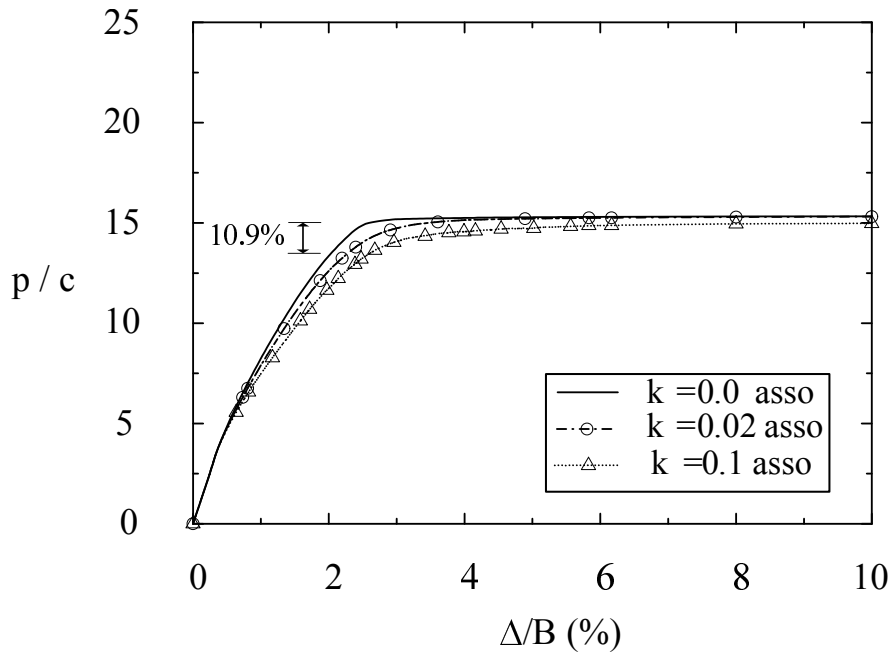
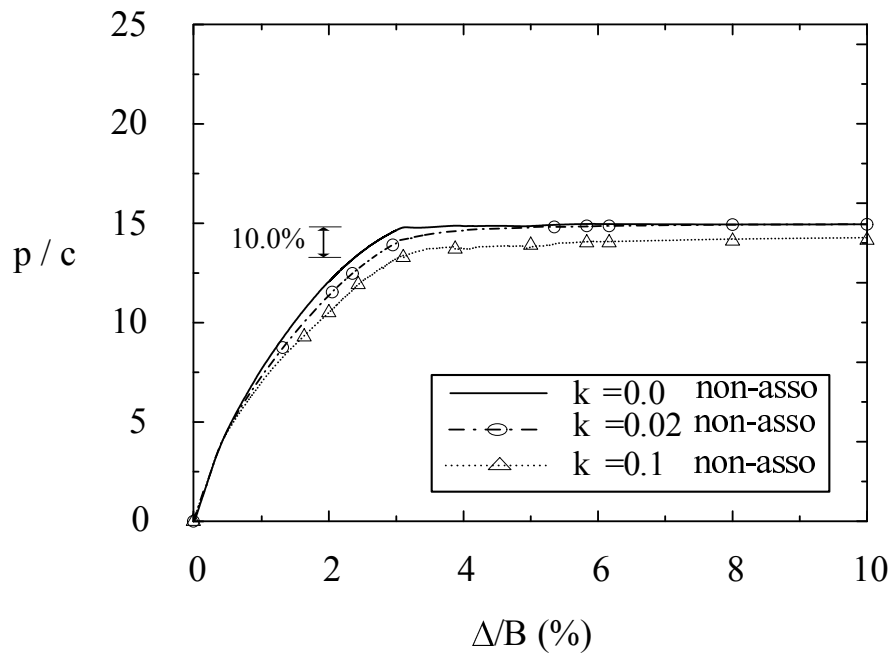
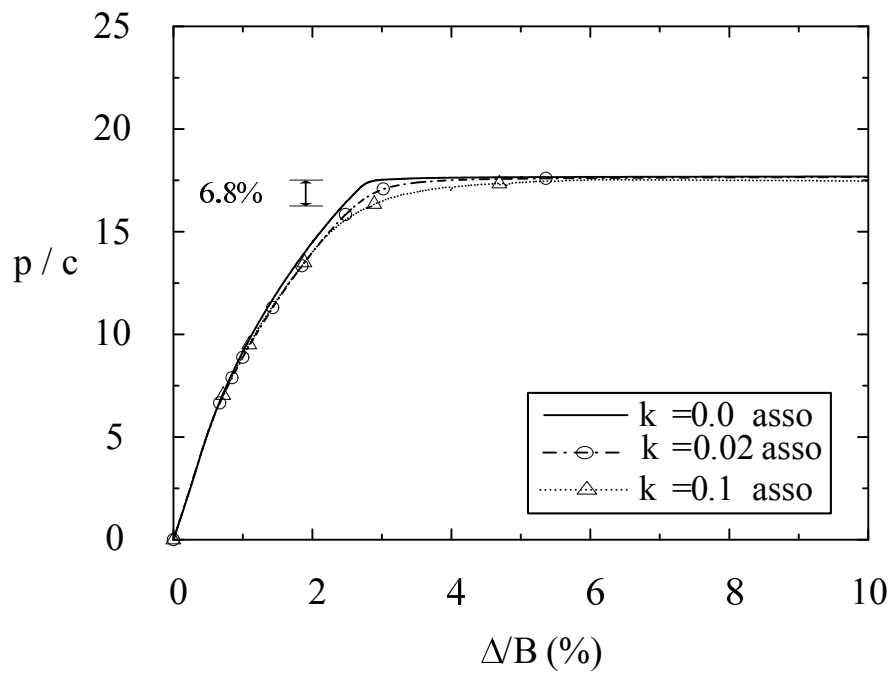


Figure 4.23 Load displacement curve of bearing capacity N_c in Test 11.

Generally, the settlement prior to collapse is larger when the non-coaxial coefficient is unequal to zero. However, the ultimate bearing capacity N_c is not significantly affected. Its values virtually tend to be identical, irrespective of the values of the anisotropic coefficient and flow rules. The predicted prior settlement increases with the increase in non-coaxial coefficient k . This indicates that the soil is softened when non-coaxial plasticity is applied. For particular cases (as shown in Figures 4.26 and 4.27), non-coaxial modelling results with $k = 0.1$ match closely with those of $k = 0.0$.

With respect to the maximum difference R_r between $k = 0.0$ and $k = 0.1$, it seems that the anisotropic coefficients n and β highly affect the influence of non-coaxiality on the bearing capacity N_c . As indicated in Figure 4.23, the maximum difference $R_r = 13.5\%$. However, the difference decreases with a reduction in n and β . For cases when $n = 0.707$ and $\beta = 0^\circ$, R_r is as low as 4.6%. In other words, non-coaxiality rarely affects the settlement and ultimate failure load for this special case.

Figures 4.24 and 4.27 present results by using the nonassociativity in the conventional plastic flow rule. The maximum difference between non-coaxial coefficient $k = 0.0$ and $k = 0.1$ is not obviously affected by using the associativity and nonassociativity

Figure 4.24 Load displacement curve of bearing capacity N_c in Test 12.Figure 4.25 Load displacement curve of bearing capacity N_c in Test 13.

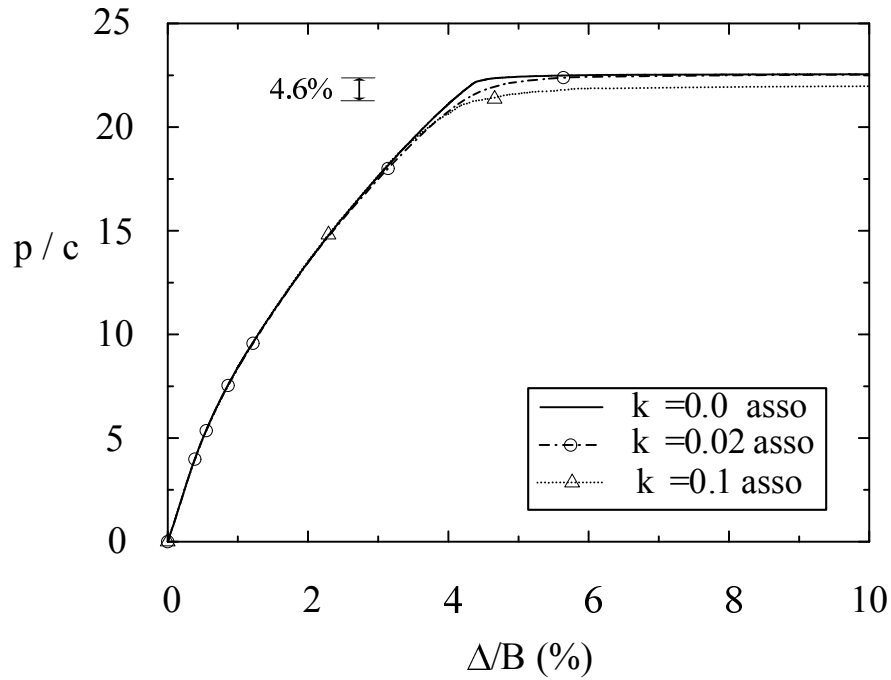


Figure 4.26 Load displacement curve of bearing capacity N_c in Test 14.

in the conventional plastic flow rule respectively. As shown in Figures 4.23 - 4.27, the difference $R_r = 10.9\%$, $R_r = 6.8\%$ and $R_r = 4.6\%$ by using the associativity in the conventional plastic flow rule, as compared to $R_r = 10.0\%$ and $R_r = 4.9\%$ by using the nonassociativity in the conventional plastic flow rule respectively.

All the values of the maximum difference of the normalised pressure and the displacement for the computation of N_c are shown in Table 4.4.

Table 4.4 Material properties for all numerical simulations

Cases	Anisotropic coefficient		R_r	R_s
	n	$\beta(\circ)$		
Test 8	1.0	N/A	12.4%	26.9%
Test 9			13.1%	34.3%
Test 10	0.85	45	13.5%	34.6%
Test 11	0.707	45	10.9%	31.7%
Test 12			10.0%	27.5%
Test 13			6.8%	17.6%
Test 14	0	0	4.6%	12.5%
Test 15			4.9%	10.5%

Figures 4.28 and 4.29 show the principal stress rotations of only those elements at the corner of the footing (see red elements in the model). The bond lines are obtained from cases when non-coaxial coefficient $k = 0.02$; whereas the dash lines represent results obtained when non-coaxial coefficient $k = 0.0$. The influence of the anisotropic

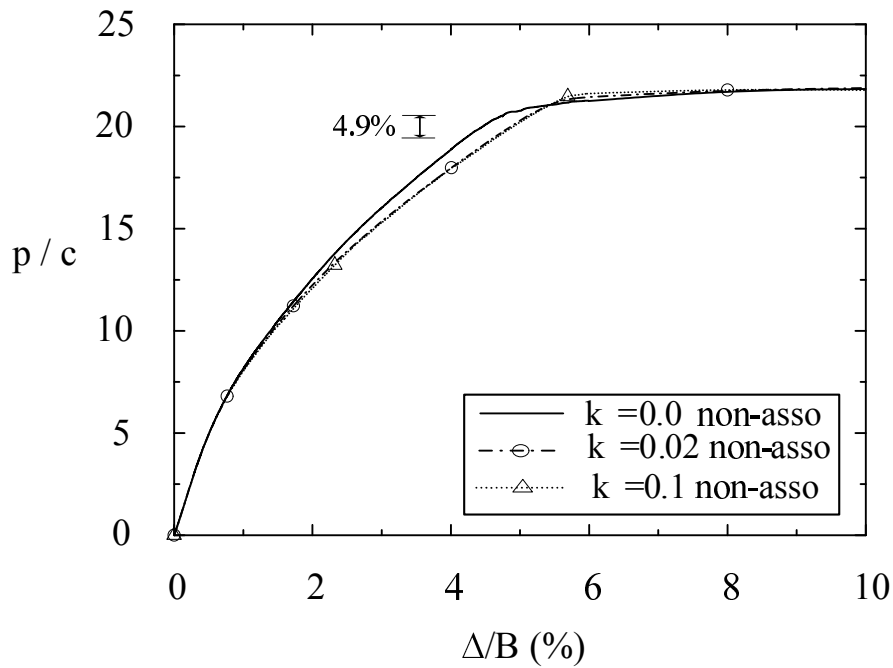


Figure 4.27 Load displacement curve of bearing capacity N_c in Test 15.

coefficient and the dilation angle on non-coaxial modelling is presented and analysed. In Figure 4.28, the variation of the principal stress rotation (Θ) from -6° to 8° is much less significant for the case when $n = 0.707$ and $\beta = 0^\circ$ (see blue lines) as compared to the other two cases (see red lines and black lines); the degree of which approximately ranges from -13° to 12° . This results in the lessened effect of non-coaxiality on prior settlements, which has been proven in Figure 4.26 since $R_r = 4.6\%$. As shown in Figure 4.29, the change in the principal stress rotation (Θ) by using the nonassociativity in the conventional plastic flow rule is less obvious (see red lines) as compared to the change by using the associativity in the conventional plastic flow rule (see black lines). Likewise, this leads to a less influence of non-coaxiality on prior settlements, of which evidence can be found in Figure 4.23 ($R_r = 10.9\%$) and Figure 4.24 ($R_r = 10.0\%$).

4.3.3.2 The computation of bearing capacity due to the contribution of surface surcharge N_q

In this subsection, a thorough investigation of N_q is presented using the newly proposed non-coaxial model. The footing is located on a weightless, cohesionless frictional soil. A uniform surface surcharge of 100 kPa is applied. The calculation of N_q is performed to include the contribution of surface surcharge. Contributions from other bearing capacity factors are eliminated in this situation. The coefficient of earth pressure at rest

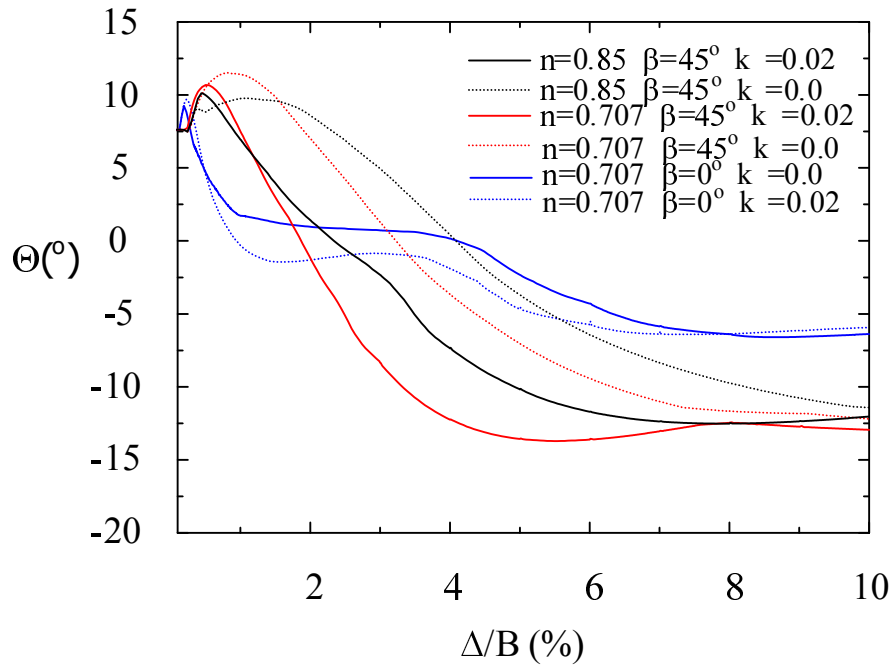


Figure 4.28 Principal stress rotation regarding different values of the anisotropic coefficient.

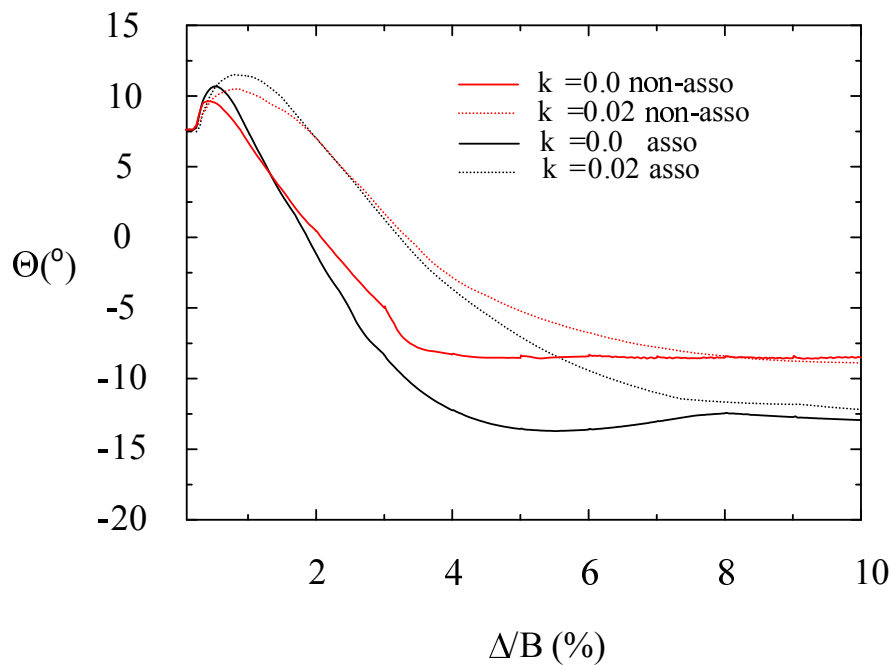


Figure 4.29 Principal stress rotation with regarding associativity and nonassociativity in the conventional plastic flow rule ($n = 0.707$, $\beta = 45^\circ$).

K_0 is assumed as 0.5 for normally consolidated soil and $K_0 = 2.0$ for over-consolidated soil. Both the associativity and nonassociativity in the conventional plastic flow rule are used in this instance. The maximum peak internal friction angle is always set as $\phi_{max} = 30^\circ$. Details of material properties for all cases are shown in Table 4.5.

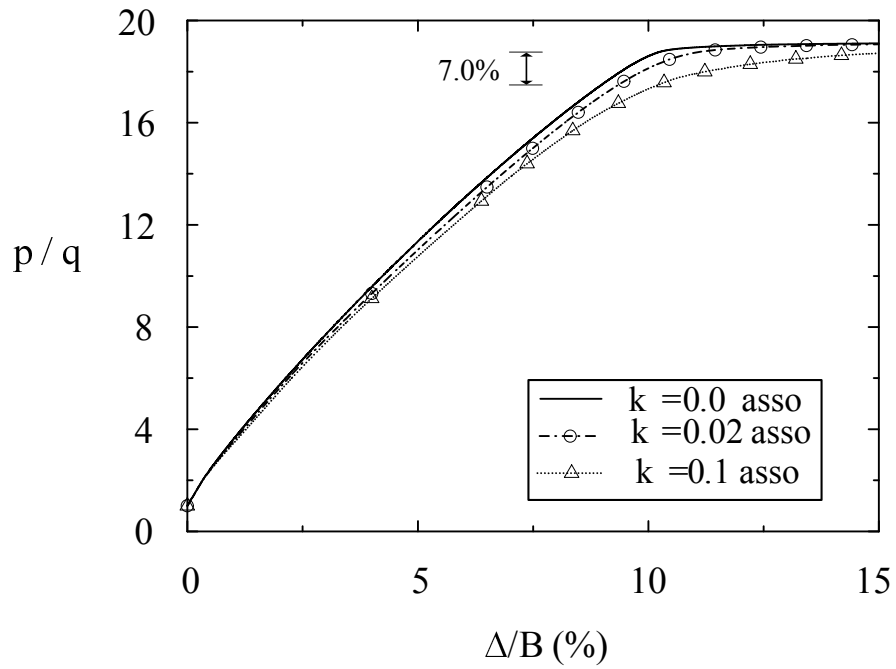
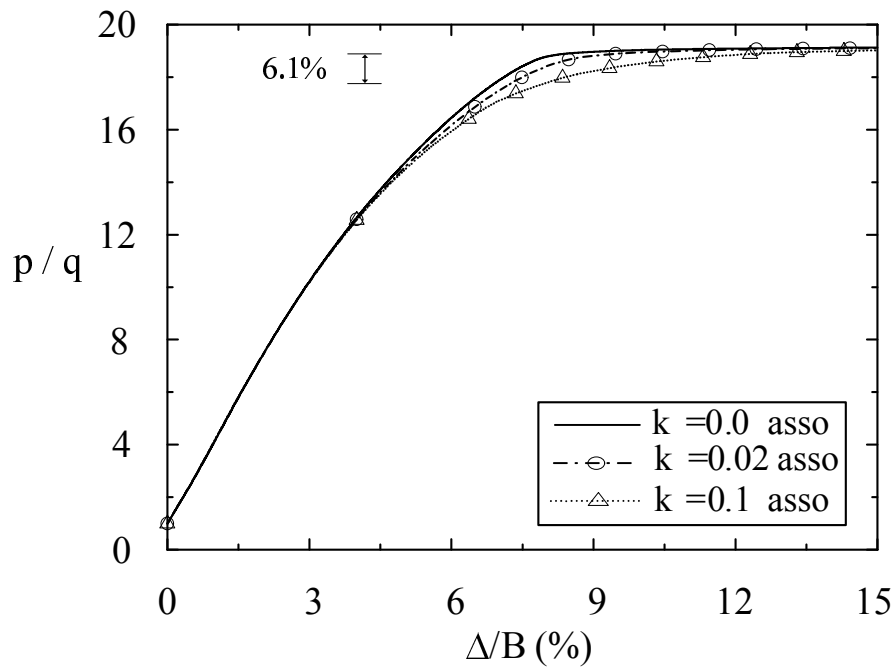
Table 4.5 Material properties for all numerical simulations

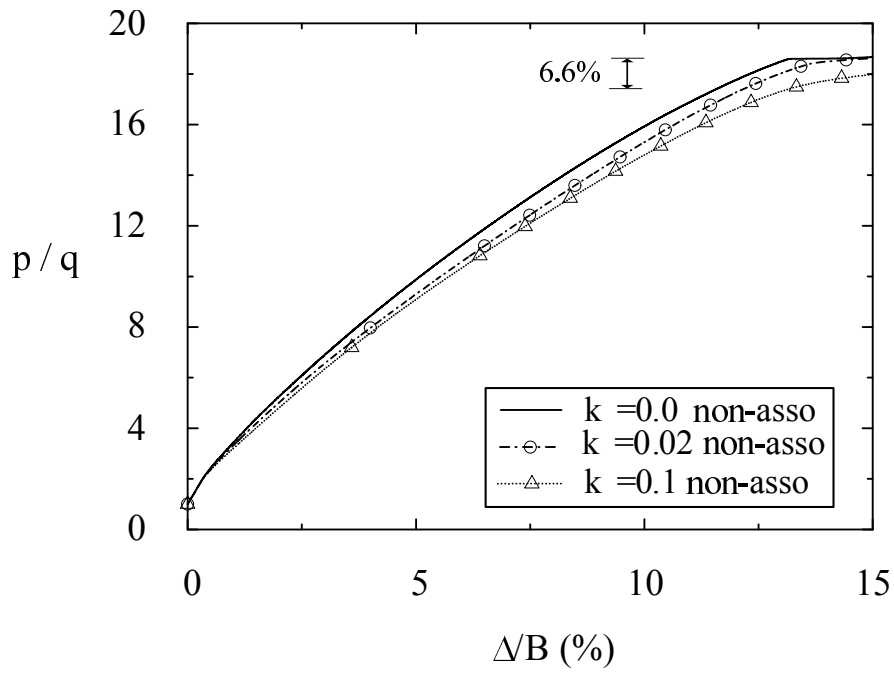
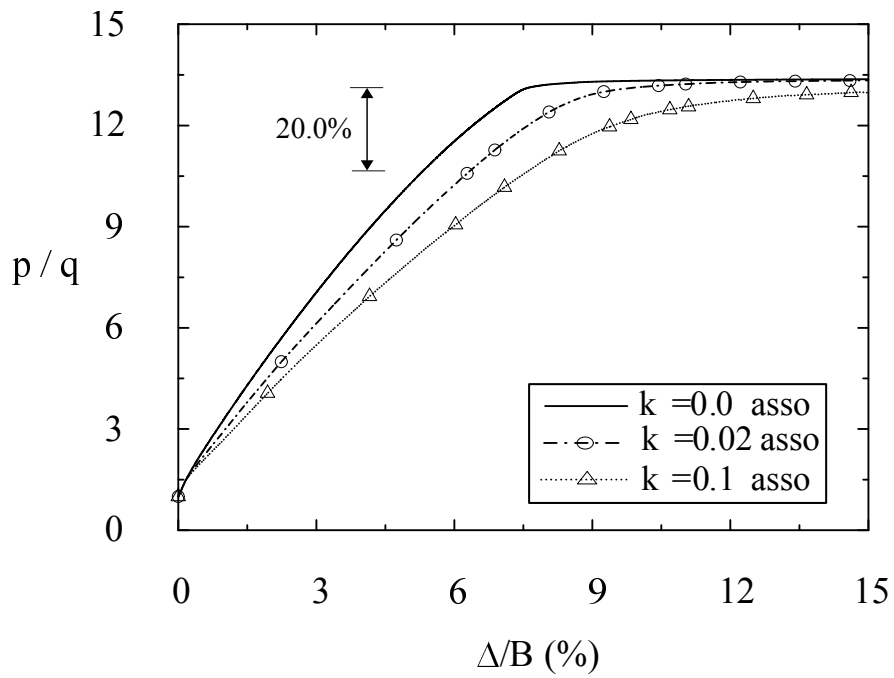
Cases	Anisotropic coefficient		Flow rule	Dilation angle	Lateral stress ratio	Non-coaxial coefficient			
	n	$\beta(^\circ)$	0-asso 1-non-asso	$\psi_{max}(^\circ)$	K_0	k			
Test 17	1.0	N/A	0	30	0.5	(0.0, 0.02, 0.1)			
Test 18					2.0				
Test 19					1		20	0.5	
Test 20	0.85	45	0	30	0.5	(0.0, 0.02, 0.1)			
Test 21					0.5				
Test 22					45		0	30	2.0
Test 23	0.707	45	1	20	0.5	(0.0, 0.02, 0.1)			
Test 24					22.5		0	30	0.5
Test 25					0		0	30	0.5

Note: the maximum friction angle $\phi_{max} = 30^\circ$, $c = 0.001\text{kPa}$, and $q = 100\text{kPa}$.

Figures 4.30 - 4.32 illustrate the load displacement curve of the resulted pressure normalised by surface surcharge with different initial stress states and flow rules when the isotropic Mohr-Coulomb yield criterion is recovered ($n = 1.0$). Generally, the ultimate value of the bearing capacity N_q is rarely affected by non-coaxial plasticity. All lines tend to be identical with the increase in the stress level. Non-coaxial modelling affects the settlement prior to collapse. The maximum difference between coaxial and non-coaxial predictions is $R_r = 7.0\%$ when using the associativity in the conventional plastic flow rule, which is slightly larger than that of $R_r = 6.6\%$ when using the non-associativity in the conventional plastic flow rule. This indicates that the non-coaxial effect is not highly affected by flow rules. Similar conclusions drawn with the computation of N_c that the soil is stiffer when using the associativity in the conventional plastic flow rule, are also suitable to the computation of N_q .

Figures 4.33 - 4.38 present the influence of non-coaxiality on the bearing capacity N_q in the context of soil anisotropy. For all cases, non-coaxiality has negligible influence on the ultimate value of the bearing capacity N_q ; however, the settlement prior to collapse is relatively largely affected by non-coaxial modelling. The influence of non-coaxiality is pronounced in test numbers 20, 21 and 23, when the anisotropic coefficients $n = 0.85$, $\beta = 45^\circ$ and $n = 0.707$ and $\beta = 45^\circ$ for both the associativity and

Figure 4.30 Load displacement curve of bearing capacity N_q in Test 17.Figure 4.31 Load displacement curve of bearing capacity N_q in Test 18.

Figure 4.32 Load displacement curve of bearing capacity N_q in Test 19.Figure 4.33 Load displacement curve of bearing capacity N_q in Test 20.

nonassociativity in the conventional plastic flow rule.

It is apparent that the maximum difference R_r between modelling when $k = 0.0$ and $k = 0.1$ is highly affected by the values of anisotropic coefficients n and β . As indicated in Figure 4.33 ($R_r = 20.0\%$) and 4.34 ($R_r = 28.3\%$), the value of R_r increases with a decrease in the value of n . However, when comparing Figure 4.34, 4.37 and 4.38, the difference R_r sharply decreases with smaller values of β . The values drops from $R_r = 28.3\%$ to $R_r = 3.4\%$ for such a scenario.

Figures 4.34 and 4.35 show the influence of the dilation angle (flow rules) on non-coaxial modelling. When the associativity in the conventional plastic flow rule is applied to soil, the medium is stiffer than a non-dilatant material. The difference R_r is small, with $R_r = 28.3\%$ and 24.4% when using the associativity and nonassociativity in the conventional plastic flow rule respectively.

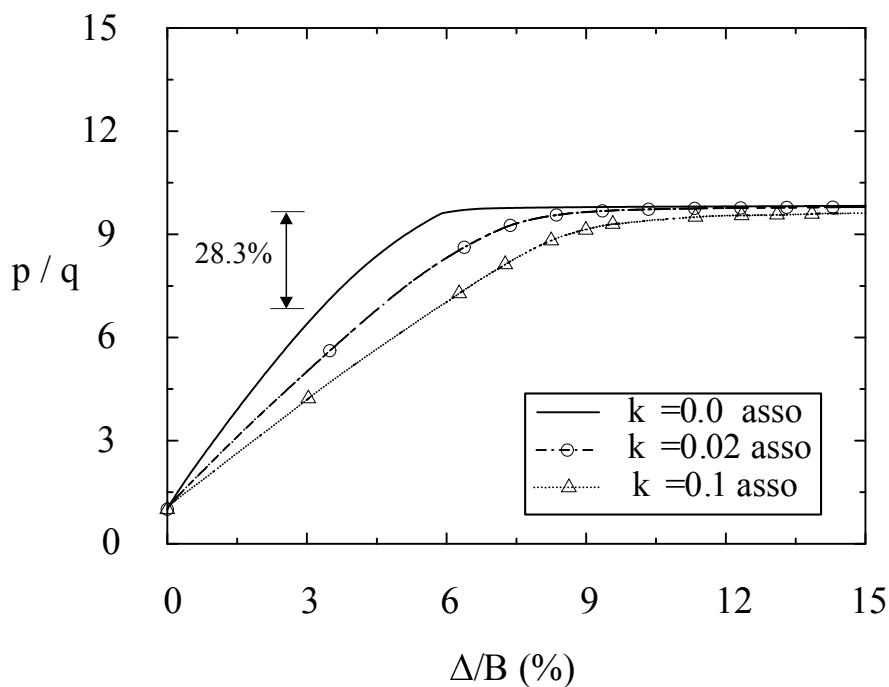
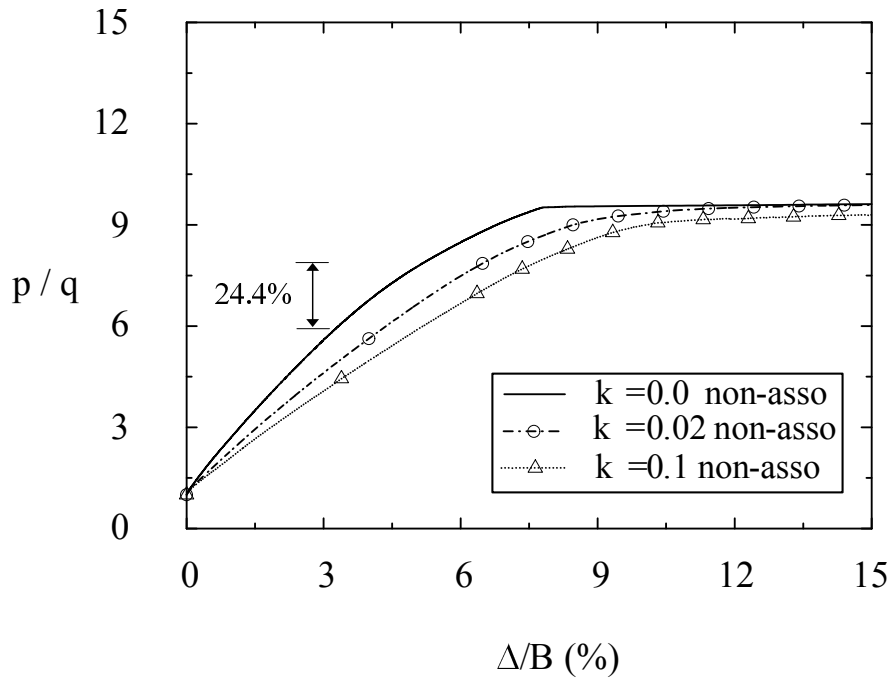
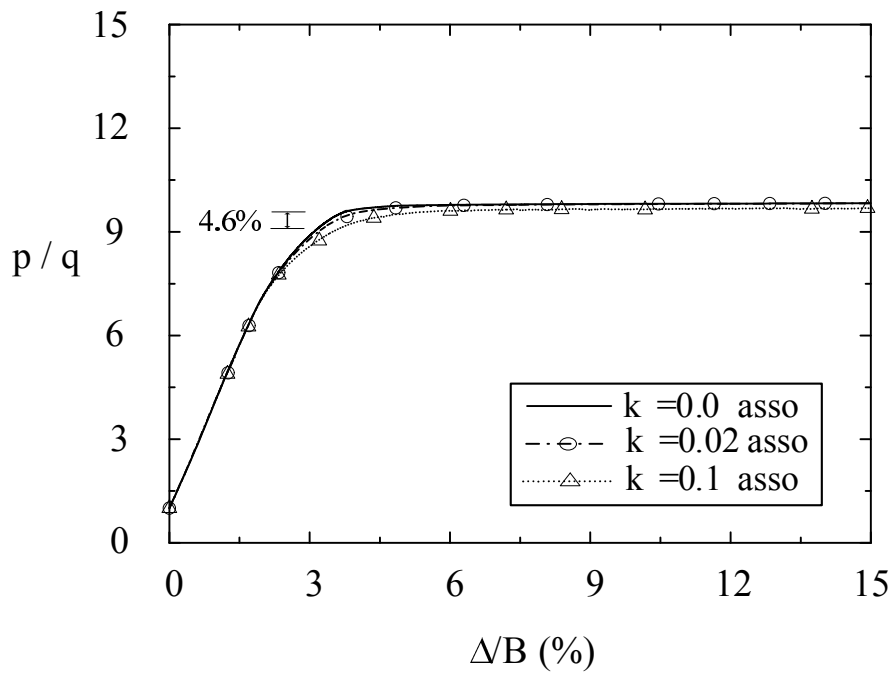
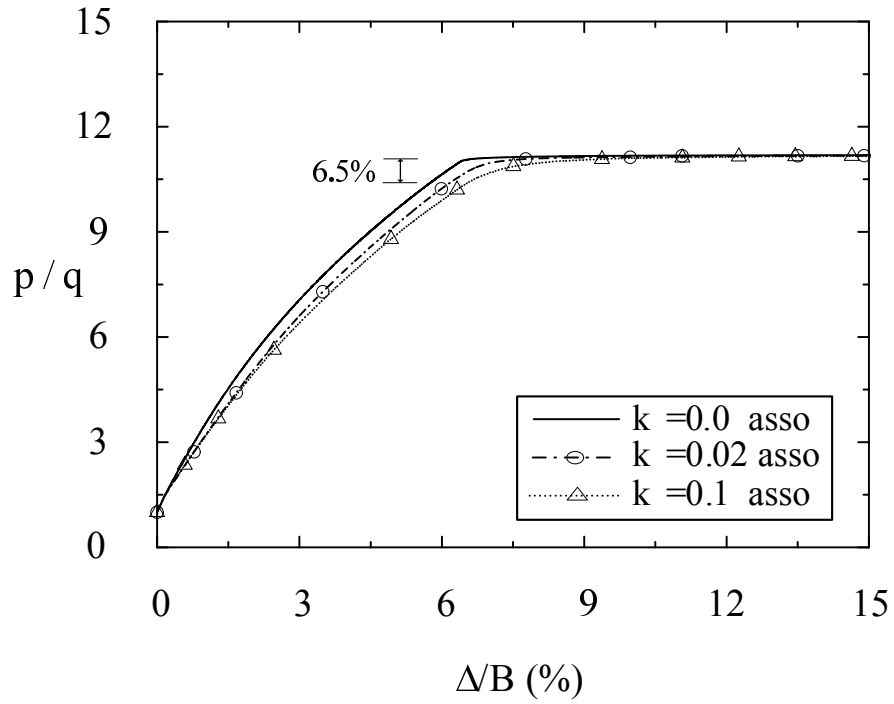
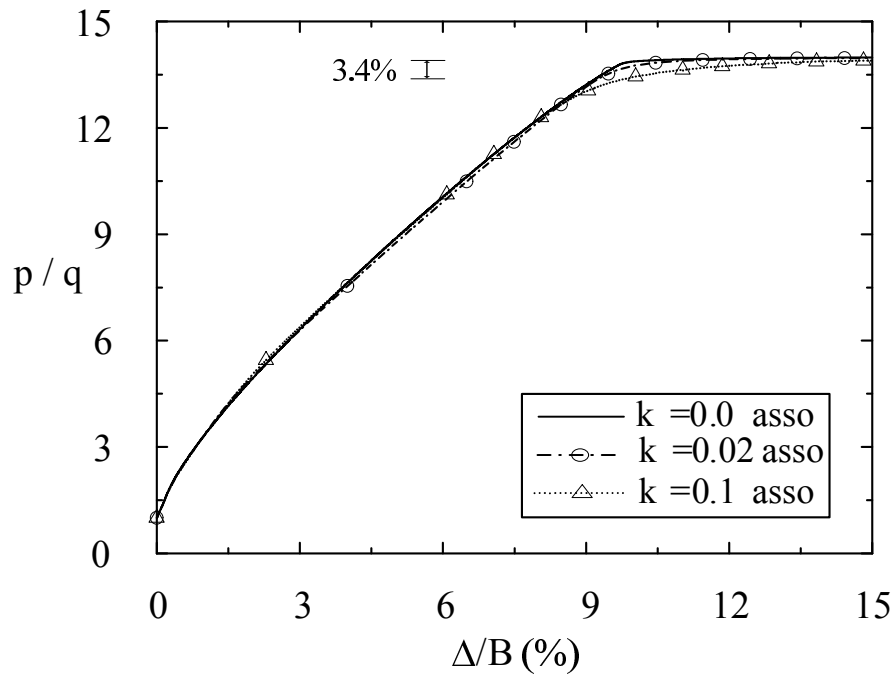


Figure 4.34 Load displacement curve of bearing capacity N_q in Test 21.

It seems that the initial stress state in terms of lateral stress ratio K_0 has a severe effect on non-coaxial modelling, which can be seen in Figures 4.34 and 4.37. For normally consolidated soil, the difference R_r is as high as 28.3%. For over-consolidated soil, there is little difference between coaxial and non-coaxial predictions, for which

Figure 4.35 Load displacement curve of bearing capacity N_q in Test 23.Figure 4.36 Load displacement curve of bearing capacity N_q in Test 22.

Figure 4.37 Load displacement curve of bearing capacity N_q in Test 24.Figure 4.38 Load displacement curve of bearing capacity N_q in Test 25.

$R_r = 4.6\%$.

All the values of the maximum difference of the normalised pressure and the displacement for the computation of N_q are shown in Table 4.6.

Table 4.6 Material properties for all numerical simulations

Cases	Anisotropic coefficient		Lateral stress ratio	R_r	R_s	
	n	$\beta(^{\circ})$	K_0			
Test 17	1.0	N/A	0.5	7.0%	14.2%	
Test 18			2.0	6.1%	17.2%	
Test 19			0.5	6.6%	13.6%	
Test 20	0.85	45	0.5	20.0%	43.3%	
Test 21	0.707	45	0.5	28.3%	73.0%	
Test 22			2.0	4.6%	16.3%	
Test 23			0.5	24.4%	53.8%	
Test 24			22.5	0.5	6.5%	14.1%
Test 25			0	0.5	3.4%	6.5%

Figures 4.39 and 4.40 show the principal stress rotations of only those elements at the corner of the footing under the respective conditions. The influence of anisotropic coefficients n and β and the initial stress state on the change of principal stress rotation are analysed, which in return provide mechanism evidence that non-coaxial behaviour in some cases is apparent. As shown in Figure 4.39, the black lines indicate the most severe principal stress rotations that have a range between -12.5° and 12.5° . This results in the highest difference $R_r = 28.3\%$ for cases when $n = 0.707$ and $\beta = 45^{\circ}$, which is demonstrated in Figure 4.40. The variation of principal stress rotations for blue lines corresponding to $n = 1.0$ is from approximately -7.5° to 7.5° , whereas that for red lines corresponding to $n = 0.707$ and $\beta = 0^{\circ}$ is from approximately -7.5° to 4.8° . Hence the value of R_r for these two conditions is 7.0% and 3.4% respectively. Taking the influence of the initial stress state into consideration, it is illustrated in Figure 4.40 that when the anisotropic coefficient $n = 0.707$ and $\beta = 45^{\circ}$, there are few fluctuations in red lines which represent over-consolidated soil. This results in $R_r = 4.6\%$ for this case, which is much lower as compared to $R_r = 28.3\%$ corresponding to black lines that represent normally consolidated soil. It is concluded that the values of initial stress state and the anisotropic coefficients have drastic effects on non-coaxial modelling.

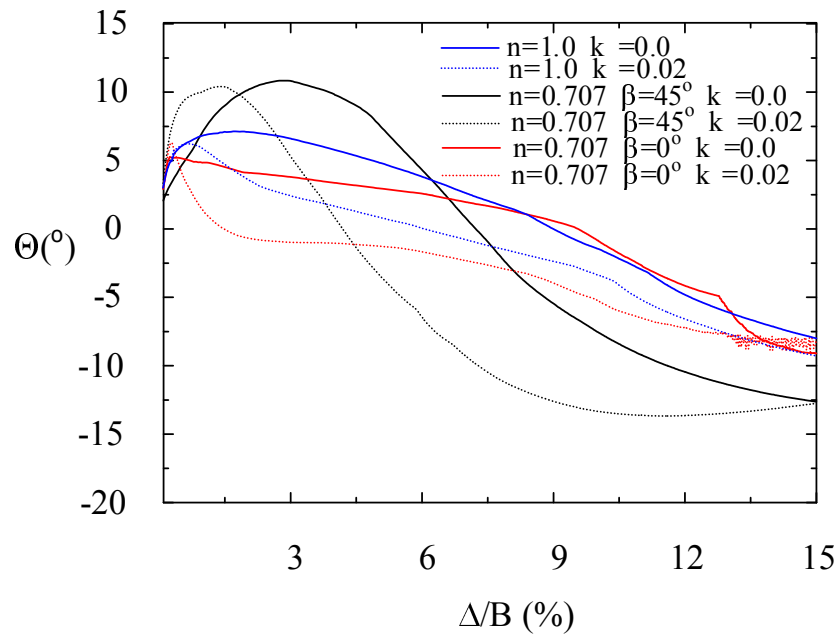


Figure 4.39 Principal stress rotation with different values of the anisotropic coefficient.

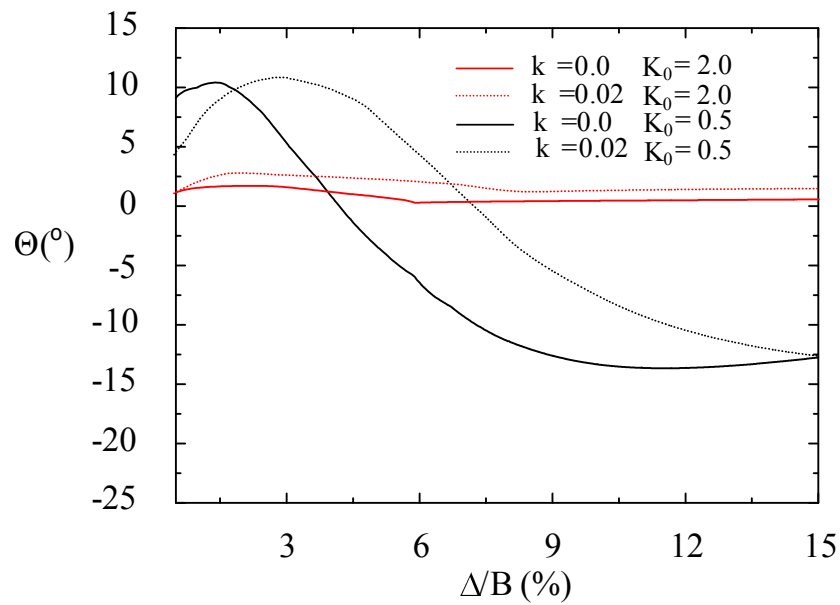


Figure 4.40 Principal stress rotation with different values of the anisotropic coefficient ($n = 0.707, \beta = 45^\circ$).

4.3.3.3 Displacement patterns

Figures 4.41 - 4.44 demonstrate the displacement patterns for both coaxial and non-coaxial plasticity in terms of the isotropic and anisotropic Mohr-Coulomb yield criterion respectively. The orientation of these vectors indicates the direction of movement and their lengths and colours indicate the magnitude of movement. The patterns are obtained at each step $\frac{\Delta}{B}$ in terms of the maximum difference R_r . The two categories shown in Table 4.1 are examined. In these figures, red arrows indicate the largest magnitude of displacement. It is obvious that the failure zone is more concentrated adjacent to or at the edge of the footing when non-coaxial behaviour is involved.

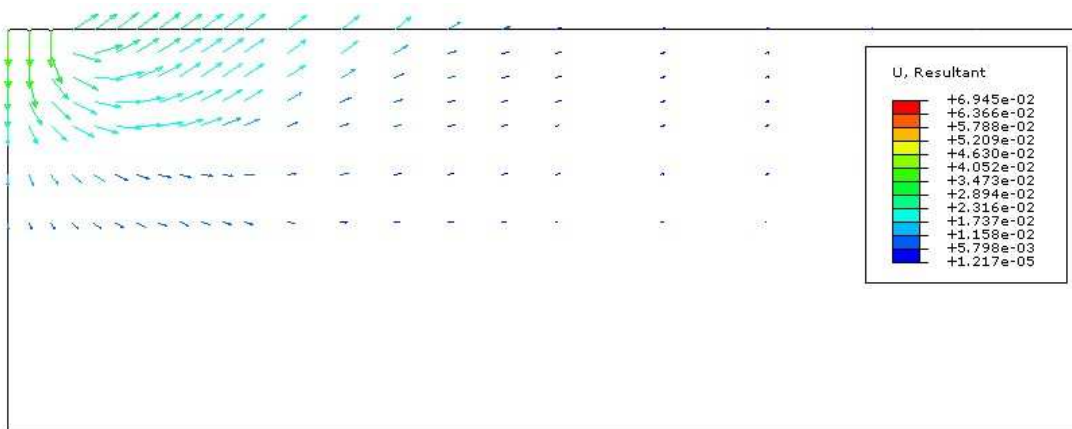


Figure 4.41 Displacement patterns of the soil mass with ($n = 0.85$ $\beta = 45^\circ$ $n = 0.0$) at $\frac{\Delta}{B} = 0.4$.

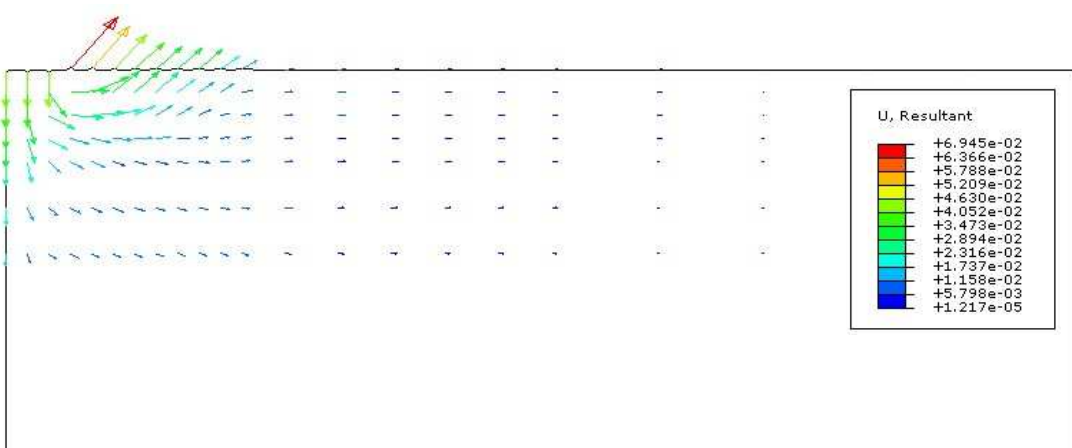


Figure 4.42 Displacement patterns of the soil mass with ($n = 0.85$ $\beta = 45^\circ$ $n = 0.1$) at $\frac{\Delta}{B} = 0.4$.

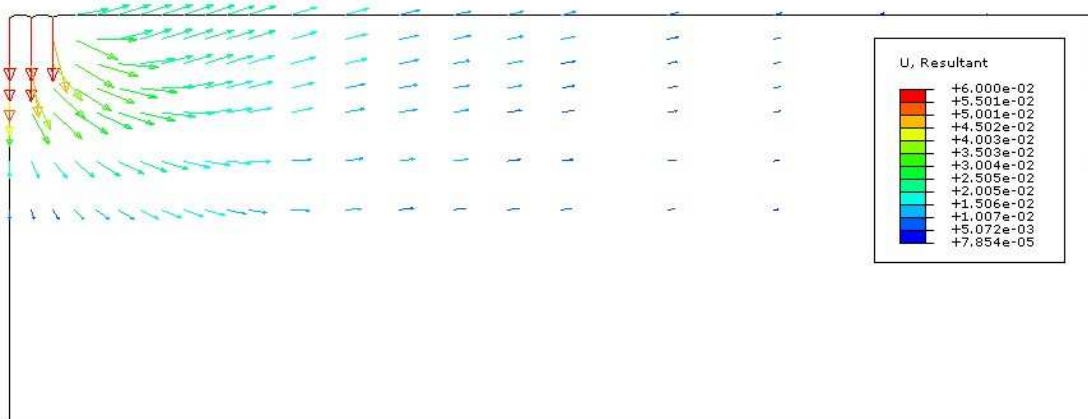


Figure 4.43 Displacement patterns of the soil mass with ($n = 0.707$ $\beta = 45^\circ$ $n = 0.0$) at $\frac{\lambda}{B} = 0.6$.

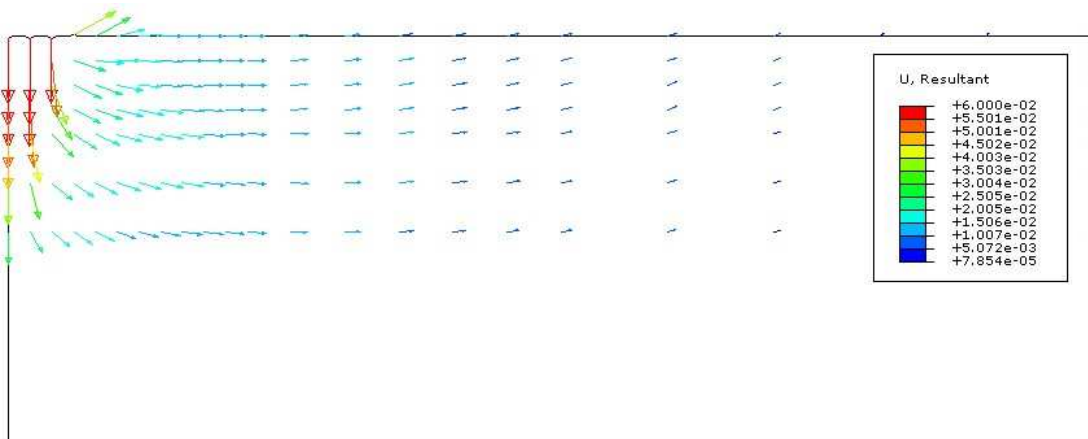


Figure 4.44 Displacement patterns of the soil mass with ($n = 0.707$ $\beta = 45^\circ$ $n = 0.1$) at $\frac{\lambda}{B} = 0.6$.

4.4 Chapter Summary

The proposed non-coaxial soil model was applied to investigate smooth strip footing problems. Semi-analytical solutions of the bearing capacity for a strip footing resting on an anisotropic, weightless, cohesive-frictional soil based on the slip line method were developed. In particular, close-form solutions for a purely cohesive material were presented, followed by a parametric study of the influence of anisotropic coefficients. It is shown that the predicted bearing capacity was lower when soil anisotropy was involved.

Verification of the numerical results excluding non-coaxiality with semi-analytical solutions, was illustrated and the results highlighted the capability of the numerical procedures. The effect of initial stress state, soil anisotropy, dilation angle and non-coaxiality was also analysed. Conclusions were drawn that the ultimate bearing capacity factors N_c and N_q were not significantly affected by non-coaxiality. Their values virtually tended to be identical, irrespective of the values of anisotropic coefficients and dilation angles. The settlement prior to collapse was larger when the non-coaxial coefficient was unequal to zero, which indicated that the soil was softened when the non-coaxial plasticity was applied. The effect of non-coaxiality was more significant on the computation of N_q than that on N_c . The difference R_r for non-coaxial modelling between $k = 0.0$ and $k = 0.1$ was pronounced with a combination of smaller values of n and larger values of β in terms of N_c . R_r was highly influenced by the lateral stress ratio K_0 . It was found that R_r is relatively small for over-consolidated soil with $K_0 = 2.0$.

Despite the encouraging results for smooth strip footings, various kinds of shallow foundations should be investigated using the proposed non-coaxial model in further work.

Chapter 5

Applications of the non-coaxial model in tunnelling

5.1 Introduction

5.1.1 Tunnelling induced ground deformations

The construction of tunnels can induce the relaxation of in-situ ground stresses and result in the movement of soils into the created opening. This is where the deformation of the surrounding ground and the ground pressure on tunnel linings is generated. Typical greenfield surface settlement troughs associated with tunnelling are presented in Figure 5.1. It should be noted here that the greenfield condition refers to the case where ground deformations are only induced by tunnelling. Following Mair and Taylor (1997), the components of ground movement can be listed as follows:

1. Deformations of the ground towards the face caused by stress relief.
2. Radial ground movements caused by over-cutting and ploughing.
3. Tail void, i.e. the gap between the tailskin of the TBMs (tunnel boring machines) and the installed lining.
4. Deflection of the lining with the development of ground loading. Consolidation settlements due to the changes of water pressure in the ground to their long-term equilibrium values.

It is obvious that tunnelling is a three-dimensional problem. However, it is useful to consider a plane-strain condition for both analytical and numerical convenience.

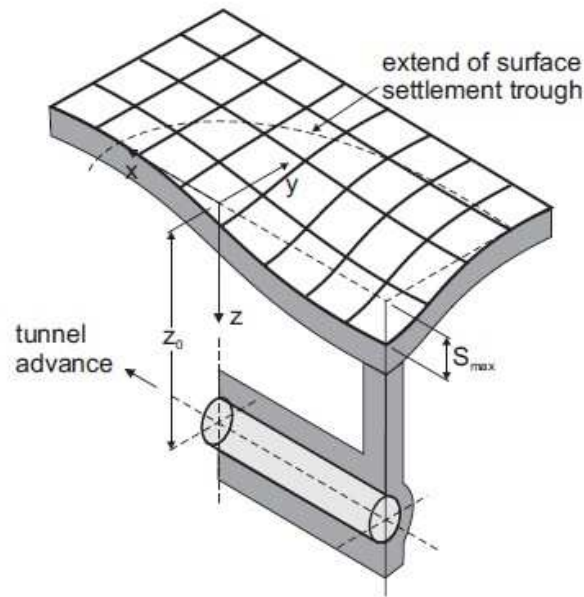


Figure 5.1 Ground movements induced by tunnelling (Attewell et al., 1986).

As shown in Figure 5.1, the $x - z$ plane is referred to as the transverse plane under a plane-strain assumption. Ground loss in the $x - z$ direction is seen as a transverse settlement trough throughout the depth of the soil above the tunnel. The analysis of this ground loss is one of the main objectives of this section. Peck (1969) first proposed an empirical Gaussian distribution curve to describe this settlement trough. It is described by the following error function (geometrical details of the parameters are shown in Figure 5.2):

$$S_v(x) = S_{vmax} \cdot \exp\left(-\frac{x^2}{2i^2}\right) \quad (5.1)$$

where S_v is the vertical displacement, S_{vmax} is the maximum vertical soil settlement at the centreline of the tunnel, x is the horizontal offset from the tunnel centreline and i is the horizontal distance from the centre line to the location of the inflexion point.

The area within the curve (V_s) can be obtained by integrating equation 5.1 with respect to x :

$$V_s = S_{vmax} \sqrt{2\pi} i \quad (5.2)$$

Clough and Schmidt (1981) analysed a huge amount of case histories and laboratory model tests and gave an approximation of the trough width parameter i from the equa-

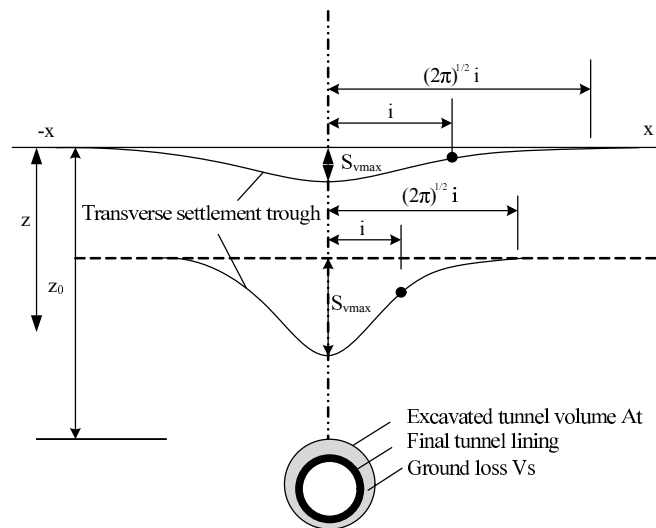


Figure 5.2 Settlement troughs defined by Gaussian distribution curve after Peck (1969).

tion:

$$i/a = \left(\frac{z_0}{2a}\right)^{0.8} \quad (5.3)$$

where a is the radius of the excavated tunnel and z_0 is the depth of the tunnel centre to the ground along the tunnel centreline.

Over the years, the Gaussian curve has been proven to have a good fit to many field tunnel settlement trough data. Recent research has also improved this distribution curve to a modified Gaussian curve, where an additional parameter α that gives an additional degree of freedom to the location of the inflexion point is included. The details can be found in Grant and Taylor (2000).

5.1.2 Lining forces

The function of the lining is to withstand ground pressure and to maintain sufficient safety of the structures during tunnelling. The effective stresses on the lining are highly dependent on installation procedures. Mair and Taylor (1997) stated that the stress can be up to 50% of the overburden stress; whereas Craig and Muirwood (1978) pointed out that the average stresses can amount up to between 50% and 70% of the equivalent overburden stress during the first few months.

Figure 5.3 illustrates various structural models with different distributions of primary

ground pressure on the tunnel lining. The stress distribution shown in Figure 5.3 a refers to a shallow tunnel, whereas Figure 5.3 b refers to a deep tunnel. When the lateral stress ratio K_0 is larger than 1.5, the numerical results of a subsurface settlement trough are strange when compared with field and experimental observations. Hence, Potts et al. (2001) proposed an approach to reduce the horizontal stresses with depth (Figure 5.3 c); however, the reason for this is not explained well in most of the literature.

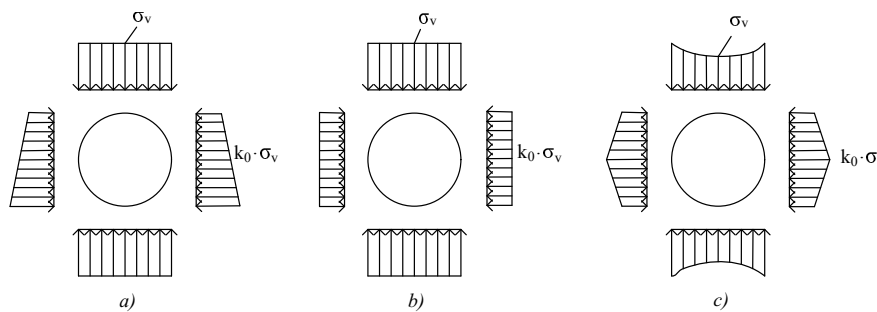


Figure 5.3 Different distributions of ground loads on tunnel linings: a) Hewett et al. (1964); b) Windels (1967); c) Fleck and Sklivanos (1978).

The assessment of bending moments and normal forces should also be taken into consideration for the design of a tunnel.

5.1.3 Installation procedures associated with 2D tunnelling

The magnitudes of tunnelling induced ground deformations and lining forces are highly dependent on the method of excavation and support sequence. No doubt, tunnel induced stress redistribution and deformations can be more properly simulated using three-dimensional numerical models. However, three-dimensional FE analyses are too complicated and time consuming. In many cases, e.g. large tunnel projects with a long excavation path and various cross-sections, three-dimensional simulations cannot be used as a design tool. Hence, two-dimensional plane strain FE-analysis is useful with the effect of the missing third dimension included in some way. Two-dimensional numerical models will be used to analyse tunnel problems in our research. A few popular installation procedures, namely the stress reduction method, the stiffness reduction method and the gap reduction method will be briefly reviewed regarding the aspects of two-dimensional approximations.

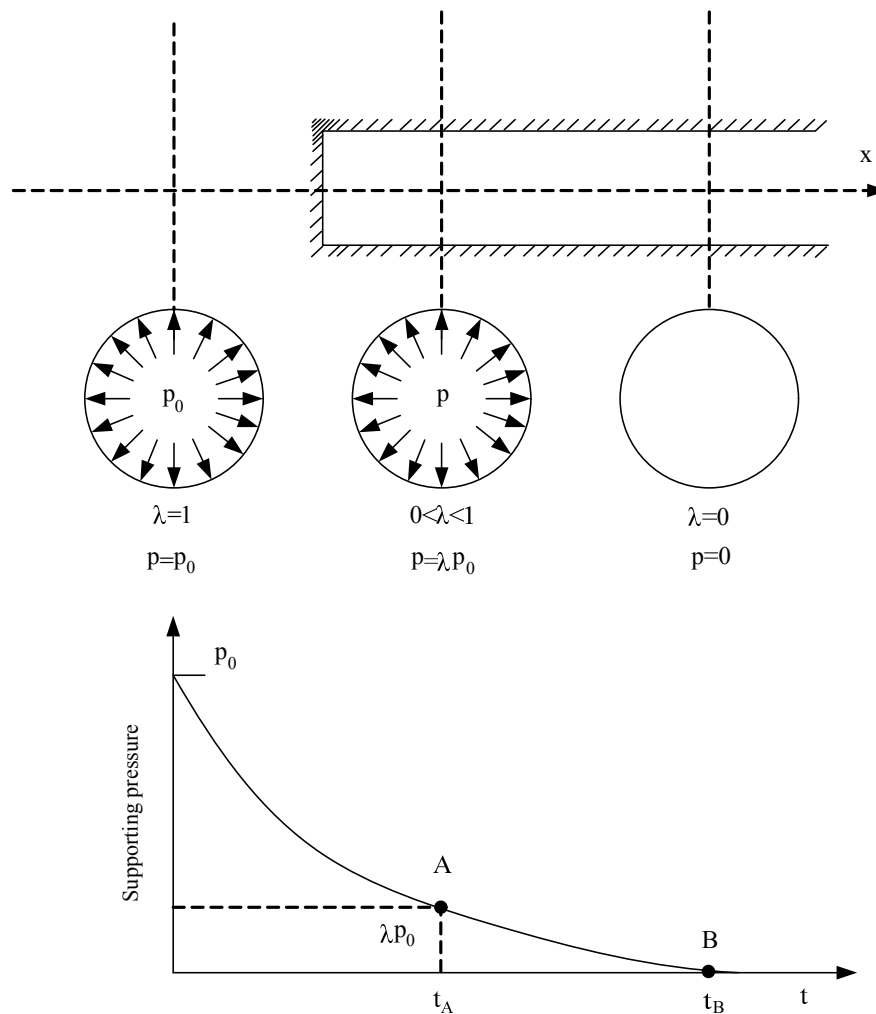


Figure 5.4 Display of the stress reduction method.

The stress reduction method

The stress reduction method is perhaps the most popular method to simulate the tunnel excavation sequence. As indicated in Figure 5.4, it can also be referred to as the λ – method. In a two-dimensional plane strain tunnelling problem, an initial radial pressure p_0 is applied on the tunnel periphery, and then reduces down to $(\lambda - p_0)$. In the case of no support, the ground pressure will eventually decrease to zero; otherwise, a lining is installed and the remaining load $(\lambda - p_0)$ is divided over the lining and the ground. Here λ is the load reduction factor, and the range of λ drops between 0 and 1.

The stiffness reduction method

As proposed by Swoboda (1979), the stiffness reduction method introduces a support core and reduces the modulus of elasticity (stiffness) of the core material by a factor of α . Thus this method is also named as the α – method. An initial value of the modulus of elasticity (E_0) is reduced down to E_s by a factor of α before the activation of the

lining. The procedure is shown in Figure 5.5, where the parameter α is the reduction amount in the original modulus of elasticity. In a review by Möller (2006), it was suggested that the values of α can have a range between 0.3 and 0.5 for partial excavations without an immediate closure of the lining ring.

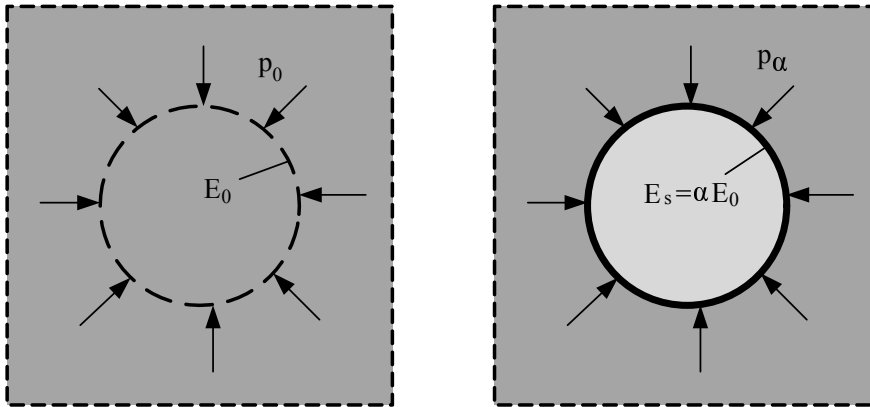


Figure 5.5 Display of the stiffness reduction method.

The gap method

The gap method, especially applied for closed shield tunnelling, was first proposed by Rowe et al. (1983) and developed by Lee and Rowe (1991). As indicated in Figure 5.6, the gap is composed of three parts where two physical gaps are denoted by the geometric clearance between the initial position of the tunnel crown and the lining, and the third physical gap corresponds to the ground loss caused by the workmanship effect. The expression is shown below:

$$GAP = U + (2\Delta + \delta) \quad (5.4)$$

$$U = U_{3D}^* + \omega \quad (5.5)$$

where ω is the ground loss, U_{3D}^* is the amount of over excavation resulting from 3D effects, Δ is the thickness of the tail piece and δ is the space allowance for installation of the lining.

Several other excavation methods have also been used in previous years; namely the Hypothetical Modulus of Elasticity (HME) soft lining method proposed by Powell et al. (1997); the Disk calculation method applied by Schikora and Ostermeier (1988); the Volume loss control method proposed by Addenbrooke and Potts (2001) and Potts et al. (2001) and so forth.

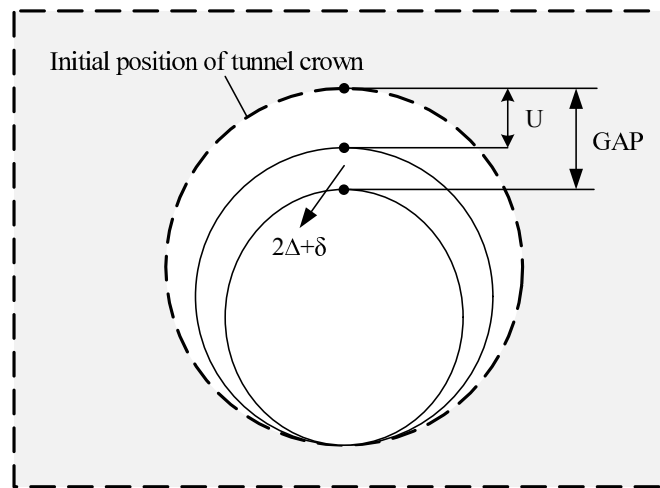


Figure 5.6 Illustration of the gap method parameters (after Rowe et al., 1983).

5.1.4 Numerical difficulties of modelling subsurface settlement troughs

As first summarised by Peck (1969) and developed by Ward and Pender (1981), the three most significant requirements that satisfy the successful design and construction of a tunnel are stability, ground movements and their effects and performance of linings. Over the decades, different design methods have been used in engineering practice; namely simple empirical, analytical and finite element analyses. Finite element analysis has been widely adopted over recent years. With the rise of computer capacity, complex geometries, excavation procedures and support installation sequences of tunnelling can be simulated more realistically. These advantages made the FE method attractive in the realm of tunnelling design practice. However, notable literature has shown that the numerical results of the subsurface settlement trough induced by tunnelling are too wide when compared with field data if a sand tunnel is investigated or a high value of the earth coefficient at rest (K_0) is involved. Several studies have focused on the reasons that could account for this discrepancy. All the parameters that may lead to the discrepancy have to be thoroughly investigated as the major concern in constructing such tunnels in urban areas is to reduce and control the subsurface settlements. These studies can be classified into two categories:

1. The selection of proper constitutive models;
2. The excavation and support sequence.

Gunn (1993) identified the reason why finite element calculations were much shallower and wider than those obtained from model tests or observations on site by investigating through a tunnelling research programme at Cambridge University in the late 1970s

and early 1980s. The reason was quickly identified as the elastic part of any constitutive model which was used to represent the stress-strain behaviour of soil, was assumed to be linear and isotropic. Lee and Rowe (1989) made the first attempt to incorporate the influence of cross-anisotropic parameters in their linear elastic-perfect-plastic constitutive equations. They concluded that the ratio of the independent shear modulus to the vertical modulus has a great impact on predicting surface settlement. Their study was restricted to a soil with a coefficient of earth pressure at rest $K_0 < 1.0$. However, Gunn (1993) provided a contrary conclusion that the tunnelling induced ground settlements are not influenced by the anisotropic shear modulus. Simpson et al. (1996) found out that the finite-element calculations of tunnelling induced subsurface settlements are remarkably influenced by cross-anisotropic parameters pre-failure, but influenced minutely by non-linearity.

As these findings are contradictory, Addenbrooke and Potts (2001) in referring to those models mentioned above, re-evaluated aspects of all the models, including isotropic and anisotropic, linear and non-linear pre-failure deformation behaviour as well as loading reversals. Their study was concerned with plane strain conditions in stiff clay. They pointed out that introducing anisotropic parameters appropriate to London Clay into a non-linear model has few improvements on the isotropic results. Only unrealistic soil stiffness, a very soft independent shear modulus in the anisotropic stiffness matrix, can improve predictions of surface settlement above a greenfield tunnel excavation with a high coefficient of the lateral earth pressure at rest ($K_0 > 1.5$). In order to investigate the influences of soil anisotropy and K_0 on ground movements induced by tunnelling, Franzius et al. (2005) presented a suite of both 2D and 3D FE analyses of tunnel construction in London Clay. They concluded from their comparison between 3D and 2D results that 3D modelling and soil anisotropy have little improvements on the shape of the transverse surface settlement trough, which remains too wide when compared with field data. Similar conclusions were drawn by Guedes and Santos Pereira (2000), who performed a suite of FE studies adopting an elastic soil model. Their results showed that 3D predictions have a negligible effect on the shape of the surface settlement trough for both $K_0 = 0.5$ and $K_0 = 1.5$. Dolezalova (2002) also supported these findings from his FE studies using both a linear elastic perfectly plastic and a non-linear elastic perfectly plastic constitutive model. Parallel to the studies of

pre-failure parameters, Oettl et al. (1998) presented a comparison of elastic-plastic soil models for 2D FE analyses of tunnelling concluding that all the current assumptions of constitutive models cannot describe the response of soil with a desired accuracy.

To obtain a good fit with numerically model testing results and laboratory tests or field data through numerical investigations of tunnelling induced settlement troughs, remains an attractive research aspect. Both constitutive models and excavation procedures are significant. In this chapter, we mainly focus on the impacts of constitutive models. It is generally identified that there exist severe stress rotations when the tunnel is excavated in non-homogeneous soils. Hence, non-coaxial modelling can have some effects on the material response under this case. Numerical applications of the non-coaxial model to analyse tunnel excavations are presented in the following subsections.

5.1.5 Chapter structure

This chapter begins with the numerical application of the non-coaxial soil model to investigate the subsurface displacement of a general two-dimensional tunnel. Results from the stiffness reduction method, also known as the α – method, are first detailed in Section 5.3. Subsequently, results from the stress reduction method, which also refers to the λ – method, are presented in Section 5.4. The discussion of the two methods is presented in Section 5.5. Then a case study is performed on Zhou’s centrifuge tests in the subsequent Section 5.6, before the chapter is concluded by a summary of the advantages and disadvantages of applying non-coaxiality into tunnelling in Section 5.7.

5.2 Model and parameters

Practical geotechnical problems usually demonstrate a three-dimensional condition and involve a complex sequence of construction steps. The construction details determine the appropriate analysis method that can be used to represent these steps accurately. However, the aim of this chapter is to find out what improvements may be achieved by introducing non-coaxiality in the context of soil anisotropy as compared to the original isotropic coaxial modelling. Construction details have been avoided for the sake of simplifying the illustration and a two-dimensional condition is taken into

consideration in this regard.

Generally, since numerical excavation procedures significantly affect results induced by tunnelling, two simple and popular excavation methods are employed: the stiffness reduction method (α -method) and the stress reduction method (λ -method). As indicated in Figure 5.7, half of the model size is assumed to be 60 m in length and 60 m in width to avoid boundary influence. The diameter of the tunnel is 8 m, and the tunnel is located 16 m down below the ground surface. The tunnel is assumed to be excavated in clay, with a Young's modulus of 200 MPa and a Poisson's ratio of 0.3. The cohesion of the material $c = 30$ kPa. The maximum peak internal friction angle for all cases is assumed to be $\phi_{max} = 30^\circ$ ($\phi = 30^\circ$ for the Mohr-Coulomb yield model in ABAQUS). The material surrounding the excavation (including the excavation zone for the stiffness reduction method) is discretised with first order 4-node plane strain elements (element type *CPE4*). The left-hand boundary represents a vertical symmetry axis, whereas the far-field condition on the right-hand-side boundary allows for vertical displacement. The condition on the bottom boundary is fixed in both the vertical and horizontal directions.

An initial stress field due to gravitational and tectonic forces exists throughout the depth of the soil. It is assumed that this stress varies linearly with depth and that the ratio between the horizontal and vertical stress components K_0 is 0.5. The self weight of the clay is 20.0 kPa.

The 150-mm-thick liner is discretised with one layer of incompatible node elements (element type *CPE4I*). These elements are recommended in regions where the bending response must be modelled accurately. The dimensions and locations of the liner are shown in Figure 5.8.

Since our aim is to look at what difference the non-coaxial modelling may introduce, the model size and model mesh are assumed simple. It follows the assumption of Fei and Zhang (2009). In addition, the elastic material parameters are generally selected. In other words, they are just particular cases within the catalogue of clay.

5.3 Stiffness reduction method

The stiffness reduction method is detailed in Section 5.1.3. In this section, the excavation of the tunnel material is accomplished by reducing the initial value of Young's modulus (E_0) inside the excavation core. The initial value of Young's modulus should be reduced down to an empirical value (E_s) by a factor of α before the activation of the lining. The value of α is assumed to be 0.1. The results of this parameter set can be seen as an extreme example of how soil anisotropy and non-coaxiality affects tunnel-induced settlement predictions. The tunnel material inside the excavation core will be removed after the activation of the lining. The lateral stress ratio is always set as $K_0 = 0.5$.

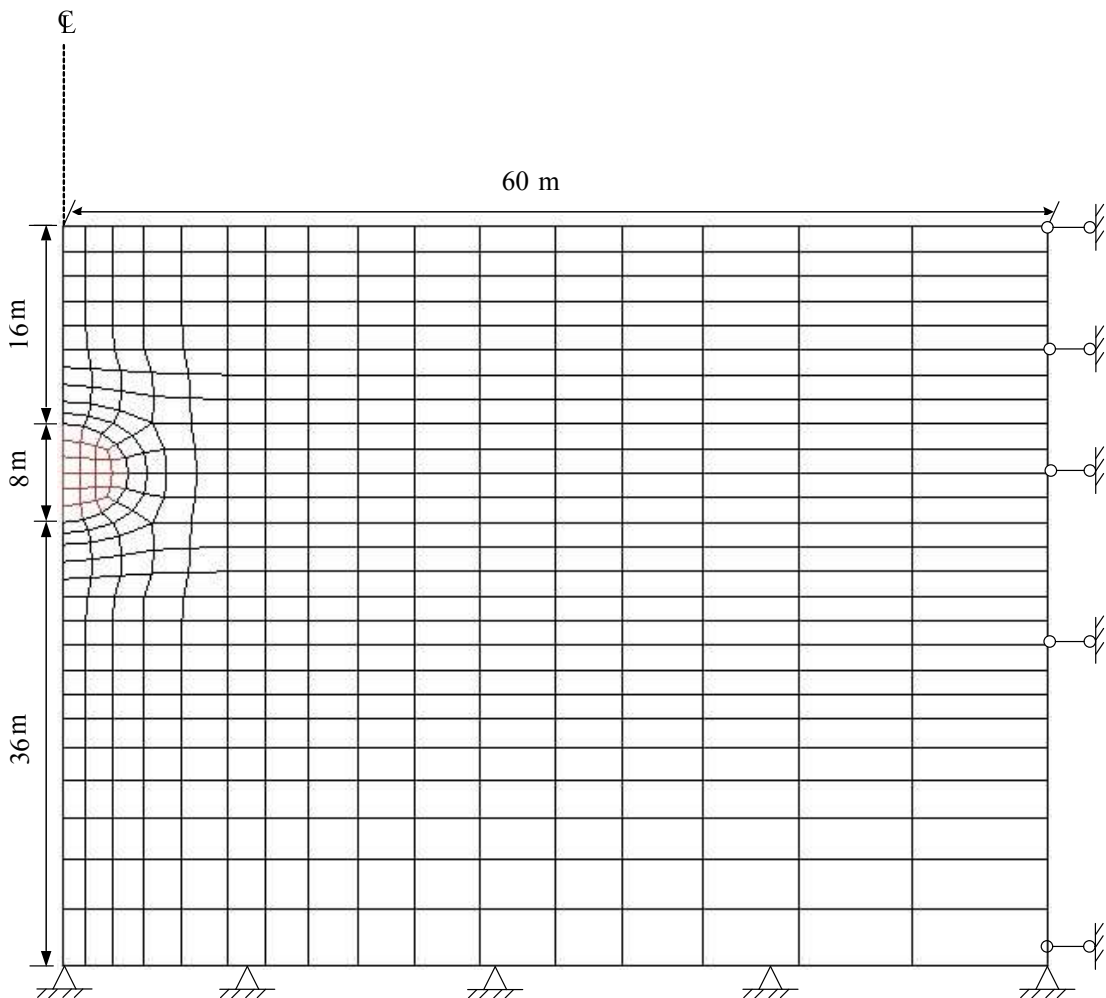


Figure 5.7 Geometry and finite element discretisation of the tunnel model.

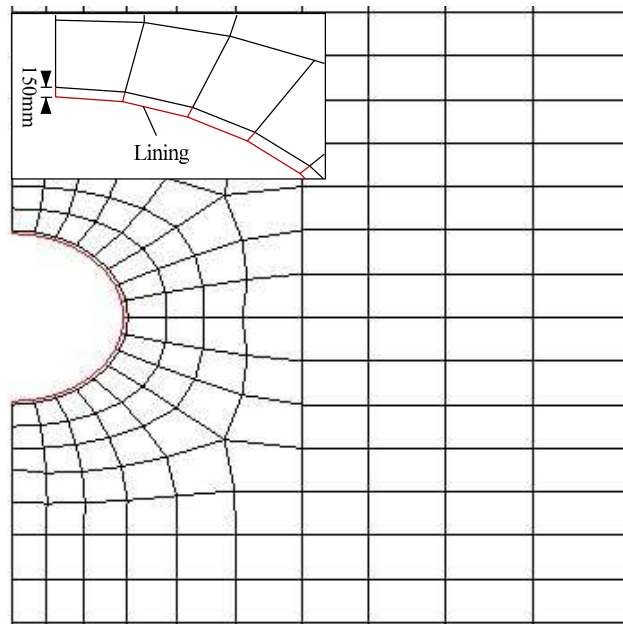


Figure 5.8 The installation of the liner.

5.3.1 Subsurface settlements

Figures 5.9 and 5.10 present the subsurface settlement troughs in a low- K_0 regime ($K_0 = 0.5$). The influence of anisotropic coefficients n and β and the influence of non-coaxial coefficient k are detailed in Figure 5.9 and Figure 5.10 respectively. As indicated in Figure 5.9, the shape pattern of the settlement trough obtained by using the Mohr-Coulomb model of ABAQUS (see black line with circle markers) is almost consistent with that (see black line) obtained by using the proposed non-coaxial model when the isotropic Mohr-Coulomb yield criterion is recovered ($n = 1.0$). It testifies the user-developed computational procedures. There exists a deformation heave along the surface soil. This can be caused by the large stiffness of the liner, which results in uplifting of the unloading force at the bottom of the tunnel. In addition, the constitutive model can be a reason. It shows that the reduction of n leads to an increase in the tunnelling induced maximum vertical displacement. The case with $\beta = 45^\circ$ predicts the largest magnitude of the maximum vertical displacement along the centre line. Generally, non-coaxiality results in a slightly larger magnitude of the maximum vertical displacement.

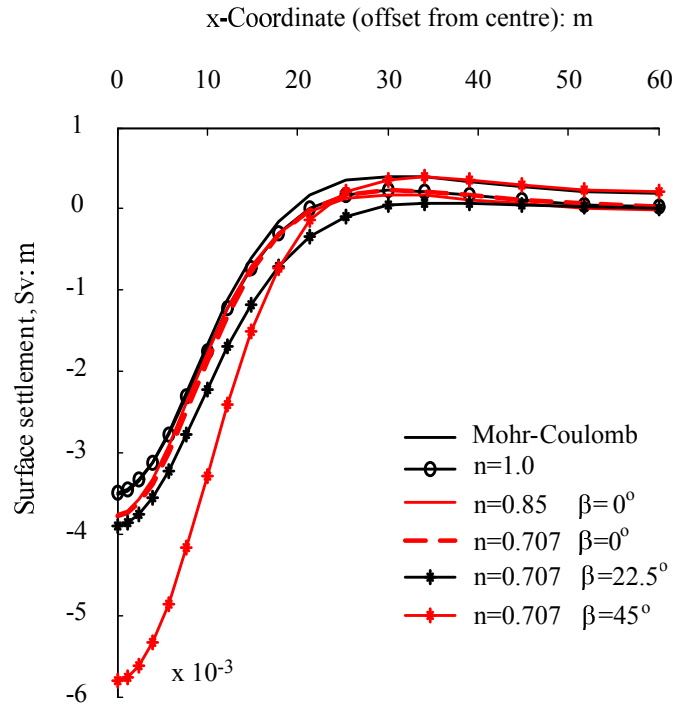


Figure 5.9 Vertical displacement with the influences of n and β ($\alpha = 0.1$).

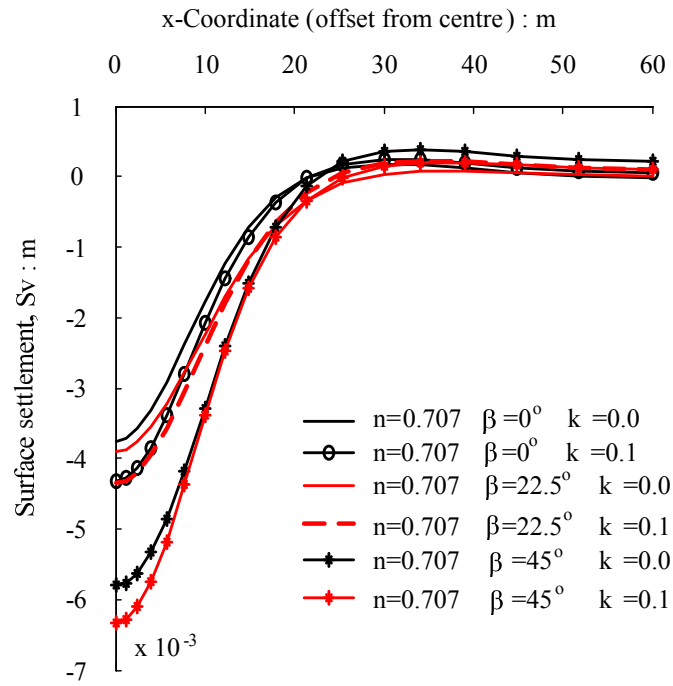


Figure 5.10 Vertical displacement with the influence of k ($\alpha = 0.1$).

5.3.2 Horizontal displacement

It is generally accepted that horizontal displacement can result in damage of buildings when tunnels in urban areas are constructed. Figures 5.11 and 5.12 show the horizontal displacement with respect to various magnitudes of anisotropic coefficients and non-coaxial coefficient. As indicated in Figure 5.11, the horizontal displacement curve obtained by using the Mohr-Coulomb model is consistent with that obtained when soil isotropy is recovered using the proposed non-coaxial model. The maximum magnitude of horizontal displacement decreases with a reduction in the anisotropic coefficient n . The anisotropic coefficient β shows a pronounced influence on the magnitude of the maximum horizontal displacement. Conclusions can be drawn that the case with $n = 0.707$ and $\beta = 45^\circ$ gives the largest maximum horizontal displacement. However, the shape of the curve is not improved by introducing soil anisotropy. As shown in Figure 5.12, a larger value of non-coaxial coefficient k leads to a larger value of the maximum horizontal displacement.

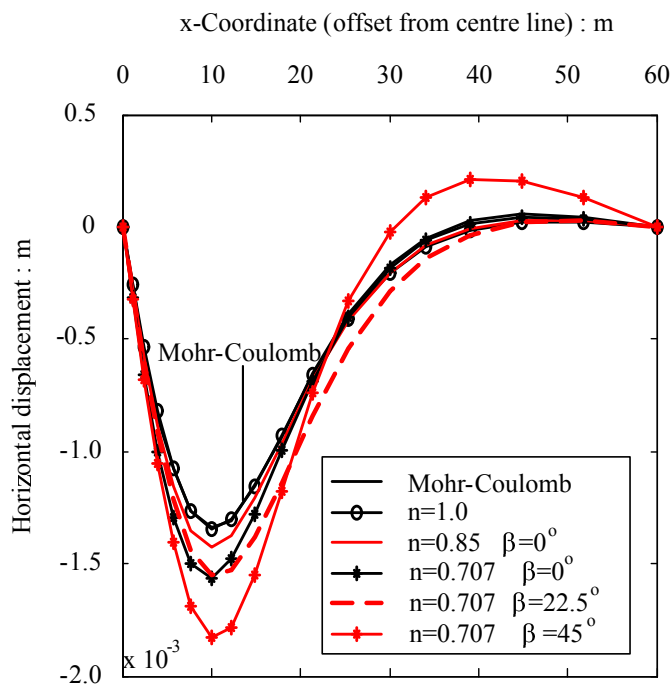


Figure 5.11 Horizontal displacement with the influences of n and β ($\alpha = 0.1$).

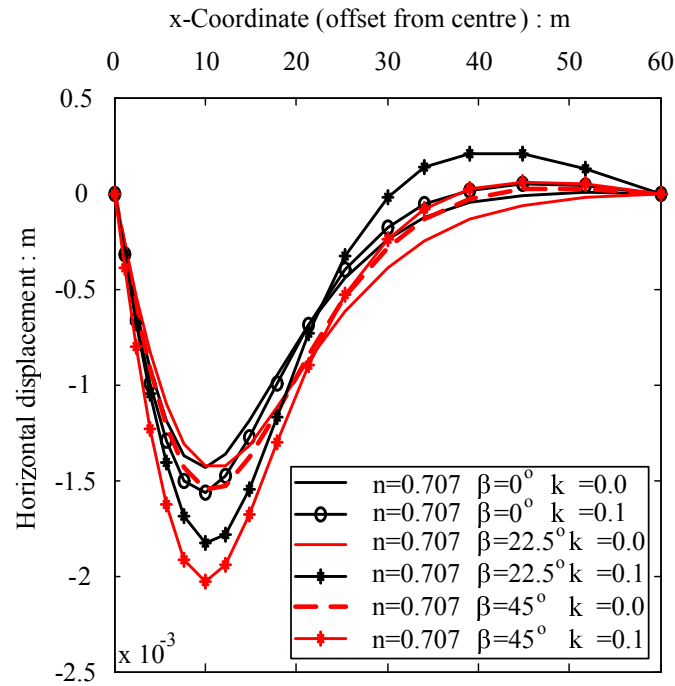


Figure 5.12 Horizontal displacement with the influence of k ($\alpha = 0.1$).

5.4 Stress reduction method

For the stress reduction method, which is also named as the λ – method, two stages of excavation procedure are applied. In the first step, an independent analysis will be observed to obtain the nodal forces applied on the perimeter of the tunnel. These forces are required to maintain equilibrium with the initial stress state in the surrounding material. In the second step, the applied nodal force will be reduced by an unloading factor of $\lambda = 0.1$. Then the lining will be activated and the remaining forces will be reduced to zero in the end.

5.4.1 Subsurface settlements

Figures 5.13 and 5.14 present the subsurface settlement troughs in terms of various values of anisotropic coefficients and non-coaxial coefficient. The result obtained from the Mohr-Coulomb model in ABAQUS is plotted in Figure 5.13 (see the black line). It is coincident with the result obtained from the proposed non-coaxial model with $n = 1.0$ and $k = 0.0$, in which soil isotropy is recovered. This validates the correctness of the numerical procedure. It is obvious from Figure 5.13 that the maximum magnitude of the surface settlement increases with the decrease in the anisotropic coefficient n . The anisotropic coefficient β also has a great impact on the magnitude of the settlement

and it demonstrates that the case with $\beta = 0^\circ$ results in the largest magnitude. This result is different from that obtained by using the stiffness reduction method, which demonstrates that the case with $\beta = 45^\circ$ gives the maximum magnitude. In Figure 5.14, the influence of non-coaxiality on the prediction of settlement troughs is pronounced. For the case with $n = 0.707$ and $\beta = 0^\circ$, the maximum magnitude of surface settlement $S_{vmax} = 58.1$ mm with non-coaxial coefficient $k = 0.1$, which is over twice that of $S_{vmax} = 24.8$ mm when the non-coaxial coefficient k equals to zero.

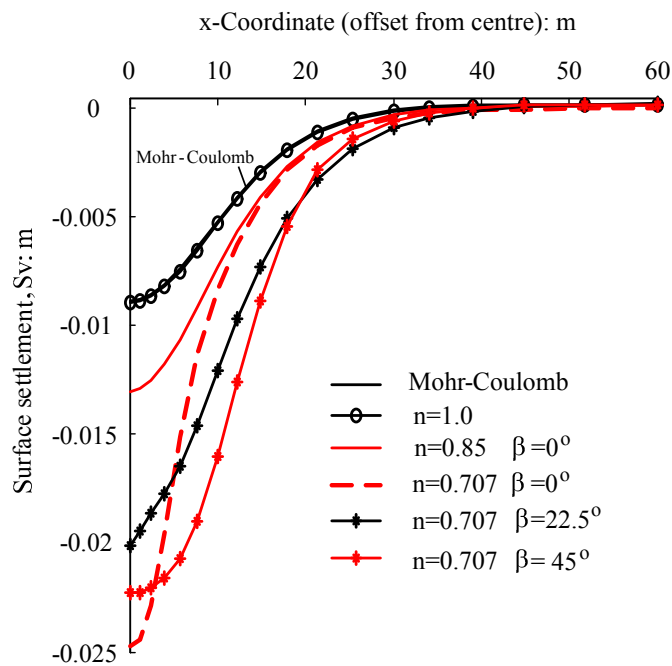


Figure 5.13 Vertical displacement with the influences of n and β ($\lambda = 0.1$).

5.4.2 Horizontal displacement

The horizontal displacement curves with respect to the influences of anisotropic coefficients and non-coaxial coefficient are illustrated in Figures 5.15 and 5.16. Likewise, the horizontal displacement curve obtained by using the Mohr-Coulomb model in ABAQUS is consistent with that obtained by using the proposed non-coaxial model with $n = 1.0$ and $k = 0.0$ as shown in Figure 5.15. Similar conclusions can be drawn that the magnitude of the maximum horizontal displacement increases with the decrease in n . And it increases with the increase in the non-coaxial coefficient k , excluding a special case when $n = 0.707$ and $\beta = 0^\circ$. In this case, the horizontal displacement curve is wider and narrower for $k = 0.1$ as compared to $k = 0.0$. The maximum horizontal displacement is highly affected by the value of β . It is interesting to see that the

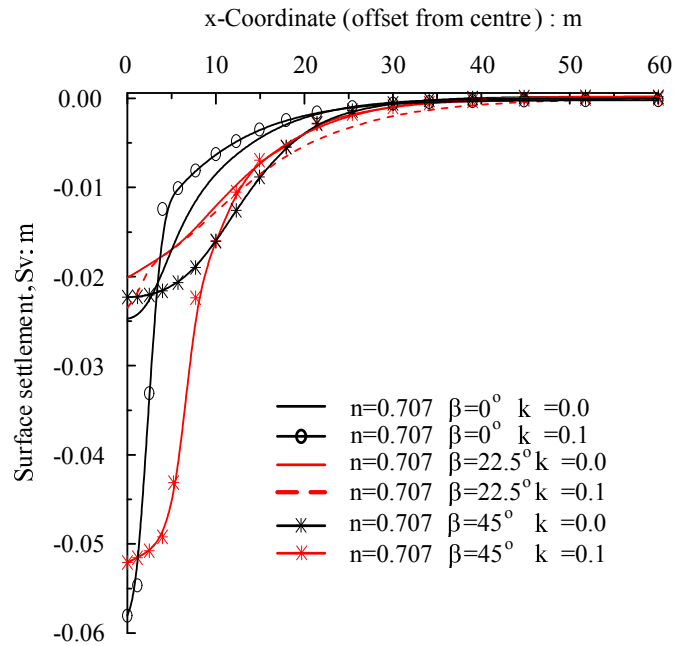


Figure 5.14 Vertical displacement with the influence of non-coaxiality ($\lambda = 0.1$).

shape of the curve is slightly different as compared to others with $n = 0.707$ and $\beta = 0^\circ$.

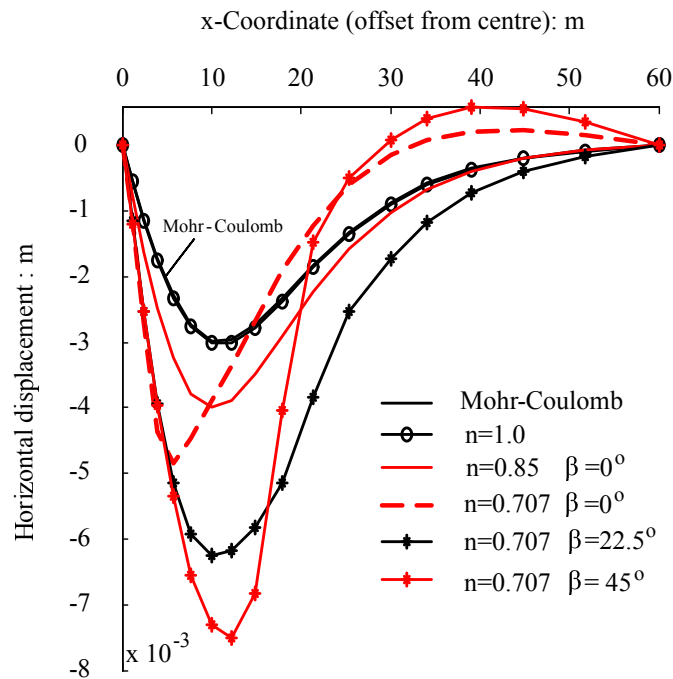


Figure 5.15 Horizontal displacement with the influences of n and β ($\lambda = 0.1$).

5.5 Discussion

The application of the proposed non-coaxial model to the analysis of tunnelling induced settlements was presented in this section. Two excavation procedures, namely

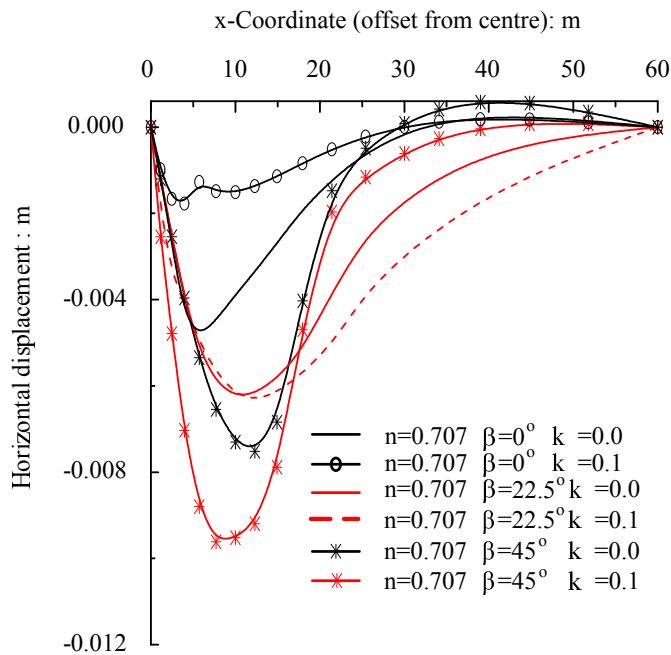


Figure 5.16 Horizontal displacement with the influence of non-coaxiality ($\lambda = 0.1$).

the stiffness reduction method (the α -method) and the stress reduction method (the λ -method) were employed. The influences of anisotropic coefficients n and β and the non-coaxial coefficient k on the subsurface settlement troughs, the horizontal displacement curves; were analysed.

In general, both vertical displacement and horizontal displacement were larger with a larger magnitude of anisotropic coefficient n and non-coaxial coefficient k in spite of some particular cases. The maximum vertical and horizontal displacement were relatively pronounced when comparing the stress reduction method and stiffness reduction method. This is due to more severe stress rotations induced by the reduction of stresses. The shape of the subsurface settlement trough is apparently influenced by the magnitude of the anisotropic coefficient β ; however, irrespective of the value of non-coaxial coefficient. The reason can be that tunnel excavation is highly affected by the elasticity of materials; however, non-coaxial behaviour is assumed to have an effect only when the material reaches plasticity. In future work, non-linear and anisotropic elasticity can be incorporated to advance the proposed non-coaxial soil model.

5.6 Case study compared with centrifuge tests

5.6.1 Assumption

Testing scaled models of actual prototype structures provides a controlled method of studying geotechnical problems. However for this case, we consider a model of a geotechnical structure scaled down by a factor of N under normal gravity conditions ($1g$). Therefore, the model should be accelerated so that gravity g is increased N times (Ng), to make sure the stress conditions in the model match those of the prototype. This is how the centrifuge works.

Zhou (2015) performed a series of greenfield tunnelling centrifuge tests on Fraction E Leighton Buzzard silica dense sand with a density of 16.03 kg/m^3 . Zhao (2008) performed a series of triaxial tests on the E silica sand to test its material properties. He concluded that the value of the Young's modulus drops in between 30 - 50 MPa. Hence in the presented numerical modelling, an average value of 40 MPa is selected. The results of subsurface settlement troughs from centrifuge tests will be used to validate the numerical results using the proposed non-coaxial model.

As shown in Figure 5.17, the model dimensions are half of the real tunnel dimensions designed for centrifuge tests, of which the length is 25.6 m and height is 30.8 m. This set of model dimensions is exactly consistent with Bo's centrifuge tests. The tunnel is assumed to have been excavated in sand. Hence, the cohesion is assumed to be 1.0 kPa in order to avoid the singularity problem. The maximum friction angle associated with the proposed non-coaxial model is $\phi_{max} = 30^\circ$. Typical elastic constants are set as Young's modulus $E = 40 \text{ MPa}$ and Poisson's ratio $\nu = 0.25$. The diameter of the tunnel is 7.2 m, and the tunnel is excavated 14.4 m below the ground surface. The material surrounding the excavation is discretised with first-order 4-node plane strain elements (element type *CPE4*). On the right-side boundary, the infinite extent of the soil is represented by a 25.6-m-wide mesh that extends offset from the centre-line to a length of 51.2 m. On the bottom boundary, the infinite extent of the soil is represented by a 18-m-wide mesh that extends from the surface to a depth of 48.8 m below the surface. The left-hand boundary represents a vertical symmetry axis. Far-field conditions on the bottom and right-hand-side boundaries are modelled by infinite ele-

ments (element type *CINPE4*). No mesh convergence studies have been performed to establish if these boundary conditions are placed far enough away from the excavation.

An initial stress field due to gravitational and tectonic forces exists throughout the depth of the soil. This stress is assumed to vary linearly with depth and the ratio between the horizontal and vertical stress components is $K_0 = 0.5$. The self-weight of the sand is 16.03 kN/m^3 .

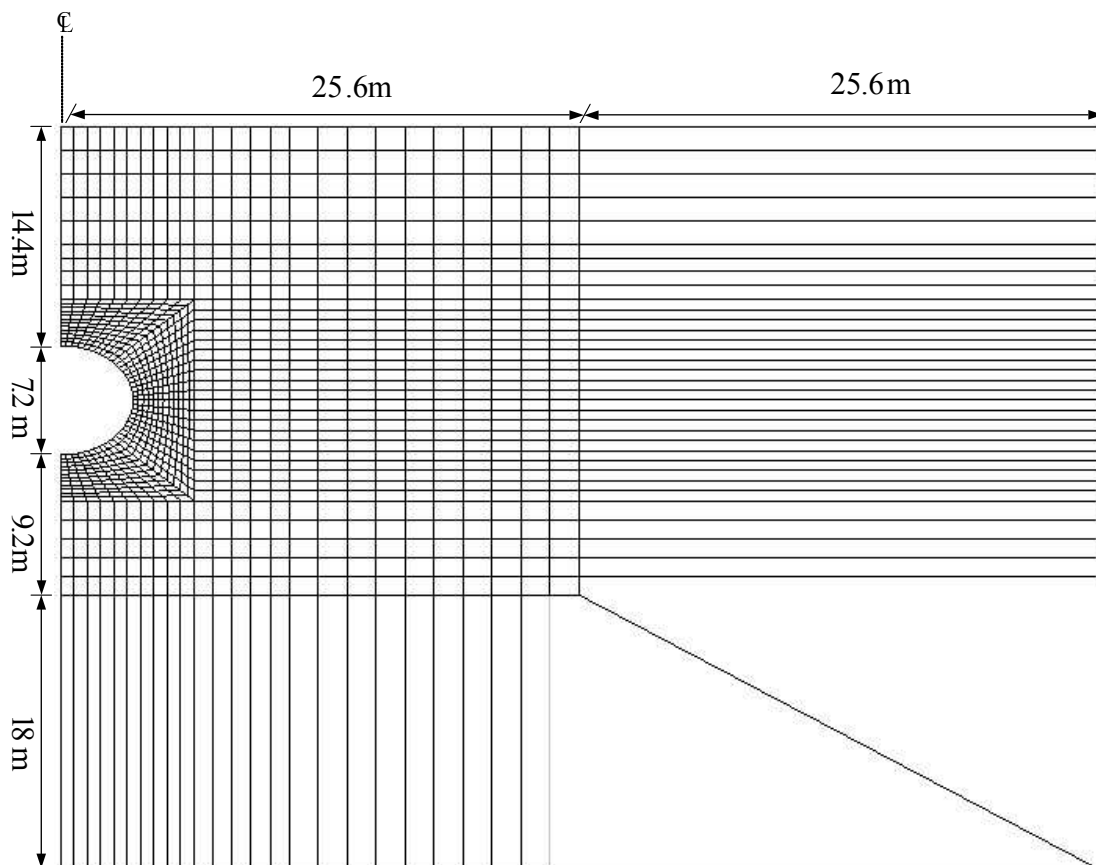


Figure 5.17 Geometry and finite element discretisation: real size with Zhou's centrifuge tests.

The nodal forces that are required to maintain equilibrium with the initial stress state in the surrounding material as loads on the perimeter of the tunnel, are obtained from an independent analysis where the displacements on the tunnel perimeter are constrained. In all cases, an initial stress regime with $K_0 = 0.5$ is adopted.

The stress reduction type of approach, which was first suggested by Wood (1975), seems to be most popular. An appropriate stress reduction factor, being referred to as the unloading or λ factor, is applied in combination with the stress reduction method.

Two calculation phases are introduced under this circumstance. Starting from initial stresses, the stresses inside the tunnel are reduced stepwise in a first calculation phase and the resulting volume loss (also known as ground loss as no pore pressure is considered) is calculated after each increment. In a second calculation phase, the simulation is terminated immediately after the prescribed ground volume loss is reached at the corresponding pressure. The corresponding pressure can be matched by applying an appropriate stress reduction factor λ .

5.6.2 Volume loss

No pore pressure is taken into consideration in our numerical modelling. In other words, fully drained conditions are assumed. Hence for simplicity, the resulting volume loss around the crown due to the reduction in the stresses inside the tunnel core, represents the ground volume loss as well. The value of the volume loss is calculated as:

$$V_l[\%] = \frac{V_s}{A_t} \cdot 100 \quad (5.6)$$

where V_s is the resulting volume around the crown, $A_t = \pi D_s^2/4$ and D_s is the tunnel diameter.

The approximate calculation of the resulting volume loss is shown in Figure 5.18. It should be noted that only a 2D condition is considered. As indicated in Figure 5.18, the black curve refers to the original size of the tunnel crown. The green lines represent the deformable shape of the tunnel after excavation. The crown diameter is D_s , and the area covering the red dash lines is equal to the resulting volume V_s . V_s is required to be calculated in order to obtain the volume loss V_l . The approximate value of V_s can be calculated geometrically by dividing the zone into a reasonable number (n) of small rectangles, having an area A_s . Then V_s can be defined by the following equation:

$$V_s = \sum_i^n A_s \quad (5.7)$$

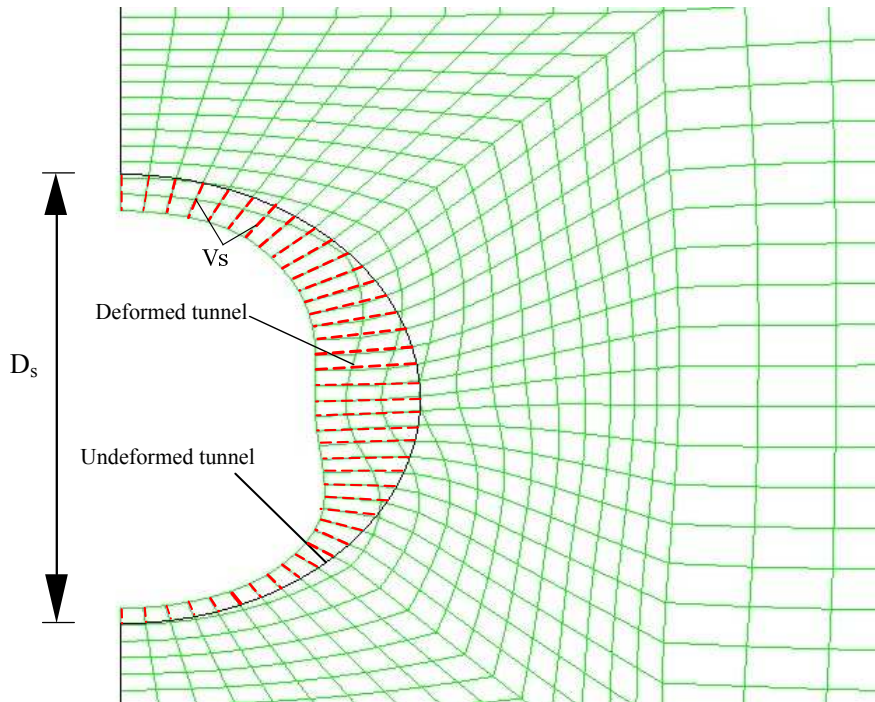


Figure 5.18 The illustration of volume loss calculation.

5.6.3 Subsurface settlement troughs

In the centrifuge tests conducted by Zhou (2015), four degrees of volume loss have been investigated, namely $V_l = 0.86\%$, $V_l = 2.0\%$, $V_l = 3.23\%$, and $V_l = 5.16\%$ respectively. Numerical simulation is also performed using the Mohr-Coulomb model provided in ABAQUS. When the proposed non-coaxial model is employed, the maximum friction angle is always set as $\phi_{max} = 30^\circ$ ($\phi = 30^\circ$ for the Mohr-Coulomb yield criterion in ABAQUS). Only a rotational ellipse yield curve is investigated for simplicity. The anisotropic coefficient n is equal to 0.707 and β varies as 0° , 22.5° and 45° . The value of non-coaxial coefficient $k = 0.0$, $k = 0.02$, and $k = 0.1$ for the same case. As mentioned previously, an appropriate stress reduction factor λ should be selected to reach a corresponding pressure, which results in a desired volume loss in numerical simulations.

Figures 5.19 - 5.26 present settlement profiles normalised against the maximum settlement S_{vmax} corresponding to a desired volume loss, and compare the results with centrifuge test data from Zhou (2015). Figures 5.28 and 5.30 illustrate the vertical displacement troughs under the same value of stress reduction factor λ (the same increment) with various values of anisotropic coefficients and the non-coaxial coefficient. The influences of soil anisotropy and non-coaxiality on tunnelling induced displace-

ment are detailed in these figures.

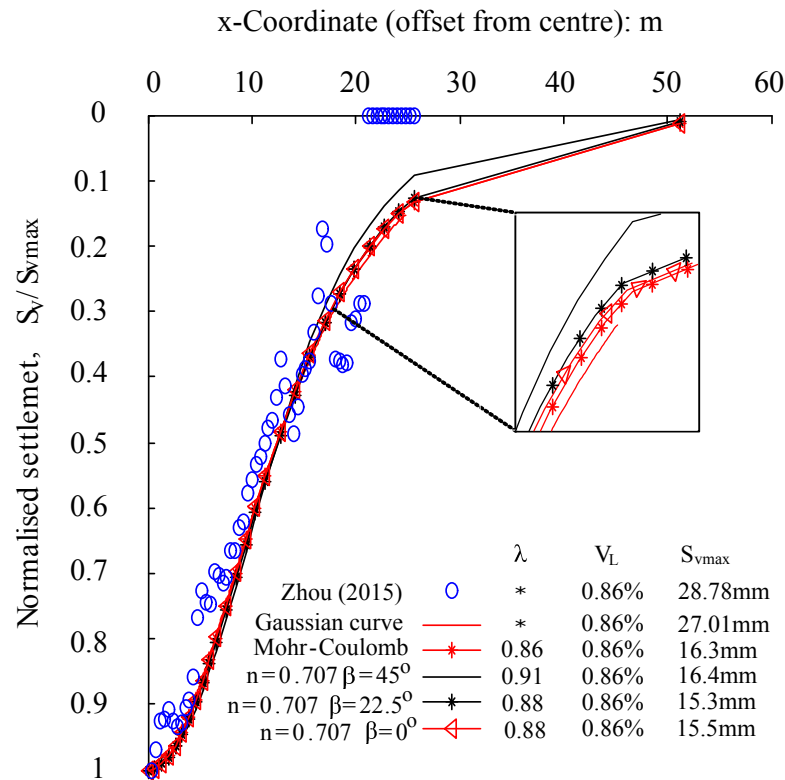


Figure 5.19 Normalised settlement profiles in terms of $V_l = 0.86\%$.

Figures 5.19 and 5.20 show the normalised ground settlement troughs for these analyses taken from increments that achieved a volume loss of approximately $V_l = 0.86\%$ and $V_l = 2.0\%$ respectively. In these figures, the non-coaxial coefficient is set as $k = 0.0$. This amount of volume loss is obtained from the centrifuge test of Zhou (2015). The figures also list the Gaussian curve fitted to the test data and the normalised settlement curve obtained by using the isotropic Mohr-Coulomb model in ABAQUS. The stress reduction factor in which the desired volume loss is achieved, and values of maximum settlement are listed in these figures as well. As indicated in these two figures, different values of λ are applied in order to achieve the same volume loss. Normally, the desired value of λ for the Mohr-Coulomb model in ABAQUS is lower than that for the proposed non-coaxial model. This may result in larger maximum vertical displacement for the proposed non-coaxial model involving soil anisotropy than the isotropic Mohr-Coulomb model in ABAQUS. The predicted settlement curves lie close to each other by using the Mohr-Coulomb model in ABAQUS and the proposed non-coaxial model. In addition, the general shape of the ground settlement curve is similar for both the Gaussian settlement curve which fits to the test data and numerical

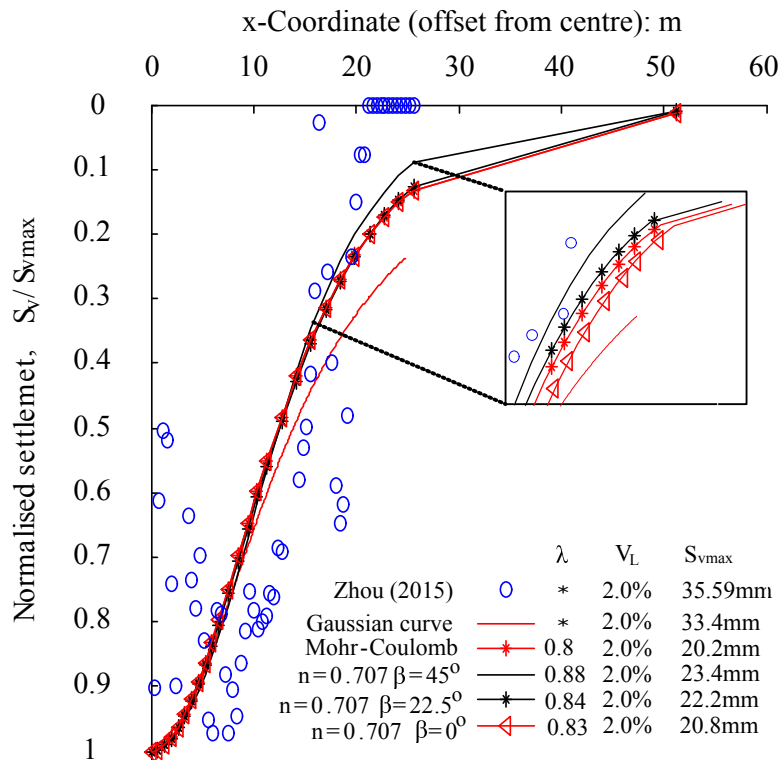


Figure 5.20 Normalised settlement profiles in terms of $V_L = 2.0\%$.

analyses.

Figures 5.21 and 5.22 present the normalised ground settlement troughs for these analyses taken from increments that achieved a volume loss of approximately $V_L = 3.23\%$ and $V_L = 5.16\%$ respectively. Comparing the settlement curves for the Gaussian settlement trough with those for the numerical analyses, shows that the surface settlement trough becomes wider when obtained from numerical simulations. However, adopting the anisotropic coefficient β improves the settlement curve further.

As indicated in both Figure 5.21 and Figure 5.22, the combination of anisotropic coefficients $n = 0.707$ and $\beta = 0^\circ$ leads to a much narrower normalised subsurface settlement trough (see red line with triangular marker). This curve is almost the same as the Gaussian curve, and fits to the field data. The reason for this behaviour is that the influence of anisotropic coefficients is pronounced for a higher stress unloading factor that results in a wider plastic zone.

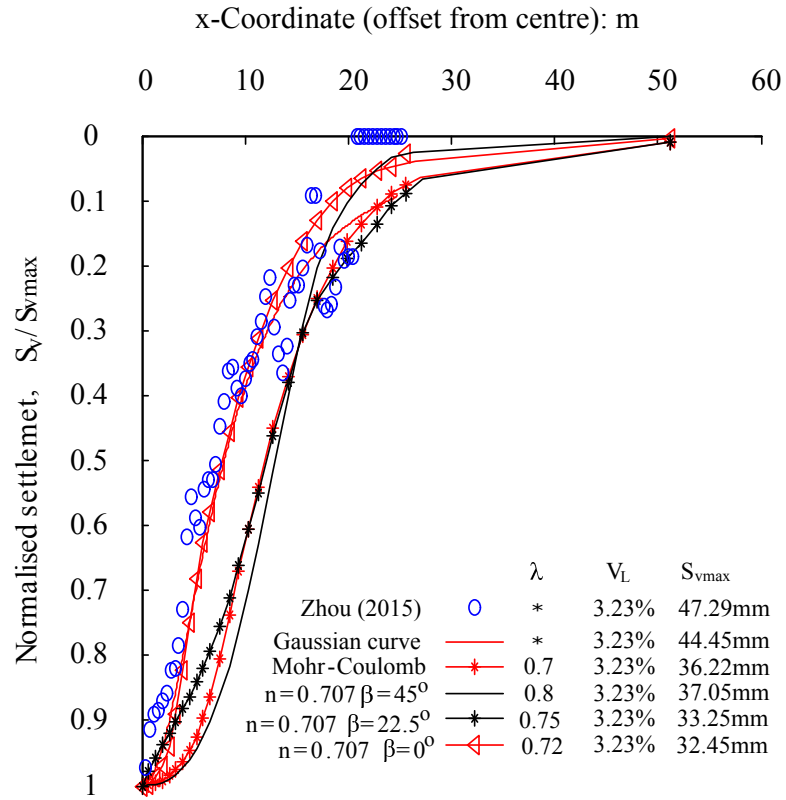


Figure 5.21 Normalised settlement profiles in terms of $V_L = 3.23\%$.

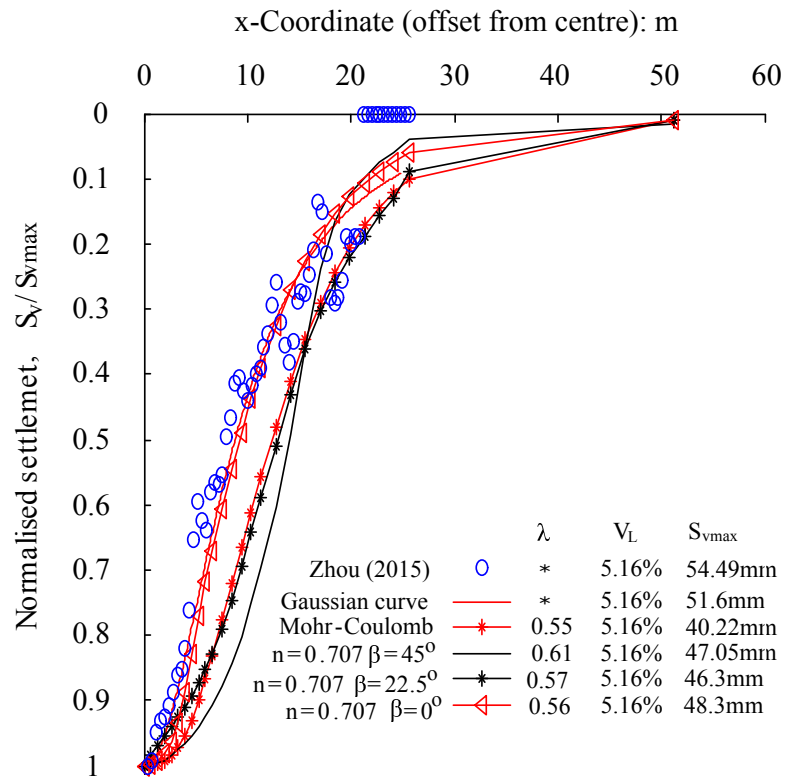


Figure 5.22 Normalised settlement profiles in terms of $V_L = 5.16\%$.

The influence of the non-coaxial coefficient k on the normalised ground settlement troughs in terms of a desired volume loss of $V_l = 3.23\%$ and $V_l = 5.16\%$, is illustrated in the following four figures (Figures 5.23 - 5.26). As analysed previously, the case with $n = 0.707$ and $\beta = 0^\circ$ leads to a close match of the normalised settlement curve to a Gaussian curve and field data; and similar observations can be found in Figure 5.23 and Figure 5.25. In contrast, the case with $n = 0.707$ and $\beta = 45^\circ$ results in a wider normalised settlement curve as shown in Figures 5.24 and 5.26. It is interesting to see that the inclusion of non-coaxial behaviour is unlikely to affect the shape of the normalised ground settlement troughs. Further discussion can be found in Figure 5.30. The figures demonstrate that only adoption of the anisotropic coefficient β can improve the normalised settlement trough.

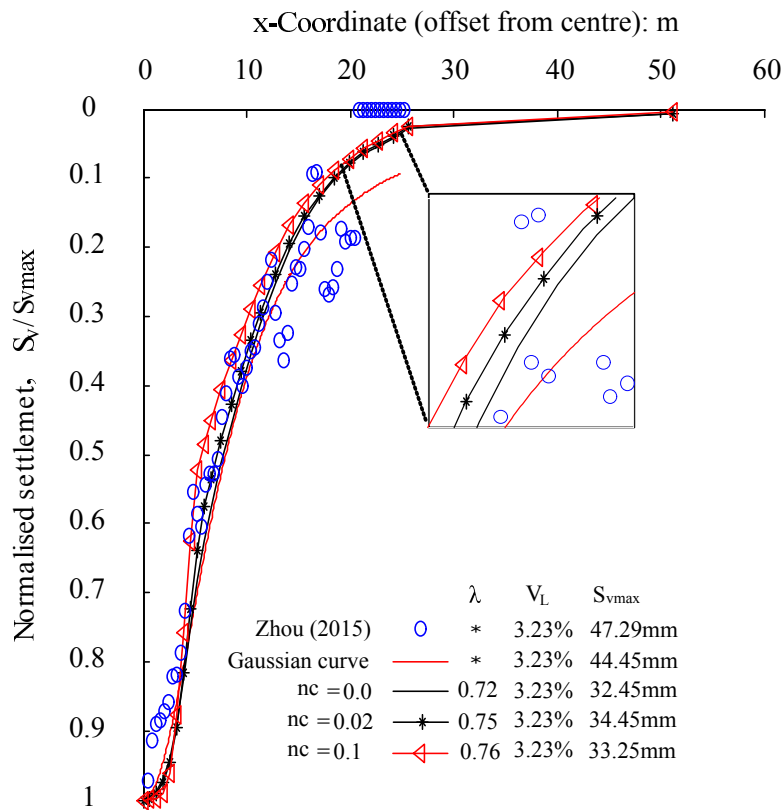


Figure 5.23 Normalised settlement profiles in terms of $V_l = 3.23\%$ in terms of non-coaxial effects when $n = 0.707$ $\beta = 0^\circ$.

As analysed previously, the value of λ in which the same desired volume loss is achieved is always lower for the Mohr-Coulomb model in ABAQUS than for the proposed non-coaxial model. However, the relative magnitude resulting from the influence of anisotropic coefficient β varies. It is necessary to investigate the subsurface settlement shape with various values of anisotropic coefficients and non-coaxial coefficient

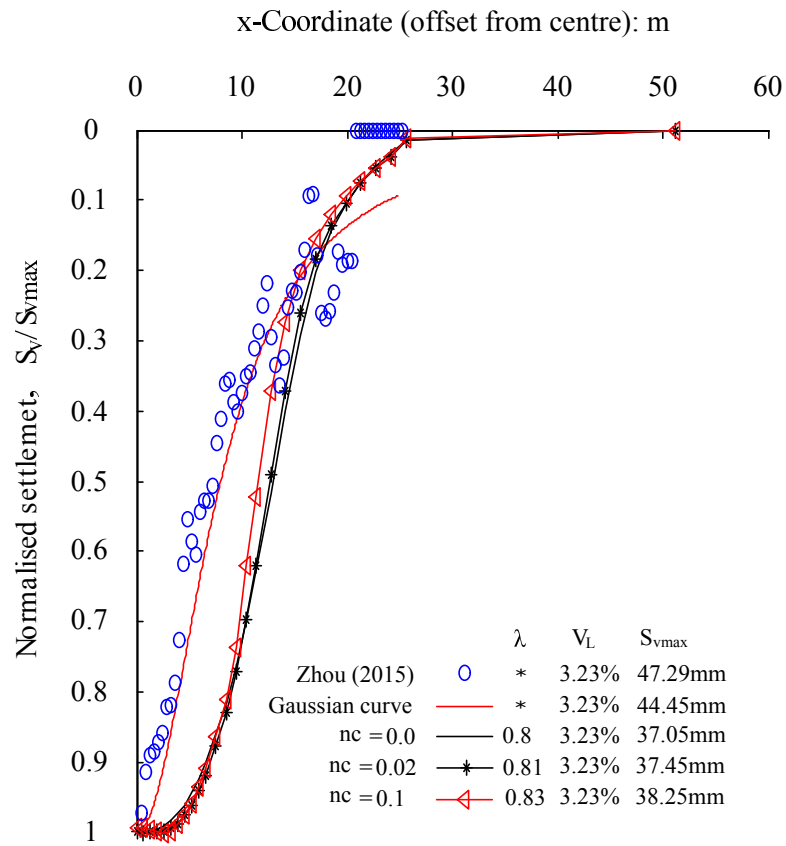


Figure 5.24 Normalised settlement profiles in terms of $V_L = 3.23\%$ in terms of non-coaxial effects when $n = 0.707$ $\beta = 45^\circ$.

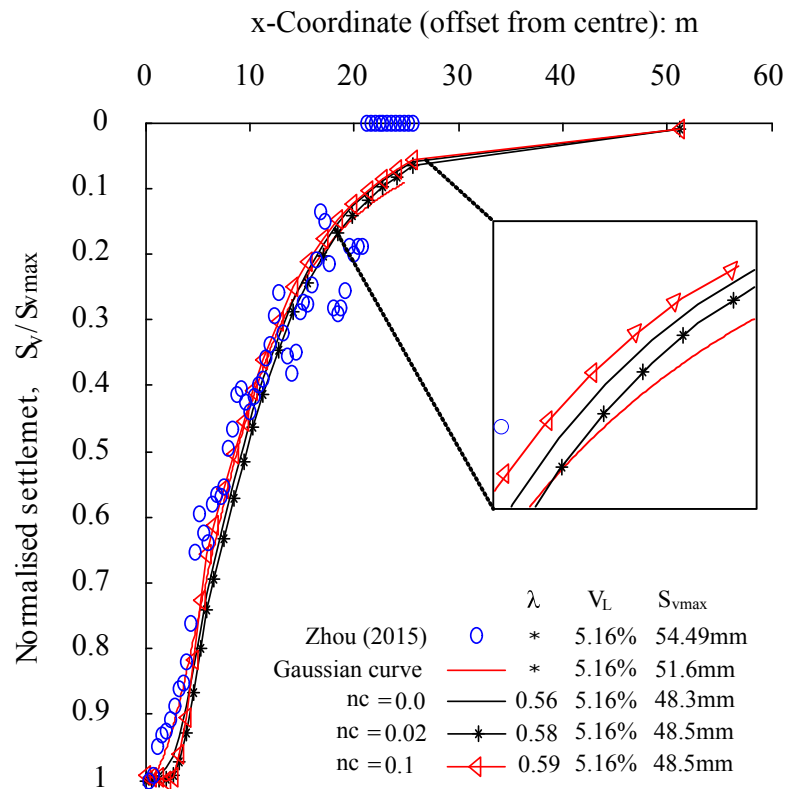


Figure 5.25 Normalised settlement profiles in terms of $V_L = 5.16\%$ in terms of non-coaxial effects when $n = 0.707$ $\beta = 0^\circ$.

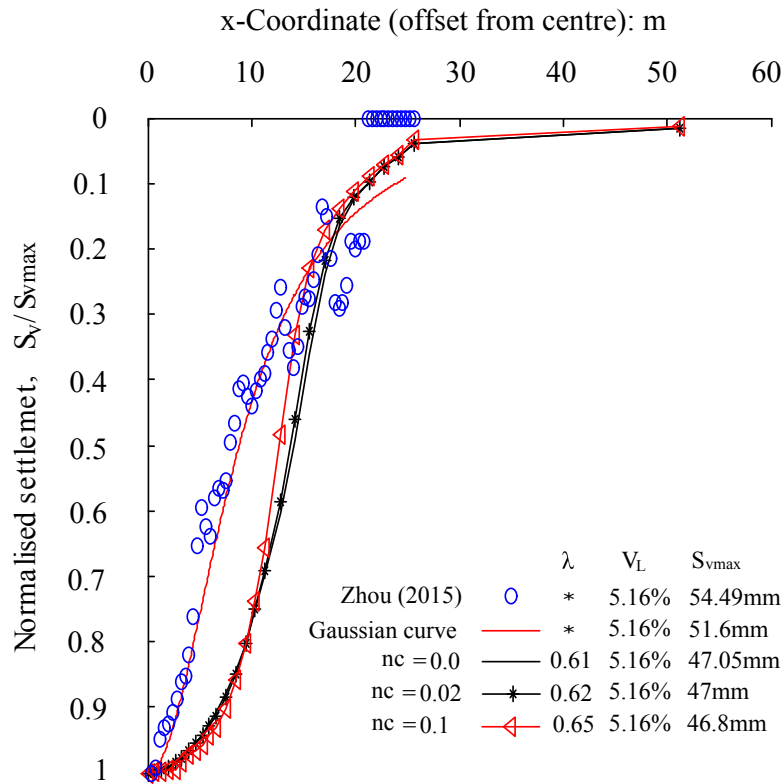


Figure 5.26 Normalised settlement profiles in terms of $V_L = 5.16\%$ in terms of non-coaxial effects when $n = 0.707$ $\beta = 45^\circ$.

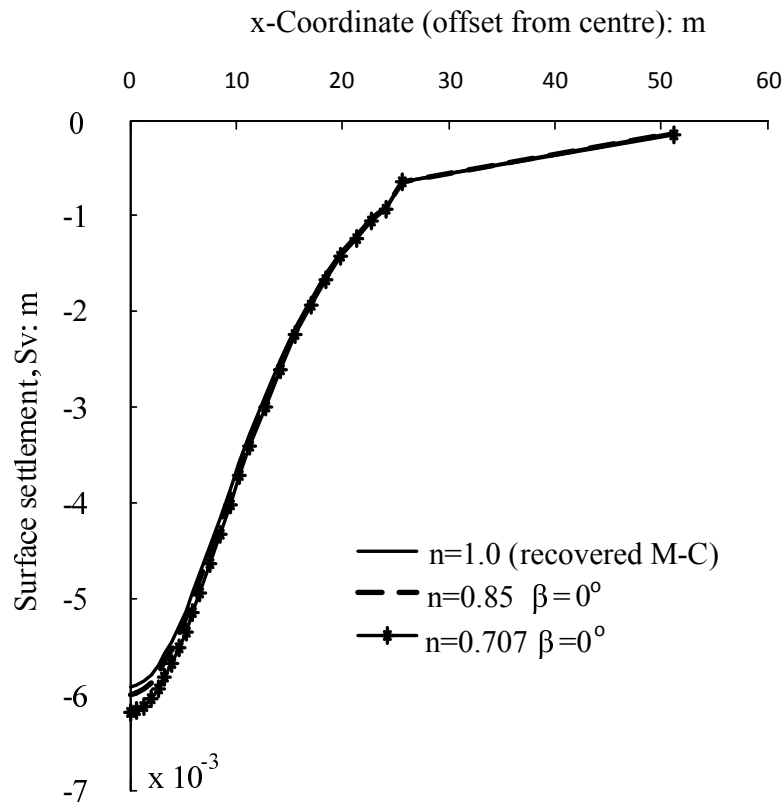
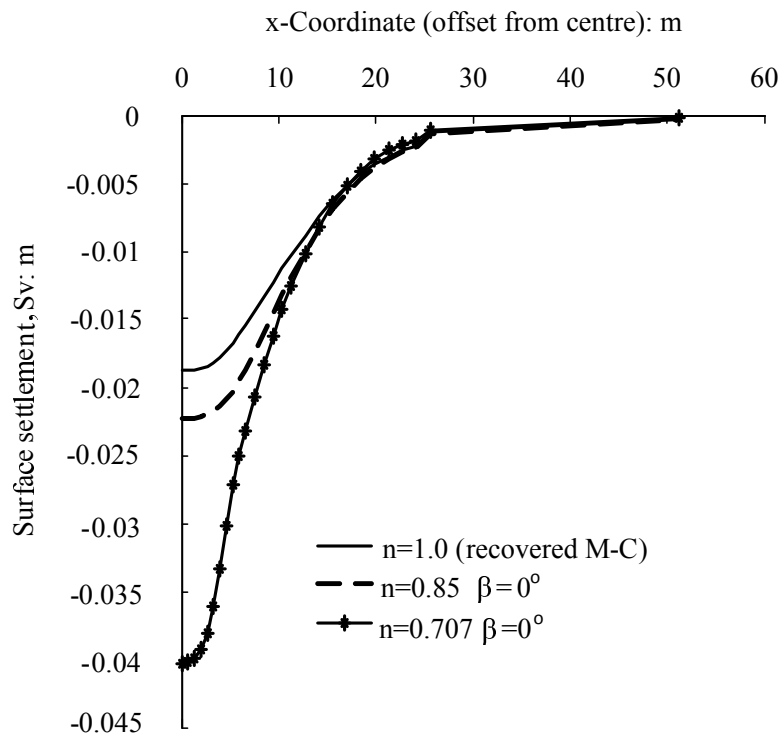
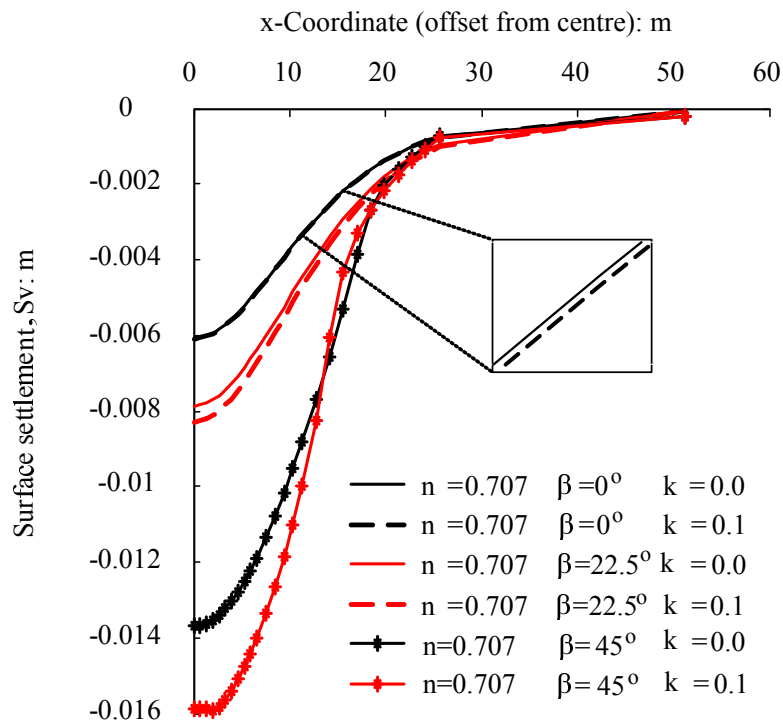


Figure 5.27 Vertical displacement with the influence of n ($\lambda = 0.92$).

at the same excavation step (the same value of λ). For the sake of argument, two excavation steps are investigated, with unloading factor $\lambda = 0.92$ and $\lambda = 0.6$. Figures 5.28 and 5.27 present the influence of anisotropic coefficient n on the subsurface settlement profile; whereas Figures 5.30 and 5.29 present the influences of anisotropic coefficient β and non-coaxial coefficient k on the settlement curve. The maximum vertical displacement is slightly larger with a lower magnitude of n when unloading factor λ equals 0.92. Evidence can be reinforced from Figures 5.19 and 5.20 that exhibit a similar normalised settlement curve with a lower value of λ , irrespective of soil anisotropy and non-coaxiality. As indicated in Figure 5.28, it is obvious that a smaller value of anisotropic coefficient n leads to a narrower and steeper settlement trough when the unloading factor λ equals 0.6. With respect to Figure 5.30, it is consistent with the conclusions drawn from the figures illustrating the normalised settlement profiles in which the settlement trough is narrower and steeper for a case with $\beta = 0^\circ$ for a smaller magnitude of unloading factor λ ($\lambda = 0.6$). For a larger magnitude of unloading factor λ ($\lambda = 0.92$), the maximum vertical displacement obtained from the case with $\beta = 45^\circ$ is higher than that with $\beta = 0^\circ$; however, the pattern of the curve is similar. Non-coaxiality is unlikely to affect the shape of the settlement curve; however, it results in higher magnitudes of the maximum vertical displacement along the centre line. In addition, the magnitude of the anisotropic coefficient β shows a strong effect on the maximum vertical displacement.

Figure 5.28 Vertical displacement with the influence of n ($\lambda = 0.6$).Figure 5.29 Vertical displacement with the influence of β ($\lambda = 0.92$).

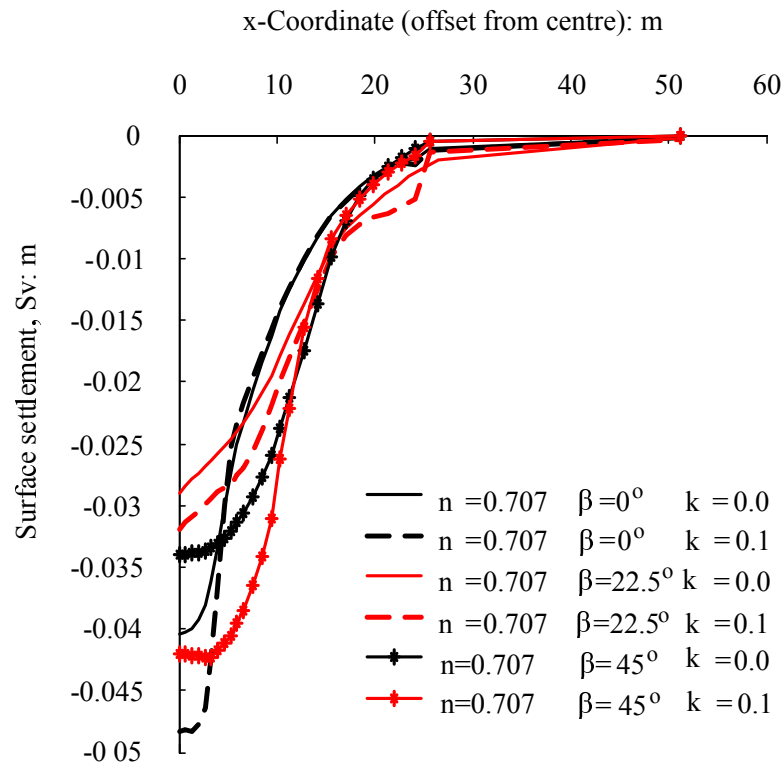


Figure 5.30 Vertical displacement with the influence of β ($\lambda = 0.6$).

5.7 Chapter Summary

The numerical application of the proposed non-coaxial model into tunnelling presented in this chapter provided an investigation of soil anisotropy and non-coaxiality on the tunnelling induced displacement. Both the stiffness reduction excavation method and the stress reduction excavation method were applied and analysed. Conclusions can be drawn that the influence of non-coaxiality was pronounced by using the stress reduction method as compared to the stiffness reduction method. The anisotropic coefficients n and β and the non-coaxial coefficient k affected the maximum magnitude of the vertical displacement and the horizontal displacement. However, the shape of the settlement trough and the horizontal displacement curve were only affected by the value of the anisotropic coefficient β . Normalised subsurface settlement troughs (S_v/S_{vmax}) were presented corresponding to a desired volume loss, and the results were compared with centrifuge test data from Zhou (2015). Numerical results became much wider when compared to test data and fitted Gaussian curves with higher volume loss. Adopting the anisotropic coefficient β resulted in an improvement of the settlement curve.

Chapter 6

Conclusions and recommendations for future work

A plane strain, elastic perfectly plastic non-coaxial soil model was developed in the framework of inherent soil anisotropy. The anisotropic Mohr-Coulomb yield criterion was developed by generalising the conventional isotropic Mohr-Coulomb yield criterion to include the effects of inherent soil anisotropy. The inherent soil anisotropy was described by the variation of internal friction angles with the direction of the principal stress. For mathematical simplicity, the shape of the yield curve in the deviatoric space ($\frac{\sigma_x - \sigma_y}{2}, \sigma_{xy}$) was assumed to be either a rotational ellipse or an eccentric ellipse. The nonassociativity in the conventional plastic flow rule was also developed to overcome the drawbacks while simulating simple shear tests. The newly proposed soil model was then implemented in a commercial numerical software ABAQUS via UMAT. A hyperbolic approximation of the yield function was used to eliminate the computational difficulties due to the gradient discontinuities that occur at the tip of the yield surface. The explicit modified Euler scheme was used to integrate the constitutive law. Simple shear problems were selected to validate the numerical implementation of the non-coaxial soil model. Further on, numerical applications were performed on smooth strip footings and tunnel excavations using the newly proposed non-coaxial soil model. This chapter presents the main conclusions drawn from each part of the research in Section 6.1, and provides recommendations for further possible areas of research on this topic in Section 6.2.

6.1 Conclusions

6.1.1 On simple shear problems

Numerical simulations have been performed on simple shear tests using the newly proposed non-coaxial soil model. Numerical results of the shear stress ratio and non-coaxial orientations of the principal stress and principal plastic strain rate were analysed. The evolutions of stress paths in the deviatoric plane were also presented.

- The analytical expressions of the ultimate stress ratio $(\frac{\sigma_{xy}}{\sigma_y})_{ultimate}$ proposed by Davis (1968) and the peak point of the stress ratio $(\frac{\sigma_{xy}}{\sigma_y})_{peak}$ proposed by Hansen (1961) were used to verify the numerical results obtained from the simple shear tests by using the non-coaxial soil model, neglecting soil anisotropy and non-coaxiality. It showed that the numerical results were consistent with the analytical solutions for both the rotational and eccentric ellipse yield criterion. This in turn testifies the correctness of the finite element implementation procedures of the newly proposed non-coaxial soil model.
- The numerical predictions of the shear stress ratio in terms of soil anisotropy were lower than those in terms of soil isotropy. The anisotropic coefficients n and β had a great effect on the magnitudes of the ultimate shear stress ratio. The initial lateral stress ratio K_0 indicated negligible effect on the ultimate shear stress ratio; however, it affected the shape of the stress-strain curve by producing a strain-softening response after reaching its peak value for over-consolidated soil ($K_0 > 1.0$), when the nonassociativity in the plastic flow rule was involved. The non-coaxial coefficient k had few effects on the ultimate shear stress ratio. A larger value of the non-coaxial coefficient resulted in a softening response of stress-strain evolutions for normally-consolidated soils ($K_0 < 1.0$). Nevertheless, in some special cases for over-consolidated soils ($K_0 = 3.0$), the numerical results of the shear stress ratio remained the same, irrespective of using a different non-coaxial coefficient k when using the associativity in the conventional plastic flow rule.
- The ultimate orientations of the principal stress and principal plastic strain rate were verified by the study of Davis (1968), who pointed out that any horizontal plane was always inclined at $45^\circ + \frac{\psi}{2}$ at the ultimate failure. With respect to the

rotational ellipse yield criterion, there existed non-coincidence of the direction of the principal stress and principal plastic strain rate throughout the loading procedure with $k = 0.0$ when the associativity in the conventional plastic flow rule was involved, which violated experimental investigations. Hence, a nonassociativity in the conventional plastic flow rule was introduced to overcome this drawback. It showed that the directions of the principal stress and principal plastic strain increment were coincident with $k = 0.0$ for the nonassociativity in the conventional plastic flow rule. When the non-coaxial coefficient was unequal to zero, a distinct non-coincidence of the direction of the principal stress and principal plastic strain rate was observed at the initial stage in the shear stress level. The degree of non-coaxiality decreased with the increase in the shear stress level. The non-coincidence vanished when achieving large shear strain at the limit state. In addition, a larger value of the non-coaxial coefficient k resulted in a higher degree of non-coaxiality at the beginning of the loading procedure. With respect to the eccentric ellipse yield criterion, similar conclusions can be drawn when compared with the rotational ellipse yield criterion. Moreover, the eccentric ellipse yield criterion can ideally model the coaxiality of the direction of the principal stress and plastic strain rate even for the associativity in the conventional plastic flow rule. For the particular case of over-consolidated soils ($K_0 = 3.0$) modelled by an eccentric ellipse yield criterion with the associativity in the conventional plastic flow rule, the orientations were coincident. The reason can be that the sample was subjected to few principal stress rotations as analysed before under this circumstance. The pattern of the orientations was in good agreement with previous experimental observations (e.g. (Roscoe et al., 1967)) and numerical investigations (e.g. (Yuan, 2005)).

- It should be noted that an elastic perfectly plastic condition was assumed, and hence the stress paths may move along the yield surface once plastic deformations develop. The anisotropic coefficients n and β affected the shapes of the yield curve in the deviatoric space, which resulted in different distances that the stress paths travelled in the purely elastic regime before reaching the plastic state. Hence, the time span for reaching coaxiality of the direction of the principal stress and principal plastic strain rate was affected. The stress paths reached the same final position on the yield curve, independent of the initial lateral stress ratio K_0 ,

and anisotropic coefficients n and β and non-coaxial coefficient k .

6.1.2 On strip footing problems

The non-coaxial soil model has been applied to investigate smooth strip footing problems, drawing particular emphasis on the influence of soil anisotropy and non-coaxiality on the bearing capacity of the strip footing. Semi-analytical solutions of the bearing capacity for a smooth strip footing resting on an anisotropic, weightless, cohesive-frictional soil were developed based on the slip line method. In particular, a close-form solution for a purely cohesive material was also presented. Prandtl's solution was recovered when the anisotropic Mohr-Coulomb yield criterion was reduced to the conventional isotropic Mohr-Coulomb yield criterion.

- Parametric studies in terms of the anisotropic coefficients n and β with various magnitudes of the maximum peak internal friction angle ϕ_{max} were performed on the computations of bearing capacity factors N_c and N_q . The bearing capacity factors N_c and N_q were lower when the soil was resting on an anisotropic soil as compared to their isotropic counterpart. For smaller values of ϕ_{max} (i.e. $\phi_{max} \leq 30^\circ$), the anisotropic predictions and isotropic predictions were close for both N_c and N_q ; however, the difference between the anisotropic predictions and isotropic predictions was pronounced with larger magnitudes of ϕ_{max} . A smaller value of n and larger value of β resulted in lower values of bearing capacity factors N_c and N_q .
- Without accounting for non-coaxial plasticity (i.e. $k = 0.0$), the numerical application of the non-coaxial soil model on the analyses of strip footing problems was conducted in two scenarios: with and without surface loading. In order to avoid the singularity problem for numerical simulations when ϕ_{max} was relatively small, the cohesion c of the soil was always set as 30kPa. Hence, two bearing capacity factors N_c and q_t/q were computed. Several numerical tests were conducted in light of various values of anisotropic coefficients n and β . The numerical results were slightly larger when compared with the semi-analytical solutions in each test, but within a tolerable range. The results highlighted the capability of numerical procedures. With respect to the rotational ellipse yield criterion, the soil was stiffer with an increase in β in the load displacement curve.
- The numerical computations of bearing capacity factors N_c and N_q were per-

formed in terms of a rotational ellipse yield criterion to investigate the influence of soil anisotropy, non-coaxiality, the initial stress state and the dilation angle. The numerical results showed that the initial lateral stress ratio K_0 , the dilation angle ψ_Θ and the non-coaxial coefficient k rarely affected the ultimate bearing capacity of the strip footing. However, the settlement prior to collapse was larger with a larger value of k , which indicated that the soil softened when the non-coaxial coefficient was unequal to zero. Parameters R_r and R_s were introduced as the maximum difference of the normalised pressure and the corresponding settlement prior to collapse between coaxial and non-coaxial modelling with $k = 0.0$ and $k = 0.1$. These parameters can be used to describe the effect of non-coaxiality on the numerical modelling of the bearing capacity. The numerical predictions of R_r and R_s for both N_c and N_q were close for different values of k by using the associativity and nonassociativity in the conventional plastic flow rule respectively. The values of anisotropic coefficients n and β and the lateral stress ratio K_0 had a significant influence on R_r . Generally, a smaller value of n and a larger value of β resulted in a pronounced value of R_r . For the computation of N_c , the influence of non-coaxiality on the bearing capacity was most significant for the case with $n = 0.85$ and $\beta = 45^\circ$, where $R_r = 13.5\%$. For the computation of N_q , the influence of non-coaxiality was most significant for the case with $n = 0.707$ and $\beta = 45^\circ$, where $R_r = 28.3\%$. This can be up to 4 times the value of R_r ($R_r = 7.0\%$) for the case with the recovered isotropic Mohr-Coulomb yield criterion ($n = 1.0$). This data highlighted the importance of modelling non-coaxial behaviour of the soil in the content of soil anisotropy. The effect of non-coaxial plasticity was negligible for over-consolidated soil ($K_0 = 2.0$) with a small value of $R_r = 4.6\%$. The variation of principal stress rotations obtained from only those elements at the corner of the footing proved the influence of non-coaxiality. It showed that a severe range of principal stress rotations was between -1.25° and 12.5° , which corresponded to the case of $n = 0.707$ and $\beta = 45^\circ$ with $R_r = 28.3\%$.

- The displacement patterns were plotted at the step $\frac{\Delta}{B}$ when the maximum difference R_r was obtained. It was concluded that the failure zone was more concentrated adjacent to or at the edge of the footing when non-coaxial behaviour was involved. The reason can be that these areas experienced more significant stress rotations when compared to other areas.

6.1.3 On tunnelling

The non-coaxial soil model was also applied to analyse tunnelling induced displacement and lining forces. Both the stiffness reduction method (α – method) and the stress reduction method (λ – method) were employed. In particular, a case study was presented and the results were compared with centrifuge test data from Zhou (2015). The lateral stress ratio was always set as $K_0 = 0.5$. The rotational ellipse yield criterion was used.

- With respect to the stiffness reduction method, the initial value of Young's modulus E_0 was reduced down to an empirical value of E_s by a factor of α before the activation of the lining, and $\alpha = 0.9$. The material inside the excavation core was then removed. The subsurface settlement troughs obtained by applying the non-coaxial soil model with $n = 1.0$ and the troughs obtained from the Mohr-Coulomb model in ABAQUS were consistent, which testifies the user-developed computational procedures. A smaller magnitude of the anisotropic coefficient n led to a larger maximum vertical settlement along the centre line. The case with $\beta = 45^\circ$ predicted the largest value of the maximum vertical displacement. In addition, the magnitude of the maximum vertical displacement was slightly higher when compared to the results from non-coaxial modelling with $k = 0.0$ and $k = 0.1$. For the horizontal displacement curves, the maximum magnitude of horizontal displacement decreased with a reduction in the anisotropic coefficient n . Similarly, the case with $\beta = 45^\circ$ gave the maximum horizontal displacement. A larger value of non-coaxial coefficient k resulted in a larger magnitude of the maximum horizontal displacement. The inclusion of soil anisotropy and non-coaxiality predicted larger axial forces on the lining.
- With respect to the stress reduction method, the initial value of the nodal forces applied on the perimeter of the tunnel were reduced by an unloading factor λ , where $\lambda = 0.9$. The lining was activated afterwards and the remaining forces were reduced to zero in the end. The subsurface settlement troughs obtained by applying the non-coaxial soil model with $n = 1.0$ and the troughs obtained from the Mohr-Coulomb model in ABAQUS were consistent, which testifies the user-developed computational procedures. The anisotropic coefficients n and β and the non-coaxial coefficient k had a pronounced effect on the subsurface settlement

trenches. A smaller value of n and a larger value of k resulted in the maximum magnitude of the maximum subsurface vertical displacement. In addition, the case with $\beta = 45^\circ$ gave the maximum magnitude of the maximum subsurface vertical displacement for all cases. Similar conclusions were found in the plots of horizontal displacement curves. In addition, the influence of non-coaxiality and soil anisotropy on the tunnelling induced displacement was pronounced using the stress reduction method when compared with the stiffness reduction method.

- A case study of numerical simulation was performed based on the centrifuge test from Zhou (2015). The nodal forces applied on the perimeter of the tunnel was reduced by a factor of λ and the resulting volume loss was calculated after each increment. The simulation was terminated immediately after the prescribed ground volume loss was reached at the corresponding pressure. Normalised settlement troughs were obtained by the Gaussian settlement troughs over the maximum settlement S_{vmax} . Results showed that for smaller volume loss with $V_l = 0.86\%$ and $V_l = 2.0\%$, the normalised subsurface settlement curves obtained by using the isotropic Mohr-Coulomb model in ABAQUS and the proposed non-coaxial model, were close to those curves obtained from centrifuge test and fitted Gaussian curves. For a larger volume loss with $V_l = 3.23\%$ and $V_l = 5.13\%$, the normalised settlement curves obtained from numerical simulations were wider as compared with the centrifuge results and the fitted Gaussian curves. However, adopting the anisotropic coefficient β improved the normalised settlement curves further. It was concluded that for the case with $n = 0.707$ and $\beta = 0^\circ$, the normalised settlement curves fitted well to the centrifuge results and fitted Gaussian curves. The non-coaxial plasticity had a negligible effect on the normalised settlement curves; however, a larger value of anisotropic coefficient n and non-coaxial coefficient k resulted in a higher magnitude of the maximum vertical displacement along the centre line at the same excavation step.

Overall, a plain strain, perfect plasticity, non-coaxial soil model has been developed in the context of soil yield anisotropy. The advantage of the proposed model was that there were only two shape parameters added to the original isotropic Mohr-Coulomb yield criterion, both of which had clear physical meanings. The formulation of the constitutive model was simple and can be easily implemented into finite element software. The finite element implementation procedures have been validated using the single

element simple shear test. The proposed model can reproduce the non-coaxiality of principal stresses and principal plastic strain rates. The settlement prior to failure in the strip footing simulation was larger under non-coaxial modelling. In addition, the soil yield anisotropy contributed to the difference between the coaxial and non-coaxial modelling. Both the maximum settlement and horizontal displacement were larger with larger values of the non-coaxial coefficient. Hence, it was concluded that failure to account for non-coaxiality may result in unsafe design in geotechnical engineering, especially the problems where severe principal stress rotations were induced.

6.2 Recommendations for further work

Based on the development of a non-coaxial soil model in the framework of inherent soil anisotropy, there are several aspects where further research on advancing the model and numerical applications in geotechnical problems can be undertaken.

- The current model is concerned with the plane strain, elastic-perfectly plastic condition. Further steps can be taken to advance the proposed soil model to include strain hardening. The soil anisotropy is described by the variation of the peak internal friction angles with the direction of the principal stress. On the other hand, the soil anisotropy can be presented by the variation of the cohesion with direction. Non-linear elasticity and cross elastic anisotropy can be incorporated into the model.
- The semi-analytical solutions were developed in the stress field at the state of plastic failure. Further steps can be taken to find a satisfactory velocity field that exhibits associativity with such a stress field and also satisfies the displacement boundary conditions. Hence, the semi-analytical solutions can be improved to analyse problems using nonassociativity in the conventional plastic flow rules. Different shapes of the shallow foundation should be analysed. Non-coaxial plastic modelling should be applied to other complicated geotechnical problems which may be subject to severe stress rotations, e.g. silo problems, anchor problems and so forth.
- Fabric tensors, which link the micro-mechanics and the constitutive modelling, can be used to develop the non-coaxial soil model. The results can be compared

to ours to gain more information regarding non-coaxiality.

- The newly developed model can be widely applied to investigate boundary value problems, e.g., silo, pile penetration to look insight how soil yield anisotropy and non-coaxiality can affect the stress-strain response of these problems.

Appendix 1

A.1 Eccentric ellipse

As indicated in Figure 1, another assumption is made that the anisotropic yield criterion with a constant Z is suggested to be an eccentric ellipse in the deviatoric stress space (Z, Y) . Likewise, the length OD changes due to the variation of peak internal friction angles with the direction of the principal stress. The maximum peak internal friction angle is assumed to be obtained when the major principal stress is parallel to the deposition direction. In other words, the Y -axis of the original Cartesian coordinate $X - Y$ moves to a new $X' - Y'$ coordinate by a positive length e along the horizontal axis. The X -axis remains unchanged in the new Cartesian coordinate in terms of a geometrical expression.

It is not difficult to assess that the length of OQ depends on the maximum peak internal friction angle ϕ_{max} . This case refers to the condition when the major principal stress is parallel to the deposition direction ($\Theta_p = 0^\circ$). Now we can obtain a peak internal friction angle ϕ_Ω by assuming that the major principal stress is perpendicular to the deposition direction ($\Theta_p = \frac{\pi}{2}$); hence, the length OP is a function of ϕ_Ω . A shape parameter n is introduced as the since ratio of the minor axis divided by the major axis of the ellipse. This parameter is empirical and needs to be determined for a given material, e.g. the simple shear test can be used to determine the n value by comparing numerical investigations with experimental results. The range of n is between 0 and 1. On this occasion, the isotropic Mohr-Coulomb yield criterion can be retrieved when $\phi_{max} = \phi_\Omega$ and $n = 1.0$.

When compared to the rotational ellipse anisotropic Mohr-Coulomb yield criterion,

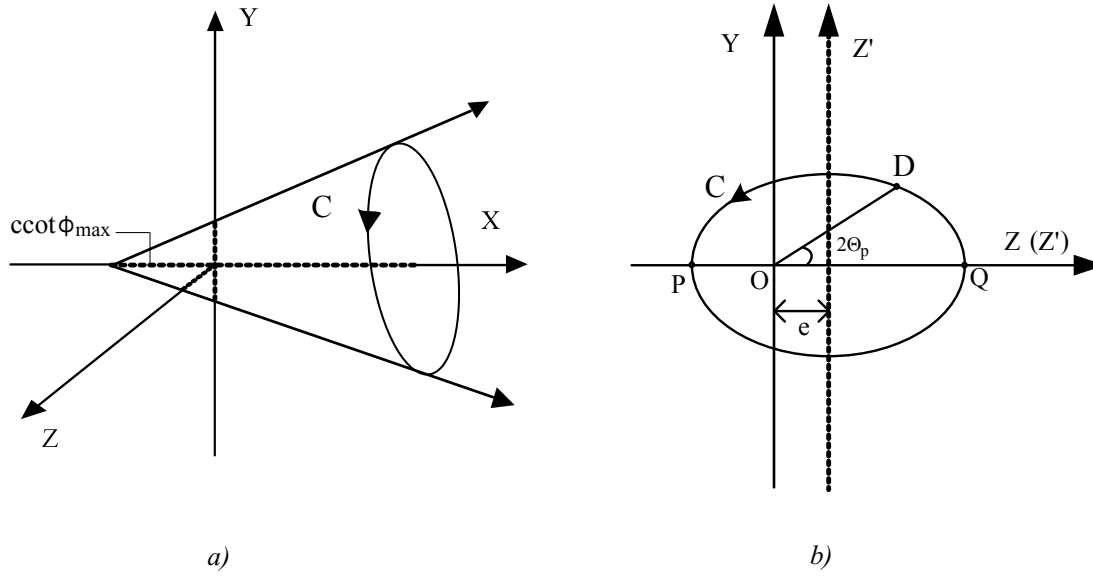


Figure 1 The eccentric ellipse anisotropic Mohr-Coulomb yield surface in: a) (X, Y, Z) space; b) (Z, Y) space.

only the formulation of the peak internal friction angle is different, as:

$$\sin\phi(\Theta_p) = \frac{n^2(\sin\phi_{max} - \sin\phi_{\Omega})\cos 2\Theta_p + B}{2n^2\cos^2(2\Theta_p) + 2\sin^2(2\Theta_p)} \quad (1)$$

where

$$B = \sqrt{n^4(\sin\phi_{max} + \sin\phi_{\Omega})^2\cos^2(2\Theta_p) + 4n^2\sin^2(2\Theta_p)\sin\phi_{max}\sin\phi_{\Omega}} \quad (2)$$

In addition, for the eccentric ellipse anisotropic Mohr-Coulomb yield criterion, the definition of m_{Θ_p} is:

$$m_{\Theta_p} = \frac{YY'\sqrt{YY^2 + TT^2} - (YY^2 + TT^2)'YY}{2\cos(2m) \cdot (YY^2 + TT^2)} \quad (3)$$

where

$$\begin{aligned} YY &= 2n^2 \cdot e \cdot (-\sin(2\Theta_p)) \cdot BB \cdot CC \\ &+ (n^2DD^2 - n^2e^2 - n^4DD^2) \cdot \sin(4\Theta_p) \\ &- (2 - 2n^2)\sin(4\Theta_p) \cdot (DD + BB) \cdot BB \end{aligned} \quad (4)$$

$$TT = CC \cdot (DD + BB)^2 \cdot BB \quad (5)$$

$$DD = n^2 \cdot e \cdot \cos(2\Theta_p) \quad (6)$$

$$BB = \sqrt{n^4 A^2 \cos^2(2\Theta_p) - n^2 (e^2 - A^2) \sin^2(2\Theta_p)} \quad (7)$$

$$CC = n^2 \cos^2(2\Theta_p) + \sin^2(2\Theta_p) \quad (8)$$

$$e = \frac{1}{2} (p + c \cot \phi_{max}) (\sin \phi_{max} - \sin \phi_{\Omega}) \quad (9)$$

A.1.1 Numerical results on simple shear tests with an eccentric ellipse yield criterion

In this section, results from a non-coaxial soil model with the eccentric anisotropic Mohr-Coulomb yield criterion are presented. The lateral stress ratio $K_0 = 0.5$ for normally consolidated soil and $K_0 = 3.0$ for over-consolidated soil respectively. The internal friction angles corresponding to various directions of the principal stress are obtained from the experimental results presented by Oda et al. (1978) ($\sigma_3 = 196$ kPa). σ_3 refers to the consolidation pressure. A higher value of σ_3 results in a more stable K_0 . This is the reason why we select $\sigma_3 = 196$ kPa instead of $\sigma_3 = 49$ kPa. Details of the material properties used in the numerical simulations are shown in Table 1. In this circumstance, the isotropic Mohr-Coulomb yield condition will be retrieved when $\phi_{max} = \phi_{\Omega} = 49.5^\circ$ and $n = 1.0$.

Table 1 Material properties for all numerical simulations

Cases	Anisotropic parameters			Flow rule	Dilation angle	Non-coaxial coefficient	lateral stress ratio
	$\phi_{max(\circ)}$	$\phi_{\Omega(\circ)}$	n	0-asso 1-non-asso	$\psi_{\Theta_p(\circ)}$	k	K_0
Test 13	49.5	49.5	1.0	0	30	(0.0, 0.02)	(0.5, 3.0)
Test 14				1	0		
Test 15	49.5	44.3	0.92	0	30	(0.0, 0.02, 0.05)	(0.5, 3.0)
Test 16				1	0		
Test 17	49.5	44.3	0.877	0	30	(0.0, 0.02, 0.05)	(0.5, 3.0)
Test 18				1	0		

Note: the maximum peak internal friction angle $\phi_{max} = 30^\circ$, $c = 0.001$ kPa, and $q = 100$ kPa.

A.1.1.1 Shear stress ratio

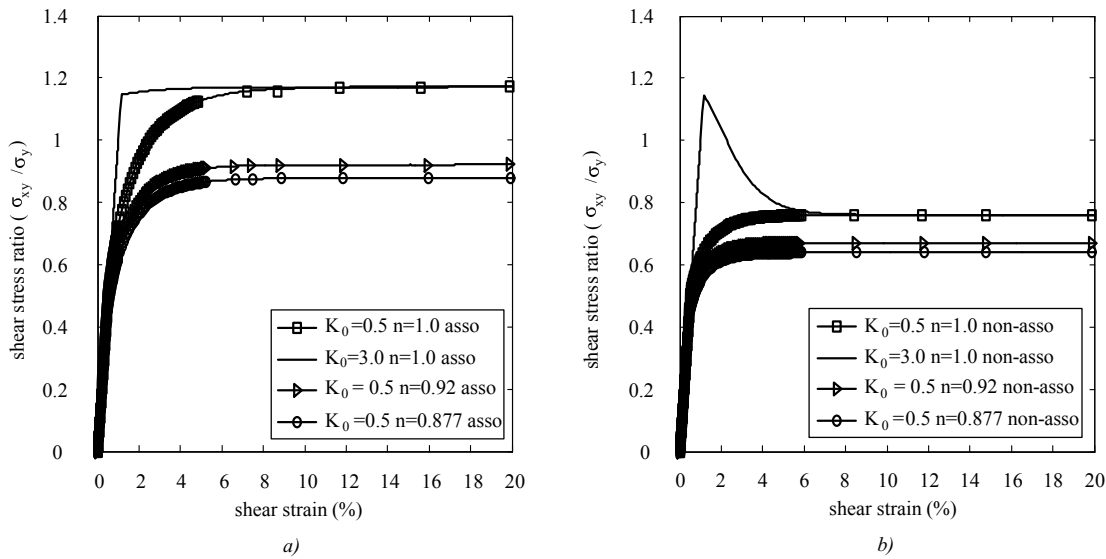


Figure 2 Shear stress ratio obtained from various values of anisotropic coefficient n : a) associativity in the conventional plastic flow rule; b) nonassociativity in the conventional plastic flow rule.

As indicated in Figure 2, soil anisotropy exhibits a significant effect on the ultimate shear stress ratio as expected. A smaller value of the anisotropic coefficient n results in a lower ultimate plastic shear stress at failure. To the contrary, the non-coaxial coefficient k and the initial lateral stress ratio K_0 demonstrate a negligible effect on the ultimate plastic shear stress at failure. This can be exhibited by Figures 2 b and 3 which show that the predicted shear stress tends to be identical irrespective of the magnitudes of k and K_0 . However, the two coefficients show a great influence on the shape of the stress-strain evolution. In Figure 2 b by invoking a nonassociativity in the conventional plastic flow rule, the shear stress is softened after reaching its peak value. The non-coaxial behaviour softens the shear stress-strain evolution immediately after the soil enters the plastic shearing phase.

A.1.1.2 Orientations of the principal stress and principal plastic strain rate

The influence of soil anisotropy, non-coaxiality, the dilation angle and the initial stress state on the orientations of the principal stress and principal plastic strain increment are investigated.

When compared to the results from a rotational ellipse yield surface, similar conclu-

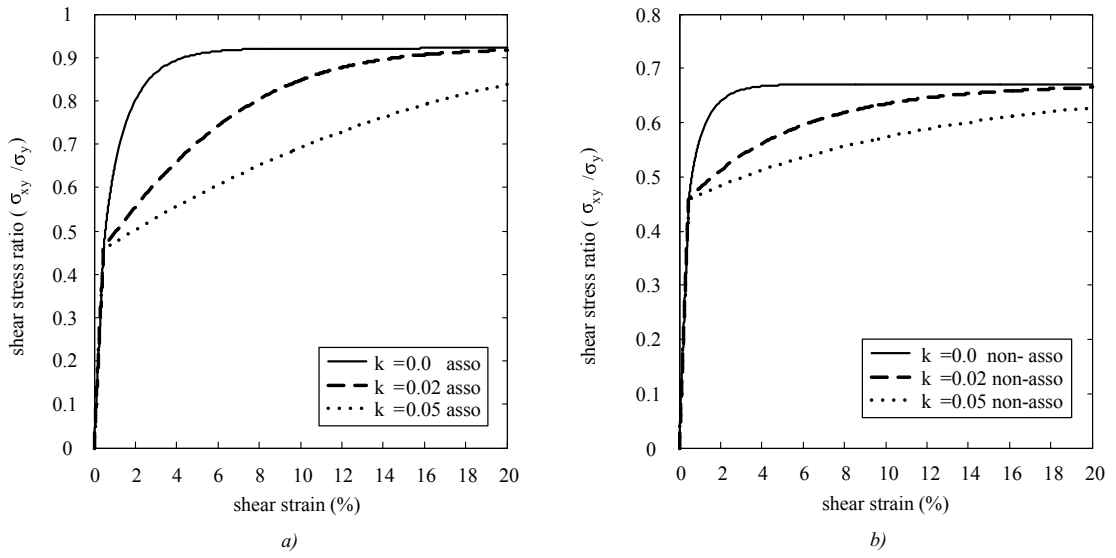


Figure 3 Shear stress ratio obtained from various values of non-coaxial coefficient k with $K_0 = 0.5$ in :
 a) Test 15; b) Test 16.

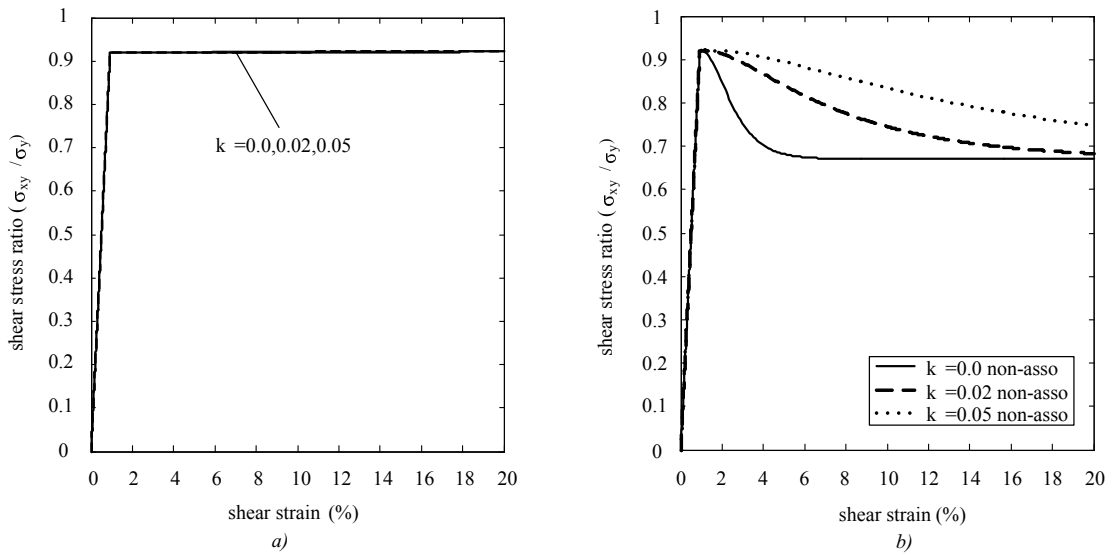


Figure 4 Shear stress ratio obtained from various values of non-coaxial coefficient k with $K_0 = 3.0$ in:
 a) Test 15; b) Test 16.

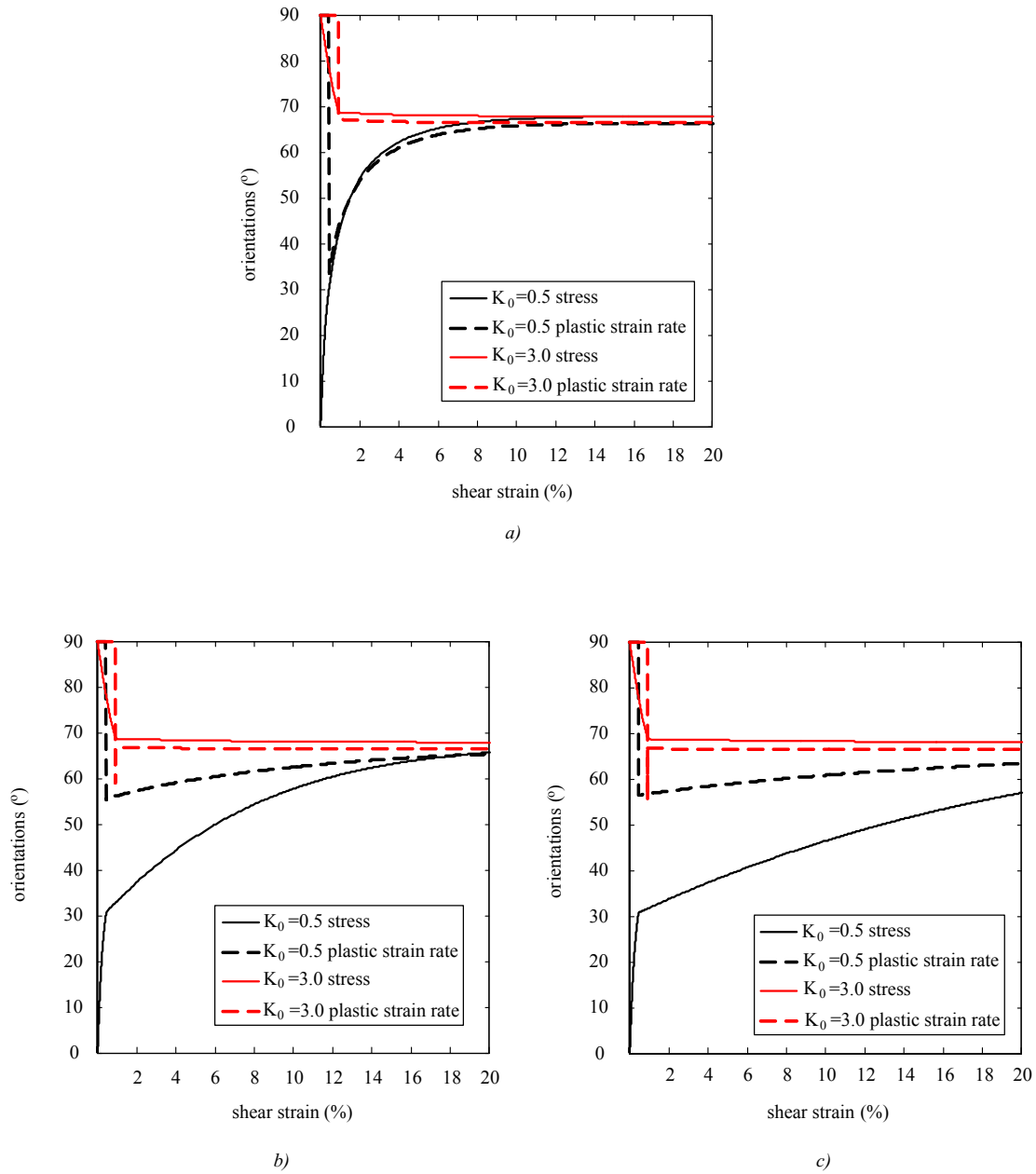
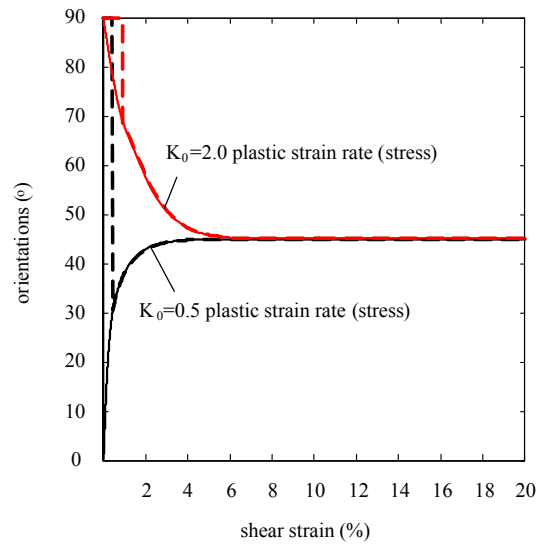
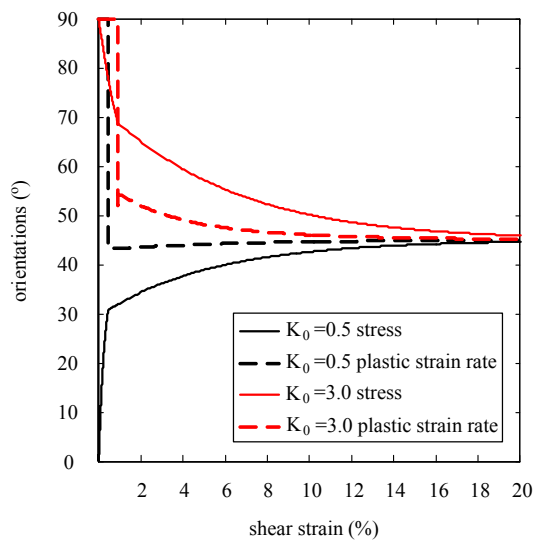


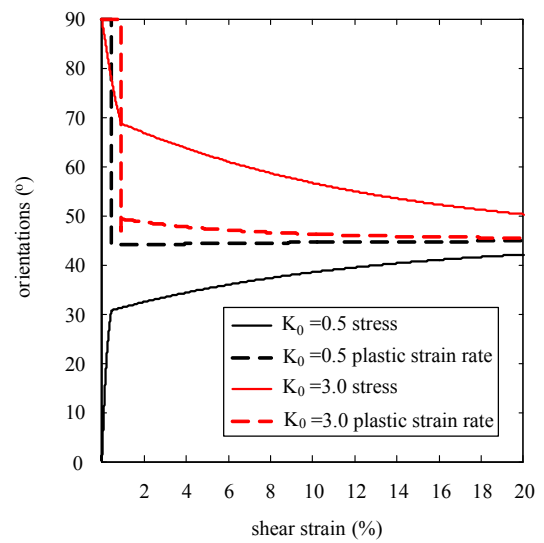
Figure 5 Numerical results of principal orientations of stress and plastic strain increment in Test 15 : a) $k = 0.0$; b) $k = 0.02$; c) $k = 0.05$.



a)



b)



c)

Figure 6 Numerical results of principal orientations of stress and plastic strain increment in Test 16: a) $k = 0.0$; b) $k = 0.02$; c) $k = 0.05$.

sions can be drawn that non-coaxiality is pronounced at the initial stage of the shear stress level and decreases with the increase in the shear strain when the non-coaxial coefficient k is not equal to zero. It should be noted here that due to the convergence problem the substeps for the elastic part are given as 120. As a result, there would be some fluctuations at the very beginning loading stage (e.g. Figures 5 b and c). The degree of non-coaxiality demonstrates an increase with larger values of the non-coaxial coefficient k . However, the eccentric ellipse yield surface can ideally model the coaxiality of the direction of the principal stress and principal plastic strain increment when using the associativity in the conventional plastic flow rule as shown in Figure 5 a. Recalling that there is no change in shear stress for over-consolidated soil with different values of the non-coaxial coefficient k as shown in Figure 4 a, negligible non-coincidence should thus be expected. This is evident from Figure 5. The directions of the principal stress and principal plastic strain rate that are represented by red lines are almost coincident, irrespective of values of the non-coaxial coefficient k .

A.2 Strip footings

A.2.1 Calculations of m for Rotational ellipse

The yield function:

$$F(p, \Theta) = (p + c \cot \phi_{max}) \cdot \sin \phi(\Theta) \quad (10)$$

where

$$\sin \phi(\Theta) = \frac{n \sin \phi_{max}}{\sqrt{n^2 \cos^2(2\Theta - 2\beta) + \sin^2(2\Theta - 2\beta)}} \quad (11)$$

$$\sin 2m = \frac{D}{\sqrt{C^2 + D^2}} \quad (12)$$

$$\cos 2m = \frac{C}{\sqrt{C^2 + D^2}} \quad (13)$$

where,

$$C = 2(n^2 - 1) \cos^2(2\Theta - 2\beta) + 2 \quad (14)$$

$$D = (1 - n^2)\sin(4\Theta - 4\beta) \quad (15)$$

so,

$$D = (1 - n^2)\sin(4\Theta - 4\beta) \quad (16)$$

$$\sin 2(m + \nu) = \sin(2m)\cos(2\nu) + \cos(2m)\sin(2\nu) \quad (17)$$

$$\frac{2\sin\phi(\Theta)}{\sin 2(m + \nu)} = \frac{2\sqrt{2}\sin\phi_{max}(C^2 + D^2)}{\sqrt{2n\sin\phi_{max}DC + \sqrt{C^5 + D^2C^3 - 2C^4(n\sin\phi_{max})^2}}} \quad (18)$$

A.2.2 Calculations of m for Eccentric ellipse

The yield function:

$$F(p, \Theta) = (p + c\cot\phi_{max}) \cdot \sin\phi(\Theta) \quad (19)$$

where

$$\sin\phi(\Theta) = \frac{(B + Q)}{2A} \quad (20)$$

and,

$$E_1 = \sin(\phi_{max}) + \sin(\phi_{\Omega}) \quad (21)$$

$$E_1 = \sin(\phi_{max}) - \sin(\phi_{\Omega}) \quad (22)$$

$$A = n^2\cos^2(2\Theta) + \sin^2(2\Theta) \quad (23)$$

$$B = n^2E_2\cos(2\Theta) \quad (24)$$

$$C = n^4E_1^2\cos^2(2\Theta) \quad (25)$$

$$D = n^2(E_1^2 - E_2^2)\sin^2(2\Theta) \quad (26)$$

$$Q = \sqrt{(C+D)} \quad (27)$$

where

$$\tan(2m) = \frac{1}{2F} \frac{\partial F}{\partial \Theta} \quad (28)$$

$$\left(\frac{(B+Q)}{2A}\right)' = \frac{(B'+Q')A - (B+Q)A'}{2A^2} \quad (29)$$

and,

$$A' = 2(1 - n^2)\sin(4\Theta) \quad (30)$$

$$B' = -2n^2E_2\sin(2\Theta) \quad (31)$$

$$C' = -4n^4E_1^2\cos(2\Theta)\sin(2\Theta) = -2n^4E_1^2\sin(4\Theta) \quad (32)$$

$$D' = 2n^2(E_1^2 - E_2^2)\sin(4\Theta) \quad (33)$$

$$Q' = (C+D)'/2Q \quad (34)$$

so,

$$\tan(2m) = \frac{(B'+Q')A - (B+Q)A'}{2A(B+Q)} \quad (35)$$

denote:

$$XX = (B'+Q')A - (B+Q)A' \quad (36)$$

$$YY = 2A(B+Q) \quad (37)$$

hence,

$$\sin(2m) = \frac{XX}{\sqrt{XX^2 + YY^2}} \quad (38)$$

$$\cos(2m) = \frac{YY}{\sqrt{XX^2 + YY^2}} \quad (39)$$

A.2.3 Close-form solutions for a rotational ellipse anisotropic Mohr-Coulomb yield criterion

The failure load q_t in this case under the assumption that the limit value of ϕ_{max} is approaching zero, can be obtained as follows:

$$q_t = \lim_{\phi_{max} \rightarrow 0} q_t \quad (40)$$

$$q_t = (1 - \sin\phi(\Theta_2)) \cdot p_2 - c \cot\phi_{max} \cdot \sin\phi(\Theta_2) \quad (41)$$

where $\Theta_2 = 0$.

Hence, for a rotational ellipse Mohr-Coulomb yield criterion:

$$q_t = (1 + \sqrt{\frac{2}{M}} n \sin\phi_{max}) \cdot p_2 + \sqrt{\frac{2}{M}} n c \cos\phi_{max} \quad (42)$$

$$q_t = \lim_{\phi_{max} \rightarrow 0} q_t = \lim_{\phi_{max} \rightarrow 0} p_2 + \sqrt{\frac{2}{M}} n c \quad (43)$$

Substituting for p_2 from Equation 4.29 into Equation 43 gives us:

$$q_t = \lim_{\phi_{max} \rightarrow 0} p_2 + \sqrt{\frac{2}{M}} n c \quad (44)$$

$$\lim_{\phi_{max} \rightarrow 0} p_2 = \lim_{\phi_{max} \rightarrow 0} \left(\frac{q\sqrt{M} \cdot e^{\int_0^{\frac{\pi}{2}} G(\Theta) d\Theta} + \sqrt{2} n c \cos\phi_{max}}{\sqrt{M} - \sqrt{2} n \sin\phi_{max}} + \frac{e^{\int_0^{\frac{\pi}{2}} G(\Theta) d\Theta} - 1 + \sqrt{M} c \cos\phi_{max}}{(\sqrt{M} - \sqrt{2} \sin\phi_{max}) \sin\phi_{max}} \right) \quad (45)$$

The subsequent derivation for $G(\Theta)$ when $\nu = \frac{\pi}{4}$ is:

$$G(\Theta) = \frac{2\sqrt{2} n \sqrt{C^2 + D^2}}{3^{1/2} \sqrt{C}} \quad (46)$$

where:

$$C = 2[(1 - n^2)\sin^2(2\Theta - 2\beta) + n^2] \quad (47)$$

$$D = (n^2 - 1)\sin(4\Theta - 4\beta) \quad (48)$$

The Equation 45 can be solved using *L'Hospital's* rule by assuming that:

$$\lim_{\phi_{max} \rightarrow 0} p_2 = qe^{\int_0^{\frac{\pi}{2}} G(\Theta)d\Theta} + (e^{\int_0^{\frac{\pi}{2}} G(\Theta)d\Theta})'c + \sqrt{\frac{2}{M}}nc \quad (49)$$

By solving Equation 49, the ultimate failure load can be obtained as:

$$q_t = q + 2nc\sqrt{\frac{2}{M}} + 2\sqrt{2}nc \int_0^{\frac{\pi}{2}} \frac{\sqrt{C^2 + D^2}}{\sqrt[3]{2}C} d\Theta \quad (50)$$

In Equation 50, q refers to surface surcharge. The most simple case $q = 0$ is taken (i.e. no surface loading is accounted for in the equation).

Booker and Davis (1972) and Yu (2006) provided a general solution of the ultimate failure load of a smooth strip footing in purely cohesive soil mass without surface surcharge and modelled on a general anisotropic yield surface. The authors suggested that the ultimate bearing capacity could be simply expressed as follows:

$$q_t = \overline{PQ} + S \quad (51)$$

where S is the minimum arc length between points P and Q (see Figure 4.2 b).

As indicated in Figure 4.2 b, the two components of q_t can be calculated geometrically. The length of S equals to half the circumference of the ellipse, and the expression for \overline{PQ} is given as:

$$\overline{PQ} = R_1 + R_2 \quad (52)$$

When a rotational ellipse yield criterion is taken into consideration, the definitions of R_1 and R_2 are shown as:

$$R_1 = \frac{n\sin\phi_{max}(p_1 + ccot\phi_{max})}{\sqrt{n^2\cos^2(2\beta) + \sin^2(2\beta)}}, \quad \Theta = \frac{\pi}{2} \quad (53)$$

$$R_2 = \frac{n \sin \phi_{max} (p_2 + c \cot \phi_{max})}{\sqrt{n^2 \cos^2(2\beta) + \sin^2(2\beta)}}, \quad \Theta = 0 \quad (54)$$

If the limit value of ϕ_{max} approaches zero, then:

$$R_{1\phi_{max} \rightarrow 0} = \sqrt{\frac{2}{M}} nc \quad (55)$$

$$R_{2\phi_{max} \rightarrow 0} = \sqrt{\frac{2}{M}} nc \cdot e^{\int_0^{\frac{\pi}{2}} G(\Theta) d\Theta} = \sqrt{\frac{2}{M}} nc \quad (56)$$

Then the expression of \overline{PQ} is:

$$\overline{PQ} = 2nc \sqrt{\frac{2}{M}} \quad (57)$$

The length of S can be calculated by the integration method of a series of parametric equations:

$$S = 2\sqrt{2}nc \int_0^{\frac{\pi}{2}} \frac{\sqrt{C^2 + D^2}}{\sqrt[3]{C}} d\Theta \quad (58)$$

By comparing Equation 50, Equations 57 and 58, it is obvious that the two equations are equal when no subsurface surcharge is applied.

In addition, it is generally acknowledged that the half circumference of an ellipse L is:

$$L = \pi b + 2(a - b) \quad (59)$$

where a is the length of the major axis and b is the length of the minor axis.

In summary, the close-form solution for the ultimate failure force for a smooth strip footing in a purely cohesive soil mass can be obtained as:

$$q_t = \pi nc + 2(1 - n)c + 2nc \sqrt{\frac{2}{M}} \quad (60)$$

A.2.4 Semi-analytical solutions for an eccentric ellipse anisotropic Mohr-Coulomb yield criterion

For an eccentric ellipse anisotropic Mohr-Coulomb yield criterion, recalling that the definition of $\sin \phi_{\Theta}$ corresponding to the eccentric anisotropic Mohr-Coulomb yield

criterion is presented as:

$$\begin{aligned} \sin\phi(\Theta) &= \frac{n^2 \cdot (\sin\phi_{max} - \sin\phi_{\Omega}) \cdot \cos 2\Theta}{2n^2 \cdot \cos^2(2\Theta) + 2 \cdot \sin^2(2\Theta)} \\ &+ \frac{(n^4 \cdot (\sin\phi_{max} + \sin\phi_{\Omega})^2 \cdot \cos^2(2\Theta) + 4n^4 \cdot \sin^2(2\Theta) \cdot \sin\phi_{max} \cdot \sin\phi_{\Omega})^{\frac{1}{2}}}{2n^2 \cdot \cos^2(2\Theta) + 2 \cdot \sin^2(2\Theta)} \end{aligned} \quad (61)$$

Then the vertical pressure at plastic collapse is shown as:

$$q_t = \frac{(1 + \sin\phi_{max}) \cdot e^{\int_0^{\frac{\pi}{2}} \frac{2\sin\phi_{max}}{\sin 2(m+\nu)} d\Theta}}{1 - \sin\phi_{\Omega}} \cdot (q + ccot\phi_{max}) - ccot\phi_{max} \quad (62)$$

The bearing capacity factor N_q is:

$$N_q = \frac{1 + \sin\phi_{max}}{1 - \sin\phi_{\Omega}} \cdot e^{\int_0^{\frac{\pi}{2}} \frac{2\sin\phi_{max}}{\sin 2(m+\nu)} d\Theta} \quad (63)$$

while the bearing capacity factor N_c is presented as:

$$N_c = (N_q - 1)cot\phi_{max} \quad (64)$$

This time Prandtl's solution can be retrieved if $n = 1.0$ and $\sin\phi_{max} = \sin\phi_{\Omega}$.

A.2.5 Close form solutions for a purely cohesive soil with the eccentric ellipse yield criterion

substituting for $\Theta = \frac{\pi}{2}$ into Equation 61 gives us:

$$R_1 = (p_1 + ccot\phi_{max}) \cdot \sin\phi_{\Omega} \quad (65)$$

and substituting for $\Theta = 0^\circ$ into Equation 61 gives us:

$$R_2 = (p_2 + ccot\phi_{max}) \cdot \sin\phi_{max} \quad (66)$$

Likewise, if the limit value of ϕ_{max} approaches zero, then *L'Hospital's* rule can be used to solve Equations 65 and 66:

$$(R_1 + R_2)_{\phi_{max} \rightarrow 0} = 2c \quad (67)$$

In addition, the half circumference of an ellipse L is:

$$L = \pi b + 2(a - b) \quad (68)$$

where,

$$a = \frac{1}{2}(p + c \cot \phi_{max})(\sin \phi_{max} + \sin \phi_{\Omega}) \quad (69)$$

$$b = na \quad (70)$$

Hence, the close-form solution for the ultimate failure force for a smooth strip footing in a purely cohesive soil mass can be obtained as:

$$q_t = (\pi - 2)nc + 4c \quad (71)$$

Likewise, for a special case of an anisotropic Tresca model with $\phi = 0$, the solution can be expressed by the same well-known form as shown in Equation 4.47 if the anisotropic yield criterion reduces to the existing isotropic Mohr-Coulomb yield criterion.

A.2.6 Parametric study

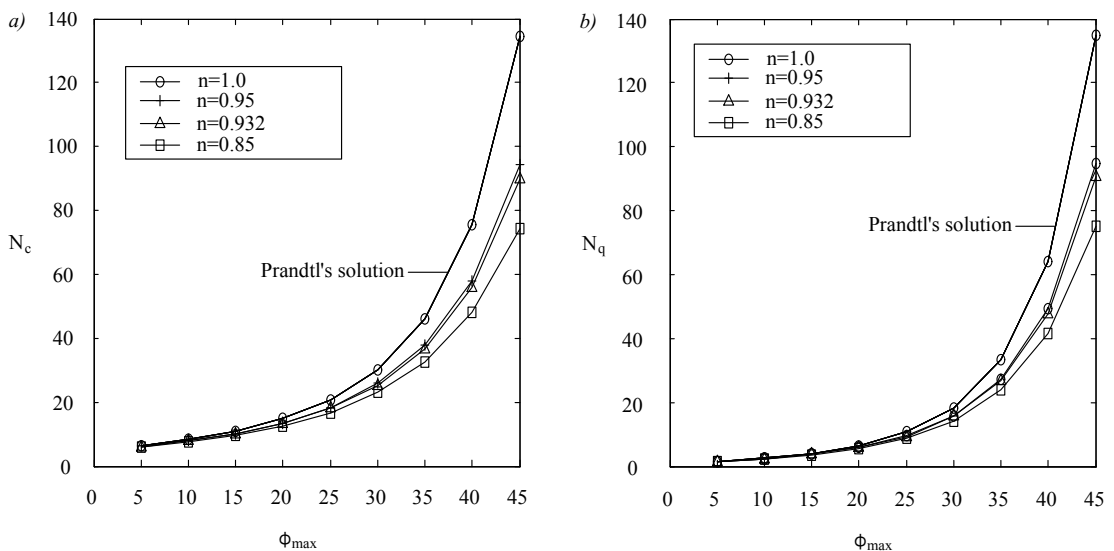


Figure 7 The bearing capacity factors versus friction angle ϕ_{max} with different values of n (eccentric ellipse): a) N_c ; b) N_q .

The bearing capacity factors N_c and N_q versus different values of the maximum peak

internal friction angle (ϕ_{max}) obtained from an eccentric ellipse are shown in Figure 7. Various values of the anisotropic coefficient n are evaluated for the parametric study of bearing capacity factors. Prandtl's solution is recovered when $n = 1.0$ and $\sin\phi_{max} = \sin\phi_{\Omega}$. For cases when n is not equal to zero, $\sin\phi_{\Omega}$ is assumed to be $\sin\phi_{\Omega} = \arcsin(0.95\sin\phi_{max})$. Similar conclusions can be drawn since the numerical results of two bearing capacity factors are lower when soil anisotropy is involved as compared to those obtained from Prandtl's solution. These two factors show a reduction with a decrease in the anisotropic coefficient n .

A.2.7 Validation of numerical results and analytical results

Table 2 Cases of simulations for eccentric ellipse

Cases	The maximum friction angle	The friction angle	Anisotropic coefficient
	$\phi_{max}(\circ)$	$\phi_{\Omega}(\circ)$	n
Test 6	(40, 35, 30, 25, 20, 15, 10, 5)	(40, 35, 30, 25, 20, 15, 10, 5)	1.0
Test 7	(40, 35, 30, 25, 20, 15, 10, 5)	(33, 29, 25, 21, 17, 12.5, 8.5, 4.2)	0.932

Note: coefficient of earth pressure at rest $K_0 = 0.5$ and the associativity in the conventional plastic flow rule is used

Figure 8 illustrates results obtained when an eccentric ellipse yield curve is taken into consideration. Figure 8 a reduces to the isotropic Mohr-Coulomb yield condition when $n = 1.0$. The anisotropic coefficient n and friction angle ϕ_{Ω} have been detailed in Table 2. The maximum friction angle ϕ_{max} is varied from 0° to 40° , and the results from numerical simulations and those from semi-analytical solutions are close for these values.

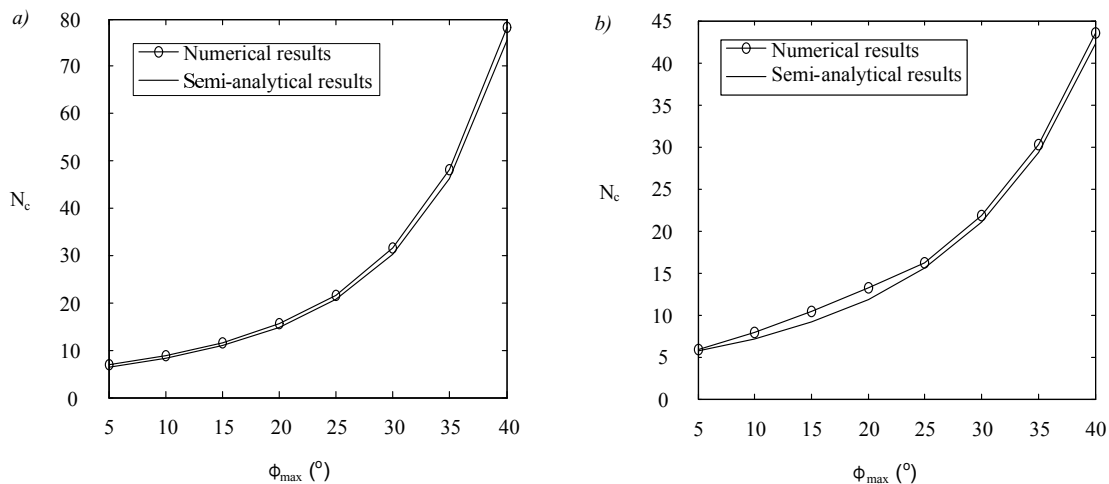


Figure 8 Bearing capacity factor N_c versus various friction angles: a) Test 6; b) Test 7.

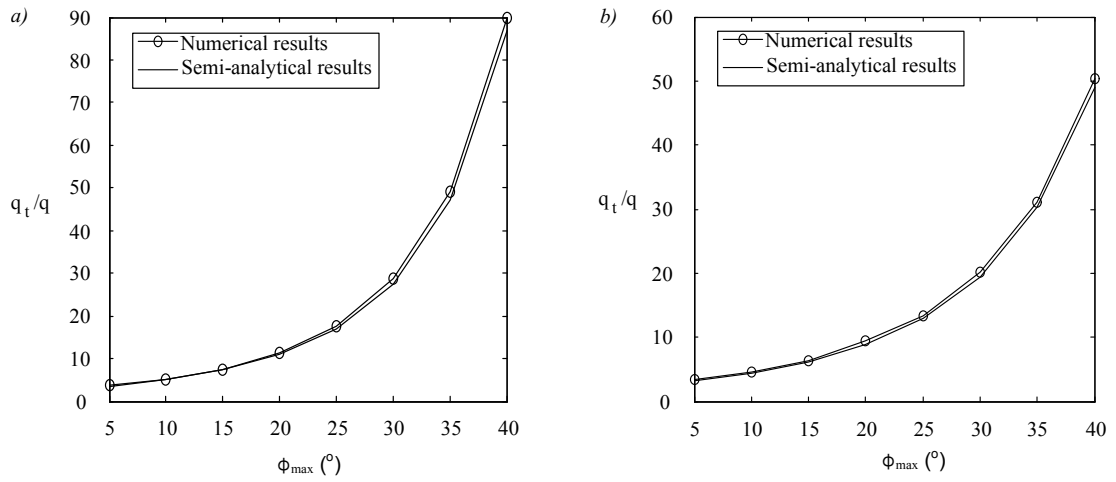


Figure 9 Ultimate failure pressure normalised by surface surcharge (q_t/q) versus various friction angles: a) Test 6; b) Test 7.

Figure 9 shows the results from the eccentric ellipse yield criterion in Test 7 in Table 2. It should be noted that Prandtl's solution can only be recovered when $n = 1.0$ and $\sin\phi_{max} = \sin\phi_{\Omega}$. It seems that the numerical results are slightly closer to the semi-analytical results in this case than those obtained from assuming a rotational ellipse yield criterion.

A.2.8 pressure-displacement curve

Figures 10 - 15 presents the pressure-displacement relationship for the computation of N_c and N_q regarding a rotational ellipse yield criterion.

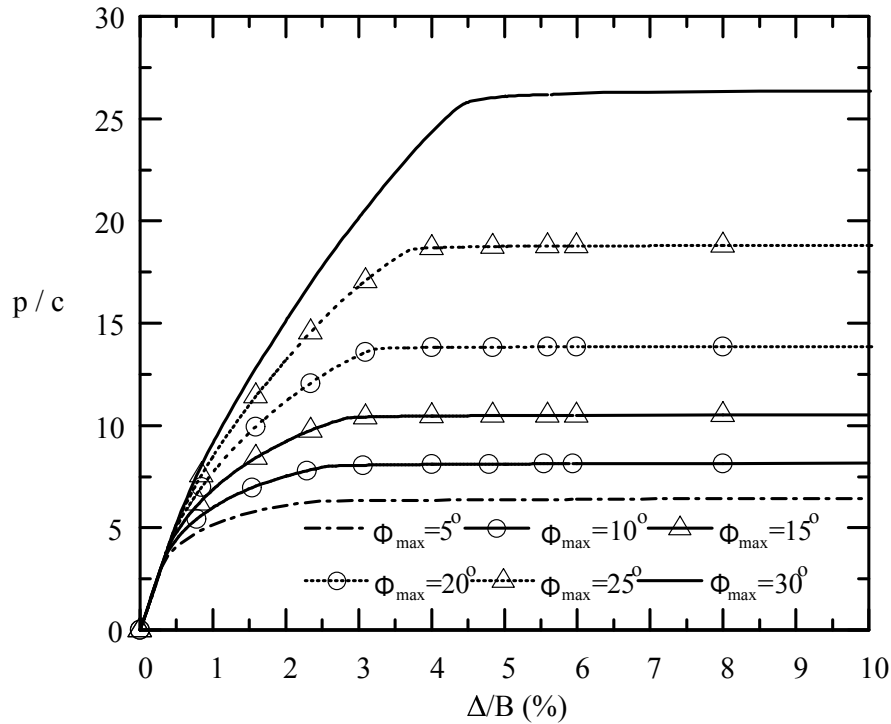


Figure 10 Load displacement curve of bearing capacity factor N_c in Test 2.

Figures 16 and 17 indicates the pressure-displacement relationship for the computation of N_c and N_q regarding an eccentric ellipse yield criterion and $n = 0.932$ respectively.

A.2.9 velocity field

Figure 18 shows the velocity field for the non-coaxial model with an eccentric ellipse anisotropic yield criterion.

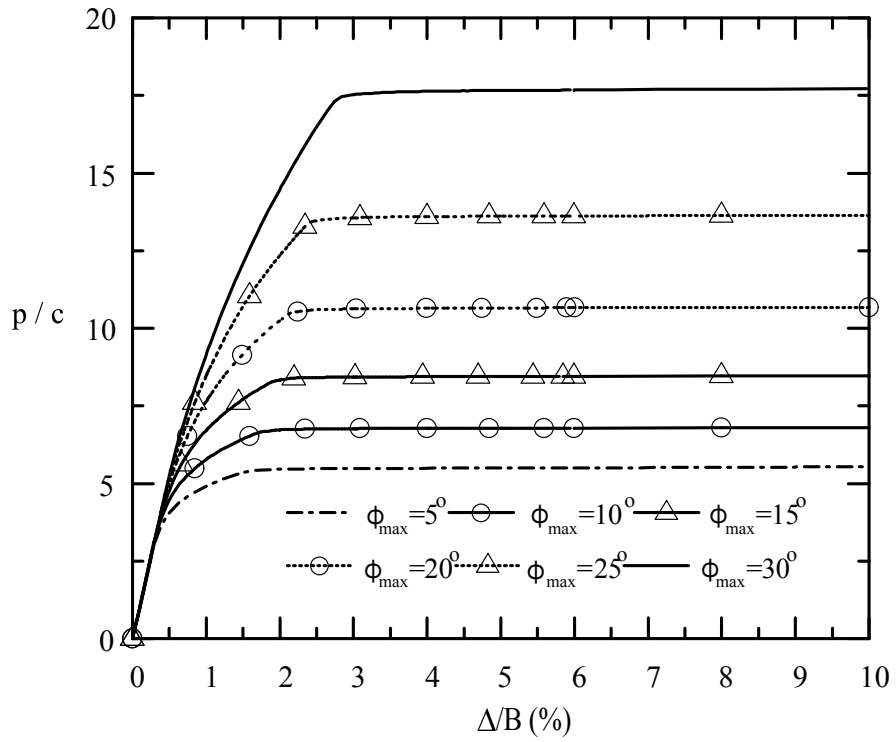


Figure 11 Load displacement curve of bearing capacity factor N_c in Test 4.

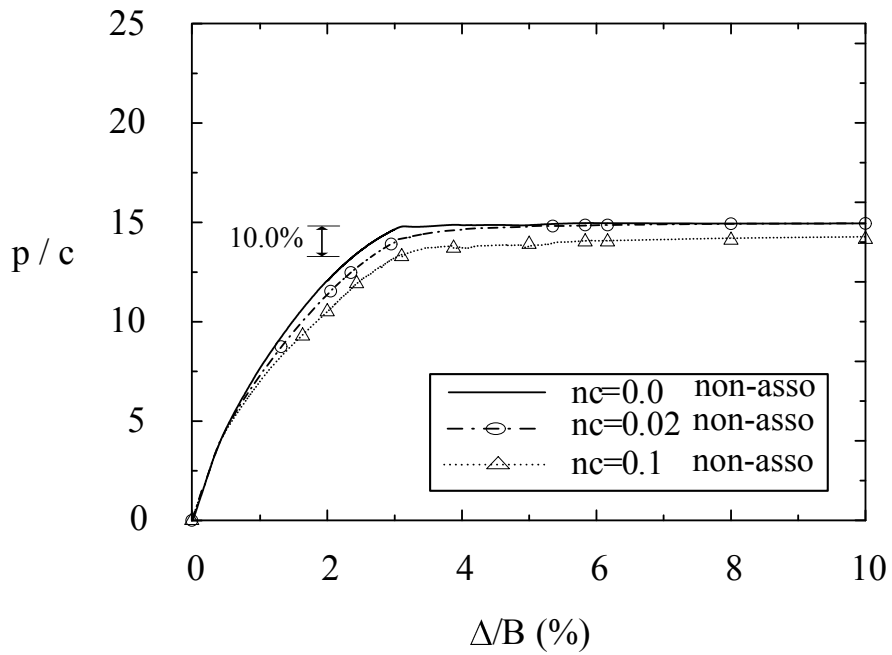


Figure 12 Load displacement curve of bearing capacity factor N_c in Test 5.

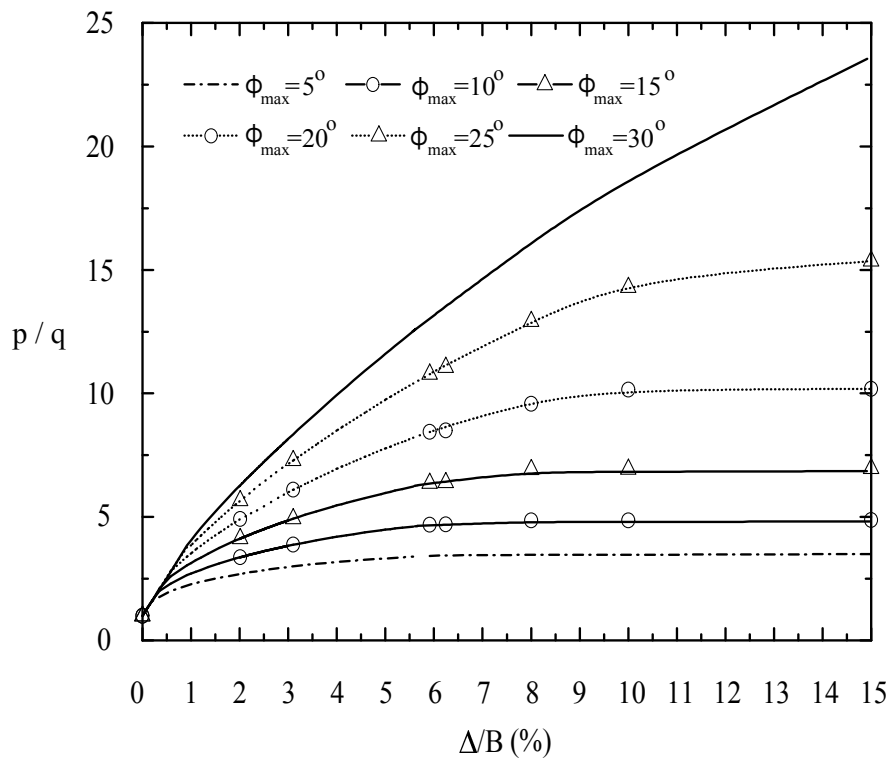


Figure 13 Load displacement curve of ultimate failure force normalised by surface surcharge q_t/q in Test 2.

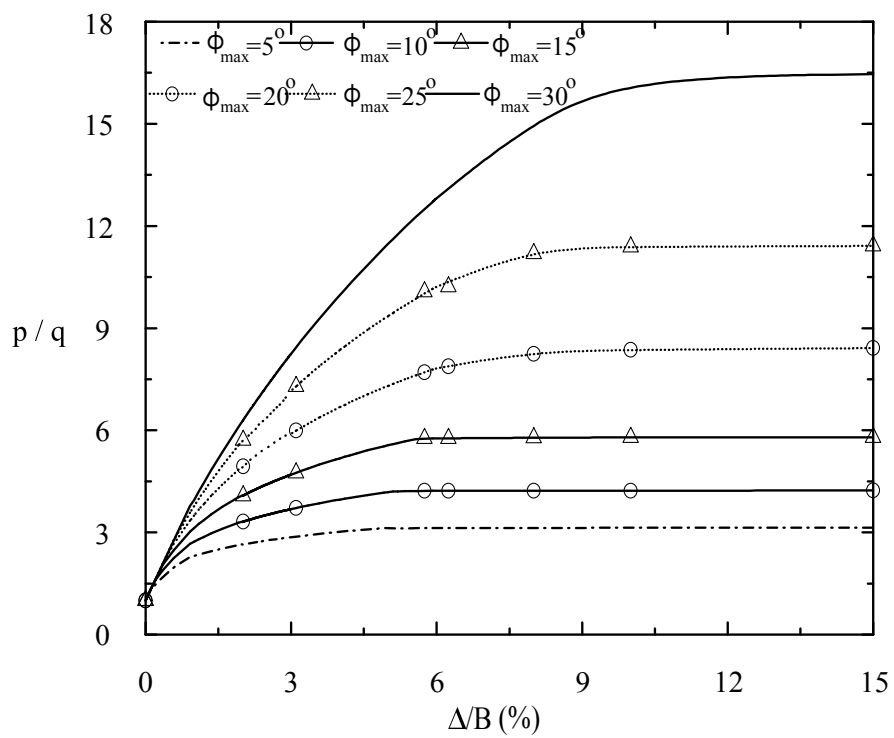


Figure 14 Load displacement curve of ultimate failure force normalised by surface surcharge q_t/q in Test 4.

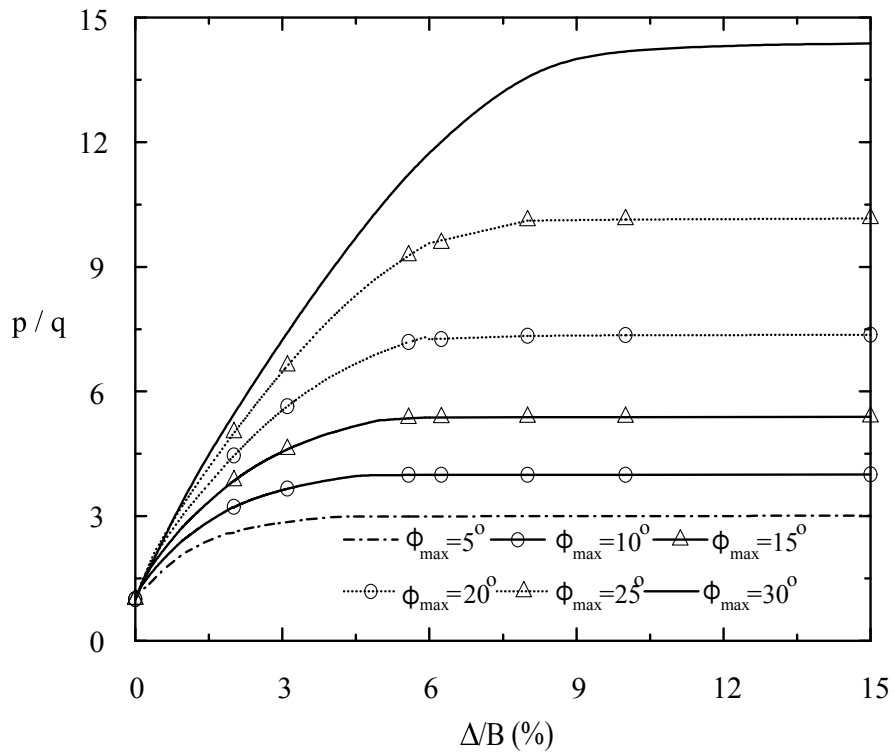


Figure 15 Load displacement curve of ultimate failure force normalised by surface surcharge q_t/q in Test 5.

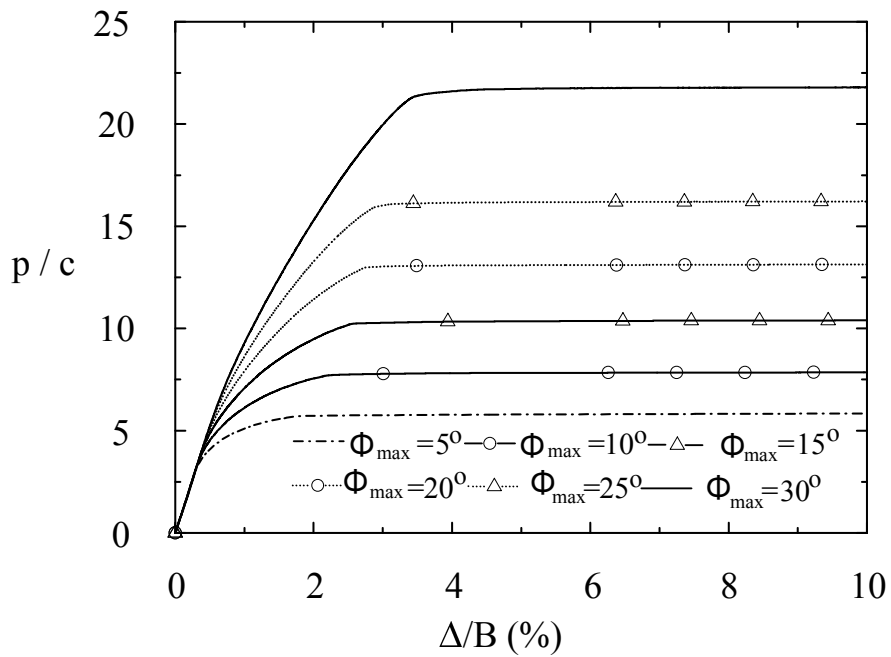


Figure 16 Load displacement curve of bearing capacity factor N_c in Test 7.

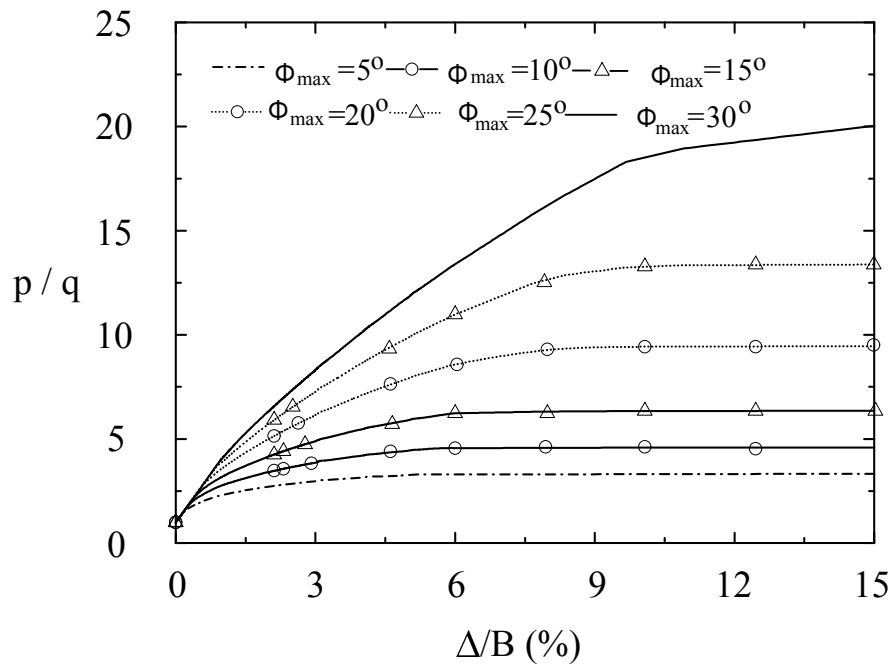


Figure 17 Load displacement curve of ultimate failure pressure normalised by surface surcharge q_t/q in Test 7.

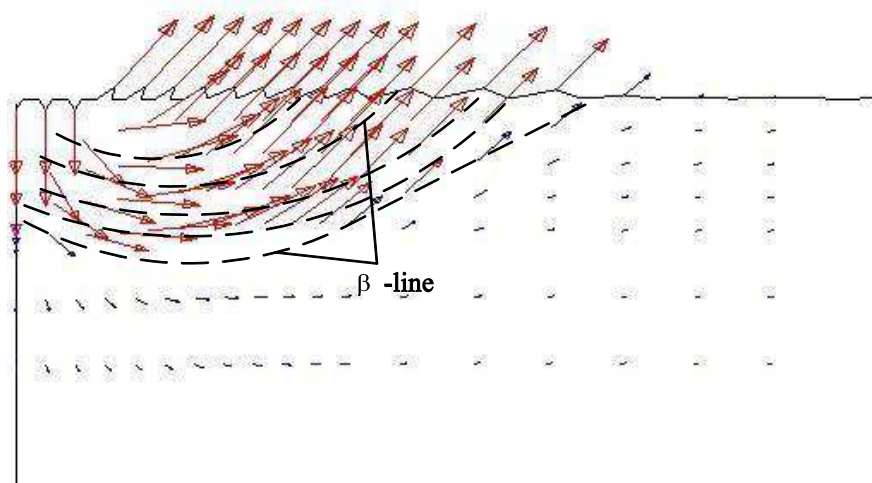


Figure 18 The velocity field for the case of eccentric ellipse Mohr-Coulomb yield criterion when $n = 0.932$.

References

- Abbo, A. J. (1997), Finite element algorithms for elastoplasticity and consolidation, PhD thesis, University of Newcastle, England.
- Abelev, A. V. and Lade, P. V. (2003), 'Effects of cross anisotropy on three-dimensional behavior of sand. i: Stress-strain behavior and shear banding', *Journal of engineering mechanics* **129**(2), 160–166.
- Addenbrooke, T. I. and Potts, D. M. (2001), 'Twin tunnel interaction: surface and subsurface effects', *International Journal of Geomechanics* **1**(2), 249–271.
- Ai, J., Langston, P. A. and Yu, H. S. (2014), 'Discrete element modelling of material non-coaxiality in simple shear flows', *International Journal for Numerical and Analytical Methods in Geomechanics* **38**(6), 615–635.
- Airey, D. W., Budhu, M. and Wood, D. M. (1985), *Some aspects of the behaviour of soils in simple shear*, Elsevier Applied Science Publishers.
- Amerasinghe, S. F. and Parry, R. H. (1975), 'Anisotropy in heavily overconsolidated kaolin', *Journal of Geotechnical and Geoenvironmental Engineering* **101**(12), 1277–1293.
- Anandarajah, A. and Dafalias, Y. F. (1986), 'Bounding surface plasticity. iii: Application to anisotropic cohesive soils', *Journal of engineering mechanics* **112**(12), 1292–1318.
- Arthur, J. R. F., Chua, K. S. and Dunstan, T. (1977), 'Induced anisotropy in a sand', *Géotechnique* **27**(1), 13–30.
- Arthur, J. R. F., del C., R., I, J., Dunstan, T. and Chua, K. S. (1980), 'Principal stress rotation: a missing parameter', *Journal of the Geotechnical Engineering Division* **106**(4), 419–433.
- Arthur, J. R. F. and Menzies, B. K. (1972), 'Inherent anisotropy in a sand', *Geotechnique* **22**(1), 115–128.
- Attewell, P. B., Yeates, J. and Selby, A. R. (1986), *Soil movements induced by tun-*

- nelling and their effects on pipelines and structures*, Blackie and Son, London.
- Baker, W. H. and Krizek, R. J. (1970), 'Mohr-coulomb strength theory for anisotropic soils', *Journal of Soil Mechanics and Foundations Division* **96**(SM1), 269–292.
- Bardet, J. P. (1991), 'Orientation of shear bands in frictional soils', *Journal of engineering mechanics* **117**(7), 1466–1485.
- Bishop, A. W. (1966), 'The strength of soils as engineering materials', *Geotechnique* **16**(2), 91–128.
- Bishop, J. F. W. (1953), 'On the complete solution to problems of deformation of a plastic-rigid material', *Journal of the Mechanics and Physics of Solids* **2**(1), 43–53.
- Bjerrum, L. and Landva, A. (1966), 'Direct simple shear tests on a norwegian quick clay', *Géotechnique* **16**(1), 1–20.
- Booker, J. R. and Davis, E. H. (1972), 'A general treatment of plastic anisotropy under conditions of plane strain', *Journal of the Mechanics and Physics of Solids* **20**(4), 239–250.
- Brewer, R. (1964), 'Fabric and mineral analysis of soils', *John Wiley and Sons, Inc* pp. 129–158.
- Budhu, M. (1984), 'Nonuniformities imposed by simple shear apparatus', *Canadian Geotechnical Journal* **21**(1), 125–137.
- Budhu, M. and Britto, A. (1987), 'Numerical analysis of soils in simple shear devices', *Soils and Foundations* **27**(2), 31–41.
- Butterfield, R. and Harkness, R. (1972), 'The kinematics of mohr-coulomb materials', *Stress Strain Behaviour of Soils* pp. 220–233.
- Cai, Y. Y. (2010), An experimental study of non-coaxial soil behaviour using hollow cylinder testing, PhD thesis, University of Nottingham.
- Cambou, B. (1993), 'From global to local variables in granular materials', *Powders and grains* **93**, 73–86.
- Cambou, B., Chaze, M. and Dedecker, F. (2000), 'Change of scale in granular materials', *European Journal of Mechanics-A/Solids* **19**(6), 999–1014.
- Casagrande, A. and Carillo, N. (1944), 'Shear failure of anisotropic materials', *Journal of Boston Society of Civil Engineers* **31**(4), 74–81.
- Chen, W. F. (1975), *Limit analysis and soil plasticity*, Elsevier, Amsterdam.
- Christoffersen, J., Mehrabadi, M. M. and Nemat-Nasser, S. (1981), 'A micromechan-

- ical description of granular material behavior', *Journal of Applied Mechanics* **48**(2), 339–344.
- Clough, G. W. and Schmidt, B. (1981), 'Excavation and tunnelling', *Soft clay engineering* (13).
- Craig, R. N. and Muirwood, A. M. (1978), A review of tunnel lining practice in the united kingdom, Technical report.
- Cundall, P. A. and Strack, O. D. L. (1979), 'A discrete numerical model for granular assemblies', *Geotechnique* **29**(1), 47–65.
- Davis, E. H. (1968), 'Theories of plasticity and the failure of soil masses', *Soil mechanics: Selected topics* pp. 341–380.
- Davis, E. H. and Christian, J. T. (1971), 'Bearing capacity of anisotropic cohesive soil', *Journal of the Soil Mechanics and Foundations Division* **97**(5), 753–769.
- De Josselin de Jong, G. (1971), 'The double sliding, free rotating model for granular assemblies', *Geotechnique* **21**(2), 155–163.
- Dolezalova, M. (2002), Approaches to numerical modelling of ground movements due to shallow tunnelling, in 'Planning and Engineering for the Cities of Tomorrow. Second International Conference on Soil Structure Interaction in Urban Civil Engineering', pp. 365–373.
- Drescher, A. (1976), 'An experimental investigation of flow rules for granular materials using optically sensitive glass particles', *Géotechnique* **26**(4), 591–601.
- Drescher, A. and De Josselin de Jong, G. (1972), 'Photoelastic verification of a mechanical model for the flow of a granular material', *Journal of the Mechanics and Physics of Solids* **20**(5), 337–340.
- Duncan, J. M. and Seed, H. B. (1966), 'Strength variation along failure surfaces in clay', *Journal of Soil Mechanics and Foundations Division* **92**(6), 81–104.
- Fei, K. and Zhang, J.-M. (2009), *Application of ABAQUS in Geotechnical Engineering*, Chinese Hydraulic and Hydro-electric.
- Fleck, H. and Sklivanos, S. (1978), 'Statische berechnung gebetteter hohlraumaussteifungen (auskleidung) bei berücksichtigung einer tangentialen bettungsmodulwirkung und vergleich mit ergebnissen nach der kontinuumstheorie', *Forschung im Ingenieurwesen A* **44**(4), 101–111.
- Franzius, J. N., Potts, D. M. and Burland, J. B. (2005), 'The influence of soil anisotropy and k_0 on ground surface movements resulting from tunnel excava-

- tion', *Géotechnique* **55**(3), 189–199.
- Grant, R. J. and Taylor, R. N. (2000), 'Tunnelling-induced ground movements in clay', *Proceedings of the ICE-Geotechnical Engineering* **143**(1), 43–55.
- Guedes, P. F. M. and Santos Pereira, C. (2000), The role of the soil k_0 value in numerical analysis of shallow tunnels, in 'of: Proc. of the International Symposium on Geotechnical Aspects of Underground Construction in Soft Ground', pp. 379–384.
- Gunn, M. J. (1993), The prediction of surface settlement profiles due to tunnelling, in 'Predictive Soil Mechanics. Proceedings of The Worth Memorial Symposium', ST Catherine's College, Oxford, pp. 27–29.
- Gutierrez, M., Ishihara, K. and Towhata, I. (1991), 'Flow theory for sand during rotation of principal stress direction', *Soils and Foundations* **31**(4), 121–132.
- Hansen, B. (1961), Shear box test on sand, in '5th Int. Conf. Soil Mech, Paris', Vol. 1, pp. 127–131.
- Harris, D. (1993), 'Constitutive equations for planar deformations of rigid-plastic materials', *Journal of the Mechanics and Physics of Solids* **41**(9), 1515–1531.
- Harris, D. (1995), 'A unified formulation for plasticity models of granular and other materials', *Proceedings of the Royal Society of London. Series A: Mathematical and Physical Sciences* **450**(1938), 37–49.
- Hashiguchi, K. (1977), 'Isotropic hardening theory of granular media', *Proc. JSCE* **227**, 45–60.
- Hashiguchi, K. (1979), Constitutive equations of granular media with an anisotropic hardening, in 'Proc. 3rd Int. Conf. Numer. Meth. Geomech., Aachen. AA Balkema, Rotterdam', pp. 438–439.
- Hashiguchi, K. and Tsutsumi, S. (2001), 'Elastoplastic constitutive equation with tangential stress rate effect', *International Journal of Plasticity* **17**(1), 117–145.
- Hashiguchi, K. and Tsutsumi, S. (2003), 'Shear band formation analysis in soils by the subloading surface model with tangential stress rate effect', *International Journal of Plasticity* **19**(10), 1651–1677.
- Hewett, B. H. M., Johannesson, S., Schürholz, R. and Apel, F. (1964), *Schild-und Druckluft-Tunnelbau*, Werner.
- Hight, D. W., Gens, A. and Symes, M. J. (1983), 'The development of a new hollow cylinder apparatus for investigating the effects of principal stress rotation in

- soils', *Géotechnique* **33**(4).
- Hill, R. (1950), *The mathematical theory of plasticity*, Oxford University Press.
- Hill, R. (1951), 'Lxxxviii. on the state of stress in a plastic-rigid body at the yield point', *Philosophical Magazine* **42**(331), 868–875.
- Hu, N. (2015), On Fabric Tensor-based Constitutive Modelling of Granular Materials: Theory and Numerical Implementation, PhD thesis, University of Nottingham, England.
- Jahanandish, M. and Haghghat, A. E. (2004), 'Analysis of boundary value problems in soil plasticity assuming non-coaxiality', *Iranian Journal of Science and Technology* **28**, 583–594.
- Jiang, M. and Yu, H. S. (2006), 'Application of discrete element method to geomechanics', *In Modern Trends in Geomechanics* (106), 241–269.
- Kavvadas, M. J. (1983), A constitutive model for clays based on non-associated anisotropic elasto-plasticity, *in* 'Proceedings of the International Conference on Constitutive Laws for Engineering Materials—Theory and Application. Tucson, Arizona, January', pp. 10–14.
- Kjellman, W. (1951), 'Testing the shear strength of clay in sweden', *Géotechnique* **2**(3), 225–232.
- Ko, H.-Y. and Sture, S. (1981), 'State of the art: Data reduction and application for analytical modeling', *Laboratory Shear Strength of Soil. ASTM STP 740*, 329–386.
- Kowalczyk, K. and Gambin, W. (2004), 'Model of plastic anisotropy evolution with texture-dependent yield surface', *International Journal of Plasticity* **20**(1), 19–54.
- Kumruzzaman, M. D. and Yin, J. H. (2010), 'Influence of principal stress direction on the stress-strain-strength behaviour of completely decomposed granite', *Facta universitatis-series: Architecture and Civil Engineering* **8**(1), 79–97.
- Lade, P. V. (1978), 'Cubic triaxial apparatus for soil testing', *Geotech. Test. J.* **14**(3), 231–246.
- Lade, P. V. and Abelev, A. V. (2003), 'Effects of cross anisotropy on three-dimensional behavior of sand. ii: Volume change behavior and failure', *Journal of engineering mechanics* **129**(2), 167–174.
- Lade, P. V. and Duncan, J. M. (1973), 'Cubic triaxial tests on cohesionless soil', *J. Soil*

- Mech. Found. Div.* **99**(10), 793–812.
- Lade, P. V. and Duncan, J. M. (1975), ‘Elastoplastic stress-strain theory for cohesionless soil’, *Journal of the Geotechnical Engineering Division* **101**(10), 1037–1053.
- Lashkari, A. and Latifi, M. (2008), ‘A non-coaxial constitutive model for sand deformation under rotation of principal stress axes’, *International journal for numerical and analytical methods in geomechanics* **32**(9), 1051–1086.
- Lee, K. M. and Rowe, R. K. (1989), ‘Deformations caused by surface loading and tunnelling: the role of elastic anisotropy’, *Géotechnique* **39**(1), 125–140.
- Lee, K. M. and Rowe, R. K. (1991), ‘An analysis of three-dimensional ground movements: the thunder bay tunnel’, *Canadian Geotechnical Journal* **28**(1), 25–41.
- Li, X. S. and Dafalias, Y. F. (2002), ‘Constitutive modeling of inherently anisotropic sand behavior’, *Journal of Geotechnical and Geoenvironmental Engineering* **128**(10), 868–880.
- Li, X. S. and Dafalias, Y. F. (2004), ‘A constitutive framework for anisotropic sand including non-proportional loading’, *Geotechnique* **54**(1), 41–55.
- Li, X. and Yu, H. S. (2009), ‘Influence of loading direction on the behavior of anisotropic granular materials’, *International Journal of Engineering Science* **47**(11), 1284–1296.
- Li, X. and Yu, H.-S. (2010), ‘Numerical investigation of granular material behaviour under rotational shear’, *Geotechnique* **60**(5), 381–394.
- Lo, K. Y. (1965), ‘Stability of slopes in anisotropic soils’, *Journal of Soil Mechanics and Foundations Division, ASCE* **91**(SM4), 85–106.
- Mair, R. J. and Taylor, R. N. (1997), Theme lecture: Bored tunnelling in the urban environment. 14th int, in ‘Proc., 14th ICSMFE Hamburg’, Vol. 4, pp. 2353–2385.
- Matsuoka, H., Sakakibara, K. and Suzuki, Y. (1988), ‘A constitutive model for sands and clays evaluating principal stress rotation’, *Micromechanics of Granular Materials* pp. 253–261.
- Mehrabadi, M. M. and Cowin, S. C. (1978), ‘Initial planar deformation of dilatant granular materials’, *Journal of the Mechanics and Physics of Solids* **26**(4), 269–284.
- Mitchell, R. (1972), ‘Some deviations from isotropy in a lightly overconsolidated clay’,

- Geotechnique* **22**(3), 459–467.
- Miura, K., Miura, S. and Toki, S. (1986), ‘Deformation behavior of anisotropic dense sand under principal stress axes rotation’, *Soils and Foundations* **26**(1), 36–52.
- Möller, S. (2006), Tunnel induced settlements and structural forces in linings, PhD thesis, Universitat Stuttgart, Mitteilung.
- Ng, T. T. (2004), ‘Macro-and micro-behaviors of granular materials under different sample preparation methods and stress paths’, *International journal of solids and structures* **41**(21), 5871–5884.
- Oda, M. (1972a), ‘Deformation mechanism of sand in triaxial compression tests’, *Soils and Foundations* **12**(4), 45–63.
- Oda, M. (1972b), ‘Initial fabrics and their relations to mechanical properties of granular material’, *Soil and foundation* **12**(1), 17–36.
- Oda, M. (1972c), ‘The mechanism of fabric changes during compressional deformation of sand’, *Soils and foundations* **12**(2), 1–18.
- Oda, M., Koishikawa, I. and Higuchi, T. (1978), ‘Experimental study of anisotropic shear strength of sand by plane strain test’, *Soils and foundations* **18**(1), 25–38.
- Oda, M. and Konishi, J. (1974a), ‘Microscopic deformation mechanism of granular material in simple shear’, *Soils and Foundations* **14**(4), 25–38.
- Oda, M. and Konishi, J. (1974b), ‘Rotation of principal stresses in granular material during simple shear’, *Soils and foundations* **14**(4), 39–53.
- ODA, M., NEMAT-NASSER, S. and KONISHI, J. (1985), ‘Stress-induced anisotropy in granular masses’, *Soils and foundations* **25**(3), 85–97.
- Oettl, G., Stark, R. F. and Hofstetter, G. (1998), ‘A comparison of elastic–plastic soil models for 2d fe analyses of tunnelling’, *Computers and Geotechnics* **23**(1), 19–38.
- Papamichos, E. and Vardoulakis, I. (1995), ‘Shear band formation in sand according to non-coaxial plasticity model’, *Geotechnique* **45**(4), 649–661.
- Parkin, A. K., Gerrard, C. M. and Willoughby, D. R. (1968), ‘Discussion on deformation of sand in shear’, *J. Soil Mech. Found. Div.* **94**(1), 336–340.
- Peck, R. B. (1969), Deep excavations and tunnelling in soft ground, in ‘Proc. 7th Int. Conf. on SMFE’, pp. 225–290.
- Phillips, A. B. and May, P. H. (1967), ‘A form of anisotropy in granular media’, *Special Task Report* .

- Potts, D. M., and Zdravković, L. (2001), *Finite element analysis in geotechnical engineering: application*, Vol. 2, Thomas Telford.
- Potts, D. M. and Gens, A. (1985), 'A critical assessment of methods of correcting for drift from the yield surface in elasto-plastic finite element analysis', *International Journal for Numerical and Analytical Methods in Geomechanics* **9**(2), 149–159.
- Powell, D. B., Sigl, O. and Beveridge, J. P. (1997), Heathrow express—design and performance of platform tunnels at terminal 4, in 'Tunnelling', Vol. 97, pp. 565–593.
- Prager, W. and Drucker, D. C. (1952), 'Soil mechanics and plastic analysis or limit design, 0', *Appi. Math* **10**(2), 157–165.
- Prevost, J.-H. (1978), 'Plasticity theory for soil stress-strain behavior', *Journal of the Engineering Mechanics Division* **104**(5), 1177–1194.
- Qian, J., You, Z. P., Huang, M. S. and Gu, X. Q. (2013), 'A micromechanics-based model for estimating localized failure with effects of fabric anisotropy', *Computers and Geotechnics* **50**, 90–100.
- Reddy, A. S. and Srinivasan, R. J. (1970), 'Bearing capacity of footings on anisotropic soils', *Journal of the Soil Mechanics and Foundations Division* **96**(6), 1967–1986.
- Roscoe, K. H. (1953), An apparatus for the application of simple shear to soil samples, in 'Proceedings of the 3rd international conference on soil mechanics and foundation engineering, Switzerland', Vol. 1, p. 186.
- Roscoe, K. H. (1970), 'The influence of strains in soil mechanics', *Géotechnique* **20**(2), 129–170.
- Roscoe, K. H., Bassett, R. H. and Cole, E. R. L. (1967), Principal axes observed during simple shear of a sand, in 'Proc. Geotech. Conf., Oslo', Vol. 1, pp. 231–237.
- Rowe, R. K., Lo, K. Y. and Kack, G. J. (1983), 'A method of estimating surface settlement above tunnels constructed in soft ground', *Canadian Geotechnical Journal* **20**(1), 11–22.
- Rudnicki, J. W. and Rice, J. R. (1975), 'Conditions for the localization of deformation in pressure-sensitive dilatant materials', *Journal of the Mechanics and Physics of Solids* **23**(6), 371–394.
- Saada, A. S. and Baah, A. K. (1967), 'Deformation and failure of a cross anisotropic

- clay under combined stresses', *In: Proceeding of the Third Pan-American Conference on Soil Mechanics and Foundation Engineering, Caracas* **1**, 67–88.
- Savage, J. C. and Lockner, D. A. (1997), 'A test of the double-shearing model of flow for granular materials', *Journal of Geophysical Research: Solid Earth (1978–2012)* **102**(B6), 12287–12294.
- Sazzad, M. d. M. and Suzuki, K. (2010), 'Micromechanical behavior of granular materials with inherent anisotropy under cyclic loading using 2d dem', *Granular Matter* **12**(6), 597–605.
- Schikora, K. and Ostermeier, B. (1988), Two-dimensional calculation model in tunnelling-verification by measurement results and by spatial calculation, *in* 'Procedures of The Sixth International Conference on Numerical Methods in Geomechanics', Innsbruck, Austria, pp. 1499–1503.
- Sekiguchi, H. and Ohta, K. (1977), Induced anisotropy and time dependency in clays, *in* 'Proceedings of the 9th ICSMFE, Specialty Session 9', pp. 229–238.
- Seyedi, H. E. (2012), 'Discrete element modeling of inherently anisotropic granular assemblies with polygonal particles', *Particuology* **10**(5), 542–552.
- Shield, R. T. (1953), 'Mixed boundary value problems in soil mechanics', *Quarterly of Applied Mathematics* **11**(1), 61–75.
- Simpson, B., Atkinson, J. H. and Jovicic, V. (1996), The influence of anisotropy on calculations of ground settlements above tunnels, *in* 'of: Proc. of the International Symposium on Geotechnical Aspects of Underground Construction in Soft Ground', pp. 591–594.
- Sloan, S. W. (1987), 'Substepping schemes for the numerical integration of elastoplastic stress–strain relations', *International Journal for Numerical Methods in Engineering* **24**(5), 893–911.
- Spencer, A. J. M. (1964), 'A theory of the kinematics of ideal soils under plane strain conditions', *Journal of the Mechanics and Physics of Solids* **12**(5), 337–351.
- Swoboda, G. (1979), Finite element analysis of the new austrian tunnelling method (natm), *in* 'Proceedings of the 3rd International Conference on Numerical Methods in Geomechanics, Aachen', Vol. 2, pp. 581–586.
- Symes, M., Gens, A. and Hight, D. W. (1984), 'Undrained anisotropy and principal stress rotation in saturated sand', *Geotechnique* **34**(1), 11–27.
- Tejchman, J. and Wu, W. (2009), 'Non-coaxiality and stress-dilatancy rule in granu-

- lar materials: Fe investigation within micro-polar hypoplasticity', *International journal for numerical and analytical methods in geomechanics* **33**(1), 117–142.
- Ting, J. M. and Meachum, L. R. (1995), 'Effect of bedding plane orientation on the behavior of granular systems', *Mech. Mater. Discontinuities Heterogeneities* **201**, 43–57.
- Tobita, Y. (1993), 'Modified double slip model for anisotropic hardening behaviour of granular materials', *Mechanics of materials* **16**(1), 91–100.
- Tsutsumi, S. and Hashiguchi, K. (2005), 'General non-proportional loading behavior of soils', *International journal of plasticity* **21**(10), 1941–1969.
- Van Dyck, E. J. (2012), Effects of Principal Stress Direction and the Intermediate Principal Stress on the Stress-Strain-Strength Behavior of a Cross-Anisotropic Fine Sand Deposit, PhD thesis, The Catholic University of America.
- Ward, W. H. and Pender, M. J. (1981), Tunnelling in soft ground: general report, in 'Proceedings of the 10th International Conference on Soil Mechanics and Foundation Engineering, Stockholm', Vol. 4, pp. 261–275.
- Windels, R. (1967), 'Kreisring im elastischen kontinuum', *Der Bauingenieur Bd* **42**, 429.
- Wood, A. M. M. (1975), 'The circular tunnel in elastic ground', *Geotechnique* **25**(1), 115–127.
- Yang, D. S. (2014), Microscopic Study of Granular Material Behaviour under General Stress Paths, PhD thesis, University of Nottingham.
- Yang, L. T. (2013), Experimental study of soil anisotropy using hollow cylinder testing, PhD thesis, University of Nottingham, England.
- Yang, Y., Ooi, J., Rotter, M. and Wang, Y. (2011), 'Numerical analysis of silo behavior using non-coaxial models', *Chemical Engineering Science* **66**(8), 1715–1727.
- Yang, Y. and Yu, H. S. (2006a), 'Application of a non-coaxial soil model in shallow foundations', *Geomechanics and Geoengineering: An International Journal* **1**(2), 139–150.
- Yang, Y. and Yu, H. S. (2006b), 'Numerical simulations of simple shear with non-coaxial soil models', *International journal for numerical and analytical methods in geomechanics* **30**(1), 1–19.
- Yang, Y. and Yu, H. S. (2010a), 'Finite element analysis of anchor plates using non-coaxial models', *Journal of Rock Mechanics and Geotechnical Engineer-*

- ing* **2**(2), 178–187.
- Yang, Y. and Yu, H. S. (2010*b*), ‘Numerical aspects of non-coaxial model implementations’, *Computers and Geotechnics* **37**(1), 93–102.
- Yang, Z. X., Li, X. S. and Yang, J. (2008), ‘Quantifying and modelling fabric anisotropy of granular soils’, *Geotechnique* **58**(4), 237–248.
- Yu, H. S. (1998), ‘Casm: A unified state parameter model for clay and sand’, *International Journal for Numerical and Analytical Methods in Geomechanics* **22**(8), 621–653.
- Yu, H. S. (2006), *Plasticity and Geotechnics*, Springer, USA.
- Yu, H. S. (2008), Non-coaxial theories of plasticity for granular materials, in ‘The 12th international conference of international association for computer methods and advances in geomechanics (IACMAG)’, Goa, India, pp. 361–378.
- Yu, H. S. and Netherton, M. D. (2000), ‘Performance of displacement finite elements for modelling incompressible materials’, *International Journal for Numerical and Analytical Methods in Geomechanics* **24**(7), 627–653.
- Yu, H. S. and Sloan, S. W. (1994), ‘Limit analysis of anisotropic soils using finite elements and linear programming’, *Mechanics Research Communications* **21**, 545–554.
- Yu, H. S. and Yuan, X. (2005), The importance of accounting for non-coaxial behaviour in modelling soil-structure interaction, in G. Barla and M. Barla, eds, ‘IACMG11’, Vol. 4, pp. 545–554.
- Yu, H. S. and Yuan, X. (2006), ‘On a class of non-coaxial plasticity models for granular soils’, *Proceedings of the Royal Society A: Mathematical, Physical and Engineering Science* **462**(2067), 725–748.
- Yuan, X. (2005), Non-coaxial plasticity for granular materials, PhD thesis, University of Nottingham, England.
- Zhang, L. (2003), The behaviour of granular material in pure shear, direct shear and simple shear, PhD thesis, Aston University.
- Zhao, Y. (2008), In situ soil testing for foundation performance prediction, PhD thesis, University of Cambridge.
- Zhou, B. (2015), Tunnelling-Induced Ground Displacements in Sand, PhD thesis, University of Nottingham.
- Zhu, H., Mehrabadi, M. M. and Massoudi, M. (2006*a*), ‘Incorporating the effects of

- fabric in the dilatant double shearing model for planar deformation of granular materials', *International journal of plasticity* **22**(4), 628–653.
- Zhu, H., Mehrabadi, M. M. and Massoudi, M. (2006b), 'Three-dimensional constitutive relations for granular materials based on the dilatant double shearing mechanism and the concept of fabric', *International journal of plasticity* **22**(5), 826–857.
- Zienkiewicz, O. C. and Pande, G. N. (1977), 'Some useful forms of isotropic yield surfaces for soil and rock mechanics', *Finite elements in geomechanics* pp. 179–198.